

WARSAW UNIVERSITY OF TECHNOLOGY

DISCIPLINE OF SCIENCE MECHANICAL ENGINEERING
FIELD OF SCIENCE ENGINEERING AND TECHNICAL SCIENCES

Ph.D. Thesis

Grzegorz Marcin Gruszczyński, M.Sc.

**Applications of the
Lattice Boltzmann Method
to solving
advection-diffusion-reaction problems
coupled with Navier-Stokes equations**

Supervisor

Prof. Jacek Szumbarski, D. Sc. Ph. D.

Additional Supervisor

Łukasz Łaniewski-Wołk, Ph. D.

WARSAW 2023

WARSAW UNIVERSITY OF TECHNOLOGY

DOCTORAL THESIS

Applications of the
Lattice Boltzmann Method
to solving
advection-diffusion-reaction problems
coupled with Navier-Stokes equations

Author:

Grzegorz GRUSZCZYŃSKI

Supervisor:

Prof. dr hab. inż. Jacek
SZUMBARSKI

Additional Supervisor:

Dr Łukasz ŁANIEWSKI-WOŁŁK

*A thesis submitted in fulfillment of the requirements
for the degree of Doctor of Philosophy
in the*

Division of Aerodynamics
Institute of Aeronautics and Applied Mechanics
Faculty of Power and Aeronautical Engineering

May 18, 2023

Declaration of Authorship

I, Grzegorz GRUSZCZYŃSKI, declare that this thesis titled, “Applications of the Lattice Boltzmann Method to solving advection-diffusion-reaction problems coupled with Navier-Stokes equations” and the work presented in it are my own. I confirm that:

- This work was done wholly or mainly while in candidature for a research degree at this University.
- Where I have consulted the published work of others, this is always clearly attributed.
- Where I have quoted from the work of others, the source is always given. With the exception of such quotations, this thesis is entirely my own work.
- I have acknowledged all main sources of help.
- Where the thesis is based on work done by myself jointly with others, I have made clear exactly what was done by others and what I have contributed myself.

Authorship contribution statement according to the Contributor Roles Taxonomy (CRediT) [1, 2].

The doctoral dissertation is based on a series of three publications [3, 4, 5] in which I am the first author. To avoid repetitions and unify the symbols, the common parts (like introduction the lattice Boltzmann method) from [3, 4, 5] have been consolidated. Below, I list the contributions of other authors to the aforementioned publications which implies that they also contributed to this thesis.

- Chapters 2 and 4 are aligned with manuscript [3]:
 - G. Gruszczyński: Writing original draft, Review & Editing, Conceptualization, Methodology, Software, Data curation, Validation, Visualization, Formal analysis, Investigation.
 - Michał Dzikowski: Formal analysis, Conceptualization, Investigation.
 - * Sections 2.4, 4.4.2.1 and 4.4.2.2 Writing, Software, Data curation, Validation, Visualization.

- Ł. Łaniewski-Wołosz: Formal analysis, Investigation.
 - * Table 2.1 and Section 4.4.1: Writing, Software, Data curation, Validation, Visualization.
- Chapter 5:
 - G. Gruszczyński: Writing original draft, Review & Editing, Conceptualization, Methodology, Software, Data curation, Validation, Visualization, Formal analysis, Funding acquisition, Investigation.
 - Ł. Łaniewski-Wołosz
 - * Sections 5.3.3, 5.3.4 and 5.4.1: Conceptualization, Investigation, Formal analysis.
 - Michał Dzikowski: Review.
- Chapter 7:
 - G. Gruszczyński: Writing original draft, Formal analysis.
 - Ł. Łaniewski-Wołosz: Supervision, Conceptualization, Formal analysis.
- Chapter 9 is based on article [4]:
 - G. Gruszczyński: Writing original draft, Review & Editing, Conceptualization, Methodology, Software, Data curation, Validation, Visualization, Formal analysis, Funding acquisition, Investigation.
 - Ł. Łaniewski-Wołosz: Supervision, Formal analysis, Software.
 - Christopher Leonardi: Review & Proofreading.
 - Michał Dzikowski: Review.
- Chapter 11 is based on article [5]:
 - G. Gruszczyński: Writing original draft, Review & Editing, Conceptualization, Methodology, Software, Data curation, Validation, Visualization, Formal analysis, Investigation.
 - Travis Mitchell: Writing - Review & Editing.
 - * Sections 11.3.4 and 11.3.5: Writing, Investigation, Data curation, Conceptualization, Validation, Visualization.

- Christopher Leonardi: Review & Editing, Supervision.
- Ł. Łaniewski-Wołk: Review & Editing, Supervision.
- Tracie Barber: Review & Editing, Supervision.

Signed:

Date:

Declaration of Competing Interest

I, Grzegorz GRUSZCZYŃSKI, declare that I have no known competing financial interests or personal relationships that could have appeared to influence the work reported in this dissertation.

Signed:

Date:

Dissemination

Publications included in this thesis

- 1 G. Gruszczyński *et al.*, “Revisiting the second-order convergence of the lattice boltzmann method with reaction-type source terms,” *arXiv*, 2021 (In review)
- 2 G. Gruszczyński and L. Łaniewski-Wołk, “A comparative study of 3d cumulant and central moments lattice boltzmann schemes with interpolated boundary conditions for the simulation of thermal flows in high prandtl number regime,” *International Journal of Heat and Mass Transfer*, vol. 197, p. 123 259, 2022
- 3 G. Gruszczyński *et al.*, “A cascaded phase-field lattice boltzmann model for the simulation of incompressible, immiscible fluids with high density contrast,” *Computers and Mathematics with Applications*, vol. 79, no. 4, pp. 1049–1071, 2020

Conferences

- 1 “A comparative study of 3D Cumulant and Central Moments lattice Boltzmann schemes with interpolated boundary conditions for the simulation of thermal flows in high Prandtl number regime”, The 18th International Conference for Mesoscopic Methods in Engineering and Science (ICMMES 2022), La Rochelle, France, 28 June - 1 July, 2022.
- 2 “A comparative study of 3D Cumulant and Central Moments lattice Boltzmann schemes with interpolated boundary conditions for the simulation of thermal flows in high Prandtl number regime”, 8th European Congress on Computational Methods in Applied Sciences and Engineering (ECCOMAS 2022), Oslo, Norway, 5 - 9 June, 2022.
- 3 “Templated CUDA Lattice Boltzmann Method: generic CFD solver for single and multi-phase problems”, Supercomputing Frontiers Europe 2020, Online (Warsaw), Poland, 23 - 26 March, 2020

- 4 “On recovering the second-order convergence of the Lattice Boltzmann Method with reaction-type source terms, The 17th International Conference for Mesoscopic Methods in Engineering and Science”, Online (Hammamet), Tunis, 12 - 16 July, 2021.
- 5 “Modelling of immiscible multiphase flows using phase-field, Cascaded Lattice Boltzmann Method”, Helmholtz Zentrum Dresden-Rossendorf, XVI Multiphase Flow Conference & Short Course, Dresden, Germany, 13-16 November, 2018
- 6 “Adjoint Lattice Boltzmann Method for Optimal Control, European Postgraduate Fluid Dynamic Conference”, Warsaw, Poland, 6 - 9 July, 2016

“If the page is empty there are too many choices. And the choices are usually a bit stressful...”

Abstract

[EN] *Keywords: lattice Boltzmann method, computational fluid dynamics, multiphase flows, heat transfer, reactive flows.*

The aim of this work is to present the application of the lattice Boltzmann method to simulate the advection-diffusion-reaction equations. These equations may be viewed as a key building block in computational fluid dynamics modelling. In all cases, the Navier-Stokes equations describing the motion of a fluid are coupled with equation belonging to the advection-diffusion-reaction family to simulate multiphase flow, solidification, dynamics of an epidemic or heat transfer. Although the physical phenomena may appear distant, the mathematical structure of the underlying equations is similar.

[PL] *Słowa kluczowe: gaz siatkowy Boltzmann, numeryczna mechanika płynów, przepływy wielofazowe, wymiana ciepła, modelowanie reakcji.*

Celem pracy jest przedstawienie zastosowania metody gazu siatkowego Boltzmann do symulacji równań adwekcji-dyfuzji-reakcji. Mogą być one postrzegane jako podstawowy element konstrukcyjny w modelowaniu w obliczeniowej mechanice płynów. We wszystkich analizowanych przypadkach równania Naviera-Stokesa opisujące ruch płynu są sprzężone z równaniem należącym do rodziny adwekcji-dyfuzji-reakcji, aby symulować przepływ wielofazowy, solidyfikację, dynamikę epidemii lub wymianę ciepła. Chociaż opisywane zjawiska fizyczne mogą wydawać się odległe, matematyczna struktura równań jest podobna.

Acknowledgements

“The struggle ends when the gratitude begins...”

– Neale Donald Walsch

First of all, I would like to state my greatest gratitude to my family who sacrificed their time for me - to have more the time to complete my PhD. In princile, these includes my wife Bożena Gruszczyńska; my mum, Katarzyna Gruszczyńska; and my mother in law, Genowefa Książek. My lovely daughter Lena and arrival of the newborn Tobiasz offered me the courage to finish my thesis as quickly as possible.

Next, I would like to thank my scientific supervisors. Most importantly, I would like express my appreciation to Dr Łukasz Łaniewski-Wołk, wonderful co-supervisor, for his patience and brilliant explanation of each detail I asked. His scientific support was absolutely crucial for my progress. Without his deep mathematical insight the success would not be possible.

My supervisor, Prof. Jacek Szumbarski is acknowledgement for his never-ending support, understanding, and encouraging references despite my (lack of) progress. I am happy that I have been given a complete freedom in the choice of my research.

Starting in 2017, I was fortunate to spend half a year at the University of New South Wales in Sydney. I would like to thank prof. Tracie Barber for hosting me during the very vague beginnings of my PhD.

Dr Travis Mitchell is admitted for insightful discussions regarding the multi-phase flows and his writing skills.

Dr Wojciech Regulski is recognized for his business energy and organizational talent. I was happy to work on thermal problems in your CFD company, QuickerSim.

Dr Michał Dzikowski is appreciated for countless discussions and impressive work at the Interdisciplinary Centre for Mathematical and Computational Modelling, University of Warsaw. His expertise in computer science, high performance computing and LBM is enormous. Together with prof. Piotr Szymczak, they also managed to draw my honest interest to geophysics and porous media flows.

Prof. Mathias Krausse is acknowledged for invitation to Karlsruhe Intitute of Technology and the opportunity to work with the OpenLB team.

Funding

My research was possible owing to the following funding:

- travel grants: *Grant Dziekański 2018*, *CWM/PROM PW 2/2019/1*, *Pakiet Mobilnościowy I*, *PW 2022*.
- *Panther* scholarship, which allowed me for a half-year research visit at the University of New South Wales, Sydney.
- industrial funds granted by QuickerSim Ltd. and internal funds from Warsaw University of Technology, namely *Rada Naukowa Dyscypliny Inżynieria Mechaniczna*.
- computational resources provided by Interdisciplinary Center for Mathematical and Computational Modelling of the University of Warsaw and resources granted for the *Massively Parallel LBM simulations with TCLB* project developed on the *Prometheus* cluster at Cyfronet supercomputing center.
- IDUB grants: *Modelling of epidemic spreading with Lattice Boltzmann Method*, funded by Warsaw University of Technology and *High-performance numerical model supporting the analysis of tomographic data* funded by University of Warsaw.

The simulations were completed using the open-source TCLB solver [6, 7] available at: <https://github.com/CFD-GO/TCLB>

Contents

Declaration of Authorship	iii
Abstract	xiii
Acknowledgements	xv
1 Introduction	1
1.1 [EN] Outline	1
1.1.1 Macroscopic equations of interest	4
1.1.2 Research hypotheses	5
1.1.3 Research methodology	5
1.2 [PL] Streszczenie	6
1.2.1 Równania makroskopowe	8
1.2.2 Hipotezy badawcze	9
1.2.3 Metodyka badań	10
2 The Lattice Boltzmann Method	13
2.1 From kinetic theory of gases to Boltzmann equation	14
2.1.1 Basic properties of the equilibrium and the collision operator	16
2.2 From Boltzmann equation to discrete Boltzmann equation	18
2.3 From discrete Boltzmann equation to lattice Boltzmann method	19
2.3.1 Calculation of the scalar field	22
2.3.2 Initialization	24
2.4 Example: Direct derivation of the 0D scheme from ODE	24
2.5 Notes on integration of the discrete Boltzmann equation	25
2.6 Summary	26
3 The collision kernels	29
3.1 Collision space	29
3.2 Discretisation of the velocity space	30

3.3	Moments of the distribution	31
3.3.1	Aliasing of moments	34
3.4	Discretisation of the equilibrium distribution function	34
3.5	Transformation matrices	37
3.6	Two Relaxation Time (TRT)	39
3.6.1	TRT in central moments space	41
4	Reactions	45
4.1	Introduction	46
4.1.1	Discussion on the state of the art	47
4.1.2	Structure	50
4.2	Model description	50
4.2.1	The collision operator	50
4.2.2	Streaming	51
4.3	Scaling of LBM	51
4.4	Model verification and validation	52
4.4.1	Linear advection-diffusion-reaction model	53
4.4.1.1	Second-order convergence	53
4.4.1.2	Convergence of DBE to advection-diffusion-reaction equation (ADRE)	54
4.4.1.3	Error landscape	55
4.4.2	The Allen-Cahn equation — illustrative advection-diffusion-reaction problem.	57
4.4.2.1	Uniform reaction benchmark — comparison with an analytical solution	60
4.4.2.2	Reaction-diffusion benchmark (2D, periodic) — comparison with a finite-element solution	61
4.4.2.3	Advection-diffusion-reaction benchmark (2D, periodic) — self-convergence study	63
4.5	Comparison of approaches to the source term integration	67
4.6	Conclusions	68
4.7	Future outlook - system of equations	70
5	Role of diffusion-reaction equations in epidemic modelling	73
5.1	Introduction	74
5.1.1	Limitations of the 0D SIR model	75

5.1.2	Numbers or fractions?	76
5.1.3	The nondimensional form equations	76
5.2	Under which conditions one may be lucky enough to not get infected? . . .	76
5.2.1	Stability of linear systems	78
5.2.2	SI Streamlines	79
5.3	The simple spatial SIR model	81
5.3.1	The 1D queue case	81
5.3.2	The spatial effect	81
5.3.3	Choice of the <i>infectious</i> operator	82
5.3.4	Comparison of "infectious" operators in the frequency domain . . .	82
5.4	The spatial SIR system (SIR-Peng model)	84
5.4.1	The low diffusivity issue and the spatial WSIR remedy	85
5.4.2	The nondimensional form equations - revisited	85
5.4.3	Remarks on other SIR-diffusion models	86
5.5	Similarity numbers in SIR-like models	87
5.5.1	SIR with <i>independent</i> (naive) diffusion	87
5.5.2	SIR-Peng model	88
5.5.3	WSIR model	89
5.5.4	Numbers or fractions - revisited	89
5.6	Benchmarks of the spatial WSIR and SIR-Peng models	91
5.6.1	Uniform population density	91
5.6.2	Spatially variable population density	92
5.7	Conclusions	95
5.8	Future outlook	95
6	Conservation laws: energy balance	97
6.1	The general framework	98
6.2	Total energy	99
6.3	Kinetic energy	99
6.4	Internal energy	100
6.5	Internal energy and enthalpy	100
6.5.1	Ideal gas - assumptions	101
6.6	Stress tensor	101
6.7	Balance of internal energy in terms of enthalpy	102
6.8	Balance of total energy in terms of enthalpy	103

7	Recovering Energy transfer	105
7.1	Macroscopic equation	105
7.1.1	Way I: The 'basic' approach	106
7.1.1.1	Scaling	109
7.2	Conjugate Heat Transfer — future outlook	112
7.2.1	Way II: Why variable ρc_v causes problem	112
7.2.2	Way III: Calculate the right moments (or correction by weights)	114
7.2.2.1	The equilibrium distribution function (EDF) in central moments space (CMS)	116
7.2.3	Way IV: Correction by source term	118
7.2.4	Way V: Two passive scalar worlds tied by BC at the interface.	120
8	Boundary Conditions in LBM	121
8.1	Link-wise approach: the bounce- back (BB)	122
8.2	The magic (Ginzburg) parameter	124
8.2.1	Velocity inlet or a moving wall	124
8.2.2	Pressure inlet/outlet	125
8.2.3	Concentration	125
8.2.4	Gradient at the boundary	126
8.3	Moments of a link-wise BC	126
8.3.1	Future outlook: heat flux boundary condition	131
8.4	Interpolated (anti)-bounce-back BC	135
8.5	Summary	137
9	Thermal Flows in high Prandtl number regime	139
9.1	Introduction	140
9.2	Model description	145
9.2.1	Moments of the distribution functions	145
9.2.1.1	Considered collision kernels	146
9.3	Model verification and validation	149
9.3.1	Advection-Diffusion of a Gaussian hill	150
9.3.2	Advection-diffusion of a square indicator function	152
9.3.3	Heat conduction between two concentric cylinders	155
9.3.4	Steady, forced convective heat transfer from a confined cylinder	156
9.4	Future outlook	163
9.5	Conclusions	164

9.6	Source term treatment	164
10	Multiphase Flows	167
10.1	The separation flux	167
10.2	Phase field - modified EDF	169
10.3	Phase field - forcing term	171
10.4	Phase field - forcing term - anti diffusion	173
11	A cascaded phase-field lattice Boltzmann model for the simulation of incompressible, immiscible fluids with high density contrast	175
11.1	Introduction	176
11.2	Model description	179
11.2.1	Macroscopic equations	179
11.2.1.1	Navier-Stokes equations	179
11.2.1.2	Interface tracking	180
11.2.2	Lattice Boltzmann equations	180
11.2.2.1	Physical interpretation of moments	180
11.2.2.2	Collision	181
11.2.2.3	Central moments of equilibrium distribution functions and force vectors	182
11.2.2.4	Streaming	183
11.2.3	Forcing terms	183
11.2.3.1	Forcing terms for hydrodynamics	183
11.2.3.2	Forcing term for the phase-field	185
11.3	Model verification and validation	185
11.3.1	Two phase Poiseuille flow	185
11.3.2	Interpolation of the relaxation rate in the diffuse interface	187
11.3.3	Effect of the moving reference frame	189
11.3.4	Planar Taylor bubble analysis	194
11.3.4.1	Problem definition	194
11.3.4.2	Results	195
11.3.5	Planar Taylor bubble in a moving reference frame	197
11.3.5.1	Problem definition	198
11.3.5.2	Results	199
11.3.6	Computational Efficiency	200
11.4	Remarks on orthogonalization of moments and relaxation	201

11.5	Remarks on discretization of the distribution functions	202
11.6	Discretization of the force term	205
11.7	Conclusions	208
11.8	Future Outlook	208
12	Summary	211
13	References	213

Acronyms

ABB anti-bounce-back

ADE advection-diffusion equation

ADRE advection-diffusion-reaction equation

BB bounce-back

BC boundary condition

BE Boltzmann equation

CFD computational fluid dynamics

CHT Conjugate Heat Transfer

CM central moments

CMS central moments space

DBE discrete Boltzmann equation

DF distribution function

EDF equilibrium distribution function

EQ equilibrium scheme

FD finite difference

FEM finite element method

HIT Herd Immunity Treshold

IABB interpolated-anti-bounce-back

IBB interpolated-bounce-back

IBM immersed boundary method

LB lattice Boltzmann

LBM lattice Boltzmann method

MRT multiple relaxation time

NS Navier Stokes

Nu Nusselt number

ODE ordinary differential equation

PDE partial differential equation

Pr Prandtl number

Re Reynolds number

SRT single relaxation time

TRT two relaxation time

List of Symbols

General properties

f_i	i -th distribution function of the hydrodynamic field
h_i	i -th distribution function of the advected field
g_i	i -th distribution function of interest
ϕ	density of the advected field

Lattice Boltzmann properties

Ω	collision operator
\mathcal{W}	transformation to <i>(central) moments</i> or <i>cumulants</i>
c_s	lattice speed of sound
Q	macroscopic source term
Υ	raw moment of distribution function
κ	central moment of distribution function
c	cumulant of distribution function
τ	relaxation time
s_i	i -th relaxation frequency
lu	lattice unit
Γ	dimensionless DF
\mathcal{C}	forward cumulant transform
\mathbb{M}	transformation matrix
\mathbb{N}	shift matrix
\mathbb{S}	relaxation matrix
\mathbf{F}	force vector
\mathbf{x}	position vector
\mathbf{w}	weight factor vector
\mathbf{e}	characteristic lattice velocity
\mathbf{u}	macroscopic velocity vector
ξ	mesoscopic (continuous) particle velocity space

Hydrodynamic properties

ρ	fluid density
ν	kinematic viscosity
ζ	bulk viscosity
μ	dynamic viscosity
Phase-field properties	
σ	surface tension
γ	phase interface thickness
M	mobility (phase field diffusion coefficient)
ϕ	phase field
Thermal properties	
h	specific internal energy (per unit mass)
H	internal energy
\mathfrak{h}	specific enthalpy (per unit mass)
\mathcal{H}	enthalpy
T	temperature
k	thermal conductivity
c_v	specific heat capacity at constant volume
c_p	specific heat capacity at constant pressure
$\alpha = \frac{k}{\rho c_p}$	thermal diffusivity
ρ	density of the medium
\dot{q}	specific heat source
Epidemic modelling	
W	viral load
S	susceptible
I	infected
R	recovered
γ	rate of recovery
β	average number of contacts per person per time unit
R_0	basic reproduction number
Other	
i	Imaginary number
Superscripts	
eq	equilibrium
\wedge	variables from the next time step (t+1)

\star	post-collision variable
\sim	redefined (shifted) distribution function or its moment
H	quantity related to internal energy field
Numerical Benchmarks	
N	number of spatial dimensions
T	number of time iterations (time steps)
t^*	dimensionless time
L	number of lattice elements per length
Δx	spatial resolution ($1/L$)
Δt	temporal resolution ($1/T$)

Chapter 1

Introduction

“Dissertation est omnis divisa in partes tres.”

– Julius Caesar

Contents

1.1	[EN] Outline	1
1.1.1	Macroscopic equations of interest	4
1.1.2	Research hypotheses	5
1.1.3	Research methodology	5
1.2	[PL] Streszczenie	6
1.2.1	Równania makroskopowe	8
1.2.2	Hipotezy badawcze	9
1.2.3	Metodyka badań	10

1.1 [EN] Outline

Key words: Lattice Boltzmann Method, advection-diffusion-reaction, heat transfer, multiphase-flows.

The doctoral dissertation is based on a series of three publications presenting the formulation and application of the lattice Boltzmann method (LBM) for numerical solving of advection-diffusion-reaction equations (ADRE) coupled with Navier-Stokes equations. From the macroscopic perspective, these equations model, among others multiphase flows, solidification, dynamics of epidemiological processes and heat transfer. Although these

phenomena may seem quite distant, the structure of the equations is similar. As an alternative to solving discrete macroscopic equations, the lattice Boltzmann method focuses on a mesoscale description of the distribution of hypothetical gas particles. This distribution determines the density of some physical quantity, such as mass, chemical concentration or internal energy. It can be viewed as the probability of finding the particle at a certain time and place. In each iteration, distributions are passed to adjacent mesh nodes. This step requires data exchange between nodes. Then, a local collision step is performed where the distributions are relaxed towards an equilibrium distribution. The selection of the relaxation coefficients and the proper space in which the collision is carried out has a fundamental impact on the precision and stability of the simulation. In general, most of the effort has been made to separate the relaxation frequencies of the observable quantities in order to achieve independence from one another. Moreover, the number of connections between the individual lattice nodes along which the distributions can move (velocity discretization) affects the number of moments that can be reproduced on the lattice. Another factor is the order of discretization of the equilibrium distribution. Over the past decades, many variants of collision operators have been proposed. The recently published textbooks [8, 9, 10] and review articles [11, 12, 13] provide a broad presentation of the current state of knowledge. The multitude of macroscopic physical models, combined with various implementations at the LBM level, is a challenge in analysing factors influencing a given approach's potential success. This work focuses on numerical properties and LBM theory, particularly on simulating the advection-diffusion-reaction equations. In subsequent parts of the thesis, improvements to the models available in the literature are presented, and their numerical properties are compared.

The first part of the work introduces the lattice Boltzmann method and describes the modelling of the advection-diffusion-reaction equations with an implicit source term (Chapters 2 to 4). The original achievement is a thorough analysis of the methodology that allows the addition of an entangled source element (depending on the intensity of the transported field) while maintaining the LBM-specific, second-order convergence both in time and in space. Due to the general form of deliberations, the publication containing this part of the work was entitled “Revisiting the second-order convergence of the lattice Boltzmann method with reaction-type source terms” and was submitted for review. Next, the system of differential equations used in consolidated epidemiological models was analysed (Chapter 5). It is similar in nature to the equations which can be found in the heat and mass transfer problems. In particular, they can be considered as a system of diffusion-reaction equations. In classical terms, a fixed-sized population is divided into

three groups: the susceptible (S) who may be ill; infected (I) who get sick; and healed (R) who were infected and then became immune. One of the methods of taking into account the spatial distribution of the population and the contacts between its individuals leading to the spread of the disease is to use the analogy to diffusion processes. Another issue is the density of the population. In this case, works related to heat transfer are a good source of inspiration.

The second part of the work is focused on the heat transfer in fluids. The Chapters 6 to 8 provide a theoretical background. Modelling of fluids characterized by a high Prandtl number (Chapter 9) has been recently published [4]. The problem is numerically challenging because the transfer of momentum and heat occurs at different time scales. In order to take into account the very low thermal conductivity while maintaining the Courant-Friedrichs-Lewy condition, the numerical diffusion of the scheme should be limited. Consequently, numerical artefacts are dominated by dispersion errors known as wiggles. Research focuses on possible countermeasures in terms of LBM through the use of novel collision kernels, lattices with a large number of discrete velocities (D3Q27) and second-order boundary conditions. For the first time, a collision operator based on the so-called cumulants has been used to simulate both hydrodynamic and thermal fields. The results of the numerical simulations confirm that in order to obtain the benefit of using a lattice with a large number of discrete velocities, it is not enough to relax the first-order moments/cumulants of the advected field. In all of the performed benchmarks, the kernel based on two relaxation times (TRT) proved to be better than the counter candidates.

The third part of the work (Chapters 10 and 11) is devoted to the modelling of an incompressible and immiscible two-phase fluid based on a phase-field approach. In this model, the phase is determined on the basis of the marker function. For example, a value of 0 indicates phase A, while a value of 1 indicates phase B. The phase field is carried (advected) in the direction of the fluid's movement. In order to avoid mixing components, the so-called anti-diffusion term is added. The implementation of this part of the work has been described in the article "A cascaded phase-field lattice Boltzmann model for the simulation of incompressible, immiscible fluids with high density contrast." The original achievement is the introduction of a cascade kernel to incompressible phase-field LBM models, which improved the stability of the schema and Galilean invariance.

1.1.1 Macroscopic equations of interest

The advection-diffusion-reaction equation may be viewed as a key building block in CFD modelling. In its simplest form, it describes the transport of scalar fields such as temperature, or concentrations of different chemical components across the spatial domain. The equation can be extended by addition of a source terms to account for chemical reactions, or heat generation. Once the density of a medium is introduced, the energy transfer can be properly modelled. Finally, a much more complex, nonlinear Navier Stokes (NS) equation describe the motion of a fluid.

1. **Hydrodynamics:** The continuity and momentum equations,

$$\begin{cases} \frac{\partial \rho}{\partial t} + \nabla \cdot \rho \mathbf{u} = 0 \\ \rho \left(\frac{\partial \mathbf{u}}{\partial t} + \mathbf{u} \cdot \nabla \mathbf{u} \right) = -\nabla p + \nabla \cdot (\mu [\nabla \mathbf{u} + (\nabla \mathbf{u})^\top]) + \mathbf{F}. \end{cases}$$

2. **Reactive flows:** General form of the advection-diffusion-reaction equation (ADRE),

$$\frac{\partial \phi}{\partial t} + \nabla \cdot \phi \mathbf{u} = \nabla \cdot M \nabla \phi + Q(\phi).$$

With a bit of tuning, the ADRE can be transformed to a more case-specific equation, which describe processes such as:

- (a) **Heat transfer:** The internal energy equation,

$$\frac{\partial}{\partial t}(\rho c_v T) + \nabla \cdot (\mathbf{u} \rho c_v T) = \nabla \cdot (k \nabla T) + \dot{q}.$$

- (b) **Multiphase flows:** Phase field evolution equation,

$$\frac{\partial \phi}{\partial t} + \nabla \cdot \phi \mathbf{u} = \nabla \cdot M \left(\nabla \phi - \frac{\nabla \phi}{|\nabla \phi|} \frac{[1 - 4(\phi - \phi_0)^2]}{\gamma} \right).$$

(c) **Dynamics of an epidemic:** Set of spatial WSIR equations,

$$\begin{cases} \frac{\partial}{\partial t} W &= \beta_W \left[\frac{r^2}{8} \Delta W + (I - W) \right] \\ \frac{\partial}{\partial t} S &= -\beta \frac{S}{N} W \\ \frac{\partial}{\partial t} I &= \beta \frac{S}{N} W - \gamma I \\ \frac{\partial}{\partial t} R &= \gamma I. \end{cases}$$

The detailed meaning of the symbols will be described in subsequent chapters.

1.1.2 Research hypotheses

The issues arising during the development of the model relate to the expansion of the possibilities of numerical simulations based on LBM. What is the best description of a given phenomenon through mathematical equations? How to solve it numerically using LBM? How much better results will be obtained? More specifically, one can ask:

1. How to correctly, i.e. with second-order accuracy, discretize an implicit source term in which the reaction intensity depends on the value of the simulated scalar field?
2. How to describe the dynamics of an epidemic process using a set of spatial SIR equations with a variable density of the population?
3. Which model should be used to simulate a heat transfer in a fluid characterized by a high Prandtl number? How will the results be influenced by the higher order boundary condition (interpolated anti-bounce-back) and by the advanced operator of the collision (cascaded and cumulant collision kernel)?
4. Will the introduction of a kernel implementing a collision of distribution functions in a moving frame of reference allow to an increase in the accuracy and stability of the two-phase flow simulation based on the 'phase-field' approach?

To the best of the author's knowledge, there are no answers to the above questions in the literature. The answer requires both analytical derivation and numerical experiments.

1.1.3 Research methodology

The rapid increase of the available computing power opens up new possibilities for methods with good scalability. Due to the local nature of computations, the scalability of LBM

on high-performance computers (HPC) is almost linear. In this work, the open source TCLB solver is used, which is being developed, at the Faculty of Power and Aeronautical Engineering of the Warsaw University of Technology, University of Queensland and the University of Warsaw. Thanks to the use of TCLB, it is possible to perform large-scale calculations on multi-GPU architectures. Source code and instructions are available at:

<https://github.com/CFD-GO/TCLB>

<https://docs.tclb.io/>

In order to carry out the research, a set of programming tools was developed. They enable automatic generation of the source code as well as symbolic integration and calculation of moments of the Maxwell-Boltzmann equilibrium distribution function both in the continuous and discrete versions, which is of key importance in the analysis of macroscopic equations.

1.2 [PL] Streszczenie

Słowa kluczowe: metoda gazu siatkowego Boltzmanna, równania adwekcji-dyfuzji-reakcji, wymiana ciepła, przepływy wielofazowe.

Niniejsza rozprawa doktorska oparta jest o cykl trzech publikacji przedstawiających sformułowanie i zastosowanie metody gazu siatkowego Boltzmanna (LBM) do numerycznego rozwiązywania równań typu adwekcji-dyfuzji-reakcji (ADRE) sprzężonych z równaniami Navier-Stokes’a. Z perspektywy makroskopowej równania te modelują m. in. przepływy wielofazowe, solidyfikację, dynamikę procesów epidemiologicznych oraz wymianę ciepła. Chociaż zjawiska te mogą wydawać się dość odległe, struktura równań jest podobna.

Alternatywnie do rozwiązywania dyskretnych równań makroskopowych, metoda gazu siatkowego Boltzmanna koncentruje się na mezoskalowym opisie ruchu dystrybucji cząstek hipotetycznego gazu sieciowego. Dystrybucja określa gęstość danej wielkości fizycznej. Można ją postrzegać jako prawdopodobieństwo znalezienia cząstki w określonym czasie i miejscu. W każdej iteracji, dystrybucje przekazywane są do sąsiednich węzłów siatki. Krok ten wymaga wymiany danych między węzłami. Następnie, wykonywany jest lokalny krok kolizji, w którym dystrybucje relaksowane są w kierunku rozkładu równowagowego. Dobór współczynników relaksacji oraz właściwej przestrzeni w której realizowana jest kolizja ma fundamentalny wpływ na precyzję i stabilność symulacji. Ogólnie rzecz biorąc,

większość wysiłku ma na celu oddzielenie częstotliwości relaksacji wielkości obserwowalnych w celu uzyskania ich wzajemnej niezależności. Ponadto, liczba połączeń pomiędzy poszczególnymi węzłami siatki po których mogą przemieszczać się dystrybucje (dyskretyzacja prędkości) rzutuje na liczbę momentów jakie można oddać na kracie. Kolejnym czynnikiem jest rząd dyskretyzacji rozkładu równowagowego. W ciągu ostatnich dziesięcioleci zaproponowano wiele wariantów operatorów kolizji. Szeroką prezentację aktualnego stanu wiedzy zawierają wydane niedawno monografie [8, 9, 10] oraz prace porównawcze [11, 12, 13]. Mnogość makroskopowych modeli fizycznych, w połączeniu z różnorodnymi implementacjami na poziomie LBM stanowi wyzwanie w analizie czynników wpływających na potencjalny sukces danego podejścia.

Niniejsza praca skupia się na własnościach numerycznych oraz teorii LBM ze szczególnym naciskiem na symulację równań adwekcji-dyfuzji-reakcji. Rozprawa rozpoczyna się wprowadzeniem do metody gazu siatkowego Boltzmann (rozdziały 2 i 3). Następnie można wyróżnić trzy części opisujące różne zastosowania równań adwekcji-dyfuzji-reakcji. W ramach poszczególnych części, przedstawiono udoskonalenia modeli dostępnych w literaturze, a następnie porównano ich własności numeryczne.

Pierwsza część pracy (rozdziały 4 i 5) opisuje modelowanie równań adwekcji-dyfuzji-reakcji z uwikłanym członem źródłowym. Oryginalnym osiągnięciem jest dokładne przeanalizowanie metodyki pozwalającej na dodanie uwikłanego członu źródłowego (zależącego od intensywności transportowanego pola) z zachowaniem właściwego dla LBM, drugiego rzędu zbieżności zarówno w czasie jak i w przestrzeni. Ze względu na ogólną formę rozważań publikacja zawierająca tę część pracy otrzymała tytuł “Revisiting the second-order convergence of the lattice Boltzmann method with reaction-type source terms” i została złożona do recenzji [3]. Ponadto, przeanalizowany został układ równań różniczkowych stosowanych w skonsolidowanych modelach epidemiologicznych. Ma on podobny charakter do równań spotykanych w zagadnieniach transportu ciepła i masy. W szczególności można je rozważać jako układ równań typu dyfuzji-reakcji. W klasycznym ujęciu populację o stałej wielkości dzieli się na trzy grupy: podatni (S), które mogą chorować; zainfekowani (I), którzy chorują; i ozdrowiali (R), którzy zostali zarażeni, a następnie stali się odporni. Jedną z metod uwzględnienia przestrzennego rozmieszczenia populacji oraz kontaktów pomiędzy jej osobnikami, a w konsekwencji rozprzestrzeniania się choroby jest wykorzystanie analogii do procesów dyfuzji. Osobnym zagadnieniem jest kwestia gęstości ośrodka (populacji). W tym przypadku dobrym źródłem inspiracji są prace poświęcone wymianie ciepła.

Druga część pracy (rozdziały 6,7 i 9) przedstawia zagadnienia związane z wymianą

ciepła dla przepływów z wysoką liczbą Prandlta, i została opublikowana [4]. Zagadnienie uwarunkowane w ten sposób stanowi wyzwanie numeryczne, ponieważ transfer momentu i ciepła występuje w różnych skalach czasowych. Aby uwzględnić bardzo niską przewodność cieplną z zachowaniem warunku Couranta-Friedrichsa-Lewy’ego należy ograniczyć numeryczną dyfuzję schematu. W konsekwencji artefakty numeryczne są zdominowane przez błędy dyspersji znane jako wiggles. Badania skupiają się na możliwych środkach zaradczych w ramach LBM poprzez zastosowanie nowatorskich kerneli kolizyjnych, krat o dużej liczbie dyskretnych prędkości (D3Q27) oraz warunków brzegowych drugiego rzędu. Po raz pierwszy operator zderzeń oparty o tzw. kumulanty został wykorzystywany do symulacji zarówno pola hydrodynamicznego jak i termicznego. Wyniki symulacji numerycznych potwierdzają, że aby uzyskać korzyść z zastosowania kraty o większej liczbie prędkości dyskretnych, nie wystarczy relaksować pierwszego rzędu momenty/kumulanty adwekowanego pola. We wszystkich przeprowadzonych testach kernel oparty na dwóch czasach relaksacji (two relaxation time, TRT) okazał się lepszy od kontrkandydatów.

Trzecia część pracy (rozdziały 10 i 11) poświęcona jest modelowaniu niemieszalnego i nieściśliwego płynu dwufazowego w oparciu o podejście typu phase-field. W modelu tym fazę określa się na podstawie funkcji wskaźnikowej. Przykładowo, wartość 0 wskazuje na fazę A, podczas gdy wartość 1 wskazuje na fazę B. Pole fazowe jest unoszone (adwekcja) zgodnie z kierunkiem ruchu płynu. Aby uniknąć wymieszania się składników do r. adwekcji-dyfuzji pola fazowego wprowadza się tzw. człon antydyfuzyjny. Realizacja tej części pracy została opisana w artykule “A cascaded phase-field lattice Boltzmann model for the simulation of incompressible, immiscible fluids with high density contrast” [5]. Oryginalnym osiągnięciem jest wprowadzenie kaskadowego jądra (ang. kernela) do nieściśliwych modeli typu phase-field LBM, co pozwoliło na poprawienie stabilności schematu oraz niezmienniczości Galileusza.

1.2.1 Równania makroskopowe

Równanie adwekcji-dyfuzji-reakcji (ADRE) może być postrzegane jako podstawowy element konstrukcyjny w modelowaniu w obliczeniowej mechanice płynów. W najprostszej formie, opisuje ono transport pól skalarnych, takich jak temperatura lub stężenie składników chemicznych w domenie przestrzennej. Dodanie członu źródłowego pozwala na zamodelowanie reakcji chemicznych lub generacji ciepła. Po uwzględnieniu gęstości ośrodka, równanie umożliwia modelowanie transportu energii. Wreszcie, znacznie

bardziej złożone, nieliniowe równania Navier-Stokes'a (NS) opisują ruch płynu.

1. **Hydrodynamika:** Równanie ciągłości i transportu pędu,

$$\begin{cases} \frac{\partial \rho}{\partial t} + \nabla \cdot \rho \mathbf{u} = 0 \\ \rho \left(\frac{\partial \mathbf{u}}{\partial t} + \mathbf{u} \cdot \nabla \mathbf{u} \right) = -\nabla p + \nabla \cdot (\mu [\nabla \mathbf{u} + (\nabla \mathbf{u})^\top]) + \mathbf{F}. \end{cases}$$

2. **Przepływy reaktywne:** Ogólna forma równania adwekcji-dyfuzji-reakcji,

$$\frac{\partial \phi}{\partial t} + \nabla \cdot \phi \mathbf{u} = \nabla \cdot M \nabla \phi + Q(\phi).$$

Po niewielkich modyfikacjach, równanie adwekcji-dyfuzji-reakcji może zostać użyte do opisu procesów takich jak:

- (a) **Transport ciepła:** Równanie transferu energii wewnętrznej,

$$\frac{\partial}{\partial t}(\rho c_v T) + \nabla \cdot (\mathbf{u} \rho c_v T) = \nabla \cdot (k \nabla T) + \dot{q}.$$

- (b) **Przepływy wielofazowe:** Równanie ewolucji pola-fazowego,

$$\frac{\partial \phi}{\partial t} + \nabla \cdot \phi \mathbf{u} = \nabla \cdot M \left(\nabla \phi - \frac{\nabla \phi}{|\nabla \phi|} \frac{[1 - 4(\phi - \phi_0)^2]}{\gamma} \right)$$

- (c) **Dynamika procesów epidemiologicznych:** Układ równań WSIR,

$$\begin{cases} \frac{\partial}{\partial t} W &= \beta_W \left[\frac{r^2}{8} \Delta W + (I - W) \right] \\ \frac{\partial}{\partial t} S &= -\beta \frac{S}{N} W \\ \frac{\partial}{\partial t} I &= \beta \frac{S}{N} W - \gamma I \\ \frac{\partial}{\partial t} R &= \gamma I. \end{cases}$$

Znaczenie poszczególnych symboli zostało przedstawione w kolejnych rozdziałach.

1.2.2 Hipotezy badawcze

Zagadnienia jakie pojawiają się w trakcie rozwoju modelu dotyczą poszerzania możliwości symulacji numerycznych opartych o LBM. Jak najlepiej możemy opisać dane

zjawisko przy pomocy równań matematycznych, a następnie jak rozwiązać je numerycznie przy użyciu LBM? O ile lepsze wyniki uda się uzyskać? Bardziej konkretnie, można zapytać:

1. Czy wprowadzenie jądra (ang. kernel) realizującego kolizję funkcji dystrybucji w ruchomym układzie odniesienia pozwoli zwiększyć dokładność i stabilność symulacji przepływu dwufazowego modelowanego w ujęciu typu ‘phase-field’?
2. Jak poprawnie, czyli z dokładnością drugiego rzędu, zdyskretyzować uwikłany człon źródłowy, w którym intensywność reakcji zależy od wartości symulowanego pola skalarnego?
3. Jak opisać model rozwoju epidemii w oparciu o przestrzenne równania typu SIR z uwzględnieniem zmiennej gęstości populacji?
4. Jakiego modelu użyć do symulacji przepływu z wymianą ciepła charakteryzującego się wysoką liczbą Prandtla? Jaki wpływ na wyniki będzie miał warunek brzegowy wyższego rzędu (interpolated anti-bounce-back), a jaki zaawansowany operator kolizji (cascaded and cumulant collision kernel)?

Według najlepszej wiedzy autora, w literaturze brak jest odpowiedzi na powyższe pytania. Poszukiwanie rozwiązań wymaga zarówno wyprowadzeń analitycznych jak i eksperymentów numerycznych.

1.2.3 Metodyka badań

Gwałtowny wzrost dostępnej mocy obliczeniowej otwiera nowe możliwości dla metod cechujących się dobrą skalowalnością. Dzięki lokalnemu charakterowi obliczeń, skalowalność LBM na systemy obliczeniowych o dużej wydajności (High-performance computing, HPC) jest niemalże liniowa. W pracy badawczej używany jest solver TCLB o otwartym kodzie źródłowym, który jest rozwijany m.in. na Wydziale Mechanicznym Energetyki i Lotnictwa Politechniki Warszawskiej, University of Queensland oraz Uniwersytecie Warszawskim. Dzięki wykorzystaniu TCLB, możliwe jest wykonywanie wielkoskalowych obliczeń na architekturach typu multi-GPU. Kod źródłowy oraz instrukcja dostępne są na:

<https://github.com/CFD-GO/TCLB>

<https://docs.tclb.io/>

W celu realizacji badań rozwinięty został zestaw narzędzi programistycznych.

Umożliwiają one automatyczne generowanie kodu źródłowego, oraz symboliczne całkowanie i obliczanie momentów funkcji dystrybucji równowagowej Maxwella-Boltzmanna zarówno w wersji ciągłej oraz dyskretnej, co ma kluczowe znaczenie przy analizie równań makroskopowych.

Chapter 2

The Lattice Boltzmann Method

“There are no foreign lands. It is the traveller only who is foreign.”

– Robert Louis Stevenson

Part of this chapter (Sections 2.3 to 2.5) is based on the manuscript, which is available online [3].

Contents

2.1	From kinetic theory of gases to Boltzmann equation	14
2.1.1	Basic properties of the equilibrium and the collision operator .	16
2.2	From Boltzmann equation to discrete Boltzmann equation .	18
2.3	From discrete Boltzmann equation to lattice Boltzmann method	19
2.3.1	Calculation of the scalar field	22
2.3.2	Initialization	24
2.4	Example: Direct derivation of the 0D scheme from ODE . . .	24
2.5	Notes on integration of the discrete Boltzmann equation . .	25
2.6	Summary	26

The LBM is a widely used numerical scheme for solving both the NS equations and ADRE. Its popularity has significantly risen in the recent three decades due to its ability to handle complex boundary shapes and its relative ease of implementation and parallelisation. Several numerical methods are currently used across academia and industry for solving both the Navier Stokes and advection-diffusion equations. These include, but are not confined to, finite difference, finite volume [14], and finite element method (FEM) [15], which all discretise the macroscopic equations directly. Alternatively to solving discretised

macroscopic equations, the LBM focuses on the evolution of a particle distribution function. As a consequence, LBM has specific features (see Figure 2.5), some of which will be discussed in details throughout the thesis.

2.1 From kinetic theory of gases to Boltzmann equation

Between the description of a continuous flow and movement of individual molecules there is a mesoscopic scale, as shown in Figure 2.1. At this scale, we investigate a representative set of molecules in terms of their distribution. The distribution function defines the density

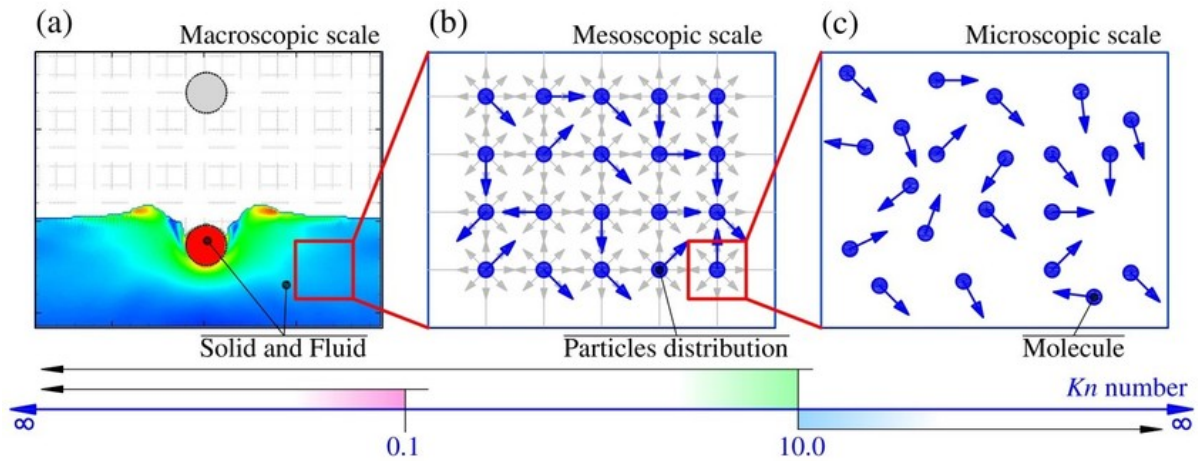
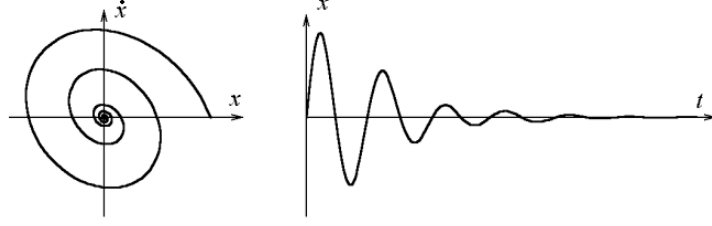


FIGURE 2.1: Illustration of fluid flow in different scales. The Knudsen number (\mathbf{Kn}) describes the ratio of the mean free path of the gas molecules to the macroscopic length of the flow domain. Figure from [16].

of some macroscopic physical quantity (such as mass or chemical concentration) across space. From the mesoscopic perspective, it can be viewed as the probability of finding a quantity-carrying particle with a given velocity and coordinates at a given time. In the discretised form, the set of velocities is finite. In each iteration, the discretised distributions are passed to neighbouring nodes along these velocities, in a step called streaming. This requires exchange of information with neighbouring nodes. Next, a local collision step is performed in each node, which relaxes the distribution function toward some form of an equilibrium. Let us investigate what kind of physical processes can be described by the lattice Boltzmann equation. To do so, consider a continuous distribution function $g(t, \mathbf{x}, \boldsymbol{\xi})$ which describes a probability of finding a particle in a phase space. Assume (for a while)


 FIGURE 2.2: Phase space (left) for a damped oscillator $g = g(t, \mathbf{x}, \dot{\mathbf{x}})$

that particles are travelling but not interacting with one another. In an infinitesimally small volume of the phase space $d\mathbf{x}d\boldsymbol{\xi}$, the system can be described as,

$$g_{no\ collisions}(t + dt, \mathbf{x} + d\mathbf{x}, \mathbf{u} + d\boldsymbol{\xi})d\mathbf{x}d\boldsymbol{\xi} = g_{no\ collisions}(t, \mathbf{x}, \boldsymbol{\xi})d\mathbf{x}d\boldsymbol{\xi} \quad (2.1)$$

Now, we are ready to include the collision term $\Omega(g)$:

$$g(t + dt, \mathbf{x} + d\mathbf{x}, \boldsymbol{\xi} + d\boldsymbol{\xi})d\mathbf{x}d\boldsymbol{\xi} = g(t, \mathbf{x}, \boldsymbol{\xi})d\mathbf{x}d\boldsymbol{\xi} + \Omega(g)d\mathbf{x}d\boldsymbol{\xi}dt \quad (2.2)$$

Expand into Taylor series,

$$g(t + dt, \mathbf{x} + d\mathbf{x}, \boldsymbol{\xi} + d\boldsymbol{\xi}) = g(t, \mathbf{x}, \boldsymbol{\xi}) + \frac{\partial g}{\partial t}dt + \nabla_{\mathbf{x}}g d\mathbf{x} + \nabla_{\boldsymbol{\xi}}g d\boldsymbol{\xi} \quad (2.3)$$

Plug Equation (2.3) into Equation (2.2),

$$\left[g(t, \mathbf{x}, \boldsymbol{\xi}) + \frac{\partial g}{\partial t}dt + \nabla_{\mathbf{x}}g d\mathbf{x} + \nabla_{\boldsymbol{\xi}}g d\boldsymbol{\xi} \right] d\mathbf{x}d\boldsymbol{\xi} = \left[g(t, \mathbf{x}, \boldsymbol{\xi}) + \Omega(g)dt \right] d\mathbf{x}d\boldsymbol{\xi} \quad (2.4)$$

Next we have to reformulate the mesoscopic velocity $\boldsymbol{\xi} = \frac{d\mathbf{x}}{dt}$ and acceleration $\frac{d\boldsymbol{\xi}}{dt} = \mathbf{a} = \frac{\mathbf{F}}{\Upsilon_{00}^G}$, where Υ_{00}^G is the zeroth order moment of the g distribution, i.e., $\Upsilon_{00}^G = \int g d\boldsymbol{\xi}$. The result, has been formulated by Ludwig Boltzmann in 1872 [17] and is known as the Boltzmann Equation (2.5). It can be viewed as a substantial derivative (of an intensive quantity g) which is equal to the collision term Ω applied to the distribution function of g :

$$\boxed{\frac{\partial g}{\partial t} + (\boldsymbol{\xi} \cdot \nabla_{\mathbf{x}})g + \left(\frac{\mathbf{F}}{\Upsilon_{00}^G} \cdot \nabla_{\boldsymbol{\xi}} \right)g = \Omega(g)} \quad (2.5)$$

Depending how we interpret g , different macroscopic partial differential equation (PDE) can be recovered from the streaming and collision routine:

$$\underbrace{g(t + dt, \mathbf{x} + d\mathbf{x}, \boldsymbol{\xi} + d\boldsymbol{\xi})d\mathbf{x}d\boldsymbol{\xi}}_{\text{Streaming}} = \underbrace{g(t, \mathbf{x}, \boldsymbol{\xi})d\mathbf{x}d\boldsymbol{\xi} + \Omega(g)d\mathbf{x}d\boldsymbol{\xi}dt}_{\text{Collision}} \quad (2.6)$$

2.1.1 Basic properties of the equilibrium and the collision operator

The collision operator, $\Omega(g)$, has to obey the conservation laws.

$$\int \Omega(g)\chi(\boldsymbol{\xi})d\boldsymbol{\xi} = \mathbf{0} \quad (2.7)$$

To simulate the NS, we will require $\chi(\boldsymbol{\xi}) = \{1, \boldsymbol{\xi}, \frac{\boldsymbol{\xi}^2}{2}\}$. Moreover, the moments of the mesoscopic distributions have to match macroscopic quantities such as density, ρ , momentum, $\rho\mathbf{u}$, and total energy, ρE . Let us denote the distributions corresponding to hydrodynamic field with $f = f(\mathbf{x}, \boldsymbol{\xi}, t)$.

$$\rho = \int f d\boldsymbol{\xi} \quad (2.8)$$

$$\rho\mathbf{u} = \int f\boldsymbol{\xi} d\boldsymbol{\xi} \quad (2.9)$$

$$\rho E = \rho \left(\frac{u^2}{2} + e \right) = \frac{1}{2} \int f \boldsymbol{\xi}^2 d\boldsymbol{\xi} \quad (2.10)$$

Observe, that the internal energy, e , is the second central moment (also known as the variance) of the distribution function,

$$\rho e = \int \frac{\|\boldsymbol{\xi} - \mathbf{u}\|^2}{2} f \boldsymbol{\xi}^2 d\boldsymbol{\xi} \quad (2.11)$$

$$(2.12)$$

as \mathbf{u} is the mean (macroscopic) velocity weighted by the particle distribution function.

The relationship between pressure, temperature and internal energy is described by an equation of state. For an ideal gas, one can write,

$$e = c_v T \quad (2.13)$$

$$p = \rho R_{gas} T \quad (2.14)$$

where $c_v = \frac{D}{2} R_{gas}$ is the heat capacity at constant volume of mono-atomic gas, D is the number of spatial dimensions and $R_{gas} = k_b/m$ is the gas constant.

The simplest collision model has been proposed by Bhatnagar, Gross and Krook [18] in 1954. It applies a single relaxation time τ towards an equilibrium state,

$$\Omega(g) = -\frac{1}{\tau}(g - g^{eq}). \quad (2.15)$$

The local thermodynamic equilibrium shall maximize the entropy and is given by [17],

$$\begin{aligned} g^{eq} &= \Psi^{M-B, eq}(\Upsilon_{00}, \sigma, \boldsymbol{\xi}, \boldsymbol{\mu}) \\ &= \frac{\Upsilon_{00}}{(2\pi\sigma^2)^{D/2}} \exp\left[-\frac{(\boldsymbol{\xi} - \boldsymbol{\mu})^2}{2\sigma^2}\right] \\ &= \frac{\Upsilon_{00}}{(2\pi c_s^2)^{D/2}} \exp\left[-\frac{(\boldsymbol{\xi} - \boldsymbol{u})^2}{2c_s^2}\right] \end{aligned} \quad (2.16)$$

where the scalar quantity of interest (like density, phase-field or internal energy) is equal to the sum of the distribution, $\Upsilon_{00} = \int \Psi^{M-B, eq} d\boldsymbol{\xi}$, the macroscopic velocity is the mean value of the distribution $\boldsymbol{u} = \boldsymbol{\mu}$, the lattice speed of sound corresponds to the variance of the distribution $c_s^2 = R_{gas} T_0 = \sigma^2$. Assuming isothermal equation of state, the ideal gas law can be expressed as $p = \rho R_{gas} T_0$, where T_0 is a constant, reference temperature. The heat transfer simulated in this thesis is based on a *decoupled* model [19]. It is assumed that the change of temperature does not affect properties (such as density or viscosity) of the fluid. The buoyancy effect, can be obtained using the Boussinesq Approximation [19] or change the variance of the distribution [20].

To simulate advection-diffusion-reaction equation coupled with NS, another set of distribution functions $h = h(\boldsymbol{x}, \boldsymbol{\xi}, t)$ is introduced. This additional set evolves between the same lattice nodes and at the same time-steps as the hydrodynamic one (further discussion is provided in Chapter 9). Denoting the advected field with ϕ , the moments

of h for a weakly compressible scheme reads,

$$\rho\phi = \int h d\xi, \quad (2.17)$$

$$\rho\phi\mathbf{u} = \int h\xi d\xi. \quad (2.18)$$

The procedure of recovering of the macroscopic ADRE is discussed in Chapter 7.

2.2 From Boltzmann equation to discrete Boltzmann equation

To construct a numerical scheme from the Boltzmann equation (BE) (see Equation (2.5)), the mesoscopic velocity space, ξ , has to be discretized Figure 2.3. Unfortunately, the de-

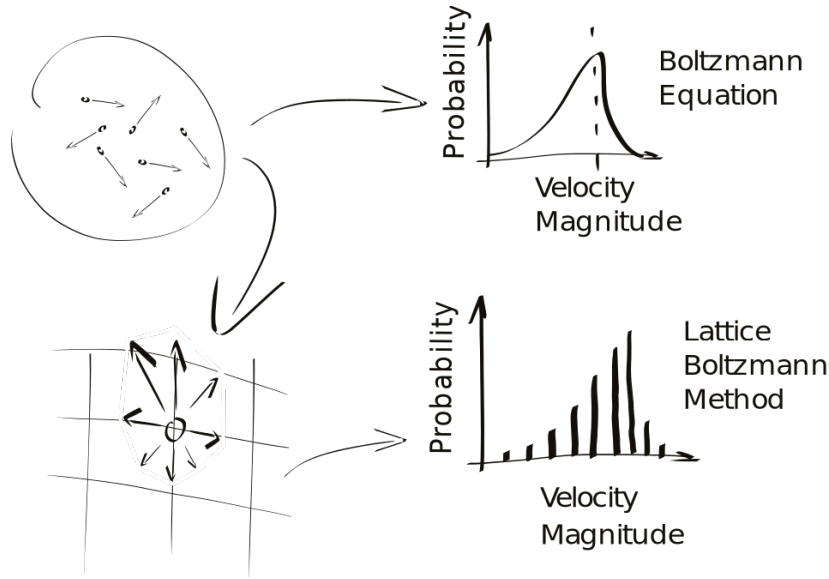


FIGURE 2.3: Discretization of the velocity space: $\xi \rightarrow e_i$.
Figure courtesy of M. Dzikowski [21].

pendence of the unknown particle distribution function, g , on the mesoscopic velocity ξ is unknown. To approximate the gradient $\mathbf{a} \cdot \nabla_{\xi} g$ (where $\mathbf{a} = \frac{d\xi}{dt} = \frac{\mathbf{F}}{\Upsilon_{00}^G}$ is the acceleration) He et al. [22] proposed to approximate g by its dominant, equilibrium part $\mathbf{a} \cdot \nabla_{\xi} g^{eq}$. Assuming that the LBM scheme is formulated in a weakly compressible form (see Sections 11.5

and 11.6 for the incompressible formulation),

$$\begin{aligned} \mathbf{F}_{\text{He}}(\boldsymbol{\xi}) &= \left(\frac{\mathbf{F}}{\Upsilon_{00}^G} \cdot \nabla_{\boldsymbol{\xi}} \right) \overbrace{\Psi^{M-B, eq}(\Upsilon_{00}^G, \boldsymbol{\xi}, \mathbf{u})}^{g^{eq}} \\ &\approx \frac{\mathbf{F}}{\Upsilon_{00}^G} \cdot \nabla_{\boldsymbol{\xi}} g^{eq} = -\frac{\mathbf{F}}{\Upsilon_{00}^G} \frac{(\boldsymbol{\xi} - \mathbf{u})}{c_s^2} g^{eq}. \end{aligned} \quad (2.19)$$

Introducing the discrete velocity vectors as \mathbf{e}_i , the discrete Boltzmann equation reads,

$$\frac{\partial}{\partial t} g_i + e_i^j \frac{\partial}{\partial x_j} g_i + (a^j \cdot \nabla_{\boldsymbol{\xi}}) g_i^{eq} = \frac{1}{\tau} (g_i^{eq}(\Upsilon_{00}^G, \mathbf{u}) - g_i) + q_i(g, \mathbf{x}, t), \quad (2.20)$$

and plugging in Equation (2.19),

$$\boxed{\frac{\partial}{\partial t} g_i + e_i^j \frac{\partial}{\partial x_j} g_i - \frac{F^j}{\Upsilon_{00}^G} \frac{(e_i^j - u^j)}{c_s^2} g_i^{eq} = \frac{1}{\tau} (g_i^{eq}(\Upsilon_{00}^G, \mathbf{u}) - g_i) + q_i(\Upsilon_{00}^G, \mathbf{x}, t),} \quad (2.21)$$

where $q_i(g, \mathbf{x}, t)$ is an additional source term.

2.3 From discrete Boltzmann equation to lattice Boltzmann method

In general, the derivations of the conventional LBM numerical schemes present in the literature, can be broadly divided into two groups. First one is referred as *bottom-up* and the second one as *top-down* approach.

The *bottom-up* procedure starts from an *a priori* postulated discrete evolution scheme. It proceeds with an expansion procedure (such as Chapman-Enskog) to recover the macroscopic equations and to analyse its order of accuracy. Knowing the difference between the target and recovered equation, one can apply corrections to account for the unbalanced terms. Regarding the advection-diffusion-reaction equation, the missing terms are recognised as spatio-temporal derivatives of the source term. To regain second-order accuracy of the numerical scheme, two approaches can be distinguished. Shi et al. [23, 24] evaluated the derivatives using standard finite-difference stencils. On the other hand, Seta [25] and Chai *et al.* [26] realised that a redefinition of variables allowed the problem to be resolved, while preserving the locality of the underlying scheme. An analogous analysis regarding the forcing term in the NS equations have been done by Guo *et al.* [27].

In the *top-down* approach, the DBE is first constructed. It is then integrated along its characteristics to derive the fully discrete scheme [28, 29, 30]. In most cases, the resulting time integration scheme will be implicit. Again, redefinition of variables can be used to transform it into explicit equations [31]. Finally, it is interesting to notice, that some alternative LBM schemes are also being developed [32, 33, 34].

Readers interested in a detailed discussion on analysis methods are referred to [35, 36, 37]. In this work the iterative scheme is derived using the *top-down* approach, i.e. by direct integration of the DBE.

Given an advection-diffusion-reaction equation,

$$\frac{\partial}{\partial t}\phi + \nabla \cdot (\mathbf{u}\phi) = \nabla \cdot (M\nabla\phi) + Q(\phi, \mathbf{x}, t), \quad (2.22)$$

where ϕ denotes the scalar field, \mathbf{u} refers to an advection velocity, M is a diffusion coefficient, and Q is the source term. The DBE reads,

$$\frac{\partial}{\partial t}h_i + e_i^j \frac{\partial}{\partial x_j}h_i = \frac{1}{\tau} (h_i^{\text{eq}}(\phi, \mathbf{u}) - h_i) + q_i(\phi, \mathbf{x}, t), \quad (2.23)$$

where h^{eq} is the equilibrium distribution, q is the source term, $\phi = \sum_i h_i$ is the scalar field, and \mathbf{u} is the advection velocity. It is important to reiterate here that the source term depends on the investigated scalar field. To the best of the authors' knowledge, such a form has not been discussed in the literature. With an appropriate choice of equilibrium distribution [10], this equation can be shown to represent the advection-diffusion-reaction equation with, $\phi = \sum_i h_i$, and $Q = \sum q_i$. The equations for the equilibrium distribution are presented in Section 3.3. An important property of the equilibrium that will be used, is,

$$\sum_i h_i^{\text{eq}}(\phi, \mathbf{u}) = \phi. \quad (2.24)$$

Contrary to classical numerical methods, such as finite-volume or finite-element method, the space and time integration can not be treated independently in the construction of a conventional LBM scheme. For a fixed i , x and t , the characteristic of DBE is given by $\mathbf{x}(\varpi) = \mathbf{x} + \varpi \mathbf{e}_i$, and $t(\varpi) = t + \varpi$. Integrating over ϖ from 0 to 1 we get,

$$\underbrace{\int_0^1 \left(\frac{\partial}{\partial t}h_i + e_i^j \frac{\partial}{\partial x_j}h_i \right) d\varpi}_{I_1} = \underbrace{\int_0^1 \left(\frac{1}{\tau} (h_i^{\text{eq}} - h_i) + q_i \right) d\varpi}_{I_2}. \quad (2.25)$$

Two integrals, I_1 and I_2 , can be identified in the integration process of the DBE. To denote the variables from the next time step, the hat superscript is used in this work. Namely, $\hat{\mathbf{x}} = \mathbf{x} + \mathbf{e}_i$, $\hat{t} = t + 1$, $\hat{\phi} = \phi(\hat{\mathbf{x}}, \hat{t})$ and $\hat{\mathbf{u}} = \mathbf{u}(\hat{\mathbf{x}}, \hat{t})$. The first integral can be evaluated directly, as it is a material derivative of h_i ,

$$I_1 = \int_0^1 \left(\frac{\partial}{\partial t} h_i + e_i^j \frac{\partial}{\partial x_j} h_i \right) d\varpi = h_i(\hat{\mathbf{x}}, \hat{t}) - h_i(\mathbf{x}, t). \quad (2.26)$$

The second integral can be approximated by the trapezoidal rule,

$$\begin{aligned} I_2 &= \int_0^1 \left(\frac{1}{\tau} (h_i^{\text{eq}} - h_i) + q_i \right) d\varpi \\ &\simeq \frac{1}{2} \left[\frac{1}{\tau} \left(h_i^{\text{eq}}(\hat{\phi}, \hat{\mathbf{u}}) - h_i(\hat{\mathbf{x}}, \hat{t}) \right) + q_i(\hat{\phi}, \hat{\mathbf{x}}, \hat{t}) + \frac{1}{\tau} (h_i^{\text{eq}}(\phi, \mathbf{u}) - h_i(\mathbf{x}, t)) + q_i(\phi, \mathbf{x}, t) \right]. \end{aligned} \quad (2.27)$$

Integrating Equation (2.27) over the characteristics, and collecting the variables from the next time step (which depend on $\hat{\mathbf{x}}$ and \hat{t}) on the left hand side gives,

$$\begin{aligned} &\overbrace{\left[1 + \frac{1}{2\tau} \right] h_i(\hat{\mathbf{x}}, \hat{t}) - \frac{1}{2\tau} h_i^{\text{eq}}(\hat{\phi}, \hat{\mathbf{u}}) - \frac{1}{2} q_i(\hat{\phi}, \hat{\mathbf{x}}, \hat{t})}^{\text{Equation (2.29)}} = \\ &= \left[1 - \frac{1}{2\tau} \right] h_i(\mathbf{x}, t) + \frac{1}{2\tau} h_i^{\text{eq}}(\phi, \mathbf{u}) + \frac{1}{2} q_i(\phi, \mathbf{x}, t). \end{aligned} \quad (2.28)$$

Next, a shifted distribution, \tilde{h} , is introduced to remove the implicit relation from Equation (2.28). To illustrate the idea, a simple example of variable shift in a ordinary differential equation is presented in 2.4. A general description of this procedure in the contexts of LBM can be found in the textbook by Krüger *et al.* [9, Chapter 3.5]).

The new (shifted) distribution, denoted with a tilde, is defined as,

$$\tilde{h}_i(\bullet) = \left[1 + \frac{1}{2\tau} \right] h_i(\bullet) - \frac{1}{2\tau} h_i^{\text{eq}}(\bullet) - \frac{1}{2} q_i(\bullet) \quad (2.29)$$

$$\implies h_i(\bullet) = \frac{1}{1 + \frac{1}{2\tau}} \left(\tilde{h}_i(\bullet) + \frac{1}{2\tau} h_i^{\text{eq}}(\bullet) + \frac{1}{2} q_i(\bullet) \right), \quad (2.30)$$

where \bullet is a placeholder for variables in either t or \hat{t} . Substituting Equation (2.29) into the

left-hand side of Equation (2.28) and Equation (2.30) into the right-hand side of Equation (2.28) leads to a fully explicit evolution scheme (see 2.5 for details),

$$\tilde{h}_i(\mathbf{x} + \mathbf{e}_i, t + 1) = \tilde{h}_i^*(\mathbf{x}, t) = (1 - s)\tilde{h}_i(\mathbf{x}, t) + sh_i^{\text{eq}}(\phi, \mathbf{u}) + \left(1 - \frac{s}{2}\right)q_i(\phi, \mathbf{x}, t), \quad (2.31)$$

where a relaxation frequency, $s = \frac{1}{\tau + 1/2}$, has been introduced to simplify the expression. The post-collision densities are denoted as \tilde{h}^* . It shall be underlined, that \tilde{h} is the variable being solved in the implementation of a LBM scheme. It is denoted with a tilde in this work to distinguish it from the non-shifted population, h . The differences in the discretisation schemes available in the literature are discussed in 4.5. The concept of the streaming step is illustrated in Figure 2.4.

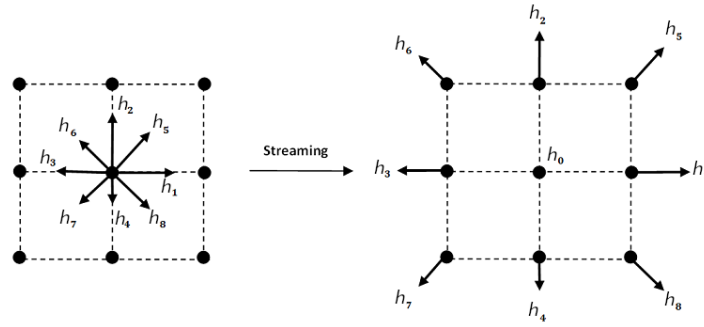


FIGURE 2.4: The streaming step on a D2Q9 lattice.

2.3.1 Calculation of the scalar field

Equation (2.31) would be an explicit iterative scheme for \tilde{h} , if not the implicit dependence on the scalar field, ϕ . One can calculate ϕ from \tilde{h} by summation of Equation (2.29) noting that both $\sum_i h_i$ and $\sum_i h_i^{\text{eq}}$ are equal to ϕ ,

$$\begin{aligned} \tilde{\phi} &= \sum_i \tilde{h}_i = \left(1 + \frac{1}{2\tau}\right) \sum_i h_i(\mathbf{x}, t) - \frac{1}{2\tau} \sum_i h_i^{\text{eq}}(\phi, \mathbf{u}) - \frac{1}{2} \sum_i q_i(\phi, \mathbf{x}, t) \\ &= \left[1 + \frac{1}{2\tau}\right] \phi - \frac{1}{2\tau} \phi - \frac{1}{2} Q(\phi, \mathbf{x}, t) \\ &= \phi - \frac{1}{2} Q(\phi, \mathbf{x}, t). \end{aligned} \quad (2.32)$$

Since the source term depends on the scalar field, $Q = Q(\phi, \mathbf{x}, t)$, one must solve the implicit equation for ϕ to retain the second-order convergence of the underlying scheme. This can be done with a sub-iteration routine, such as bisection or Newton's method, and in certain cases it can be solved analytically. In Table 2.1, a set of common source terms is presented with corresponding equations for the scalar field, ϕ . In some cases multiple solutions to the implicit equation can exist, and physical limitations must be applied to select the appropriate value. For these cases, the relevant conditions are listed in the notes. If Q is dependent only on the spatial, \mathbf{x} , and temporal, t , location, the equation reduces to, $\phi = \tilde{\phi} + \frac{1}{2}Q(\mathbf{x}, t)$, which is commonly encountered in the literature.

Class	Source term	Equation for ϕ	Notes
No source term	$Q = 0$	$\phi = \tilde{\phi}$	
ϕ independent term	$Q = Q(x, t)$	$\phi = \tilde{\phi} + \frac{1}{2}Q(x, t)$	
General 1st order term	$Q = -\lambda(\phi - \gamma)$	$\phi = \tilde{\phi} + \frac{1}{2+\lambda}\lambda(\gamma - \tilde{\phi})$	
Linear decay	$Q = -\lambda\phi$	$\phi = \frac{2}{2+\lambda}\tilde{\phi}$	
General 2nd order term	$Q = -\lambda(\phi^2 - B\phi + C)$	$\phi = \alpha + \sqrt{\frac{2}{\lambda}\tilde{\phi} + \alpha^2 - C}$	for $\phi > \alpha$, where $\alpha = \frac{B}{2} - \frac{1}{\lambda}$
Logistic model	$Q = \lambda\phi(1 - \frac{\phi}{\gamma})$	$\phi = \alpha + \sqrt{\frac{2\gamma}{\lambda}\tilde{\phi} + \alpha^2}$	for $\phi > \alpha$, where $\alpha = \gamma(\frac{1}{2} - \frac{1}{\lambda})$
Gompertz model	$Q = -\lambda\phi \ln \frac{\phi}{\gamma}$	$\phi = \alpha e^{\mathcal{W}_0(\frac{2}{\lambda}\tilde{\phi})}$	for $\phi > \alpha e^{\frac{1}{e}}$, where $\alpha = \gamma e^{-\frac{2}{\lambda}}$, and \mathcal{W} is the Lambert W function
Allen-Cahn equation	$Q = \lambda\phi(1 - \phi^2)$	$\phi = \frac{A}{C} - C$	for $\lambda < 2$, where $A = \frac{2-\lambda}{3\lambda}$, $B = \frac{\tilde{\phi}}{\lambda}$, and $C = \sqrt[3]{\sqrt{B^2 + A^3} - B}$
General term	$Q = Q(\phi, x, t)$	$\phi - \frac{1}{2}Q(\phi, x, t) = \tilde{\phi}$	implicit equation, which can be solved with sub-iterations

TABLE 2.1: Calculation of the value of the macroscopic scalar field ϕ from the sum of LBM densities $\tilde{\phi} = \sum_i \tilde{h}_i$. In cases of higher order terms, only one branch of the implicit function is selected, based on physical considerations.

Observe, that the equation for the macroscopic quantity, ϕ , is independent of the LBM scheme being used. Namely, for any collision operator, for example single relaxation time (SRT), multiple relaxation time (MRT) or cascaded LBM, and any discretisation of the source term, q_i , the equation will stay the same.

2.3.2 Initialization

As the densities simulated in the LBM are different than the DBE densities, the difference must to be taken into account in the initialization procedure. Namely, if one assumes the DBE to be initialized by the equilibrium distribution function, the LBM densities need to be initialized as,

$$\begin{aligned}\tilde{h}_i(x, 0) &= h_i^{eq}(\phi_0, \mathbf{u}_0) - \frac{1}{2}q_i(\phi_0, x, 0) \\ &= h_i^{eq}(\tilde{\phi}_0, \mathbf{u}_0),\end{aligned}\tag{2.33}$$

where ϕ_0 and \mathbf{u}_0 are the initial values of the macroscopic field and advection velocity respectively. Taking advantage of Equation (2.32), the initialization procedure can be simplified by calculating $\tilde{\phi}_0$. Omission of this crucial adjustment of the initialization procedure will result in a solution inconsistent with the desired initial condition, and will reduce the order of convergence. Note, that Equation (2.33) gives the value of the initial distribution functions after streaming and before collision.

2.4 Example: Direct derivation of the 0D scheme from ODE

As an illustrative exercise, a direct derivation of numerical scheme for an ordinary differential equation (ODE), analogous to the proposed LBM scheme, is presented. Consider an ODE,

$$\frac{d}{dt}\phi = Q(\phi, t).\tag{2.34}$$

Integrating it with the trapezoidal rule leads to the update formula,

$$\phi(t + \delta t) = \phi(t) + \frac{\delta t}{2} \left(Q(\phi(t), t) + Q(\phi(t + \delta t), t + \delta t) \right),\tag{2.35}$$

which belongs to a wider class of implicit Adams-Moulton methods. Introduction of a $\frac{\delta t}{2}$ shift, similarly to the LBM derivation presented in Section 2.3,

$$\tilde{\phi} = \phi - \frac{\delta t}{2}Q \longrightarrow \phi = \tilde{\phi} + \frac{\delta t}{2}Q, \quad (2.36)$$

allows to transform this update formula into an explicit one,

$$\tilde{\phi}(t + \delta t) + \cancel{\frac{\delta t}{2}Q(\phi(t + \delta t), t + \delta t)} = \tilde{\phi}(t) + \frac{\delta t}{2}Q(\phi(t), t) + \frac{\delta t}{2} \left(Q(t) + \cancel{Q(\phi(t + \delta t), t + \delta t)} \right), \quad (2.37)$$

as long as the transformation between ϕ and $\tilde{\phi}$ is bijective. This lead to a numerical scheme, identical to one obtained in LBM methodology,

$$\tilde{\phi}(t + \delta t) = \tilde{\phi}(t) + \delta t Q(\phi(t), t) \quad \text{where} \quad \phi(t) = \tilde{\phi}(t) + \frac{\delta t}{2}Q(\phi(t), t). \quad (2.38)$$

2.5 Notes on integration of the discrete Boltzmann equation

To ease the reading of the main text, some of the algebraic transformations are listed here. The substitutions can prove a useful reference for the reader, especially for newcomers, although similar derivations can be also found LBM textbooks [9, 10].

Substituting Equation (2.29) into the left-hand side of Equation (2.28) and Equation (2.30) into the right-hand side of Equation (2.28) gives,

$$\begin{aligned}
 \tilde{h}_i(\hat{\mathbf{x}}, \hat{t}) &= \left[1 - \frac{1}{2\tau}\right] \frac{\tilde{h}_i(\mathbf{x}, t) + \frac{1}{2\tau}h_i^{\text{eq}}(\phi, u) + \frac{1}{2}q_i(\mathbf{x}, t)}{1 + \frac{1}{2\tau}} + \frac{1}{2\tau}h_i^{\text{eq}}(\phi, u) + \frac{1}{2}q_i(\mathbf{x}, t) \\
 &= \frac{1 - \frac{1}{2\tau}}{1 + \frac{1}{2\tau}} \left[\tilde{h}_i(\mathbf{x}, t) + \frac{1}{2\tau}h_i^{\text{eq}}(\phi, u) + \frac{1}{2}q_i(\mathbf{x}, t) \right] + \frac{1}{2\tau}h_i^{\text{eq}}(\phi, u) + \frac{1}{2}q_i(\mathbf{x}, t) \\
 &= \frac{2\tau - 1}{2\tau + 1} \left[\tilde{h}_i(\mathbf{x}, t) + \frac{1}{2\tau}h_i^{\text{eq}}(\phi, u) + \frac{1}{2}q_i(\mathbf{x}, t) \right] + \frac{1}{2\tau}h_i^{\text{eq}}(\phi, u) + \frac{1}{2}q_i(\mathbf{x}, t) \\
 &= \underbrace{\frac{2\tau - 1}{2\tau + 1}}_{F_1} \tilde{h}_i(\mathbf{x}, t) + \underbrace{\frac{1}{2\tau} \left[1 + \frac{2\tau - 1}{2\tau + 1}\right]}_{F_2} h_i^{\text{eq}}(\phi, u) + \underbrace{\frac{1}{2} \left[1 + \frac{2\tau - 1}{2\tau + 1}\right]}_{F_3} q_i(\mathbf{x}, t). \quad (2.39)
 \end{aligned}$$

Next, introducing the relaxation frequency, $s = \frac{1}{\tau + 1/2}$, simplifies the expressions further,

$$F_1 = \frac{2\tau - 1}{2\tau + 1} = \frac{2\tau + 1}{2\tau + 1} - \frac{2}{2\tau + 1} = 1 - \frac{1}{\tau + 1/2} = 1 - s. \quad (2.40)$$

$$F_2 = \frac{1}{2\tau} \left[1 + \frac{2\tau - 1}{2\tau + 1}\right] = \frac{1}{2\tau} \frac{4\tau}{2\tau + 1} = \frac{2}{2\tau + 1} = s. \quad (2.41)$$

$$F_3 = \frac{1}{2} \left[1 + \frac{2\tau - 1}{2\tau + 1}\right] = \frac{2\tau}{2\tau + 1} = \frac{2\tau + 1}{2\tau + 1} - \frac{2}{2\tau + 1} = 1 - \frac{1}{2}s. \quad (2.42)$$

Substituting Equations (2.40-2.42) into Equation (2.39), the desired Equation (2.31) emerges,

$$\tilde{h}_i(\mathbf{x} + \mathbf{e}_i, t + 1) = \tilde{h}_i^*(\mathbf{x}, t) = (1 - s)\tilde{h}_i(\mathbf{x}, t) + sh_i^{\text{eq}}(\phi, u) + \left(1 - \frac{s}{2}\right)q_i(\mathbf{x}, t). \quad (2.43)$$

2.6 Summary

Figure 2.5 presents six specific features of lattice Boltzmann method. Thanks to its formulation, the collision and streaming routine makes the LBM scheme a conservative

one. As the collision is done locally and streaming involves only directly neighbouring nodes, the algorithm enjoys ideal scalability on HPC clusters. Moreover, it is well suited for GPU implementation. In each iteration, the distributions travel along the lattice links, thus the simulation can inherently capture the unsteadiness of fluid flow. The algorithm is implemented in an explicit manner and there is no global matrix inversion. However, the *shift* of variables gives the method properties of a second order implicit scheme, i.e. makes it suitable to simulate flows characterized by large diffusivity coefficient (like viscosity or conductivity). Finally, the Cartesian grid allows to import a complex geometry without meshing process in opposite to classical computational fluid dynamics (CFD) solvers.

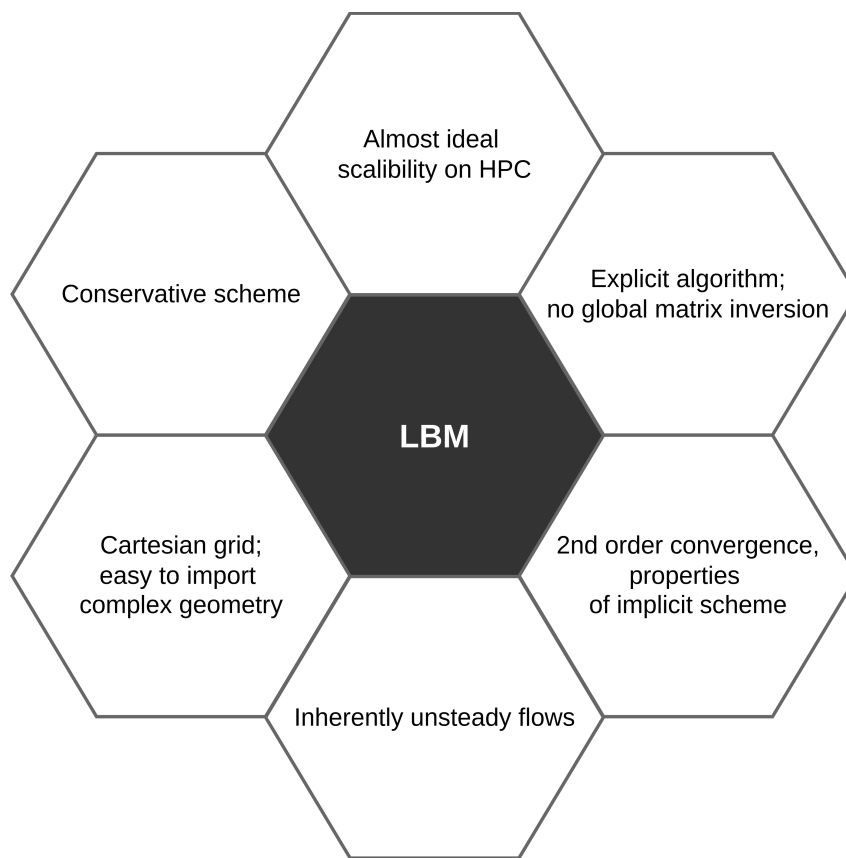


FIGURE 2.5: LBM features.

Chapter 3

The collision kernels

“The first casualty when war comes is truth.”

– Hiram Johnson

Contents

3.1 Collision space	29
3.2 Discretisation of the velocity space	30
3.3 Moments of the distribution	31
3.3.1 Aliasing of moments	34
3.4 Discretisation of the equilibrium distribution function	34
3.5 Transformation matrices	37
3.6 Two Relaxation Time (TRT)	39
3.6.1 TRT in central moments space	41

In this chapter a closer look at selected collision kernels and relaxation strategies is provided.

3.1 Collision space

During the last decades, a variety of collision operators have been proposed. For the detailed discussion of this subject, the reader is referred to the comparative works [11, 12, 13] and established textbooks [9, 10]. Substantial effort was made to use the mutual independence of the observable quantities (such as density, momentum, stress tensor components, etc.) to separate their relaxation frequencies and improve stability. In the simplest form of the collision operator, a single relaxation time (SRT) is assigned to all distribution

functions. The next concept follows from the fact that the observable quantities can be found as moments of the distribution function [38, 9]. As different relaxation rates can be assigned to each moment, the MRT name has been coined [38]. The moments can be calculated in stationary or moving reference frame and are refereed as raw or central moments (CM) respectively [39]. A method, in which the relaxation rates of odd and even raw moments are separated has been originally proposed by Ginzburg [40], and is known as two relaxation time (TRT).

The proper choice of the combination of moments used during the collision step plays important role for the stability of the scheme. Dubois *et al.* [41] have benchmarked two frequently used sets in the contexts of NS equations. Some researchers argue that the orthogonalisation of the transformation from distribution function to the moments' space shall limit the *cross-talk* between the moments [42]. On the other hand Geier *et al.* [43, Appendix I] stated that the orthogonalisation process can be the source of spurious couplings. As a remedy, a more complex, non-linear, statistically independent quantities known as cumulants has been proposed in [43]. The cumulants can be calculated from the distribution function. Their use in the LBM framework resulted in the formulation of the Cumulant Lattice Boltzmann Method, which exhibited very promising numerical properties [43, 44].

3.2 Discretisation of the velocity space

Discretisation of the velocity space in the Lattice Boltzmann Method corresponds to the number of links between each of the neighbouring nodes in the lattice. In general, the choice of the discrete velocity set is dictated by the target macroscopic equation. On the one hand, large velocity sets are expected to provide more accurate [45] and stable solutions [46]. On the other hand, they contribute to increased memory consumption, computational and communication cost, as well as complexity of boundary conditions. The velocity sets are commonly described using $DdQq$ notation, where d corresponds to the number of spatial dimensions and q accounts for the number of discrete velocities.

In order to formally discuss different LBM schemes, the concept of moments of the distribution is introduced in this section. The general formulations is first presented for the D3Q27 lattice (utilized in Chapter 9), as restrictions to smaller lattices or to two dimensions can be easily derived. Using the Euclidean basis, the discrete velocities for a

D3Q27 lattice, shown in Fig. 3.1, read,

$$\mathbf{e} = [\mathbf{e}_x, \mathbf{e}_y, \mathbf{e}_z], \quad (3.1)$$

$$\mathbf{e}_x = [0, 1, 0, 0, 1, 1, 0, -1, 0, 0, 1, 1, -1, -1, 0, 0, 1, -1, -1, 0, -1, 1, 1, 1, -1, -1, -1]^\top, \quad (3.2)$$

$$\mathbf{e}_y = [0, 0, 1, 0, 1, 0, 1, 0, -1, 0, -1, 0, 1, 0, 1, -1, 1, -1, 0, -1, 1, -1, 1, -1, 1, -1, -1]^\top, \quad (3.3)$$

$$\mathbf{e}_z = [0, 0, 0, 1, 0, 1, 1, 0, 0, -1, 0, -1, 0, 1, -1, 1, 1, 0, -1, -1, 1, 1, -1, -1, -1, 1, -1]^\top. \quad (3.4)$$

Obviously, a different set of velocity vectors \mathbf{e} can be chosen for the evolution of \mathbf{f} and \mathbf{h}

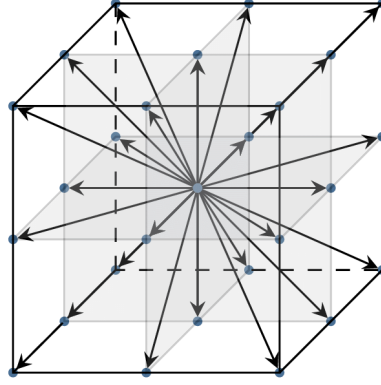


FIGURE 3.1: A D3Q27 stencil.

distributions.

3.3 Moments of the distribution

The moments of distribution function can be calculated in a stationary or a moving reference frame [39]. The so-called *cascaded* or central moments are moments calculated in a reference frame, moving with the local macroscopic velocity, \mathbf{u} . The discrete, raw and central moments are defined as,

$$\Upsilon_{mno}^G = \sum_i (e_{ix})^m (e_{iy})^n (e_{iz})^o g_i, \quad (3.5)$$

$$\kappa_{mno}^G = \sum_i (e_{ix} - u_x)^m (e_{iy} - u_y)^n (e_{iz} - u_z)^o g_i, \quad (3.6)$$

where mno is a three-index, spanning triplets of positive numbers. As many equations are formulated analogously for both \mathbf{f} and \mathbf{h} , the letter \mathbf{g} will be used as placeholder for both of these distribution functions. Notice, that for a fixed set of three-indexes mno , the Equations (3.5) and (3.6) forming the raw, \mathcal{M} , and central moment, $\tilde{\mathcal{M}}$, transforms can be expressed as matrix multiplication [47, 48, 49],

$$\Upsilon^G = \mathcal{M}(\mathbf{g}) = \mathbb{M}\mathbf{g}, \quad (3.7)$$

$$\kappa^G = \tilde{\mathcal{M}}(\mathbf{g}) = \mathbb{N}\Upsilon^G, \quad (3.8)$$

where Υ and κ denote the vector containing raw and central moments, respectively. It is essential that \mathbb{M} is a fixed matrix while the shift matrix, \mathbb{N} , is dependent on the fluid velocity, \mathbf{u} . We select all indexes mno for which m , n and o are less than 3, in the following order: [000, 100, 010, 001, 110, 101, 011, 200, 020, 002, 120, 102, 210, 201, 012, 021, 111, 220, 202, 022, 211, 121, 112, 122, 212, 221, 222]. This choice of 27 moments results in non-singular square matrices \mathbb{M} and \mathbb{N} , making the \mathcal{M} and $\tilde{\mathcal{M}}$ operators reversible. Remarks regarding assembling of the matrices can be found in Section 3.5.

Now, let us adopt the D2Q9 lattice for illustrational purposes. It is the most popular choice for discretisation of 2D problems. Here, the lattice velocities, \mathbf{e}_i , and weight coefficients are defined as,

$$\mathbf{e} = [\mathbf{e}_x, \mathbf{e}_y], \quad (3.9)$$

$$\mathbf{e}_x = [0, 1, 0, -1, 0, 1, -1, -1, 1]^\top, \quad (3.10)$$

$$\mathbf{e}_y = [0, 0, 1, 0, -1, 1, 1, -1, -1]^\top, \quad (3.11)$$

$$\mathbf{w} = \left[\frac{4}{9}, \frac{1}{9}, \frac{1}{9}, \frac{1}{9}, \frac{1}{9}, \frac{1}{36}, \frac{1}{36}, \frac{1}{36}, \frac{1}{36} \right]. \quad (3.12)$$

For moments of LBM densities, g , shifted densities \tilde{g} , post-collision densities, \tilde{g}_i^* , equilibrium distribution, g^{eq} and source term, q , we will use Υ , $\tilde{\Upsilon}$, $\tilde{\Upsilon}^*$, Υ^{eq} and \mathbf{R} respectively.

As the set of densities is finite, and the velocities \mathbf{e} are distinct, one can select a finite set of linearly independent moments to fully represent any set of densities. For the D2Q9 lattice, the following set of moments is chosen,

$$\Upsilon = \left[\Upsilon_{00} \quad \Upsilon_{10} \quad \Upsilon_{01} \quad \Upsilon_{20} \quad \Upsilon_{02} \quad \Upsilon_{11} \quad \Upsilon_{21} \quad \Upsilon_{12} \quad \Upsilon_{22} \right]^\top. \quad (3.13)$$

It is convenient to express LBM schemes in terms of moments, and not densities

themselves. This is because they represent specific mechanics and have physical interpretations, which the densities themselves do not possess. The LBM collision operator defined in equation Equation (2.31), can be expressed using moments as,

$$\tilde{\mathbf{\Upsilon}}^*(\mathbf{x}, t) = (1 - s)\tilde{\mathbf{\Upsilon}}(\mathbf{x}, t) + s\mathbf{\Upsilon}^{\text{eq}}(\phi, \mathbf{u}) + (1 - \frac{s}{2})\mathbf{R}(\phi, \mathbf{u}, \mathbf{x}, t). \quad (3.14)$$

The moments of the discrete equilibrium, $\mathbf{\Upsilon}^{\text{eq}}$, are defined to be equal to moments of the continuous Maxwell-Boltzmann distribution function, $\mathbf{\Upsilon}^{\text{eq}}(\phi, \mathbf{u}) = \phi \mathbf{\Gamma}(\mathbf{u})$, where,

$$\mathbf{\Gamma}(\mathbf{u}) = \begin{bmatrix} 1 \\ u_x \\ u_y \\ c_s^2 + u_x^2 \\ c_s^2 + u_y^2 \\ u_x u_y \\ u_y(c_s^2 + u_x^2) \\ u_x(c_s^2 + u_y^2) \\ c_s^4 + c_s^2(u_x^2 + u_y^2) + u_x^2 u_y^2 \end{bmatrix}^{\top}. \quad (3.15)$$

One can clearly see that these moments fulfil the conditions required for representation of the advection-diffusion-reaction equation by the DBE. A common choice of the speed of sound c_s is $1/\sqrt{3}$, which reduces the error in higher moments. The moments of the equilibrium distribution are truncated by some authors on the second order terms [31, 50, 51, 45, 52, 53, 54, 55, 56, 57], by not including the terms $u_x^2 u_y$, $u_x u_y^2$ and $u_x^2 u_y^2$. Furthermore, it can be truncated at first-order terms [58, 59, 60, 61, 62] giving,

$$\mathbf{\Gamma}^{\text{1st order}}(\mathbf{u}) = \begin{bmatrix} 1 & u_x & u_y & c_s^2 & c_s^2 & 0 & u_y c_s^2 & u_x c_s^2 & c_s^4 \end{bmatrix}^{\top}. \quad (3.16)$$

Formulas analogous to Equation (3.15) can be used for the D2Q5 lattice [63]. Similarly, the moments of the source term can be expressed as $\mathbf{R} = Q(\phi, \mathbf{x}, t) \mathbf{\Gamma}(\mathbf{u})$. Again, some authors simplify the source term by truncating the velocity of the equilibrium distribution function (EDF) [64, 58]. Investigation of an error related to the order of velocity expansion in the EDF has been conducted by Chopard *et al.* [65]. It has been shown that the full order velocity expansion enhances both the Galilean invariance [39, 66, 67, 68, 69] and stability of the LBM schemes [39, 69].

3.3.1 Aliasing of moments

The aliasing error causes some of the discrete moments to be indistinguishable from the others. For example, if the discrete velocities are contained in a $\{-1, 0, 1\}$ set, then $(e_i^j)^3 = e_i^j$. The first moment of the normal distribution is equal to its mean value μ , while the third order moment shall be $\mu^3 + 3\mu\sigma^2$. To reduce the aliasing error, the variance is usually set to $\sigma^2 = c_s^2 = 1/3$. In case of the hydrodynamic distributions, f , their mean, μ , corresponds to the macroscopic velocity u , thus the aforementioned error is one of the sources of the lack of the Galilean invariance in LBM schemes [43].

3.4 Discretisation of the equilibrium distribution function

Before the derivations, it is useful to comment on the factors influencing Galilean invariance and stability within the LB framework. The first issue concerning Galilean invariance originates from the use of standard lattices, which suffer from the aliasing of the third-order longitudinal moments, namely $e_{\alpha i}^3 = e_{\alpha i}$. Prasianakis et al. [70] and Geier et al. [43] sought to alleviate this issue by formulating correction terms within the standard lattice formulation. Nie et al. [66] took a different approach in which the LB scheme was extended to higher-order lattices, typically referred to as multispeed methods. According to the work of Geier et al. [39], it does not appear possible to recover the full Galilean invariance of the hydrodynamic shear rate in three dimensions when implementing a standard LBM on lower-order lattices such as the D3Q13, D3Q15, and D3Q19. Moreover, simulation of a thermal field on such a lattice could lead to defects in recovering critical Rayleigh number [45].

Secondly, the truncation order of the equilibrium distribution function has also been recognized to significantly impact the Galilean invariance of the flow [66, 67, 69]. Nie et al. [66] and De Rosi and Luo [69] were able to show that Hermite polynomials up to the sixth order were required to recover the central moments of the continuous, Maxwellian equilibrium distribution function through its discrete analog. If a lower order is used, such as the second order equilibrium commonly seen in LB schemes, the error can manifest as a *cubic* velocity dependence on the viscosity [66]. Further, De Rosi and Luo [69] supplemented their study with a linear stability analysis of the collision operator as a function of Mach number, relaxation frequency and the order of the discrete equilibrium. Similar remarks apply to the forcing term in CLBM. With the exception of the *exact*

difference method [71], the forcing schemes typically used in CLBM are built from the method derived by He et al. [22]. Premnath et al. [72] presented the extension of this into the central moments' formulation. Furthermore, Huang et al. [73] was able to show the relationship between the forcing scheme of Guo et al. [27] and the discrete, as well as continuous, schemes of He et al. [22]. Again, the difference stems from the order of the Hermite polynomial expansion used for the forcing term. As expected, an approximation which uses the full set of Hermite polynomials converges to the results obtained with a continuous equilibrium. For a discussion on the recent developments of various forcing schemes, the interested reader is pointed to the work of Fei et al. [48, 67] and Huang et al. [73].

Finally, the Galilean invariance can further deteriorate as a result of unfavourable coupling between moments of the distribution functions. Some of these spurious couplings can be removed through a non-uniform weight function in the orthogonalization process. This was shown in 2D by Dellar [74], and extended to 3D in the context of multiphase flows by Fakhari et al. [75], in what was termed the weighted multiple-relaxation-time method. Geier et al. [39] proposed an alternative solution in the form of the *Cascaded* LBM. An interesting example of the coupling between moments has been observed in the MRT collision kernel commonly introduced into the single-population, multispeed LBM for thermal flows. Although the kernel facilitated simulations with variable Prandtl number, it coupled the thermal conductivity with the velocity of the flow. Chen et al. [76] solved the problem by recognizing that the moment corresponding to energy flux must be expressed as an eigenvector of the collision matrix in the relative reference frame.

In addition to Galilean invariance, the stability of collision kernels plays a significant role in their selection and practical use. The ability to suppress higher-order, non-hydrodynamic, *ghost* moments, such as in models with multiple relaxation rates or regularization techniques, has been observed to significantly increase the range of achievable simulation parameters [77, 78].

Some authors favour the usage of the Hermite polynomials to discretise the equilibrium distribution function [69, 79]. In this section, an common alternative [39] is discussed. Let us remind Equation (2.17), which describes the continuous Maxwell-Boltzmann distribution,

$$\Psi^{M-B, eq} = \Psi^{M-B, eq}(\phi, \boldsymbol{\xi}, \mathbf{u}) = \frac{\phi}{(2\pi c_s^2)^{N/2}} \exp \left[-\frac{(\boldsymbol{\xi} - \mathbf{u})^2}{2c_s^2} \right],$$

The definition of the raw and central moments for a continuous distribution is,

$$\Upsilon_{mn} = \int_{-\infty}^{\infty} \int_{-\infty}^{\infty} (\xi_x)^m (\xi_y)^n \Psi(\phi, \boldsymbol{\xi}, \mathbf{u}) d\xi_x d\xi_y, \quad (3.17)$$

$$\kappa_{mn} = \int_{-\infty}^{\infty} \int_{-\infty}^{\infty} (\xi_x - u_x)^m (\xi_y - u_y)^n \Psi(\phi, \boldsymbol{\xi}, \mathbf{u}) d\xi_x d\xi_y. \quad (3.18)$$

To illustrate the analysis with a relatively short example, a D2Q9 lattice with the following order of the raw/central moments is investigated,

$$\boldsymbol{\Upsilon} = [\Upsilon_{00}, \Upsilon_{10}, \Upsilon_{01}, \Upsilon_{20}, \Upsilon_{02}, \Upsilon_{11}, \Upsilon_{21}, \Upsilon_{12}, \Upsilon_{22}]^{\top}. \quad (3.19)$$

$$\boldsymbol{\kappa} = [\kappa_{00}, \kappa_{10}, \kappa_{01}, \kappa_{20}, \kappa_{02}, \kappa_{11}, \kappa_{21}, \kappa_{12}, \kappa_{22}]^{\top}. \quad (3.20)$$

The resulting moments and central moments are,

$$\boldsymbol{\Upsilon}^{\phi,eq} = \Upsilon_{00}^{\phi} \begin{bmatrix} 1 \\ u_x \\ u_y \\ (u_x^2 + c_s^2) \\ (u_y^2 + c_s^2) \\ u_x u_y \\ u_y (u_x^2 + c_s^2) \\ u_x (u_y^2 + c_s^2) \\ (u_x^2 u_y^2 + c_s^2 u_x^2 + c_s^2 u_y^2 + c_s^4) \end{bmatrix} = \Upsilon_{00}^{\phi} \boldsymbol{\Gamma}(\mathbf{u}), \quad (3.21)$$

$$\boldsymbol{\kappa}^{\phi,eq} = \Upsilon_{00}^{\phi} \begin{bmatrix} 1 \\ 0 \\ 0 \\ c_s^2 \\ c_s^2 \\ 0 \\ 0 \\ 0 \\ c_s^4 \end{bmatrix}. \quad (3.22)$$

where Υ_{00}^{ϕ} is the zeroth order moment of the quantity of interest. For example, to express the internal energy one would substitute $\phi = \Upsilon_{00}^{\phi} = H = \rho c_v T$.

In general, the central moments of a physical quantity being in equilibrium should be

independent of the velocity. Next, the discrete equilibrium distribution and source term can be obtained using backward transformation from moments space,

$$\mathbf{h}^{eq} = \mathbb{M}^{-1} \boldsymbol{\kappa}^{\phi,eq}, \quad (3.23)$$

$$\mathbf{q} = \mathbb{M}^{-1} \mathbf{R}, \quad (3.24)$$

or from the central moments space

$$\mathbf{h}^{eq} = \mathbb{M}^{-1} \mathbb{N}^{-1} \boldsymbol{\kappa}^{\phi,eq}, \quad (3.25)$$

$$\mathbf{q} = \mathbb{M}^{-1} \mathbb{N}^{-1} \mathbf{R}, \quad (3.26)$$

and the result is the same as in case of full order Hermite expansion [69, 79].

3.5 Transformation matrices

The transformation from raw to central moments can be obtained by application of the shift matrix, \mathbb{N} . This matrix was originally introduced by Asinari [47], and later, reformulated by De Rosis [80]. De Rosis' approach allowed the distribution functions to be transformed directly into central moments, without first transforming into moment space. Unfortunately, the obtained matrix is dense. Moreover, each element is filled with lengthy expressions. As a consequence, the *one step* transformation is computationally costly.

The shift matrix proposed by Asinari [47] is sparser. As a result, it is more suitable to be symbolically inverted and used for automatic generation of efficient code.

From the computational point of view, it is preferred to perform the transformations to the central moments space in two steps, using Equations (3.7) and (3.8). Since

$$\boldsymbol{\kappa} = \mathbb{T} \mathbf{g} = \mathbb{N} \mathbb{M} \mathbf{g}, \quad (3.27)$$

the \mathbb{N} matrix can be easily found as

$$\mathbb{N} = \mathbb{T} \mathbb{M}^{-1}. \quad (3.28)$$

Rows of the transformation matrices are calculated analogously to Υ and κ . For a D3Q27 lattice, each row consists of $q \in \{1, 2, \dots, 27\}$ elements,

$$\mathbf{M}_{mno} = \left[M_{mno}|_1, M_{mno}|_2, \dots, M_{mno}|_i, \dots, M_{mno}|_{q-1}, M_{mno}|_q \right], \quad (3.29)$$

$$\mathbf{T}_{mno} = \left[T_{mno}|_1, T_{mno}|_2, \dots, T_{mno}|_i, \dots, T_{mno}|_{q-1}, T_{mno}|_q \right]. \quad (3.30)$$

The mno subscript refers to the order of moment, while i - th subscript indicates the index of the element in the \mathbf{M}_{mno} row. Each element can be calculated as,

$$M_{mno}|_i = (e_{ix})^m (e_{iy})^n (e_{iz})^o, \quad (3.31)$$

$$T_{mno}|_i = (e_{ix} - u_x)^m (e_{iy} - u_y)^n (e_{iz} - u_z)^o. \quad (3.32)$$

Next, the matrices are assembled row by row as,

$$\mathbb{M} = [\mathbf{M}_{000}, \mathbf{M}_{100}, \mathbf{M}_{010}, \mathbf{M}_{001}, \mathbf{M}_{110}, \mathbf{M}_{101}, \mathbf{M}_{011}, \mathbf{M}_{200}, \mathbf{M}_{020}, \mathbf{M}_{002}, \dots, \mathbf{M}_{ijk}, \dots, \mathbf{M}_{222}]^\top,$$

$$\mathbb{T} = [\mathbf{T}_{000}, \mathbf{T}_{100}, \mathbf{T}_{010}, \mathbf{T}_{001}, \mathbf{T}_{110}, \mathbf{T}_{101}, \mathbf{T}_{011}, \mathbf{T}_{200}, \mathbf{T}_{020}, \mathbf{T}_{002}, \dots, \mathbf{T}_{ijk}, \dots, \mathbf{T}_{222}]^\top.$$

For the D2Q9 lattice, utilized in Chapters 4 and 11, the matrices are presented below.

$$\mathbb{M} = \begin{bmatrix} 1 & 1 & 1 & 1 & 1 & 1 & 1 & 1 & 1 \\ 0 & 1 & 0 & -1 & 0 & 1 & -1 & -1 & 1 \\ 0 & 0 & 1 & 0 & -1 & 1 & 1 & -1 & -1 \\ 0 & 1 & 0 & 1 & 0 & 1 & 1 & 1 & 1 \\ 0 & 0 & 1 & 0 & 1 & 1 & 1 & 1 & 1 \\ 0 & 0 & 0 & 0 & 0 & 1 & -1 & 1 & -1 \\ 0 & 0 & 0 & 0 & 0 & 1 & 1 & -1 & -1 \\ 0 & 0 & 0 & 0 & 0 & 1 & -1 & -1 & 1 \\ 0 & 0 & 0 & 0 & 0 & 1 & 1 & 1 & 1 \end{bmatrix}, \quad (3.33)$$

$$\mathbb{N} = \begin{bmatrix} 1 & 0 & 0 & 0 & 0 & 0 & 0 & 0 & 0 \\ -u_x & 1 & 0 & 0 & 0 & 0 & 0 & 0 & 0 \\ -u_y & 0 & 1 & 0 & 0 & 0 & 0 & 0 & 0 \\ u_x^2 & -2u_x & 0 & 1 & 0 & 0 & 0 & 0 & 0 \\ u_y^2 & 0 & -2u_y & 0 & 1 & 0 & 0 & 0 & 0 \\ u_x u_y & -u_y & -u_x & 0 & 0 & 1 & 0 & 0 & 0 \\ -u_x^2 u_y & 2u_x u_y & u_x^2 & -u_y & 0 & -2u_x & 1 & 0 & 0 \\ -u_y^2 u_x & u_y^2 & 2u_x u_y & 0 & -u_x & -2u_y & 0 & 1 & 0 \\ u_x^2 u_y^2 & -2u_x u_y^2 & -2u_y u_x^2 & u_y^2 & u_x^2 & 4u_x u_y & -2u_y & -2u_x & 1 \end{bmatrix}. \quad (3.34)$$

The matrices have been given explicitly by Fei et al. [68], which originates from the work of Asinari [47]. The matrices can also be obtained using Equation (3.28) which was not explained clearly in [47, 68].

3.6 Two Relaxation Time (TRT)

The two relaxation time (TRT) collision operator was shown to have superior accuracy and stability [40, 81, 82, 83, 84, 85] when compared to the SRT one. The TRT approach consists of decomposing the distribution function into even (symmetric) and odd (anti-symmetric) components [40],

$$h_i^{even} = \frac{h_i + h_{\bar{i}}}{2},$$

$$h_i^{odd} = \frac{h_i - h_{\bar{i}}}{2},$$

where $\bar{i} = -i$. The discrete equilibrium distribution is treated analogously,

$$\begin{aligned} h_i^{even-eq} &= \frac{h_i^{eq} + h_{\bar{i}}^{eq}}{2}, \\ h_i^{odd-eq} &= \frac{h_i^{eq} - h_{\bar{i}}^{eq}}{2}. \end{aligned}$$

The collision reads (the source term is omitted for simplicity),

$$\mathbf{h}^*(\mathbf{x}, t) = \mathbf{h} + s_{even}[\mathbf{h}^{even-eq} - \mathbf{h}^{even}] + s_{odd}[\mathbf{h}^{odd-eq} - \mathbf{h}^{odd}]. \quad (3.35)$$

Multiplying by \mathbb{M} , the scheme can be transferred to the moment space

$$\Upsilon^{\phi,*}(\mathbf{x}, t) = \Upsilon^{\phi} + s_{even}[\Upsilon^{\phi,even,eq} - \Upsilon^{\phi,even}] + s_{odd}[\Upsilon^{\phi,odd-eq} - \Upsilon^{\phi,odd}]. \quad (3.36)$$

The TRT approach requires the odd-moments, to be relaxed with a common rate s_{odd} , while the even moments, with s_{even} . When the combination of odd and even relaxation rates is kept constant, then the steady state, non-dimensional solution of NS or advection-diffusion equation (ADE) is *exactly* controlled by the similarity numbers (Reynolds number, Péclet number, etc.) [85]. The so called magic parameter has been defined as,

$$\Lambda = \left(\frac{1}{s_{odd}} - \frac{1}{2} \right) \left(\frac{1}{s_{even}} - \frac{1}{2} \right). \quad (3.37)$$

Fixing the magic parameter at specific constant values, results in a minimisation of specific types of discretisation errors, and can improve stability and or accuracy of commonly used boundary conditions [40, 85].

It is interesting to observe, that vectors describing $\{\Upsilon^{\phi,even,eq}, \Upsilon^{\phi,even}\}$ and $\{\Upsilon^{\phi,odd}, \Upsilon^{\phi,odd}\}$ contain elements with zero values at the same indices (see Equations (3.43) and (3.44)). In other words, the symmetric component, h_j^{even} , has only even order moments, and the anti-symmetric, h_j^{odd} , component has only odd order moments that are non-zero.

The relaxation matrix \mathbb{S}^{ϕ} is diagonal. It has s_{odd} in rows corresponding to moments of odd order, and s_{even} otherwise. For D2Q9 the matrix is as follows,

$$\mathbb{S}^{\phi} = \text{diag}([s_{even}, s_{odd}, s_{odd}, s_{even}, s_{even}, s_{even}, s_{odd}, s_{odd}, s_{even}]). \quad (3.38)$$

In case of the ADRE, the relaxation rate for odd moments, s_{odd} , has to correspond to the macroscopic diffusion coefficient, k ,

$$s_{odd} = \frac{1}{\frac{k}{c_s^2 \delta t} + 1/2}. \quad (3.39)$$

This means that the Equation (3.36) can be simplified further to:

$$\begin{aligned} \Upsilon^{\phi,*}(\mathbf{x}, t) &= \Upsilon^\phi + \mathbb{S}^H(\Upsilon^{\phi,eq} - \Upsilon^\phi) \\ &= (\mathbb{I} - \mathbb{S}^\phi)\Upsilon^\phi + \mathbb{S}^\phi\Upsilon^{\phi,eq}. \end{aligned} \quad (3.40)$$

This means that the non-orthogonal matrix of raw moments, \mathbb{M} , provided in Equation (3.33), diagonalises the TRT collision operator [47]. For additional information on the TRT method, the interested reader is directed to the work of Ginzburg [40], although this particular property has not been explicitly stated there.

3.6.1 TRT in central moments space

The transformation to the central moments space can be performed in two ways. In the first approach, which follows the original idea of Ginzburg [40, 81], the Equation (3.36) is multiplied by \mathbb{N} ,

$$\kappa^{\phi,*}(\mathbf{x}, t) = \kappa^\phi + s_{even}[\kappa^{\phi,even-eq} - \kappa^{\phi,even}] + s_{odd}[\kappa^{\phi,odd-eq} - \kappa^{\phi,odd}]. \quad (3.41)$$

In the second approach, the Equation (3.40) is transformed,

$$\begin{aligned} \kappa^{\phi,*}(\mathbf{x}, t) &= \kappa^\phi + \mathbb{S}^\phi(\kappa^{\phi,eq} - \kappa^\phi) \\ &= (\mathbb{I} - \mathbb{S}^\phi)\kappa^\phi + \mathbb{S}^\phi\kappa^{\phi,eq}. \end{aligned} \quad (3.42)$$

As the structure of $\{\kappa^{\phi,even-eq}, \kappa^{\phi,even}\}$ vectors (see Equation (3.46)) do not contain zero elements, thus the Equation (3.41) does not collapse to Equation (3.42).

In Chapter 9, the full order, discrete equilibrium distribution function given in Equation (3.25) is used to express $h_i^{even-eq}$ and h_i^{odd-eq} . Their moments can be calculated using

Equations (3.5) and (3.6),

$$\Upsilon^{\phi, even-eq} = \Upsilon_{00}^{\phi} \begin{bmatrix} 1 \\ 0 \\ 0 \\ u_x^2 + c_s^2 \\ u_y^2 + c_s^2 \\ u_x u_y \\ 0 \\ 0 \\ u_x^2 u_y^2 + c_s^2 u_x^2 + c_s^2 u_y^2 + c_s^4 \end{bmatrix}, \quad \Upsilon^{\phi, odd-eq} = \Upsilon_{00}^{\phi} \begin{bmatrix} 0 \\ u_x \\ u_y \\ 0 \\ 0 \\ 0 \\ u_y (u_x^2 + c_s^2) \\ u_x (u_y^2 + c_s^2) \\ 0 \end{bmatrix}. \quad (3.43)$$

The moments of symmetric and anti-symmetric distribution function exhibits analogous structure,

$$\Upsilon^{\phi, even} = \begin{bmatrix} \Upsilon_{00}^{\phi} \\ 0 \\ 0 \\ \Upsilon_{20}^{\phi} \\ \Upsilon_{02}^{\phi} \\ \Upsilon_{11}^{\phi} \\ 0 \\ 0 \\ \Upsilon_{22}^{\phi} \end{bmatrix}, \quad \Upsilon^{\phi, odd} = \begin{bmatrix} 0 \\ \Upsilon_{10}^{\phi} \\ \Upsilon_{01}^{\phi} \\ 0 \\ 0 \\ 0 \\ \Upsilon_{21}^{\phi} \\ \Upsilon_{12}^{\phi} \\ 0 \end{bmatrix}. \quad (3.44)$$

These results extend the analysis done in [57], which was limited to raw, second-order moments and truncated (to linear and quadratic velocity terms) discrete equilibrium

function. Finally, the central moments are,

$$\boldsymbol{\kappa}^{\phi, even, eq} = \Upsilon_{00}^{\phi} \begin{bmatrix} 1 \\ -u_x \\ -u_y \\ 2u_x^2 + c_s^2 \\ 2u_y^2 + c_s^2 \\ 2u_x u_y \\ -u_y (4u_x^2 + c_s^2) \\ -u_x (4u_y^2 + c_s^2) \\ 8u_x^2 u_y^2 + 2c_s^2(u_x^2 + u_y^2) + c_s^4 \end{bmatrix}, \quad (3.45)$$

$$\boldsymbol{\kappa}^{\phi, odd, eq} = \Upsilon_{00}^{\phi} \begin{bmatrix} 0 \\ u_x \\ u_y \\ -2u_x^2 \\ -2u_y^2 \\ -2u_x u_y \\ u_y (4u_x^2 + c_s^2) \\ u_x (4u_y^2 + c_s^2) \\ -(8u_x^2 u_y^2 + 2c_s^2(u_x^2 + u_y^2)) \end{bmatrix}. \quad (3.46)$$

Chapter 4

Reactions

“Be careful how you are talking to yourself because you are listening.”

– Lisa M. Hayes

Content of this chapter is has been submitted for publication. The manuscript is available online [3].

Contents

4.1 Introduction	46
4.1.1 Discussion on the state of the art	47
4.1.2 Structure	50
4.2 Model description	50
4.2.1 The collision operator	50
4.2.2 Streaming	51
4.3 Scaling of LBM	51
4.4 Model verification and validation	52
4.4.1 Linear advection-diffusion-reaction model	53
4.4.2 The Allen-Cahn equation	
— illustrative advection-diffusion-reaction problem.	57
4.5 Comparison of approaches to the source term integration	67
4.6 Conclusions	68
4.7 Future outlook - system of equations	70

This chapter analyses an approach to consistently recover the second-order convergence of the LBM, which is frequently degraded by an improper discretisation of the required source terms. The attention is focused on advection-diffusion-reaction models, in

which the source terms are dependent on the intensity of transported fields. Such terms can be observed in reaction-type equations used in heat and mass transfer problems or multiphase flows. The investigated scheme is applicable to a wide range of formulations within the LBM framework. All considered source terms are interpreted as contributions to the zeroth-moment of the distribution function. These account for sources in a scalar field, such as density, concentration, temperature or a phase field. Further application of this work can be found in the method of manufactured solutions or in the immersed boundary method.

The second-order convergence of the proposed LBM schemes is verified on both linear and non-linear source terms. The pitfalls of the commonly used acoustic and diffusive scaling are identified and discussed. Furthermore, for a simplified case, the competing errors are shown visually with isolines of error in the space of spatial and temporal resolutions.

4.1 Introduction

In general, the explicitness of the scheme and the second-order convergence of the LBM is known in the literature [31, 9]. Unfortunately, it may be easily degraded through inconsistent discretisation of the source terms. This may lead to excessive computational requirements to achieve accuracies observed in other formulations. In this chapter, we will focus on advection-diffusion-reaction equation (see Equation (2.22)),

$$\frac{\partial}{\partial t}\phi + \nabla \cdot (\mathbf{u}\phi) = \nabla \cdot (M\nabla\phi) + Q(\phi, \mathbf{x}, t), \quad (4.1)$$

where the source term, Q , is dependent on ϕ itself, i.e., $Q = Q(\phi)$. To the best of the author's knowledge, such a form has not been analysed in the literature. Integration of the DBE with trapezoidal rule leads to implicit expressions. To transform them into an explicit scheme, a shift (redefinition) of variables is used [31, 9]. The resulting relation between the macroscopic field, ϕ , and the shifted one, $\tilde{\phi}$, can be expressed as (see Section 2.3 for details),

$$\phi - \frac{1}{2}Q(\phi, \mathbf{x}, t) = \tilde{\phi}. \quad (4.2)$$

However, in the case of Q dependent on the ϕ , the Equation (4.2) is implicit itself and potentially non-linear. The detailed analysis of this issue is the primary concern of the current work.

Finally, we clarify the potential confusion related to the way in which the convergence LBM is investigated. In classical numerical methods, spatial convergence is tested by varying the domain resolution while holding a fine, fixed time step. The idea is to keep the error of temporal discretisation much smaller than the spatial one or vice versa. Due to the relatively narrow range of parameters for which LBM is stable, its convergence is usually investigated for a special relationship between spatial and temporal scales. Usually, these relationships follow the rules of so-called acoustic and diffusive scaling. As a consequence, a biased view of convergence may be reported by looking solely at either spatial or temporal resolution, while the corresponding errors can converge at different rates. The naive discretisation of the source term (assuming $\phi = \tilde{\phi}$) reduces the order of convergence in the case of acoustic scaling. On the other hand, we will demonstrate that the same order of convergence can still be observed even for the improper treatment of the source term under diffusive scaling.

4.1.1 Discussion on the state of the art

From an application point-of-view, there is a wide range of physical phenomena which can be described by a form of the advection-diffusion-reaction equation. Models based on the LBM were developed for processes such as multicomponent reaction [86], combustion [87], solid and fluid dissolution related to underground CO_2 storage [88, 89], crystallization and melting [53, 90], Joule heating in electro-osmotic flows [91] and heat transfer [31, 50, 51, 92, 45, 93, 68, 63, 94, 95, 96]. Last but not least, the numerical solvers can be verified by the method of manufactured solutions [97, 98, 99] in which the source term modelling is extensively used. Selected studies involving the use of LBM are listed below to present both the scope of modelling approaches, and applicability of the concepts discussed in this work.

One of the earliest studies in which the LBM framework was applied to simulate reaction-diffusion equations has been conducted by Dawson *et al.* [100] in 1993. The group investigated the classical Selkov model (originating from biological studies of glycolysis). They used a hexagonal lattice with a BGK relaxation model and an explicit first-order integration of source term. The proposed technique was used to simulate pure diffusion, homogenous reaction and the formation of Turing patterns. Later, the model was reformulated on a square lattice by Blaak and Sloot [101]. The first order approximation of the source term was present in both works.

Arguably, the most widely explored application of the advection-diffusion LBM is found in coupled flow-heat transfer problems [31, 50, 51, 92, 45, 93, 68, 63, 94, 95, 96]. To model the underlying physics, a two-population approach is frequently used. One of the populations simulates the motion of the fluid, while the second one uses some form of the energy balance equation to resolve the heat transfer. The primary benefit of using the same numerical framework for fluid flow and heat transfer is that it greatly simplifies the computational implementation.

The LBM framework has also been extended to capture the conjugate heat transfer and or phase change between solid and liquid phases. Huang *et al.* [53, 90] incorporated the term responsible for the latent heat of fusion into the equilibrium distribution function. As a result, moments of equilibrium have been adjusted to recover the desired PDE. A similar effect has been obtained by Hosseini *et al.* [62], who presented a set of weight coefficients to tune the second-order moments of a source-like term, which was added to the equilibrium distribution function. Karani and Huber [60], and later Chen *et al.* [61], studied the macroscopic energy equation suitable to model conjugate heat transfer in comparison with the standard ADE. The difference was expressed as a corrective source term, and was added to the standard LBM routine for the ADRE to obtain the correct energy balance. While the aforementioned works [60, 61, 62] introduce a source term specific for conjugate heat transfer problems, they do not discuss its treatment which potentially leads to the use of explicit first-order schemes. Interested readers are referred to a comprehensive review of methods related to phase-change, heat transfer and multiphase flows by Li *et al.* [102].

The source term technique can be also used to implement a boundary condition on a moving or curved wall. The intensity of the heat source is adjusted in each iteration to match the Dirichlet, Neumann, or Robin boundary condition. Models that use this technique are commonly referred to as immersed boundary method. Seta [25] performed a comprehensive work on its thermal variant, including an analysis of the error terms present. Many authors have recognised the importance of consistently treating the source term with an appropriate scheme [103, 104, 105, 25, 106, 107, 108], however, it is not always taken into account [109, 110, 111]. An alternative approach to couple the fluid-solid interaction is through the partially saturated method [112], where a lattice node is categorised as a pure fluid, pure solid or mixed node. Recent applications can be found in the studies of heat transfer in particle suspensions [113, 56].

To simulate advection-diffusion-reaction in a compressible medium, Aursjø *et al.* [114] have defined the concentration of the scalar quantity relatively to the density of fluid.

Later, the same research group proposed a scheme for including a mass source term in the NS equations and showed its application for imposing a pressure boundary condition [115].

While problems relating to heat transfer represent the majority of work conducted with the ADRE resolved in the LBM framework, other physical phenomena are also studied. When multiple components are present in the same volume, a reaction between them may occur [100, 116, 87, 117]. Kang *et al.* [116] managed to reduce the number of equations required to solve the problem of dividing species by separating their interaction into reaction rate-, and diffusion-dominated. Again, the convergence was not discussed in [100, 116, 87].

Shi and Guo [24] and Chai *et al.* [26] provided general studies on the non-linear and anisotropic variants of the advection-diffusion equations in the LBM framework, respectively. The influence of source term treatment is highlighted, but the numerical examples are focused on other aspects of the ADRE and do not include an example of solving non-linear source term preserving both temporal and spatial derivatives. The asymptotic analysis of the LBM schemes for the ADRE have been discussed in detail by Yoshida and Nagaoka [58] and Chai and Shi [35]. The authors gave a detailed expansion analysis for both SRT and MRT collision operators for the advection-diffusion-reaction system. For the diffusive scaling, second-order accuracy was reported. However, the test cases presented did not include source terms, which were integrated with a first-order scheme.

From a theoretical point-of-view, detailed studies of LBM schemes for the 1D advection-diffusion equation have been conducted by Dellacherie [118]. The systematic analysis presented by Dellacherie provided a framework to quantify the behaviour of D1Q2 LBM schemes in L^∞ norm, allowing one to check both consistency and convergence. It is worth noting, that the author indicated a need to integrate the collision operator with a higher-order integration scheme. Additionally, a link was shown between the periodic 1D LBM schemes and the finite-difference schemes, namely, leap-frog for the temporal discretisation, centred-difference for convective terms and Du Fort-Frankel for the diffusive term. The interested reader is referred to the discussion on stability analysis and convergence of a 1D LBM in the work of Junk and Yang [119].

Although less common in the literature, the final family of discretisation schemes for the diffusion and advection-diffusion within the LBM framework were derived based on the finite-volume concept. The scheme was proposed by Onishi *et al.* [120]. It adapts the particle distribution function used to resolve the NSE to calculate the scalar flux similar to the finite-volume approach. The method was later extended by Osmanlic and Körner [121] to include an upwind-type switch in flux calculation. The interested read is directed

to the review by Küng *et al.* [122] for more information on this formulation and the details relating to it.

4.1.2 Structure

With the state of the art, and the common methodologies for deriving an LBM scheme introduced, the remainder of this chapter is structured as follows. From this, a general method which preserves the second-order nature of the underlying LBM with source terms is analysed. A simplified relaxation procedure using a moment-based collision operator is then presented in Section 4.2.1. Section 4.3 outlines the non-dimensionalisation procedure for a PDE and the required scaling of parameters on LBM grids. Subsequently, Section 4.4.1 describes how leading components of error affect the accuracy of a solution in terms of both spatial and temporal resolution. To illustrate the methodology, the proposed approach for solving a formally implicit source term is applied to the Allen-Cahn equation in Section 4.4.2. With the use of symbolic algebra, a solution with an explicit algorithm, which preserves second-order accuracy is proposed. Finally, the methodology is validated numerically by comparison with a finite-element method solution in Section 4.4.2.2 and a convergence study is provided in Sections 4.4.2.1 and 4.4.2.3. The summary of the findings and major outcomes of this work are presented in Section 4.6.

4.2 Model description

4.2.1 The collision operator

If the moments of the source term are chosen to be $\mathbf{R} = Q(\phi, \mathbf{x}, t) \mathbf{\Gamma}(\mathbf{u})$, and $\mathbf{\Upsilon}^{\text{eq}}(\phi, \mathbf{u}) = \phi \mathbf{\Gamma}(\mathbf{u})$, one can use Equations (2.32) and (3.15) to express the collision operator in three equivalent forms,

$$\tilde{\mathbf{\Upsilon}}^* = (1 - s) \tilde{\mathbf{\Upsilon}} + s \mathbf{\Upsilon}^{\text{eq}}(\phi, \mathbf{u}) + \left(1 - \frac{s}{2}\right) \mathbf{R} \quad (4.3)$$

$$= (1 - s) \tilde{\mathbf{\Upsilon}} + s \mathbf{\Upsilon}^{\text{eq}}(\tilde{\phi}, \mathbf{u}) + \mathbf{R} \quad (4.4)$$

$$= (1 - s) \left(\tilde{\mathbf{\Upsilon}} - \mathbf{\Upsilon}^{\text{eq}}(\tilde{\phi}, \mathbf{u}) \right) + \mathbf{\Upsilon}^{\text{eq}}(\tilde{\phi} + Q, \mathbf{u}). \quad (4.5)$$

The form provided in Equation (4.4) can be viewed as a simplification of a relaxation procedure expressed in central moments space by Fei and Luo [63]. On the other hand,

the form in Equation (4.5) can be interpreted as a natural extension of the exact difference method [71] for reaction-type source terms. Even though Equations (4.4) and (4.5) use $\Upsilon^{\text{eq}}(\tilde{\phi}, \mathbf{u})$ instead of $\Upsilon^{\text{eq}}(\phi, \mathbf{u})$, the implicit Equation (2.32) must still be resolved as the source term Q is dependent on ϕ .

To perform numerical benchmarks, the Equation (4.4) has been adopted to formulate the TRT collision operator (see Section 3.6).

$$\tilde{\Upsilon}^* = (1 - \mathbb{S})\tilde{\Upsilon} + \mathbb{S}\Upsilon^{\text{eq}}(\tilde{\phi}, \mathbf{u}) + \mathbf{R}. \quad (4.6)$$

For a comparison of forcing schemes, the reader is referred to the studies [27, 123, 124]. Further discussion concerning discretisation and the order of the velocity expansion of the forcing scheme in the central moment space can be found in [73, 79, 5] and references therein.

4.2.2 Streaming

As usual, the collision step, given by Equation (4.6), is followed by the streaming step,

$$\tilde{h}_i(\mathbf{x} + \mathbf{e}_i, t + 1) = \tilde{h}_i^*(\mathbf{x}, t) = \mathbb{M}^{-1}\tilde{\Upsilon}^*(\mathbf{x}, t). \quad (4.7)$$

Concluding, the order of operations in the LBM scheme can be presented as in Figure 4.1.

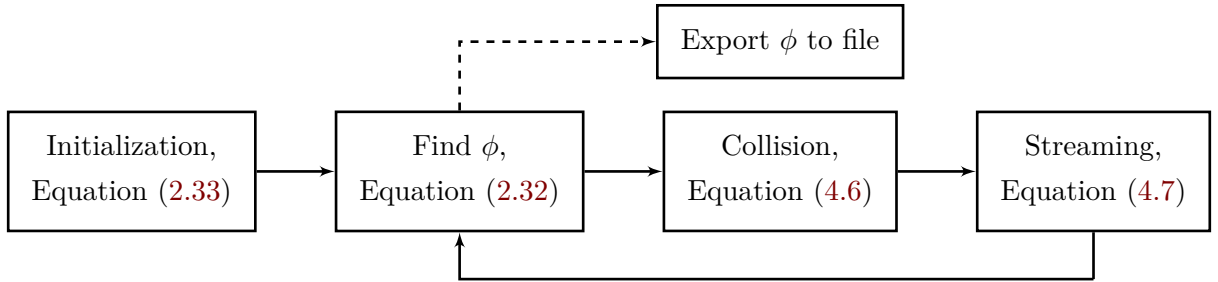


FIGURE 4.1: The order of operations performed during execution of the solver.

4.3 Scaling of LBM

To represent the same physical problem, the non-dimensional form of the investigated differential equation must be preserved on a set of LBM grids. Let us consider a source term $Q = \lambda P(\phi)$, where P has the same unit as ϕ , and λ is a scaling coefficient (see Table 2.1). Using L , T and U as reference length, time and velocity, respectively, one can

define non-dimensional coordinates $x = x^*L$, $t = t^*T$, $u = u^*U$. For a constant M one can express the Equation (2.22) in non-dimensional form [125],

$$\frac{\partial}{\partial t^*} \phi + \mathbf{Pe} \mathbf{Fo} \nabla^* \cdot (\mathbf{u}^* \phi) = \mathbf{Fo} \Delta^* \phi + \mathbf{Da} \mathbf{Fo} P(\phi), \quad (4.8)$$

where \mathbf{Fo} , \mathbf{Da} and \mathbf{Pe} are dimensionless numbers:

- Fourier number $\mathbf{Fo} = \frac{MT}{L^2}$ — the ratio of the diffusive term to the temporal term;
- (second) Damköhler number $\mathbf{Da} = \frac{\lambda L^2}{M}$ — the ratio of the reaction term to diffusive term;
- Péclet number $\mathbf{Pe} = \frac{UL}{M}$ — the ratio of the convective term to the diffusive term.

Observe, that the \mathbf{Fo} incorporates the temporal scale of the simulation and as such can be considered as a non-dimensional time. An alternative approach would be to fix $\mathbf{Fo} = 1$, and quote the time of simulation for each case.

The LBM grids are described by their characteristic length and time (L, T) expressed in number of elements and time-steps. The element size, and time-step can be expressed as their inverse, $\Delta x = \frac{1}{L}$ and $\Delta t = \frac{1}{T}$. For each grid, there are corresponding values of M , λ , and U that preserve the dimensionless numbers: $M = \mathbf{Fo} \frac{L^2}{T}$, $\lambda = \mathbf{Da} \mathbf{Fo} \frac{1}{T}$ and $U = \mathbf{Pe} \mathbf{Fo} \frac{L}{T}$.

For the so-called acoustic scaling, one uses a series of lattices with $L_k = \varepsilon_k^{-1} L_0$ and $T_k = \varepsilon_k^{-1} T_0$, for some scaling factor $\varepsilon_k \rightarrow 0$. Using the previously mentioned equations for the simulation parameters one obtains, $M_k = \varepsilon_k^{-1} M_0$, $U_k = U_0$, and $\lambda_k = \varepsilon_k \lambda_0$. This scaling is called acoustic, as it preserves the velocity scale, making the speed of sound constant across the series of LBM grids. On the other hand, for diffusive scaling, one has $L_k = \varepsilon_k^{-1} L_0$ and $T_k = \varepsilon_k^{-2} T_0$. This in turn gives, $M_k = M_0$, $U_k = \varepsilon_k U_0$, and $\lambda_k = \varepsilon_k^2 \lambda_0$. This scaling is called diffusive, as the diffusion coefficient M is constant across the series of LBM grids.

4.4 Model verification and validation

To test the numerical properties of the described LBM scheme, two equations were investigated, an advection diffusion equation, with a linear source term, and the Allen-Cahn equation. As analytical solutions are easy to obtain for the first example, a detailed analysis of error is performed in that case. Also, for the first equation, the results are compared

with the situation in which one would naively assume $\phi = \tilde{\phi}$. In the case of the Allen-Cahn equation, which has a bi-stable, highly non-linear source term, convergence is checked for both uniform, and non-trivial initial conditions.

If not stated differently, the error between the numerical solution $\phi(x_i)$ defined on the lattice points \mathbf{x}_i and the reference solution ϕ_{ref} is quantified using the \mathcal{L}_2 norm, defined as:

$$\mathcal{L}_2 \text{ norm of error} = \sqrt{\frac{1}{N} \sum_{i=1}^N (\phi(x_i) - \phi_{\text{ref}}(x_i))^2}, \quad (4.9)$$

where N is the number of points in the lattice.

4.4.1 Linear advection-diffusion-reaction model

Here, a simple equation with a linear source term is considered,

$$\frac{\partial \phi}{\partial t} + \nabla \cdot (\mathbf{u}\phi) = \nabla \cdot (M\nabla \phi) + \underbrace{\lambda(\eta(\mathbf{x}) - \phi)}_{Q=Q(\phi)}, \quad (4.10)$$

where γ is a known constant function. On a periodic domain with constant velocity, \mathbf{u} , the problem is a first order linear differential equation, which acts independently on all wavelengths. That means that for any selected wavevector \mathbf{k} , we can solve analytically the equation for initial condition $\phi|_{t=0} = Pe^{i\mathbf{k}\cdot\mathbf{x}}$ and $\eta = Ge^{i\mathbf{k}\cdot\mathbf{x}}$, where upright i denotes the imaginary unit. The analytical solution will be a transition between the initial condition and the steady state,

$$\phi_{\text{analytical}}(\mathbf{x}, t) = (e^{-at}P + (1 - e^{-at})a^{-1}\lambda G) e^{i\mathbf{k}\cdot\mathbf{x}}, \quad (4.11)$$

where $a = \lambda + i(\mathbf{u} \cdot \mathbf{k}) + M(\mathbf{k} \cdot \mathbf{k})$. As the equation is linear, one can take the imaginary or real part of the above analytical solution to obtain a real valued solution. If not specifically mentioned, the real part is used in tests. By varying P and G one can study the influence of the initial condition and the steady-state solution respectively.

4.4.1.1 Second-order convergence

To test the convergence, the Equation (4.10) was solved on a periodic domain of size $L \times L$ elements for a time t with $\mathbf{Fo} = 0.001$ and $\mathbf{Da} = 1000$. In all computations of this

case, the SRT collision operator was used. The number of time steps was increased by a factor of 2 from $T = 2^9$ to $T = 2^{15}$, while maintaining the number of elements per length, L , proportional such that $16L = T$ (acoustic scaling). The velocity was varied between $\mathbf{Pe} = 0$ and $\mathbf{Pe} = 1000$ and the wave number k was $0\frac{2\pi}{L}$, $1\frac{2\pi}{L}$ or $2\frac{2\pi}{L}$. For each setup, two cases were executed. One with $P = 1$ and $G = 0$, and the other with $P = 0$ and $G = 1$. The LBM solutions were compared with the analytical solution of Equation (4.10), and the \mathcal{L}_2 norm of the difference was computed. The proposed scheme consistently recovered second-order convergence for all the cases, with the slope varying from 1.99 to 2.2 as calculated with a least square fit.

4.2 provides an indication of the convergence for $k = 1\frac{2\pi}{L}$, $P = 1$ and $G = 0$. The convergence observed was compared to results obtained when ignoring the implicit Equation (2.32) and assuming $\phi = \tilde{\phi}$ in the calculation of Q .

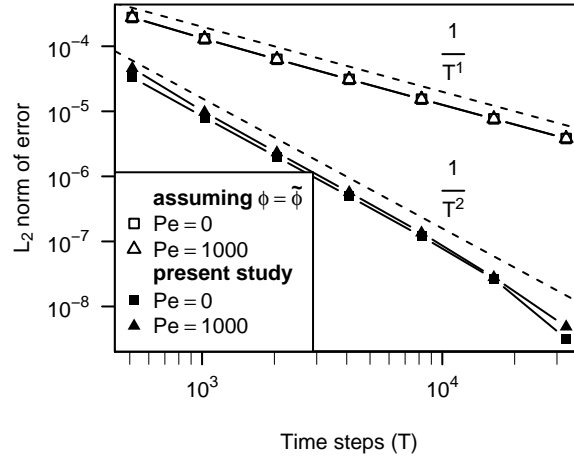


FIGURE 4.2: Convergence of the solution of Equation (4.10) compared with analytical solution given by Equation (4.11), for $k = 1\frac{2\pi}{L}$, $P = 1$ and $G = 0$.

4.4.1.2 Convergence of DBE to ADRE

The LBM can be treated as a discretisation of the DBE, which in turn converges to the ADRE that one originally wanted to solve. This means that two types of error need to be considered, namely, the error of discretisation, and the error (difference) between the DBE and ADRE. Readers interested in a more detailed study regarding equivalent partial differential equations for the lattice Boltzmann schemes are referred to the recent work of Fučík and Straka [36] and Simonis *et al.* [37].

In the case of the linear source term, $\mathbf{q} = Q(\phi)\boldsymbol{\gamma}(\mathbf{u})$, $\mathbf{h}^{\text{eq}} = \phi\boldsymbol{\gamma}(\mathbf{u})$ and $\boldsymbol{\gamma}(\mathbf{u}) = \mathbb{M}^{-1}\boldsymbol{\Gamma}(\mathbf{u})$; see Equation (3.15) for the definition of $\boldsymbol{\Gamma}(\mathbf{u})$. Assuming an uniform velocity field, \mathbf{u} , the DBE given in Equation (2.23) can be solved analytically and its solution can be conveniently expressed using matrix exponents,

$$\mathbf{h}_{\text{analytical}}^{\text{DBE}}(\mathbf{x}, t) = (e^{-\mathbf{A}t}\boldsymbol{\gamma}(\mathbf{u})P + (I - e^{-\mathbf{A}t})\mathbf{A}^{-1}\boldsymbol{\gamma}(\mathbf{u})\lambda G) e^{i\mathbf{k}\cdot\mathbf{x}}, \quad (4.12)$$

where $A_{jk} = i\delta_{jk}(\mathbf{e}_j \cdot \mathbf{k}) - \frac{1}{\tau}(\gamma_j(\mathbf{u}) - \delta_{jk}) + \lambda\gamma_j(\mathbf{u})$. Substitution of all variables indicates that the analytical solution of the ADRE is independent of L and T , as one would expect, however, the analytical solution of the DBE is only dependent on ratio of L to T (the velocity scale).

Figure 4.3 provides the \mathcal{L}_2 norm of the difference between the complex solutions of DBE and ADRE. The two components of the error can be observed, namely, the fourth-order, velocity dependent error, and second-order, velocity independent error.

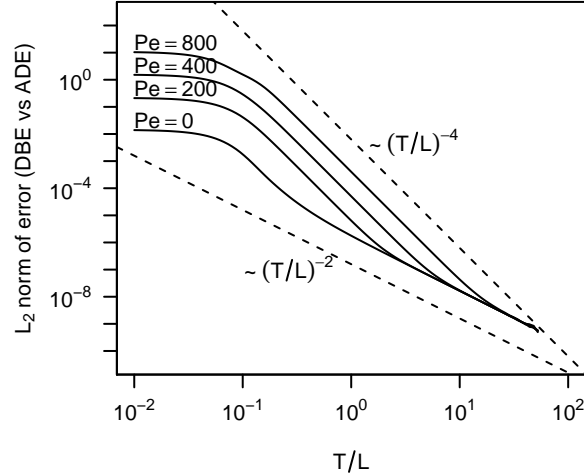


FIGURE 4.3: \mathcal{L}_2 norm of the difference between the analytical solutions of the discrete Boltzmann Equation (2.23) and the advection-diffusion-reaction Equation (2.22). Evaluated for $k = 1 \frac{2\pi}{L}$, $M = 0.001 \frac{L^2}{T}$, $G = 0$, and $P = 1$.

4.4.1.3 Error landscape

A better understanding of the behaviour of the LBM method for advection-diffusion-reaction equation, and LBM in general, can be gained by looking at the dependence of the error on both spatial and temporal resolution. In this work, this is termed the error landscape. For most of physical problems it is prohibitively expensive to calculate the full

error landscape, even if an analytical solutions is available. Nevertheless, the landscape for this case is discussed here, as the general trends and slopes of this landscape will be similar in any LBM application.

A set of 23 and 31 distinct values of L and T were selected, generating a solution set that is close to a linear distribution in log space. For each pair, two simulations were performed, one with the method presented in this chapter, and one in which Q is calculated from $\tilde{\phi}$, not ϕ . In total, 1426 simulations were performed to populate the error landscape. The results were compared to both the analytical solutions of the ADRE and DBE. Figure 4.4 presents the isolines of the error. One can observe, that the convergence to the

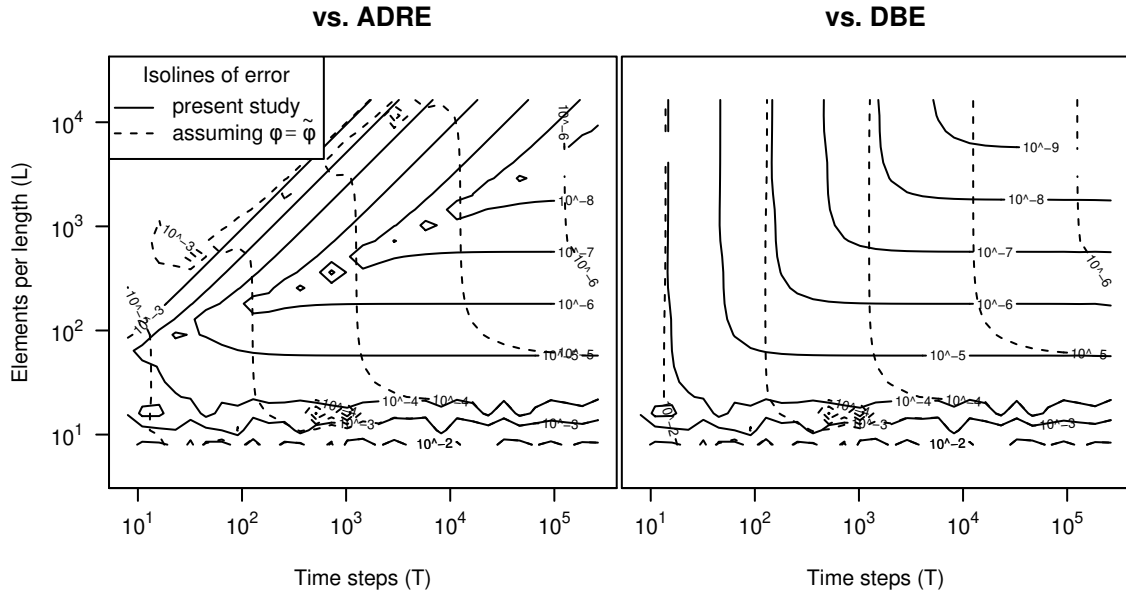


FIGURE 4.4: The isolines of error of the LBM solution against advection-diffusion-reaction equation and discrete Boltzmann equation, given by Equation (4.11) and Equation (4.12), in the T - L space. The y-axis of the left-hand and right-hand side plots are the same. Error is defined as \mathcal{L}_2 -norm of the difference between LBM solution and the reference one. All combinations of 23 and 31 distinct values of L and T respectively, were simulated. Evaluated for $k = \frac{2\pi}{L}$, $M = 0.001 \frac{L^2}{T}$, $G = 0$, $P = 1$, and $u = 0$.

DBE is only driven by competing temporal and spatial discretisation errors. On the other hand, the T/L dependent error between DBE and ADRE dominates the temporal error in convergence to ADRE. In either case, if the source term is inappropriately integrated, its first-order error reduces the accuracy greatly in almost the entire landscape (marked with dashed lines).

In order to provide a clear view of the trends present in the error landscape, approximations of all the separate errors were established to create a smoothed landscape presented in Figure 4.5.

To quantify the impact of the source term discretisation, the computational cost was compared to achieve the same level of error using either a first- or second-order scheme. Both for the present method, and for the inconsistent integration, an optimal selection of number of time-steps, T , and number of elements, L , was made, to achieve error of no more than 10^{-5} . In this specific example, the use of the inconsistent integration scheme for the source term leads to an increase in computational effort (L^2T) of the factor of 500 to achieve an equivalent level error.

The landscapes presented in Figures 4.4 and 4.5 indicate the pitfalls of analysing the convergence of LBM. It has to be reiterated that the Boltzmann equation is integrated along the characteristics, thus the space and time integration can not be treated independently in the construction of a conventional LBM scheme. As a consequence, a properly implemented LBM scheme has second-order convergence. The isolines of error, presented in Figure 4.5, are commonly traversed along the directions marked by the acoustic and diffusive scaling. Given a specific scaling, i.e. ratio of temporal to spatial resolution between subsequent refinements, a researcher may get a biased view of the error and the order of convergence. For instance, under the diffusive scaling, a second order convergence in space will be observed for both the trapezoidal and Euler's implementation of the reaction term integrator. An example of first order implementation leading to the aforementioned behaviour can be found in [126]. Next, the second order convergence in time is clearly visible in the acoustic scaling, while the diffusive scaling works as only first order in time (see Figure 4.11). Moreover, in the lower right corner of the landscape, the error caused by Euler's implementation is relatively small, thus it may not affect the order of convergence. Concluding, the same gain in accuracy can be accomplished along different pathways. The choice of the pathway will influence the computational cost. Based on this, one could select the spatio-temporal parameters of the simulation to progress along the iso-error line in order to obtain the desired result with a lower computational cost.

4.4.2 The Allen-Cahn equation

— illustrative advection-diffusion-reaction problem.

In this section a solidification problem was selected in order to illustrate the impact of the non-linear dependence of the source term on the transported scalar field. The problem

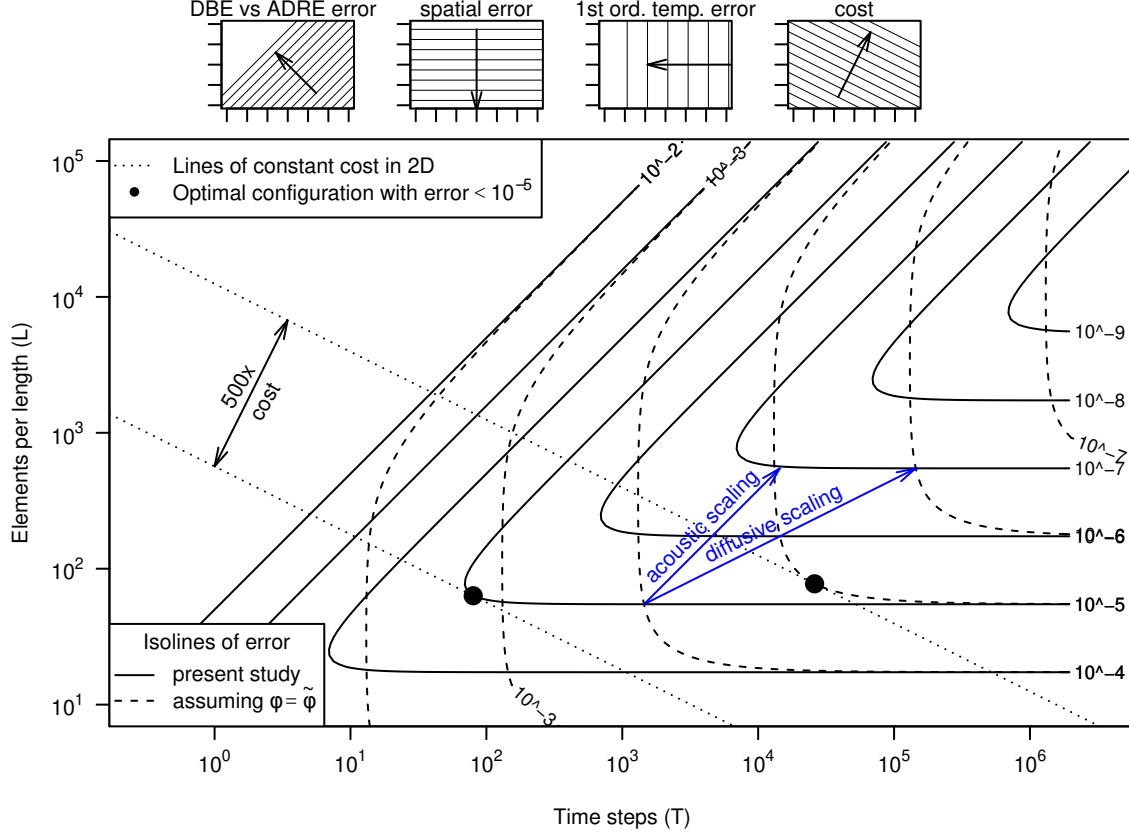


FIGURE 4.5: The schematic isolines of error in the T–L space. See Figure 4.4 for the plot of actual error, measured in simulation. First three of the top four plots show the trends of: error between discrete Boltzmann equation solution and advection-diffusion-reaction equation ($\sim (T/L)^{-2}$), error of the spatial discretisation ($\sim L^{-2}$), 1st order temporal error introduced by improper integration of the source term ($\sim T^{-1}$). The last of the top four plots presents the trend of the cost of the simulation for 2D lattice ($\sim L^2T$). The large black circles mark optimal (CPU cheapest) selections of L and T to achieve the error of no more then 10^{-5} . The ratio of the computational cost for the optimal setup in the naive approach ($\phi = \tilde{\phi}$) compared to the present study is approximately 500 times. The vectors indicate the direction of spatio-temporal refinement using either acoustic or diffusive scaling. Assuming that the length of a vector corresponds to a single refinement step, the second order convergence can be deduced (as two iso-lines of errors are crossed) when looking at the diffusive scaling and setting $\phi = \tilde{\phi}$. In other words, the slope of convergence for diffusive scaling would be the same for both the proper and naive implementation.

solved is the Allen-Cahn equation in the form,

$$\frac{\partial \phi}{\partial t} + \nabla \cdot (\mathbf{u}\phi) = \nabla \cdot (M\nabla \phi) + \underbrace{\lambda \phi (1 - \phi^2)}_{Q=Q(\phi)}, \quad (4.13)$$

where the source term is responsible for the phase change. The details for this equation can be found in the dedicated literature, for example Cahn and Hilliard [127] and Jacqmin [128]. To formulate the implicit relation between ϕ and $\tilde{\phi}$, the source term, $Q(\phi)$, was substituted into Equation (2.32),

$$\tilde{\phi} = \sum_i \tilde{h}_i = \phi - \frac{1}{2}Q(\phi) = \phi - \frac{1}{2}\lambda \phi (1 - \phi^2) = \phi \left(1 - \frac{\lambda}{2} (1 - \phi^2) \right). \quad (4.14)$$

As previously discussed, this equation has to be solved to express ϕ as a function of $\tilde{\phi} = \sum_i h_i$ to resolve the implicit relation introduced by $Q = Q(\phi)$. The exact solution can be readily derived for this third order polynomial. For $\lambda < 2$, there is only one real-valued solution,

$$\phi(\tilde{\phi}) = \frac{A}{C} - C, \text{ where } A = \frac{2 - \lambda}{3\lambda}, B = \frac{\tilde{\phi}}{\lambda}, \text{ and } C = \sqrt[3]{\sqrt{B^2 + A^3} - B}. \quad (4.15)$$

In the next sections, this analytical expression is used in the LBM collision operator to calculate ϕ , and $Q(\phi)$. Figure 4.6 illustrates the relationship between ϕ , Q and $\tilde{\phi}$. Two stable fixed points correspond to the roots of Q , present at $\phi = \tilde{\phi} = 1$ and -1 , and one unstable at 0. The round-off errors can cause the solution of Equation (4.14) to

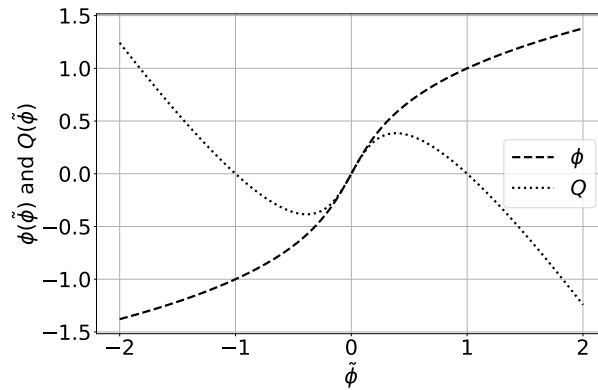


FIGURE 4.6: Plot presents the real solution of Equation (4.15), namely $\phi = \phi(\tilde{\phi})$ and $Q = Q(\tilde{\phi})$ for $\lambda = 1$.

drift from the unstable, 0, root (see Figure 4.6). Although direct implementation (as in

the present work) of Equation (4.15) and calculation of the source term as $Q = Q(\phi) = \lambda\phi(1 - \phi^2)$ generates acceptable results, one can seek to improve the stability in two ways. In the first approach, an iterative (e.g. Newton-Raphson) method can be applied to find ϕ directly from Equation (4.14) instead of Equation (4.15). Then, $Q = Q(\phi)$ is calculated as before. Alternatively, ϕ and $\tilde{\phi}$ can be calculated from Equation (4.15) and Equation (4.14) respectively, while the source term (see Equation (2.32)) would correspond to double of their difference, $Q = 2(\phi - \tilde{\phi})$.

The following subsections are ordered by the growing complexity of benchmarks. First, only the reaction term is benchmarked. Then, a non-uniform initial condition is applied to observe the diffusive effects. Finally, an external velocity field is imposed to obtain the full advection-diffusion-reaction problem.

4.4.2.1 Uniform reaction benchmark — comparison with an analytical solution

This section analyses the evolution of a uniform initial distribution of the scalar field, ϕ , in the absence of an external velocity field. The spatial derivatives in Equation (4.13) reduce to zero and the problem simplifies to ordinary differential equation,

$$\frac{d\phi}{dt} = \lambda\phi(1 - \phi^2). \quad (4.16)$$

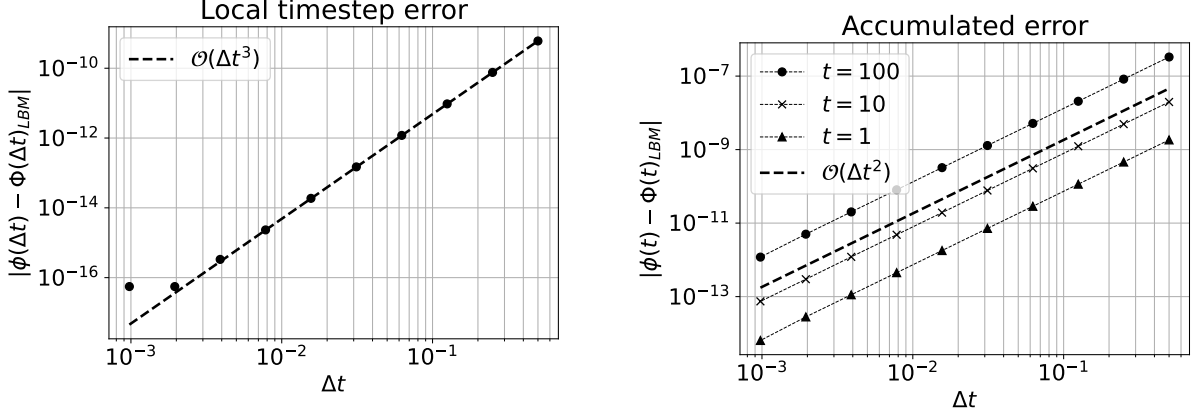
The analytical solution of this equation is,

$$\phi(t) = \pm (C_1 e^{-2\lambda t} + 1)^{-\frac{1}{2}}, \text{ where } C_1 = (\phi(0))^{-2} - 1. \quad (4.17)$$

The results obtained from LBM using the Equation (4.15), were compared with the analytical solution of the ODE. In Figure 4.7, both local and global (accumulated) truncation errors are presented. The local time-step error was calculated as the difference between the numerical and analytical solution after a single time step. For this case, the third-order convergence up to the level of computational accuracy was recovered. As there is no diffusion, the **Fo** is undefined. The global convergence rate was determined by comparison of the numerical and analytical solution after a fixed time $t \in 1, 10, 100$. The coefficient responsible for the intensity of reaction was set to $\lambda = 0.01$.

As observed in Figure 4.7b, the scheme recovered the expected second-order convergence. From this result it can be concluded that the presented implementation recovers

the trapezoidal integration scheme for the special case in which the Allen-Cahn PDE reduces to an ODE.



(A) Local truncation error for a single time step. The error reaches 10^{-16} being the limit of numerical accuracy.

(B) Convergence of total/accumulated error, evaluated for three different times $t = 1; 10; 100$.

FIGURE 4.7: Convergence study of the reaction component of the Allen-Cahn Equation (4.13), on a $D2Q9$ lattice with uniform initial condition and on periodic domain with $\lambda = 0.01$. In such a case, the problem simplifies to an ODE given by Equation (4.16). The operator $|\bullet|$ on the vertical axis denotes a scalar absolute value. It is used to evaluate the error against the analytical solution. In general, a method which converges with $\mathcal{O}(n + 1)$ local truncation error, has a global error of order $\mathcal{O}(n)$. In this example, the convergence of a local time-step error is limited by truncation error at $\approx 10^{-16}$ in local error.

It is reminded that to obtain accurate solution, a precise initialisation procedure which took into account the *shift* in calculated values (see Equation (2.33)) must be applied.

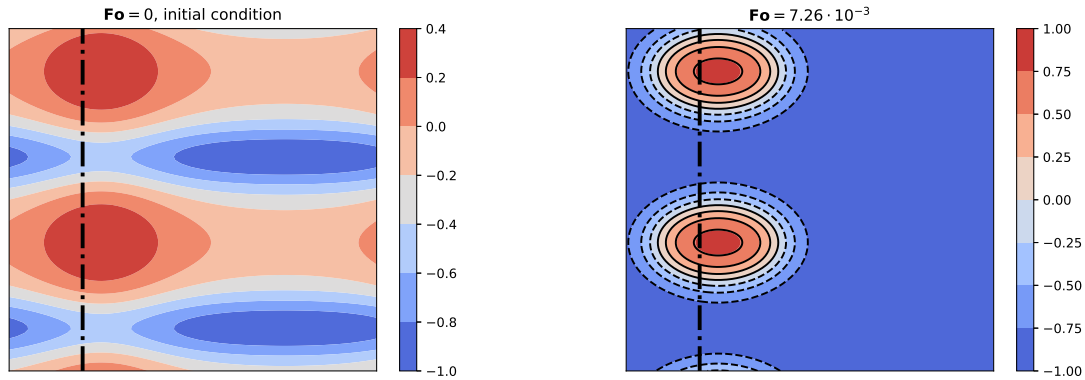
4.4.2.2 Reaction-diffusion benchmark (2D, periodic) — comparison with a finite-element solution

To ensure that the proposed collision kernel properly recovers the diffusion process, the LBM solver has been qualitatively compared against the finite element method (FEM). A spatially varying, periodic initial condition was applied on a square, unit domain using the exponential function,

$$\phi|_{t=0}(x, y) = \frac{1}{2e - e^{-1}} \left(e^{\sin\left(2\pi\frac{x}{L}\right)} - 2e^{\sin\left(4\pi\frac{y}{L}\right)} \right). \quad (4.18)$$

Figure 4.8a shows the result of the initialisation.

The FEM results were obtained using the FEniCS [129, 130] solver. We used fourth-order Lagrange interpolation for spatial discretisation. Fourth-order Runge-Kutta (ES-DIRK43a) with adaptive time-stepping was used for time integration, as implemented in Gryphon package [131]. The FEM was solved on a regular, triangular mesh in the 2D square domain of unit length. There were 25 divisions along each side of the domain resulting in $\sim 26^2$ elements in total. The time step ranged from approximately 10^{-4} to 10^{-5} . Diffusivity in FEM solver was set to one, while the reaction rate was defined by setting $\mathbf{Da} = 500$. The LBM domain was discretised with 256×256 lattice nodes and the diffusivity was set to $1/6$ in lattice units, and magic number was set to $1/12$. To match the solutions obtained by two different solvers, the results were reported for a specific non-dimensional time. There was no external velocity field, thus $\mathbf{Pe} = 0$. Figure 4.8b provides a qualitative comparison between the FEM and LBM solutions at a time defined by $\mathbf{Fo} = 7.26 \times 10^{-3}$. Here, the colour contours from the FEM solution are aligned with the dashed iso-lines of the LBM solution. Figure 4.9 quantitatively compares the time evolution of the scalar field, ϕ , computed by both solvers. through the cross section denoted by the vertical dashed line in Figure 4.8a and Figure 4.8b. The initial condition, and three subsequent times are provided in the same figure. It can be clearly seen that the LBM and FEM solutions agree.



(A) The initial condition, given by Equation (4.18), (B) The intensity of the phase field, ϕ , at the final time, $\mathbf{Fo} = 7.26 \times 10^{-3}$. Both FEM (colors) and LBM (lines) solutions are presented.

FIGURE 4.8: Comparison of the FEM and LBM solutions for reaction-diffusion problem specified in section 4.4.2.2. The LBM lattice consists of 256×256 nodes. Domain is periodic. The Péclet and Damköhler numbers are $\mathbf{Pe} = 0$, $\mathbf{Da} = 500$.

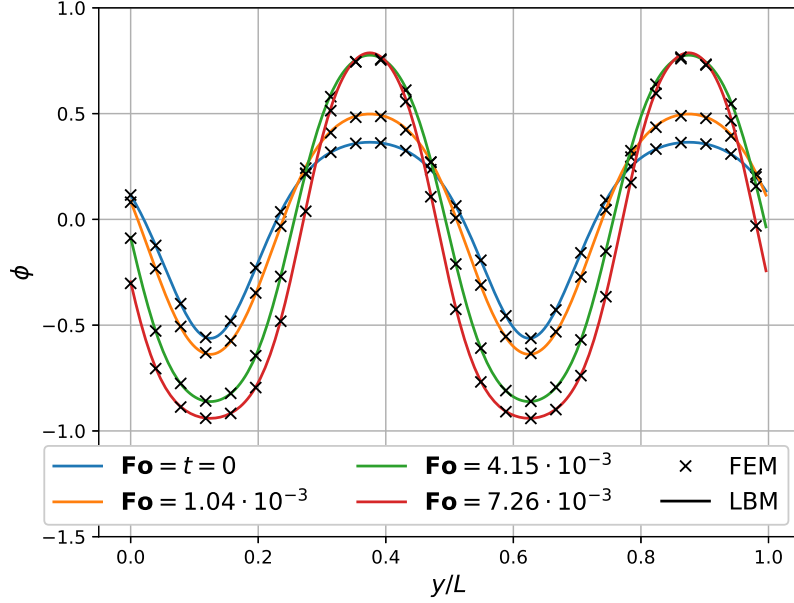


FIGURE 4.9: The time evolution of the phase field, ϕ , is captured for four different Fourier numbers at a cross-section defined at $x/L = 0.2$ (see Figures 4.8a and 4.8b). The FEM and LBM solutions are marked with crosses and lines respectively.

4.4.2.3 Advection-diffusion-reaction benchmark (2D, periodic) — self-convergence study

This section investigates the convergence of the advection-diffusion-reaction problem, given by Equation (4.13). The exponential initial condition was used again, as per Equation (4.18). For this study, a TRT collision operator was used again, with the magic coefficient, Λ , set to $1/12$ in order to cancel out the third-order spatial error and provide optimal results for advection dominated problems [132]. The scalar field was advected with a uniform external velocity, U_x , corresponding to $\mathbf{Pe} = 1 \times 10^3$. The time of the simulation was determined by setting $\mathbf{Fo} = 1 \times 10^{-6}$. The Damköhler number has been set as $\mathbf{Da} = 1 \times 10^6$, to provide a scenario in which the reaction term dominates the diffusion behaviour. The convergence of the scheme was assessed using both acoustic and diffusive scaling techniques. The parameters used during these studies are provided in Table 4.1 and Table 4.2, respectively. Here, the number of elements per the domain length, L , is provided, as is the number of iterations, T .

L	T	U_x		M	λ
4096	1024	4.00×10^{-3}	1.64×10^{-2}	9.77×10^{-4}	
2048	512	4.00×10^{-3}	8.19×10^{-3}	1.95×10^{-3}	
1024	256	4.00×10^{-3}	4.10×10^{-3}	3.91×10^{-3}	
512	128	4.00×10^{-3}	2.05×10^{-3}	7.81×10^{-3}	
256	64	4.00×10^{-3}	1.02×10^{-3}	1.56×10^{-2}	

TABLE 4.1: Simulation parameters in lattice units, acoustic scaling, for $\mathbf{Pe} = 1 \times 10^3$, $\mathbf{Fo} = 1 \times 10^{-6}$ and $\mathbf{Da} = 1 \times 10^6$.

L	T	U_x		M	λ
4096	1024	4.00×10^{-3}	1.64×10^{-2}	9.77×10^{-4}	
2048	256	8.00×10^{-3}	1.64×10^{-2}	3.91×10^{-3}	
1024	64	1.60×10^{-2}	1.64×10^{-2}	1.56×10^{-2}	
512	16	3.20×10^{-2}	1.64×10^{-2}	6.25×10^{-2}	
256	4	6.40×10^{-2}	1.64×10^{-2}	2.50×10^{-1}	

TABLE 4.2: Simulation parameters in lattice units, diffusive scaling, for $\mathbf{Pe} = 1 \times 10^3$, $\mathbf{Fo} = 1 \times 10^{-6}$ and $\mathbf{Da} = 1 \times 10^6$.

Figure 4.10 provides the result of the finest resolution simulated for the scalar variable, ϕ , and the implicit source term, $Q(\phi)$. As there does not exist an analytical solution to the complete advection-diffusion-reaction equation, this finest mesh solution is used to provide a reference point of convergence tests.

The two scaling approaches (acoustic and diffusive) are evaluated in Figure 4.11 for both the proper and naive (assuming $\phi = \tilde{\phi}$) discretization of the source term, Q . The spatial and temporal resolutions are calculated as $\Delta x = 1/L$ and $\Delta t = 1/T$, respectively. In both scenarios, the proposed scheme provided second-order convergence with respect to the grid spacing. However, when the diffusive scaling is applied, the spatial discretisation error dominates (see Fig. 4.5) which manifests as first-order dependence of the error on the time step. To understand the impact these convergence rates have in practice, the \mathcal{L}_2 error norm is shown as a function of the computational cost, defined as $CPU_{cost} = TL^2$, in Figure 4.11. Assuming that the simulation parameters will be maintained within the stability regime of the LBM (namely, $U_{max} \ll 0.1$, $\omega < 2$), one may conclude that for a given set of dimensionless numbers, it is more computationally effective to use acoustic scaling for mesh refinement, and diffusive scaling for mesh rarefaction. It is noted here,

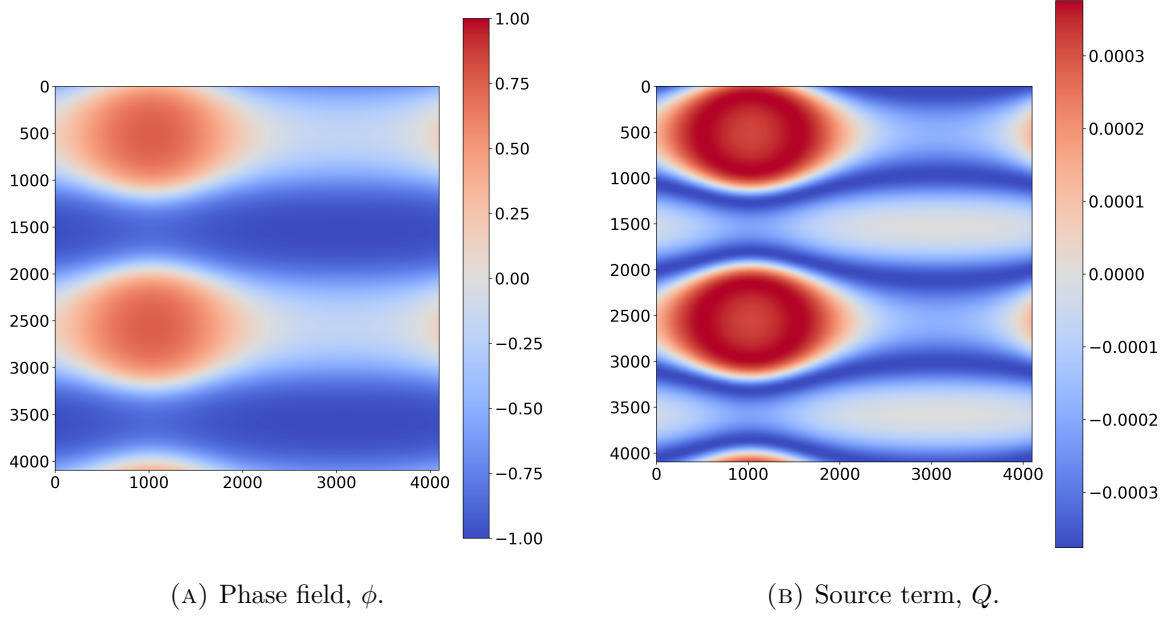
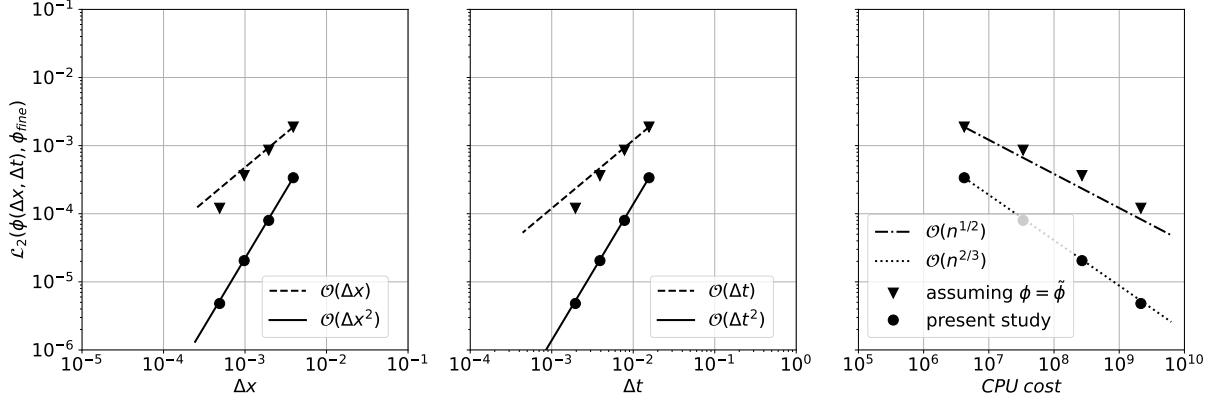


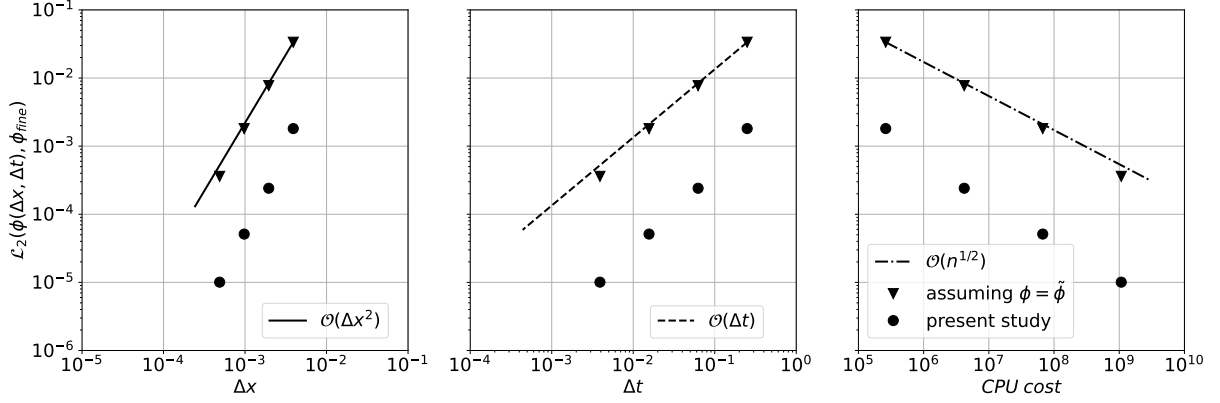
FIGURE 4.10: Contours of the reference solution on the 4096×4096 lattice, for $\mathbf{Pe} = 1 \times 10^3$, $\mathbf{Fo} = 1 \times 10^{-6}$ and $\mathbf{Da} = 1 \times 10^6$. The solver has been initialized according to Equation (4.18).

however, that a domain-specific simulation may affect the scaling approach. For example, one may prefer to use diffusive scaling in the simulation of flow through a porous medium as the effective boundary location is known to be affected by the choice of relaxation frequency [133, 134].

In addition to the above, the convergence rates reported in this test case highlight the importance of the error landscape previously introduced. The rates observed in Figure 4.11, indicate that the set of simulations were conducted below the diagonal of Figure 4.5. This apparent diagonal line sets the limit on the accuracy that could be obtained by means of a single acoustically scaled set of grids, and should be noted by practitioners looking to study the convergence of their LBM scheme. For the particular scenario investigated here, the temporal error dominates. By refining solely the time step, one can hide the source term discretization error below the spatial one and regain the second order convergence under acoustic scaling for the naive scheme.



(A) Acoustic scaling



(B) Diffusive scaling

FIGURE 4.11: Self-convergence study of an advection-diffusion-reaction Equation (4.13), on a $D2Q9$ lattice for $\mathbf{Pe} = 1 \times 10^3$, $\mathbf{Fo} = 1 \times 10^{-6}$ and $\mathbf{Da} = 1 \times 10^6$. Notice, that the formally second-order LBM scheme works as first-order with respect to time if the refinement is done along the diffusive pathway (see Section 4.4.1.3). Despite the same order of convergence under the diffusive scaling for both proper and naive (assuming $\phi = \tilde{\phi}$) discretization of the source term, the level of \mathcal{L}_2 error differs.

4.5 Comparison of approaches to the source term integration

The appropriate integration of the DBE with the trapezoidal rule and redefinition of variables allows one to derive a second-order accurate, local, and explicit evolution scheme as presented in Equation (2.31). To broaden the discussion of approaches available in the literature, this section briefly analyses the spatio-temporal derivatives of the source term that appears in the works of Shi et al. [23, 24] and Chai et al. [26, 35]. If the source term is not included in the shift of variables, then the evolution equation reads,

$$\begin{aligned}\bar{h}_i(\mathbf{x} + \mathbf{e}_i, t + 1) &= \bar{h}_i^*(\mathbf{x}, t) = \\ &= (1 - s)\bar{h}_i(\mathbf{x}, t) + sh_i^{\text{eq}}(\phi, \mathbf{u}) + q_i(\phi, \mathbf{x}, t) + \frac{1}{2} \left(\frac{\partial}{\partial t} + \mathbf{e}_i \cdot \nabla \right) q_i(\phi, \mathbf{x}, t),\end{aligned}\quad (4.19)$$

where contrary to the presented scheme, $\phi = \bar{\phi} = \sum_i \bar{h}_i$ and \bar{h} is a shifted variable, analogous to \tilde{h}_i , but without the contribution of q_i .

To understand the relation between Equation (4.19), and the one described in the present study (given by Equation (2.31)), consider the right hand side of Equation (2.25). The I_2 integral consist of two parts, first related to collision and second to the source term. In fact, any number of different numerical techniques can be applied to each of them. For example, instead of applying the trapezoidal rule, one can use a first order approximation of the source term,

$$\begin{aligned}q_i(\phi(\mathbf{x} + s\mathbf{e}_i, t + s), \mathbf{x} + s\mathbf{e}_i, t + s) &= \\ &= q_i(\phi(\mathbf{x}, t), \mathbf{x}, t) + s \frac{\partial}{\partial s} \left(q_i(\phi(\mathbf{x} + s\mathbf{e}_i, t + s), \mathbf{x} + s\mathbf{e}_i, t + s) \right) + \mathcal{O}(s^2) \\ &= q_i(\phi(\mathbf{x}, t), \mathbf{x}, t) + s \left(\underbrace{\frac{\partial t}{\partial s}}_{=1} \frac{\partial}{\partial t} + \underbrace{\frac{\partial \mathbf{x}}{\partial s}}_{=\mathbf{e}_i} \cdot \frac{\partial}{\partial \mathbf{x}} \right) q_i(\phi(\mathbf{x}, t), \mathbf{x}, t) + \mathcal{O}(s^2) \\ &\simeq q_i(\phi(\mathbf{x}, t), \mathbf{x}, t) + s \left(\frac{\partial}{\partial t} + \mathbf{e}_i \cdot \nabla \right) q_i(\phi(\mathbf{x}, t), \mathbf{x}, t).\end{aligned}\quad (4.20)$$

This approximation can be integrated giving,

$$\begin{aligned}
 & \int_0^1 q_i(\phi(\mathbf{x} + s\mathbf{e}_i, t + s), \mathbf{x} + s\mathbf{e}_i, t + s) ds = \\
 & = \left[sq_i(\phi(\mathbf{x}, t), \mathbf{x}, t) + \frac{s^2}{2} \left(\frac{\partial}{\partial t} + \mathbf{e}_i \cdot \nabla \right) q_i(\phi(\mathbf{x}, t), \mathbf{x}, t) + \mathcal{O}(s^3) \right]_0^1 \\
 & \simeq q_i(\phi, \mathbf{x}, t) + \frac{1}{2} \left(\frac{\partial}{\partial t} + \mathbf{e}_i \cdot \nabla \right) q_i(\phi, \mathbf{x}, t).
 \end{aligned} \tag{4.21}$$

In the case of the *bottom-up* approach, the last term in Equation (4.21) is usually recognised as an artefact [25]. As pointed out by Seta [25], this term can be removed by redefinition of variables or by addition of a correction with regard to the derivative of the source term. The derivative can be computed using a forward or backward finite difference (FD) expression. As one would expect, if a forward FD is used, then the result is equivalent to that obtained through the trapezoidal rule,

$$\begin{aligned}
 q_i(\phi, \mathbf{x}, t) + \frac{1}{2} \left(\frac{\partial}{\partial t} + \mathbf{e}_i \cdot \nabla \right) q_i(\phi, \mathbf{x}, t) &= q_i(\phi, \mathbf{x}, t) + \frac{1}{2} \left(q_i(\hat{\phi}, \hat{\mathbf{x}}, \hat{t}) - q_i(\phi, \mathbf{x}, t) \right) = \\
 &= \frac{1}{2} \left(q_i(\hat{\phi}, \hat{\mathbf{x}}, \hat{t}) + q_i(\phi, \mathbf{x}, t) \right).
 \end{aligned}$$

The influence of the spatial component of the derivate, $\mathbf{e}_i \cdot \nabla$, and various FD stencils has been analysed in [23]. As long as the source term does not depend on ϕ , both forward and backwards FD are computationally trivial. However, if there is a dependence, the backwards FD would require additional transfer of data, while the forward FD, without the appropriate shift of variables, results in a globally implicit scheme.

4.6 Conclusions

Since its initial formulation, the LBM has been developed and adapted to solve a variety of equations, addressing different physical scenarios. Current study has been focused on the details of the usage of LBM for ADRE in which the source term directly depends on the advected field. Such source terms arise in the study of heat and mass transfer, phase-transition or evolution of species populations. Moreover most, implementations of immersed boundary method for heat flows, use source terms to account for desired thermal boundary conditions. In this chapter, the state-of-the-art applications of the LBM for ADRE were presented, and the main differences in discretisation were discussed. A clear

framework for derivation of the LBM numerical scheme from the DBE was discussed, and the algebraic manipulations needed for it, were explicitly shown. Next, a simplification of the collision operator in the moments' space has been proposed.

The article reminds that an implicit relation (see Equation (2.32)) between the value of the macroscopic field and the zeroth-moment (sum) of the LBM densities is the key component for recovering the second-order convergence of the resulting LBM numerical scheme. Furthermore, the closed form solutions of this relation were presented for a variety of common source terms, ranging from simple linear terms to Gompertz model and the Allen-Cahn equation. Using this implicit relation, the chapter presented a local and explicit single- or TRT LBM for ADRE with source terms dependent of the transported field.

To demonstrate the order of convergence of the proposed approach, two distinct equations, involving a linear source term, and a third-order one (as in the Allen-Cahn equation) were investigated. In the case of the linear source term, analytical solutions for both ADRE and DBE were obtained, allowing for the study of the dependence of the error of the LBM on both spatial and temporal resolution. This dependence was visualized as isolines, forming an error landscape. Different competing sources of error were discussed, as was the dependence of the convergence graph on choice of scaling and initial parameters. Moreover, by investigating the isolines of error one can find the point which minimizes the computational effort for a given accuracy. In the second benchmark, the relation between the macroscopic field and the shifted one was non-linear and implicit. The analytical solution was derived and embedded into the explicit, local evaluation of the LBM collision operator. The resulting numerical scheme was evaluated on three different test problems. Firstly, the domain was initialised with a uniform initial distribution to verify the accuracy of the time integration of the source term independently. The uniform initial distribution removed the spatial derivatives from the governing equation and allowed an analytical solution to be derived. In this scenario, the proposed scheme recovered the expected second-order global, and third-order local-in-time convergence. Next, the diffusion term was included in the assessment along with a periodic initial condition based on the exponential function. The result of a two-dimensional LBM simulation was compared to a fourth-order FEM solution, as an analytical solution for such case was no longer obtainable. Finally, to introduce advective effects an external velocity field was added to drive the phase field and a self-convergence study has been performed. The TRT collision operator was required to reduce the influence of numerical artefacts in the results.

All of the examples confirmed the consistency of the proposed approach and have

shown the expected order of convergence. Observe, that the same implementation of the LBM scheme exhibits different order of convergence depending on the ratio of temporal and spatial refinements. For example, the formally second-order LBM scheme displays a first-order convergence with respect to time if the analysed with diffusive scaling (see Figure 4.11). Interestingly, in the case of this scaling, both the proper and naive (assuming $\phi = \tilde{\phi}$) discretizations will exhibit the same *slope* of convergence (see Figures 4.5 and 4.11), but the second-order scheme will result in the lower overall level of error. It is thus concluded that great care should be taken when verifying the order of the LBM scheme with tests of convergence.

4.7 Future outlook - system of equations

Let us illustrate the idea with the following system,

$$\begin{cases} \partial_t c_A + \nabla(u \cdot c_A) &= \nabla \cdot (D \nabla c_A) - k_A c_A + k_C c_C \\ \partial_t c_C + \nabla(u \cdot c_C) &= \nabla \cdot (D \nabla c_C) + k_A c_A - k_C c_C. \end{cases} \quad (4.22)$$

The variable being solved in a LBM scheme is $\tilde{\mathbf{c}}$. The implicit relation (due to 'shift' of variables) is.

$$\tilde{\mathbf{c}} = \mathbf{c} - \frac{1}{2} \mathbf{Q} \Leftrightarrow \begin{bmatrix} \tilde{c}_A \\ \tilde{c}_C \end{bmatrix} = \begin{bmatrix} c_A \\ c_C \end{bmatrix} - \frac{1}{2} \begin{bmatrix} -k_A c_A & k_C c_C \\ +k_A c_A & -k_C c_C \end{bmatrix}. \quad (4.23)$$

One can find $\mathbf{c} = \mathbf{c}(\tilde{\mathbf{c}})$ as,

$$\begin{cases} c_A = \frac{\tilde{c}_A k_C + 2\tilde{c}_A + \tilde{c}_C k_C}{k_A + k_C + 2} \\ c_C = \frac{\tilde{c}_A k_A + \tilde{c}_C k_A + 2\tilde{c}_C}{k_A + k_C + 2} \end{cases} \quad (4.24)$$

To benchmark the source term, the advective and diffusive term can be skipped, and the Equation (4.22) simplifies to system of ODE,

$$\begin{cases} \partial_t c_A &= -k_A c_A + k_C c_C \\ \partial_t c_C &= k_A c_A - k_C c_C. \end{cases} \quad (4.25)$$

Then, the general solution is,

$$\begin{cases} c_A(t) = \frac{C_1 k_C}{k_A} - C_2 e^{t(k_A + k_C)} \\ c_C(t) = C_1 + C_2 e^{t(k_A + k_C)}. \end{cases} \quad (4.26)$$

As the mathematical procedure has been outlined, the LBM scheme can be implemented and benchmarked.

Chapter 5

Role of diffusion-reaction equations in epidemic modelling

“What gets measured gets managed.”

– Peter Drucker

Contents

5.1	Introduction	74
5.1.1	Limitations of the 0D SIR model	75
5.1.2	Numbers or fractions?	76
5.1.3	The nondimensional form equations	76
5.2	Under which conditions one may be lucky enough to not get infected?	76
5.2.1	Stability of linear systems	78
5.2.2	SI Streamlines	79
5.3	The simple spatial SIR model	81
5.3.1	The 1D queue case	81
5.3.2	The spatial effect	81
5.3.3	Choice of the <i>infectious</i> operator	82
5.3.4	Comparison of "infectious" operators in the frequency domain	82
5.4	The spatial SIR system (SIR-Peng model)	84
5.4.1	The low diffusivity issue and the spatial WSIR remedy	85
5.4.2	The nondimensional form equations - revisited	85
5.4.3	Remarks on other SIR-diffusion models	86

5.5 Similarity numbers in SIR-like models	87
5.5.1 SIR with <i>independent</i> (naive) diffusion	87
5.5.2 SIR-Peng model	88
5.5.3 WSIR model	89
5.5.4 Numbers or fractions - revisited	89
5.6 Benchmarks of the spatial WSIR and SIR-Peng models . . .	91
5.6.1 Uniform population density	91
5.6.2 Spatially variable population density	92
5.7 Conclusions	95
5.8 Future outlook	95

This chapter introduces basic description of an epidemic processes from a point of view of CFD modelling. Content of this chapter has been published as an online tutorial followed by set of interactive jupyter notebooks [135].

5.1 Introduction

The history of infectious diseases and attempts to stop them has accompanied mankind since the dawn of time. Thanks to the progress of science, some pathogens, such as the bacteria *Yersinia pestis*, responsible for the plague, have been eliminated. Nevertheless, modern history is not free from epidemics. In the last century, the so-called Spanish flu, caused the death of nearly 50 million people. At the turn of the last century, we witnessed the Ebola epidemic, bovine spongiform encephalopathy (colloquially known as mad cow disease), and flu-like infections caused by zoonotic viruses such as swine and avian flu.

The first empirical, quantitative study of human deaths and diseases was conducted by Graunt in 1662 [136], it concerned the number and cause of deaths in London parishes. A century later, Bernoulli presented a deterministic model to justify the practice of vaccination against chickenpox [137]. In 1927, Kermack et al. [138] have made a significant contribution to epidemic modeling by introducing a simple but effective consolidated model. In particular, a fixed-sized population can be divided into three groups: susceptible (S), who may become ill; infected (I); and recovered (R) who became immune upon recovery. During the epidemic process, individuals may move between the compartments. Currently, the use of the classical SIR model to predict the evolution of epidemics over

time is a frequent starting point for more complex methods. It consists in solving three differential equations,

$$\frac{\partial S}{\partial t} = -\beta \frac{S}{N} I \quad \frac{\partial I}{\partial t} = \beta \frac{S}{N} I - \gamma I \quad \frac{\partial R}{\partial t} = \gamma I \quad (5.1)$$

where t is time and $N = S + I + R$ is the total population. The average number of contacts per person per day (supposing "day" is the time unit) is denoted with β . The transition rate between I and R, is γ (simply the rate of recovery, that is, number of recovered during one day). If the duration of the infection is denoted as D , then $\gamma = 1/D$, since an individual experiences one recovery in D units of time. The basic reproduction number is defined as $R_0 = \frac{\beta}{\gamma}$. Finally, the Equation (5.1) can be enriched by considering maternal immunity, immunization, exposure and incubation periods.

Observe, that the number of contacts between people (draw with replacement) is responsible for the spread of disease. Each infected person, I , has β contacts (meetings with other people). Therefore, the probability of meeting a susceptible person by an infected one is $\frac{S}{N}$.

5.1.1 Limitations of the 0D SIR model

One of the main assumptions of Equation (5.1) is the homogeneity of the environment. There is no doubt that this assumption limits the application of the equation as environmental factors differ significantly from place to place. Movement restrictions, both of a geographical nature and of administrative bans affecting a given region, can dramatically affect the spread of an epidemic. Another factor significantly influencing the dynamics of the process is the local population density. Over the past 20 years, a great deal of research has explored the importance of spatial epidemiology, showing how population diffusion influences the formation of spatial patterns [139, 140, 141, 142, 143, 144]. Apart from the consolidated models, simulations based on [145] cellular automata and [146] agent models should be mentioned. Undoubtedly, blocking the flow of people, especially the infected, is one of the reliable recipes for the spread of infectious diseases. When choosing an epidemic control strategy, the costs associated not only with the effects of the disease itself, but also with the containment of its outbreak [147, 148] are important.

5.1.2 Numbers or fractions?

Notice that $\frac{S}{N}$ corresponds to the fraction of susceptible in the total population. Dividing each of the equations by N , the SIR system can be described in terms of fractions instead of numbers:

$$\begin{cases} \frac{\partial}{\partial t}s &= -\beta si \\ \frac{\partial}{\partial t}i &= \beta si - \gamma i \\ \frac{\partial}{\partial t}r &= \gamma i \end{cases} \quad (5.2)$$

5.1.3 The nondimensional form equations

If we rescale the time as $\tau = \gamma t$, then the set of equations can be described by single similarity number - $R_0 = \frac{\beta}{\gamma}$ known as the basic reproduction number. It is a measure of contagiousness, i.e, the number of secondary infections each infected individual produces.

$$\begin{cases} \frac{\partial}{\partial \tau}s &= -R_0 si \\ \frac{\partial}{\partial \tau}i &= R_0 si - i \\ \frac{\partial}{\partial \tau}r &= i \end{cases} \quad (5.3)$$

5.2 Under which conditions one may be lucky enough to not get infected?

It is interesting to observe, that there are scenarios in which some of the population may survive the epidemic with non infected individuals (see Figure 5.1).

To start the analysis, let us denote a small perturbation, ε , in the SIR compartments as,

$$\begin{cases} s &= \bar{s} + \varepsilon s \\ i &= \bar{i} + \varepsilon i \\ r &= \bar{r} + \varepsilon r \end{cases} \quad (5.4)$$

5.2. Under which conditions one may be lucky enough to not get infected?

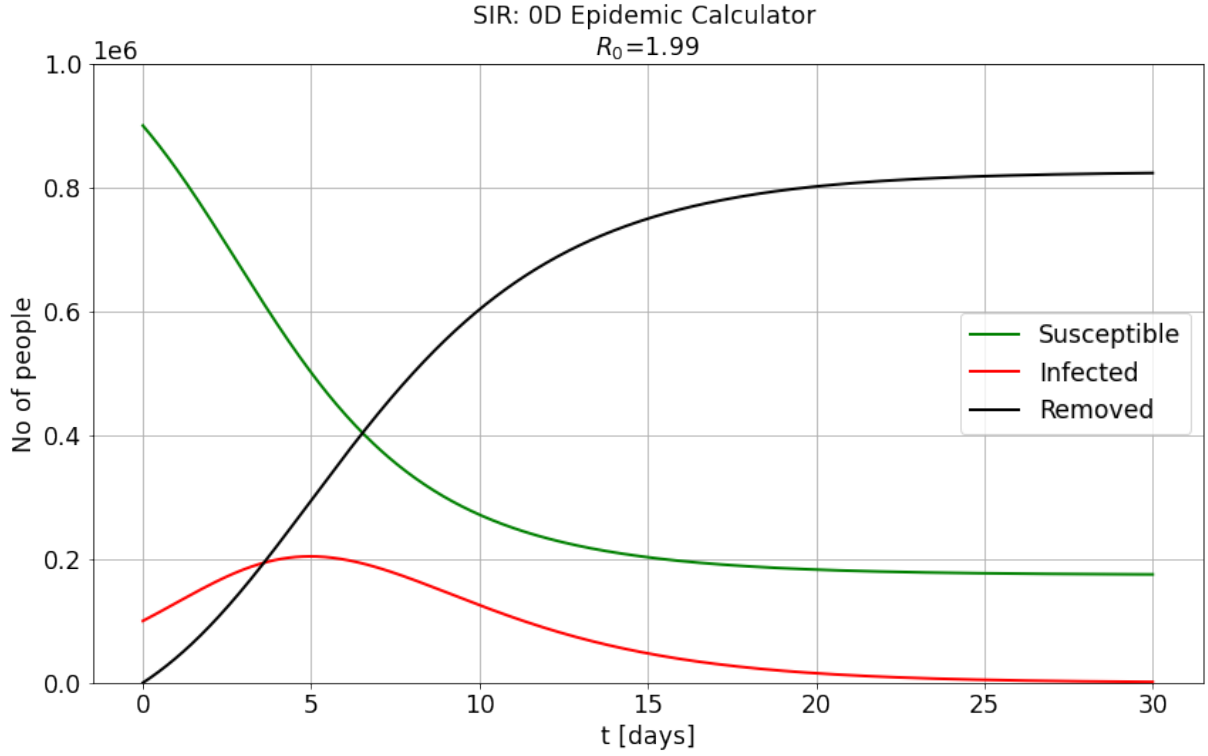


FIGURE 5.1: Parameters has been set to $\beta = 0.71$, $\gamma = 0.36$, a $S_0 = 0.9$, $I_0 = 0.1$, $R_0 = 0$

Consider a system which was initially *at rest* (no infections: $\bar{s} \neq 0, \bar{i} = 0, \bar{r} = 1 - \bar{s}$). One day, a couple of infectious patients, εi , have returned from holidays. What are the conditions to prevent the epidemic from growth? In other words, what proportion of the population should be immunized to eradicate a disease? To answer this question, we have to insert the small perturbation into the (nondimensional) system of SIR equations,

$$\begin{cases} \frac{\partial}{\partial \tau} s &= -R_0 s i \\ \frac{\partial}{\partial \tau} i &= R_0 s i - i \\ \frac{\partial}{\partial \tau} r &= i \end{cases} \quad (5.5)$$

Expanding,

$$\begin{cases} \frac{\partial}{\partial \tau} s &= -R_0(\bar{s} + \varepsilon s)\varepsilon i = -R_0\bar{s}\varepsilon i - R_0\bar{s}\varepsilon^2 i \\ \frac{\partial}{\partial \tau} i &= R_0(\bar{s} + \varepsilon s)\varepsilon i - \varepsilon i = R_0\bar{s}\varepsilon i + R_0\bar{s}\varepsilon^2 i - \varepsilon i \\ \frac{\partial}{\partial \tau} r &= \varepsilon i \end{cases} \quad (5.6)$$

Eliminating the higher order terms, ε^2 , the condition of decay of the epidemic is,

$$\begin{aligned} \frac{\partial}{\partial \tau} i < 0 &\Leftrightarrow (R_0\bar{s} - 1)\varepsilon i < 0 \\ &\Leftrightarrow R_0\bar{s} < 1 \end{aligned} \quad (5.7)$$

Since $\bar{s} = 1 - \bar{r}$, the condition can be expressed as:

$$\begin{aligned} \frac{\partial}{\partial \tau} i < 0 &\Leftrightarrow R_0(1 - \bar{r}) < 1 \\ &\Leftrightarrow \bar{r} > 1 - \frac{1}{R_0}. \end{aligned} \quad (5.8)$$

The Equation (5.8) can be refereed as Herd Immunity Treshold (HIT). It is plotted in the Figure 5.2.

5.2.1 Stability of linear systems

The perturbed, linearised, 0D SIR system can be expressed in matrix form as,

$$\underbrace{\begin{bmatrix} \dot{s} \\ \dot{i} \\ \dot{r} \end{bmatrix}}_{\dot{x}} = \underbrace{\begin{bmatrix} 0 & -R_0\bar{s} & 0 \\ 0 & R_0\bar{s} - 1 & 0 \\ 0 & 1 & 0 \end{bmatrix}}_{\mathbb{A}} \underbrace{\begin{bmatrix} \varepsilon s \\ \varepsilon i \\ \varepsilon r \end{bmatrix}}_x \quad (5.9)$$

where \dot{s} denotes $\frac{\partial}{\partial \tau} s$, etc.

The stability condition for the continuous system is $Re(eigenvalues(\mathbb{A})) < 0$ (all real parts of the eigenvalues, λ , of the matrix \mathbb{A} are negative). Intuition for ODE is fairly simple: $\dot{x} = \lambda x \rightarrow x = Ce^{\lambda t}$. Again, calculating $eigenvalues(\mathbb{A})$ we obtain condition $R_0\bar{s} - 1 < 0 \Leftrightarrow \bar{r} > 1 - \frac{1}{R_0}$. The matrix notation would be even more useful if one would like to consider additional couplings to the SIR system (like loss of the immunity of the recovered).

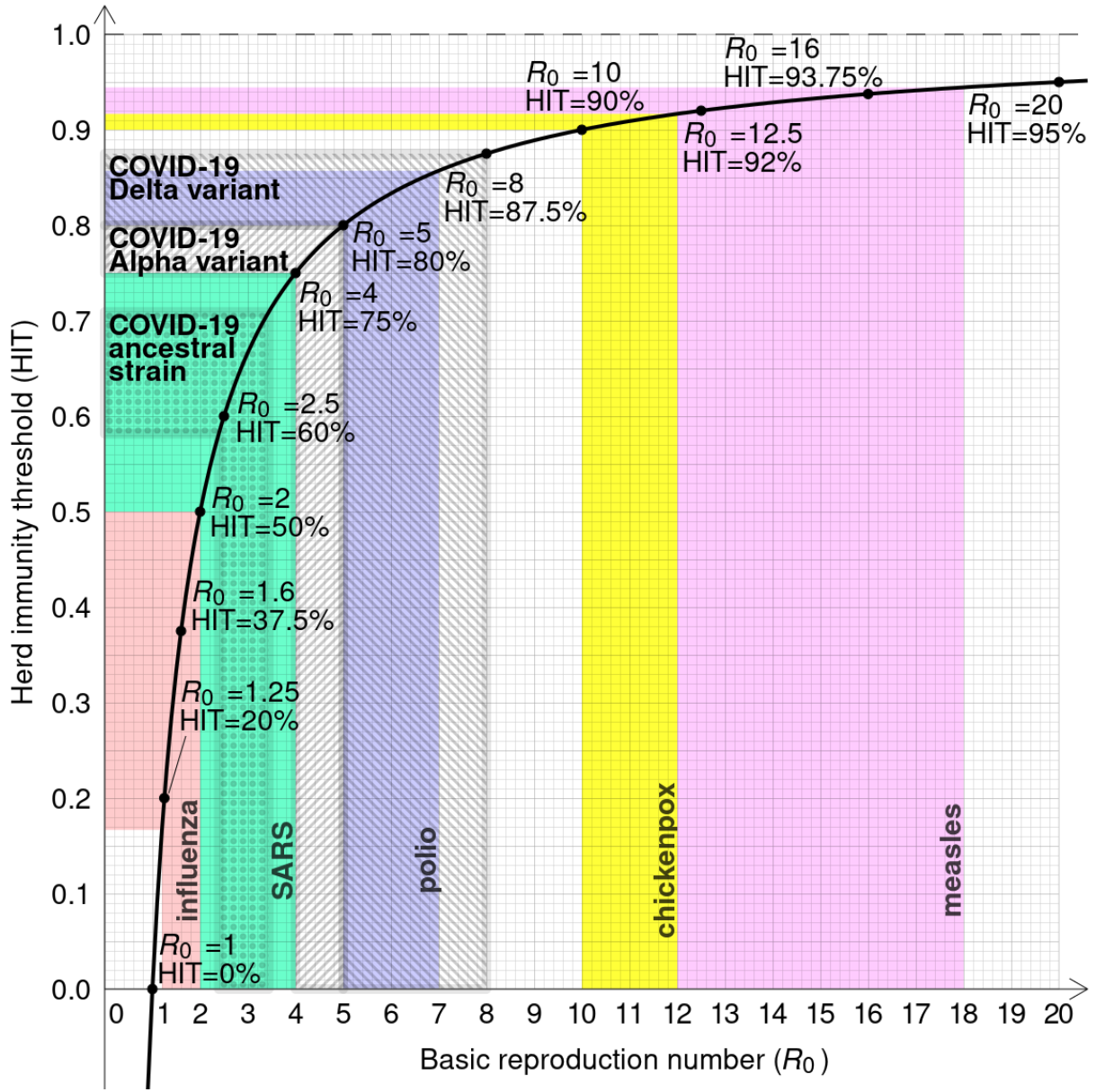


FIGURE 5.2: Herd Immunity Treshold (HIT), based on Equation (5.8).
 Image from [149]

5.2.2 SI Streamlines

It is instructive to plot the streamlines (phase portrait) of a non-dimensional SIR system. The Figure 5.3 shows fractions of susceptible and infected individuals during the epidemic.

Notice, that the R compartment can be eradicated thanks to the $R = N - I - S$ constraint.

$$\begin{cases} \frac{\partial}{\partial \tau} s &= -R_0 s i \\ \frac{\partial}{\partial \tau} i &= R_0 s i - i \\ \frac{\partial}{\partial \tau} r &= i \end{cases} \quad (5.10)$$

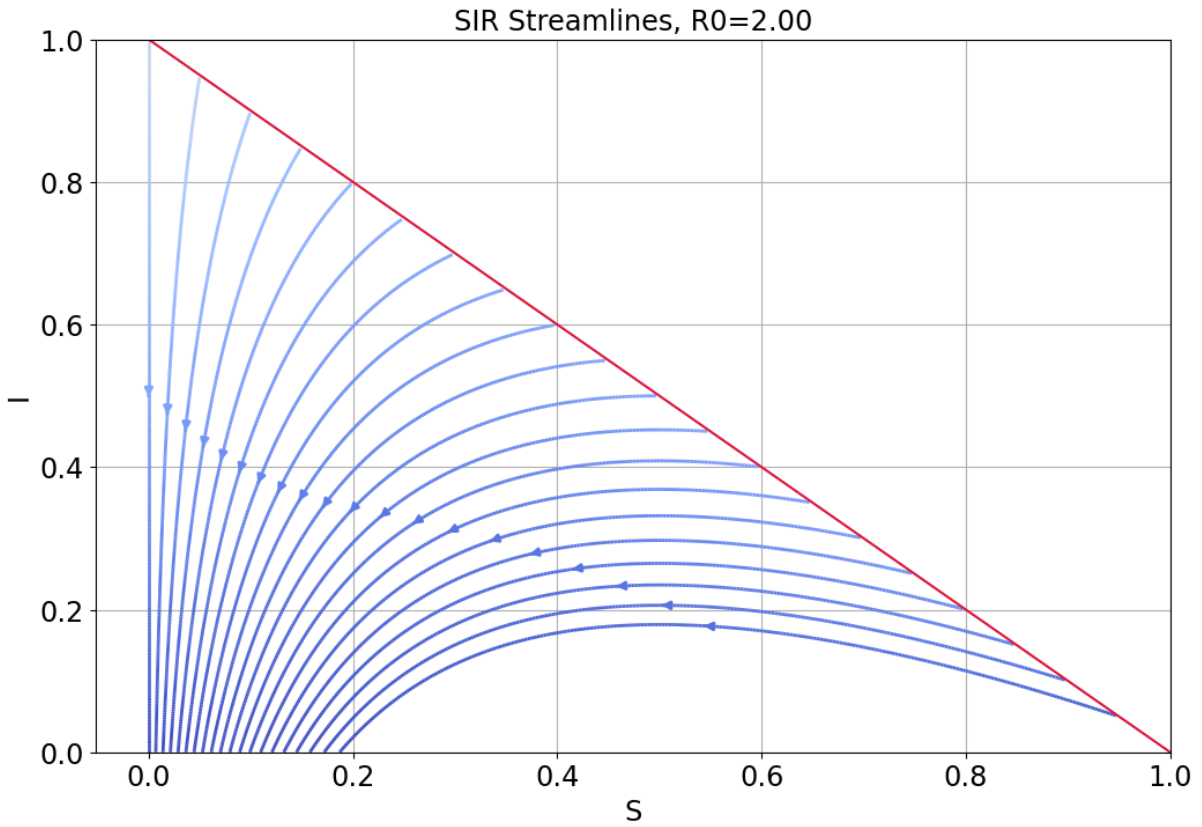


FIGURE 5.3: Starting from various initial conditions and following the $i(s)$ streamlines, one can visualise the fractions of infected and susceptible individuals in the phase space. The fraction of recovered, r can be easily found as $S + i + r = 1$. The red line corresponds to $r = 0$.

5.3 The simple spatial SIR model

5.3.1 The 1D queue case

Consider a queue of people waiting in front of a drug-store. Some of them are ill, some have just come to buy medicine for their beloved ones. Some are standing alone, some are couples or whole families... What is the probability that the susceptible people would get infected? A 1D queue example shall allow us to observe the spatial effects and make some general conclusions before setting up a more real, 2D model. How does the people behave? Do they swap their places in the queue? What is the distance at which an individual may get infected? We will start with the already presented SIR system:

$$\begin{cases} \frac{\partial}{\partial t} S &= -\beta \frac{S}{N} I \\ \frac{\partial}{\partial t} I &= \beta \frac{S}{N} I - \gamma I \\ \frac{\partial}{\partial t} R &= \gamma I \end{cases}$$

5.3.2 The spatial effect

The disease may spread to neighbours with some probability $P(r)$, where r is the *infectious* distance. Various functions can be chosen to model $P(r)$.

Comparing to 0D SIR, we have to take into account interaction between two functions. First accounts for the spatial distribution of infected individuals $I(x)$, while the second describes the distance at which infection may occur $P(r)$, where $r = x - x_0$

From a mathematical perspective, the resulting interaction can be as a convolution of these two functions. Now, the viral load, W , can be defined as,

$$W = I \star P(r). \quad (5.11)$$

Next, the rate of change of infected people can be generalized as,

$$\frac{\partial}{\partial t} I = \beta \frac{S}{N} W - \gamma I. \quad (5.12)$$

Notice, that the 0D case corresponds to $P(r) = \delta$, where δ is the Dirac distribution.

5.3.3 Choice of the *infectious* operator

Let us investigate four basic distributions.

1) The simplest choice is to assume, that an individual can become infected (with constant probability) if he/she is located within a disc of radius r .

$$W = I \star [\text{disc of radius } r]. \quad (5.13)$$

2) which can be (explicitly) approximated as [150],

$$W \approx I + \frac{r^2}{8} \Delta I. \quad (5.14)$$

3) An alternative (implicit) approximation is,

$$W - \frac{r^2}{8} \Delta W \approx I. \quad (5.15)$$

4) Finally, assuming, that the probability of getting infected at some distance has a normal distribution,

$$W = I \star \text{Gaussian}(\sigma). \quad (5.16)$$

5.3.4 Comparison of "infectious" operators in the frequency domain

Let us remind basic properties of the Fourier transform:

$$\mathcal{F}(\delta) = 1$$

$$\mathcal{F}(\Delta u) = -k^2 \mathcal{F}(u)$$

$$\mathcal{F}(u \star v) = \mathcal{F}(u) \mathcal{F}(v)$$

$$\mathcal{F}(C_1 u + C_2 v) = C_1 \mathcal{F}(u) + C_2 \mathcal{F}(v)$$

The frequency response, G describes the ratio of the output amplitude, Y , to the input amplitude, X , for each frequency ω ,

$$G(j\omega) = \frac{Y}{X}, \quad (5.17)$$

where X and Y denote the Fourier transform of the *input* and *output* signal respectively. The frequency response for each of the "infectious" operators can be calculated as follows:

$$G_1 = \frac{\mathcal{F}(I + \frac{r^2}{8}\Delta I)}{\mathcal{F}(I)} = \frac{\mathcal{F}(I) - k^2 \frac{r^2}{8} \mathcal{F}(I)}{\mathcal{F}(I)} = 1 - k^2 \frac{r^2}{8} \quad (5.18)$$

$$G_2 = \frac{\mathcal{F}(I)}{\mathcal{F}(I - \frac{r^2}{8}\Delta I)} = \frac{1}{1 + k^2 \frac{r^2}{8}} \quad (5.19)$$

$$G_3 = \frac{\mathcal{F}(I \star [\text{disc of radius } r])}{\mathcal{F}(I)} = \frac{2 * \text{bessel}J(kr, 1)}{kr} \quad (5.20)$$

$$G_4 = \frac{\mathcal{F}(I \star \text{Gaussian}(\sigma = r/2))}{\mathcal{F}(I)} = \exp((-kr)^{2/8}) \quad (5.21)$$

Notice that the input, X , in G_2 is implicit and the frequency response is related to the continuous (not discrete) operator. The gain can be defined as absolute value of the system frequency response.

Remarks

For frequencies where negative values occurs, the spread of the disease may become unphysical. The high frequency for explicit operator ($W = I + \frac{r^2}{8}\Delta I$, see Equation (5.14)) tends to infinity, thus such IC is expected to diverge.

The frequency response for the discrete operators does not follow the same plot. The response for higher frequencies becomes flattened by a discrete operator. The lower the order of a FD stencil, the more flattened the response.

Numerical stencils of various size can be used to express the discrete convolution/Laplace operator. In general, the approximation by means of Laplacian operator is in general more local than convolution. As a result, the algorithm is computationally faster. Moreover, imposing BC for an equation which includes a Laplacian term is far easier than with convolution.

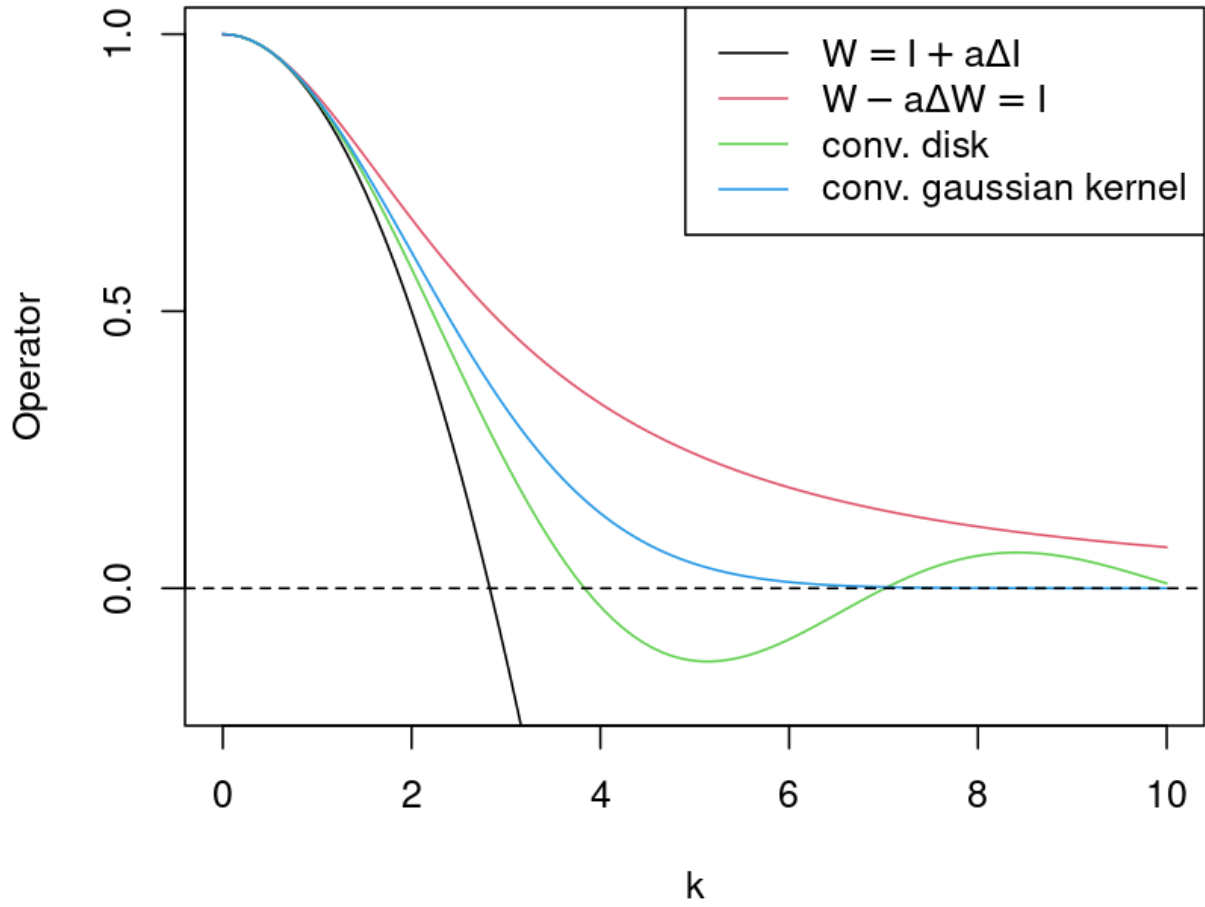


FIGURE 5.4: Frequency response of different "infectious" operators.

5.4 The spatial SIR system (SIR-Peng model)

Let us use the simplest approximation [150],

$$\begin{cases} \frac{\partial S}{\partial t} &= -\beta \frac{S}{N} (I + \frac{r^2}{8} \Delta I) \\ \frac{\partial I}{\partial t} &= \beta \frac{S}{N} (I + \frac{r^2}{8} \Delta I) - \gamma I \\ \frac{\partial R}{\partial t} &= \gamma I \end{cases} \quad (5.22)$$

Substituting $W = I + \frac{r^2}{8}\Delta I$,

$$\begin{cases} \frac{\partial S}{\partial t} &= -\beta \frac{S}{N} W \\ \frac{\partial I}{\partial t} &= \beta \frac{S}{N} W - \gamma I \\ \frac{\partial R}{\partial t} &= \gamma I \end{cases} \quad (5.23)$$

Notice that the diffusivity depends on S , which is decreasing in time. As a consequence, the any numerical scheme (LBM as well) is likely to become unstable at some point. We will reference the Equations (5.22) and (5.23) as SIR-Peng model.

5.4.1 The low diffusivity issue and the spatial WSIR remedy

Low values of the diffusivity coefficient can lead to stability problems in the numerical algorithms. To avoid numerical issues the viral load, W , is simulated as an additional field. W is relaxed (with β_W coefficient) to $W - \Delta W \frac{r^2}{8} = I$. The WSIR system reads:

$$\begin{cases} \frac{\partial W}{\partial t} &= \beta_W \left[\frac{r^2}{8} \Delta W + (I - W) \right] \\ \frac{\partial S}{\partial t} &= -\beta \frac{S}{N} W \\ \frac{\partial I}{\partial t} &= \beta \frac{S}{N} W - \gamma I \\ \frac{\partial R}{\partial t} &= \gamma I \end{cases} \quad (5.24)$$

5.4.2 The nondimensional form equations - revisited

Again, we can rescale the time as $\tau = \gamma t$, then the set of equations can be described by single similarity number $R_0 = \frac{\beta}{\gamma}$

$$\begin{cases} \frac{\partial S}{\partial \tau} &= -R_0 \frac{S}{N} (I + \frac{r^2}{8} \Delta I) \\ \frac{\partial I}{\partial \tau} &= R_0 \frac{S}{N} (I + \frac{r^2}{8} \Delta I) - I \\ \frac{\partial R}{\partial \tau} &= I \end{cases} \quad (5.25)$$

The WSIR system reads:

$$\begin{cases} \frac{\partial}{\partial \tau} W &= \frac{\beta_W}{\gamma} \left[\frac{r^2}{8} \Delta W + (I - W) \right] \\ \frac{\partial}{\partial \tau} S &= -R_0 \frac{S}{N} W \\ \frac{\partial}{\partial \tau} I &= R_0 \frac{S}{N} W - I \\ \frac{\partial}{\partial \tau} R &= I \end{cases} \quad (5.26)$$

5.4.3 Remarks on other SIR-diffusion models

There are models [151], in which the diffusion acts as an *independent* operator for each of the compartments,

$$\begin{cases} \frac{\partial}{\partial t} S &= -\beta \frac{S}{N} I + k_S \Delta S \\ \frac{\partial}{\partial t} I &= \beta \frac{S}{N} I - \gamma I + k_I \Delta I \\ \frac{\partial}{\partial t} R &= \gamma I + k_R \Delta R \end{cases} \quad (5.27)$$

where $k_{S,I,R}$ denotes the diffusion coefficient for particular compartment.

According to [150], such models does not capture physics of the epidemic because:

- (a) almost all humans moves within a small fixed radius and does not disperse in a manner such as Brownian motion.
- (b) equation cannot explain the spatial transmission by infection if individuals are at rest.
- (c) humans would move away from an increasing gradient of the infected.
- (d) humans would move away from over-crowded locations.

Consequently, the spatial transmission described in [151] is caused not by infection but by the dispersion of patients. Inspired by the heat transfer equation,

$$\frac{\partial}{\partial t} \rho T = \nabla \cdot k \nabla T + \dot{q}.$$

One can mitigate the escape of humans from *over-crowded* locations by using fractions in the laplacian term.

Notice, that this will be a *different model*: $\frac{1}{N} \nabla \cdot k_s \nabla S \neq \nabla \cdot k_s \nabla s$ because N is a spatial variable:

$$\begin{cases} \frac{\partial}{\partial t} S = \frac{\partial}{\partial t} N s &= \nabla \cdot k_s \nabla s - \beta \frac{S}{N} I \\ \frac{\partial}{\partial t} I = \frac{\partial}{\partial t} N i &= \nabla \cdot k_i \nabla i + \beta \frac{S}{N} I - \gamma I \\ \frac{\partial}{\partial t} R = \frac{\partial}{\partial t} N r &= \nabla \cdot k_r \nabla r + \gamma I \end{cases} \quad (5.28)$$

Anyway, the drawbacks mentioned in a) – c) still apply.

5.5 Similarity numbers in SIR-like models

Let us define dimensionless variables,

$$\bar{x} = \frac{x}{x_c}, \quad \bar{t} = \frac{t}{t_c}, \quad \bar{N} = \frac{N}{N_c}, \quad \bar{S} = \frac{S}{N_c}, \quad \bar{I} = \frac{I}{N_c}, \quad (5.29)$$

where the c -subscript denotes a characteristics scale.

The Fourier number, Fo , is the ratio of the diffusive term to the temporal term. It can be viewed as a non-dimensional-time.

The (second) Damköhler number is defined as the ratio of the reaction rate to the diffusive transfer rate,

$$Da = \frac{\dot{R} x_c^2}{k} \quad (5.30)$$

where $\dot{R}[1/s]$ denotes the reaction rate, $x_c[m]$ is the characteristics length and $k[m^2/s]$ is the diffusion coefficient.

5.5.1 SIR with *independent* (naive) diffusion

First, we will analyse a SIR model with *independent* (naive) diffusion. Its dimensions are,

$$\underbrace{\frac{\partial}{\partial t}}^{[1/s]} \underbrace{S}_{[individual]} = - \underbrace{\beta}_{[1/s]} \underbrace{\frac{S}{N}}^{[-]} \underbrace{I}_{[individual]} + \underbrace{k_S}_{[m^2/s]} \underbrace{\Delta}_{[1/m^2]} \underbrace{S}_{[individual]}. \quad (5.31)$$

In terms of the characteristic scales

$$\begin{aligned}
 \frac{1}{t_c} \frac{\partial}{\partial t} \bar{S} N_c &= -\beta \frac{\bar{S} N_c}{\bar{N} N_c} \bar{I} N_c + k_S \frac{N_c}{x_c^2} \frac{\partial^2}{\partial \bar{x}^2} \bar{S} \Leftrightarrow // \cdot t_c, : N_c \\
 &\Leftrightarrow \frac{\partial}{\partial \bar{t}} \bar{S} = -\beta t_c \frac{\bar{S}}{\bar{N}} \bar{I} + k_S \frac{t_c}{x_c^2} \frac{\partial^2}{\partial \bar{x}^2} \bar{S} \\
 &= -\beta \underbrace{\frac{x_c^2 \bar{I}}{k_S}}_{Da_S} \underbrace{\frac{k_S t_c}{x_c^2}}_{Fo} \bar{S} + \underbrace{\frac{k_S t_c}{x_c^2}}_{Fo} \frac{\partial^2}{\partial \bar{x}^2} \bar{S}
 \end{aligned} \tag{5.32}$$

In this model, the diffusion coefficient are independent for each fo the S,I,R compartments. As a consequence, this model will be described by three Damkohnler numbers, Da_S, Da_I, Da_R .

5.5.2 SIR-Peng model

Notice, that in the SIR-Peng model [150], the only field with diffusive term is the I compartment,

$$\frac{\partial}{\partial t} I = \beta \frac{S}{N} (I + \frac{r^2}{8} \Delta I) - \gamma I.$$

Repeating the analysis,

$$\frac{1}{t_c} \frac{\partial}{\partial t} \bar{I} N_c = \beta \frac{\bar{S} N_c}{\bar{N} N_c} \left[\bar{I} N_c + N_c \frac{r^2}{8} \frac{1}{x_c^2} \frac{\partial^2}{\partial \bar{x}^2} \bar{I} \right] - \gamma \bar{I} N_c \quad // \cdot t_c, : N_c \tag{5.33}$$

$$\tag{5.34}$$

and denoting $k = \beta \frac{r^2}{8} \frac{\bar{S}}{\bar{N}}$

$$\frac{\partial}{\partial \bar{t}} \bar{I} = \left(\beta \frac{\bar{S}}{\bar{N}} - \gamma \right) t_c \bar{I} + \frac{\overbrace{r^2 \bar{S}}^k}{8} \beta \frac{t_c}{\bar{N}} \frac{\partial^2}{x_c^2} \bar{I} \tag{5.35}$$

leads to the final form

$$\frac{\partial}{\partial \bar{t}} \bar{I} = \underbrace{\frac{x_c^2 \left(\beta \frac{\bar{S}}{\bar{N}} - \gamma \right)}{k}}_{Da_I} \underbrace{\frac{k t_c}{x_c^2}}_{Fo} \bar{I} + \underbrace{\frac{k t_c}{x_c^2}}_{Fo} \frac{\partial^2}{\partial \bar{x}^2} \bar{I}. \tag{5.36}$$

5.5.3 WSIR model

Notice, that in the WSIR model, the only field with diffusive term is the W field.

$$\frac{\partial}{\partial t} W = \beta_W \left[\frac{r^2}{8} \Delta W + (I - W) \right] \quad (5.37)$$

Repeating the analysis,

$$\frac{1}{t_c} \frac{\partial}{\partial \bar{t}} \bar{W} N_c = \beta_W N_c \left[\frac{r^2}{8} \frac{1}{x_c^2} \frac{\partial^2}{\partial \bar{x}^2} \bar{W} + (\bar{I} - \bar{W}) \right] \quad // \cdot t_c, : N_c \quad (5.38)$$

$$\frac{\partial}{\partial \bar{t}} \bar{W} = \beta_W t_c \bar{I} - \beta_W t_c \bar{W} + \overbrace{\frac{r^2}{8} \beta_W}^k \frac{t_c}{x_c^2} \frac{\partial^2}{\partial \bar{x}^2} \bar{W} \quad (5.39)$$

and denoting $k = \beta_W \frac{r^2}{8}$

$$\frac{\partial}{\partial \bar{t}} \bar{W} = \beta_W t_c \bar{I} - \frac{\beta_W x_c^2}{k} \frac{k t_c}{x_c^2} \bar{W} + \frac{k t_c}{x_c^2} \frac{\partial^2}{\partial \bar{x}^2} \bar{W} \quad (5.40)$$

$$= \beta_W t_c \bar{I} - \underbrace{\frac{8 x_c^2}{r^2}}_{Da} \underbrace{\frac{k t_c}{x_c^2}}_{Fo} \bar{W} + \underbrace{\frac{k t_c}{x_c^2}}_{Fo} \frac{\partial^2}{\partial \bar{x}^2} \bar{W}. \quad (5.41)$$

Finally, the Damköhler number for WSIR model is $Da_W = \frac{8 x_c^2}{r^2}$

5.5.4 Numbers or fractions - revisited

This time, the task is more difficult. First, let us remind the quotient rule for Laplace operator:

$$\begin{aligned} \Delta \left(\frac{f}{g} \right) &= \frac{1}{g} \Delta f - \frac{2}{g} \nabla \left(\frac{f}{g} \right) \cdot \nabla g - \frac{f}{g^2} \Delta g \\ \rightarrow \frac{1}{g} \Delta f &= \Delta \left(\frac{f}{g} \right) + \frac{2}{g} \nabla \left(\frac{f}{g} \right) \cdot \nabla g + \frac{f}{g^2} \Delta g \end{aligned} \quad (5.42)$$

Again, we can divide each of the equations by N to represent them in terms of fractions instead of numbers. Consider the spatial equation for S from [150],

$$\begin{aligned}\frac{\partial}{\partial t} S &= -\beta \frac{S}{N} \left(I + \frac{r^2}{8} \Delta I \right) && \text{dividing each side by } N... \\ \frac{\partial}{\partial t} \frac{S}{N} &= -\beta \frac{S}{N} \left(\frac{I}{N} + \frac{r^2}{8} \frac{1}{N} \Delta I \right)\end{aligned}\tag{5.43}$$

Substituting the quotient rule for Laplace operator,

$$\frac{\partial}{\partial t} \frac{S}{N} = -\beta \frac{S}{N} \left[\frac{I}{N} + \frac{r^2}{8} \left[\Delta \left(\frac{I}{N} \right) + \frac{2}{N} \nabla \left(\frac{I}{N} \right) \cdot \nabla N + \frac{I}{N^2} \Delta N \right] \right]\tag{5.44}$$

Introducing fractions $s = \frac{S}{N}, i = \frac{I}{N}, r = \frac{r}{N}$,

$$\begin{cases} \frac{\partial}{\partial t} s &= -\beta s \left[i + \frac{r^2}{8} \left(\Delta i + 2 \nabla i \cdot \frac{\nabla N}{N} + i \frac{\Delta N}{N} \right) \right] \\ \frac{\partial}{\partial t} i &= \beta s \left[i + \frac{r^2}{8} \left(\Delta i + 2 \nabla i \cdot \frac{\nabla N}{N} + i \frac{\Delta N}{N} \right) \right] - \gamma i \\ \frac{\partial}{\partial t} r &= \gamma i \end{cases}\tag{5.45}$$

Alternatively, one can easily rewrite the initial equation as,

$$\begin{cases} \frac{\partial}{\partial t} s &= -\beta s \left(i + \frac{r^2}{8} \frac{1}{N} \Delta(iN) \right) \\ \frac{\partial}{\partial t} i &= \beta s \left(i + \frac{r^2}{8} \frac{1}{N} \Delta(iN) \right) - \gamma i \\ \frac{\partial}{\partial t} r &= \gamma i \end{cases}\tag{5.46}$$

Notice that $\Delta(iN) = i\Delta N + 2\nabla i \cdot \nabla N + N\Delta i$.

Concluding, the attempt to switch from numbers to fractions in spatial model results in more complex form of the equations. According to the authors' experience, the LBM scheme for the latter form is expected to be unstable for large ratio of N ($\sim 100 \div 1000$).

5.6 Benchmarks of the spatial WSIR and SIR-Peng models

For $\beta_W \rightarrow \infty$ the W-SIR model converges to the SIR-Peng one (Equation (5.22)). The Finite-Difference scheme has been implemented to present the basic properties of the aforementioned models in 1D. The domain of length 64 units has been discretized using 129 points. The temporal discretization has been set to $\Delta t = 10^{-5}$ and the simulation was run for 100000 iterations. The infectious radius was chosen as $r_0 = 5.5$, while the average number of contacts per person per time was $\beta = 3.01$ and it took 2.8 days to recover thus $\gamma = 1/2.8$. If not stated differently, the β_W parameter for the WSIR model was set to 10^3 .

5.6.1 Uniform population density

First, the population is assumed to be distributed uniformly. The total number of people, N has been normalized, thus $N = S_{IC} + I_{IC} + R_{IC} = 1$. Next, the S, I, R compartments have been initialized as follows,

$$\begin{cases} S_{IC} = 1 - I_{IC} \\ I_{IC} = 0.05 \quad \text{for } x \in \langle \frac{1}{4}, \frac{1}{2} \rangle, \quad \text{elsewhere } I_{IC} = 0.01 \\ R_{IC} = 0 \\ N = S_{IC} + I_{IC} + R_{IC} = 1. \end{cases}$$

The initial conditions have been visualized in Figure 5.5

The Figure 5.6 show that the WSIR model is well aligned with SIR-Peng model, while it allows to alleviate problems related to low diffusivity as indicated in Sections 5.4 and 5.4.1

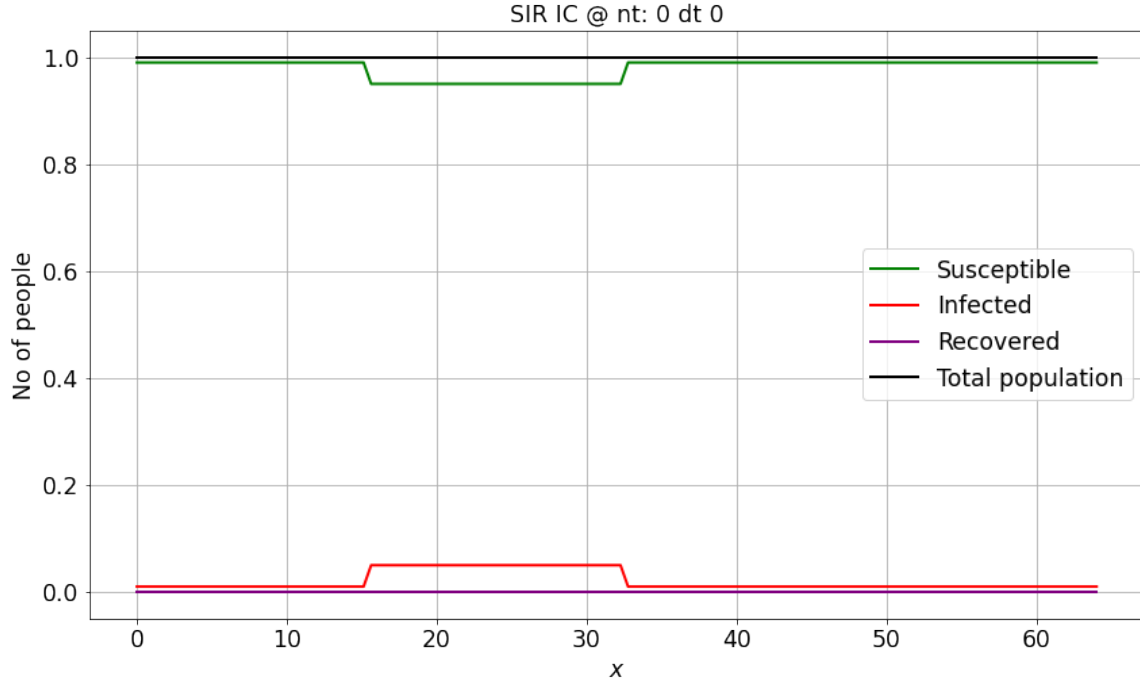


FIGURE 5.5: The initial condition.

5.6.2 Spatially variable population density

The validate the method in a nonuniformly distributed population, following conditions have been assumed,

$$\begin{cases} S_{IC} = 1 - I_{IC} \\ I_{IC} = 0.05 \quad \text{for } x \in \langle \frac{3}{8}, \frac{6}{8} \rangle, \quad \text{elsewhere } I_{IC} = 0.5 \\ R_{IC} = 0 \\ N = S_{IC} + I_{IC} + R_{IC} = 10 \quad \text{for } x \in \langle \frac{1}{4}, \frac{1}{2} \rangle, \quad \text{elsewhere } N = 1. \end{cases}$$

The initial conditions have been visualized in Figure 5.7

Due to non-uniformly distributed population in Figure 5.6, the WSIR model does not follow the SIR-Peng model as good as uniform case. Nevertheless the behaviour is the same, and the similarity can be improved by increasing the β_W coefficient at the price of smaller time steps.

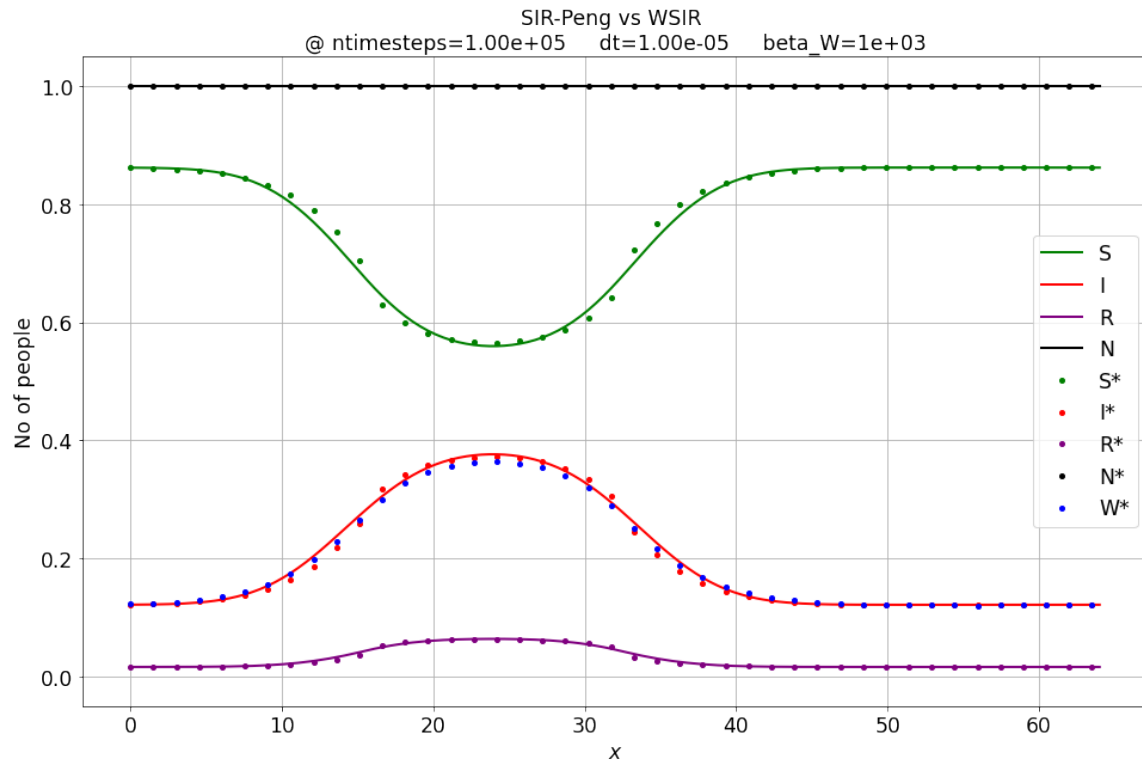


FIGURE 5.6: Comparison of the WSIR and SIR-Peng models in uniform population density.

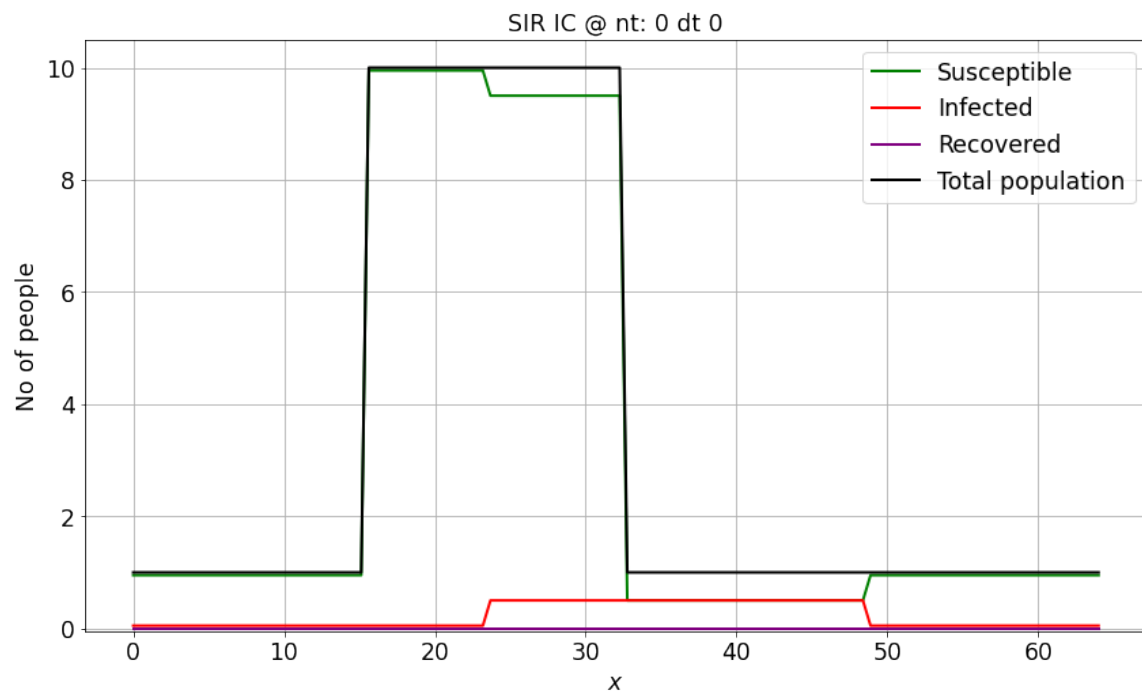


FIGURE 5.7: The initial condition.

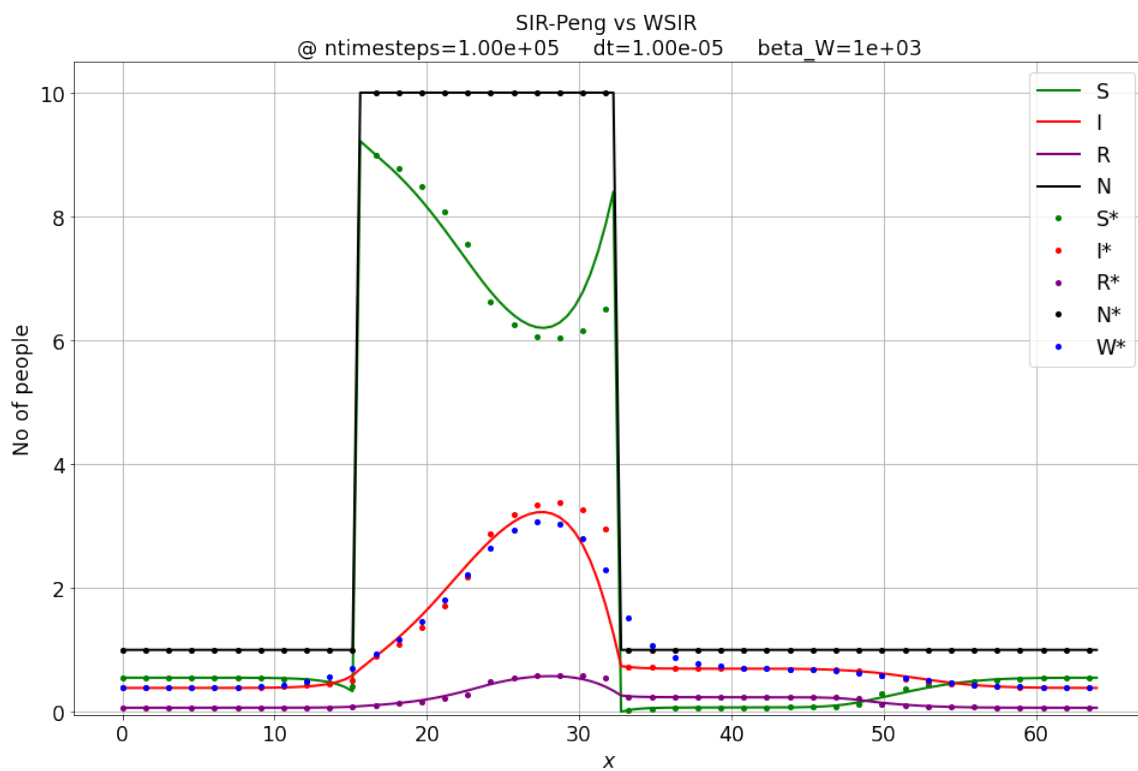


FIGURE 5.8: Comparison of the WSIR and SIR-Peng models in spatially variable population density.

5.7 Conclusions

It has been shown that the W-SIR model is the most suitable candidate for implementation in the Lattice Boltzmann Solver due to its ability to deal with low values of numerical diffusivity. From the physical perspective, it follows the idea of the SIR-Peng model [150], thus is believed to correctly capture the dynamic of an epidemic.

5.8 Future outlook

There is a trade-off between amount of control variables and accuracy. The greatest challenge is the input data and calibration of the model. Fitting the mathematical model to a real world data is multivariable optimization problem. To do limit the computational cost, application of an adjoint technique would be necessary, however such extension is beyond the scope of the current work.

Another view of epidemic modelling may point toward a control theory as indicated in Figure 5.9.

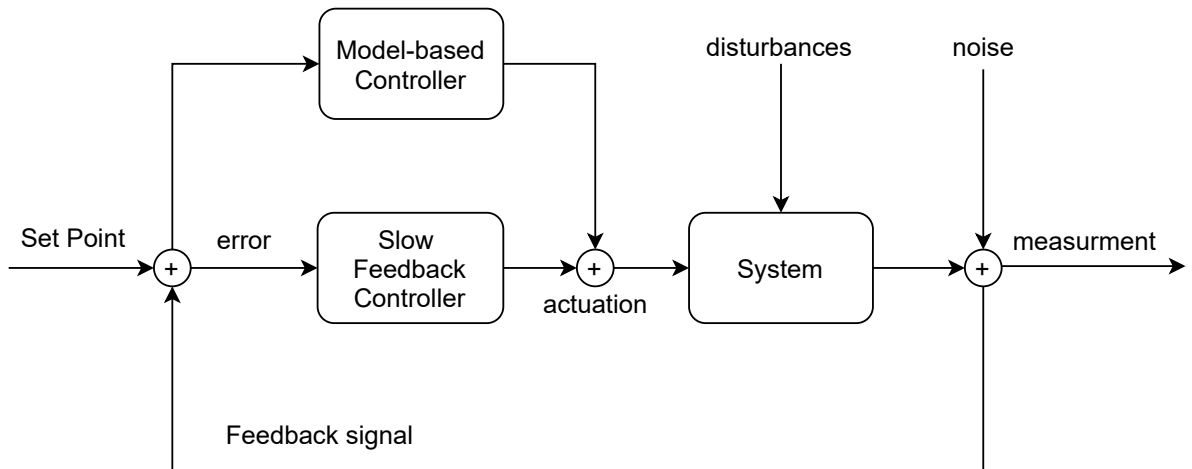


FIGURE 5.9: Control Theory and Covid-19 [152].

Last but not least, an origin-destination 'diffusion' matrix shall be implemented to account for quick movement of people between the cities Figure 5.10.

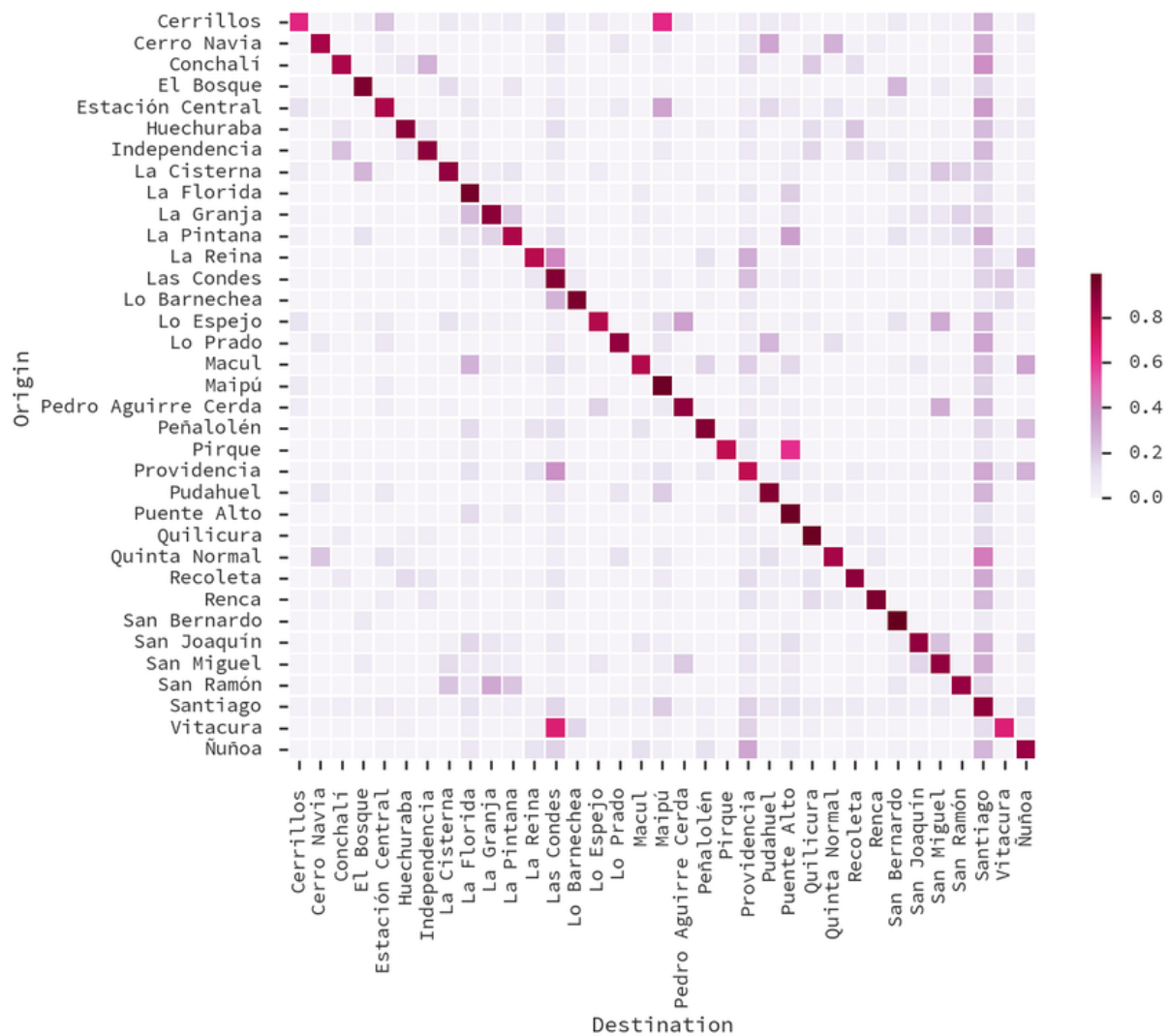


FIGURE 5.10: Example of an Origin-Destination matrix.

Chapter 6

Conservation laws: energy balance

“Laws are like sausages, it is better not to see them being made.”

– Otto von Bismarck

Contents

6.1	The general framework	98
6.2	Total energy	99
6.3	Kinetic energy	99
6.4	Internal energy	100
6.5	Internal energy and enthalpy	100
6.5.1	Ideal gas - assumptions	101
6.6	Stress tensor	101
6.7	Balance of internal energy in terms of enthalpy	102
6.8	Balance of total energy in terms of enthalpy	103

This chapter is dedicated to show relations between equations describing balance of energy.

Figure 6.1 presents intuitive ways in which energy of a physical system can be described. In this chapter, we will derive how these forms of energy are related to each other.

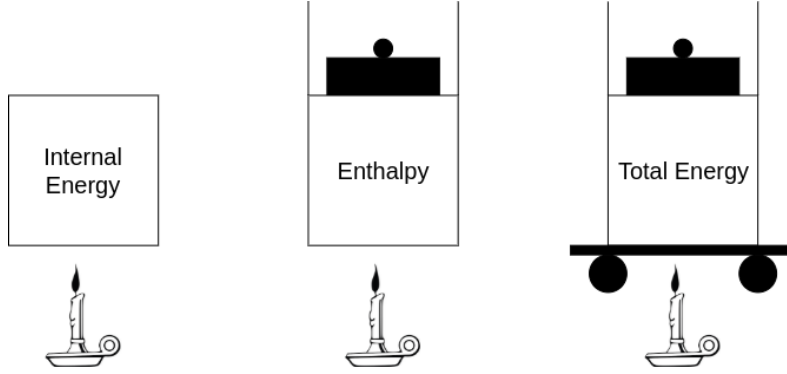


FIGURE 6.1: Intuitive concept of internal energy, enthalpy and total energy.

6.1 The general framework

Let us consider some extensive quantity, Φ , such as mass, energy, momentum, electrical charge, etc. Its spatial distribution is characterized by the mass specific density, ϕ , which can be a scalar, vector or tensor. The total amount of the quantity Φ is expressed by a volume integral,

$$\Phi = \int_V \rho \phi dV = \left. \frac{d\Phi}{dt} \right|_{\text{production}} + \left. \frac{d\Phi}{dt} \right|_{\text{flow through } \partial V} \quad (6.1)$$

$$= \int_V \frac{\partial}{\partial t}(\rho \phi) dV + \oint_{\partial V} (\rho \phi) \mathbf{u} \cdot \mathbf{n} dS \quad (6.2)$$

$$\stackrel{GGO}{=} \int_V \left[\frac{\partial}{\partial t}(\rho \phi) + \nabla \cdot (\rho \phi \mathbf{u}) \right] dV \quad (6.3)$$

$$= \int_V \phi \underbrace{\left[\frac{\partial}{\partial t} \rho + \nabla \cdot (\rho \mathbf{u}) \right]}_{\text{mass conservation eq.} = 0} dV + \int_V \rho \underbrace{\left[\frac{\partial}{\partial t} \phi + \mathbf{u} \cdot \nabla \phi \right]}_{\text{material derivative}} dV \quad (6.4)$$

$$= \int_V \rho \frac{D}{Dt} \phi dV. \quad (6.5)$$

The material derivative appeared,

$$\frac{D}{Dt}(\bullet) = \frac{\partial}{\partial t}(\bullet) + \mathbf{u} \cdot \nabla(\bullet). \quad (6.6)$$

Apart of it, we will define an *augmented* material derivative,

$$\frac{\widehat{D}}{\widehat{D}t}(\bullet) = \frac{\partial}{\partial t}(\bullet) + \nabla \cdot (\bullet \mathbf{u}). \quad (6.7)$$

Based on Equations (6.3) and (6.4) the relationship between them is,

$$\frac{\widehat{D}}{\widehat{D}t}(\rho\phi) = \rho \frac{D}{Dt}(\phi). \quad (6.8)$$

In this chapter we will use the *augmented* material derivative, as it seems to be more native to LBM (see the form of equations in Chapter 7).

6.2 Total energy

The total energy is a sum of internal and kinetic energy, $e = h + \kappa$,

$$\int \frac{\partial}{\partial t}(\rho e) dV + \oint (\rho e \mathbf{u}) \cdot \mathbf{n} dS = \oint \Xi \mathbf{n} \cdot \mathbf{u} dS + \int \rho \mathbf{g} \cdot \mathbf{u} dV - \oint \mathbf{n} \cdot \mathbf{q} dS + \int \rho \dot{q} dV \quad (6.9)$$

where $\mathbf{q} = -k\nabla T$ is the conductive heat flux through the boundary and Ξ is the stress tensor (see Equation (6.20)). Applying the GGO theorem, the equation can be rewritten in the differential form,

$$\frac{\widehat{D}}{\widehat{D}t}(\rho e) = \underbrace{\nabla \cdot (\Xi \cdot \mathbf{u})}_{\text{surface forces}} + \underbrace{\rho \mathbf{g} \cdot \mathbf{u}}_{\text{body forces}} + \underbrace{\nabla \cdot (k \nabla T)}_{\text{conductive heat flux}} + \underbrace{\rho \dot{q}}_{\text{heat source}} \quad (6.10)$$

6.3 Kinetic energy

The kinetic energy is defined as,

$$\rho \kappa = \rho \frac{1}{2} \mathbf{u}^2 = (\rho \mathbf{u}) \cdot \mathbf{u}. \quad (6.11)$$

The balance of kinetic energy is,

$$\frac{\widehat{D}}{\widehat{D}t}(\rho\kappa) = (\nabla \cdot \Xi) \cdot \mathbf{u} + \rho \mathbf{g} \cdot \mathbf{u} \quad (6.12)$$

$$= \nabla \cdot (\Xi \cdot \mathbf{u}) - \Xi : \nabla \mathbf{u} + \rho \mathbf{g} \cdot \mathbf{u}. \quad (6.13)$$

Recall, that the $:$ symbol denotes the double dot product,

$$\mathbb{A} : \mathbb{B} = a_{ij}b_{ij} = a_{11}b_{11} + a_{12}b_{12} + a_{13}b_{13} + a_{21}b_{21} + a_{22}b_{22} + a_{23}b_{23} + a_{31}b_{31} + a_{32}b_{32} + a_{33}b_{33}.$$

6.4 Internal energy

Subtracting the balance of kinetic energy Equation (6.13) from the balance of total energy Equation (6.10), we obtain the balance of internal energy:

$$\frac{\widehat{D}}{\widehat{D}t}(\rho h) = \Xi : \nabla \mathbf{u} + \nabla \cdot (k \nabla T) + \rho \dot{q}. \quad (6.14)$$

Notice the change of sign of $\Xi : \nabla \mathbf{u}$ between $\frac{\widehat{D}}{\widehat{D}t}(\rho h)$ and $\frac{\widehat{D}}{\widehat{D}t}(\rho\kappa)$. This term describes transfer of mechanical energy into internal energy (or vice versa).

6.5 Internal energy and enthalpy

Specific enthalpy is a sum of internal energy $h = c_v T$ and the work required to make space for the system at given pressure. Using equation of state for an ideal gas, $p = \rho R T$, we can express the specific enthalpy as,

$$\mathcal{H} = c_v T + \overbrace{pV}^{=RT} \quad (6.15)$$

$$= (c_v + R)T \quad (6.16)$$

$$= c_p T. \quad (6.17)$$

Where the c_p and c_v are the specific heat capacity at given constant pressure and volume respectively. Here, by enthalpy, we will mean the sensible enthalpy, which is defined as

absolute enthalpy minus enthalpy of formation,

$$\mathcal{H} = \int_{T_0}^T c_p(T) dT. \quad (6.18)$$

Enthalpy is an extensive property of the system,

$$\mathcal{H} = \int_V \rho \mathcal{H} dV. \quad (6.19)$$

6.5.1 Ideal gas - assumptions

The ideal gas model depends on the following assumptions:

- (a) The molecules of the gas are indistinguishable, small, hard spheres.
- (b) All collisions are elastic and all motion is frictionless (no energy loss in motion or collision).
- (c) Newton's laws apply.
- (d) The average distance between molecules is much larger than the size of the molecules.
- (e) The molecules are constantly moving in random directions with a distribution of speeds.
- (f) There are no attractive or repulsive forces between the molecules apart from those that determine their point-like collisions.
- (g) The only forces between the gas molecules and the surroundings are those that determine the point-like collisions of the molecules with the walls.
- (h) In the simplest case, there are no long-range forces between the molecules of the gas and the surroundings.

6.6 Stress tensor

The stress tensor is known as,

$$\begin{aligned} \Xi_{ij} &= -p\delta^{ij} + \left(\zeta - \frac{2}{3}\mu\right) \frac{\partial}{\partial x_k} u_k \delta^{ij} + \mu \left[\frac{\partial}{\partial x_i} u_j + \frac{\partial}{\partial x_j} u_i \right] \\ \Leftrightarrow \Xi &= -p\mathbb{1} + \left(\zeta - \frac{2}{3}\mu\right) (\nabla \cdot \mathbf{u}) \mathbb{1} + \mu [\nabla \mathbf{u} + (\nabla \mathbf{u})^T] \\ &= -p\mathbb{1} + \left(\zeta - \frac{2}{3}\mu\right) (\nabla \cdot \mathbf{u}) \mathbb{1} + 2\mu \mathbb{D}. \end{aligned} \quad (6.20)$$

Divergence of the stress tensor,

$$\begin{aligned}
 \frac{\partial}{\partial x_j} \Xi_{ij} &= -\frac{\partial}{\partial x_j} p \delta^{ij} + \left(\zeta - \frac{2}{3}\mu\right) \frac{\partial}{\partial x_j} \left(\frac{\partial}{\partial x_k} u_k\right) \delta^{ij} + \mu \frac{\partial}{\partial x_j} \left[\frac{\partial}{\partial x_i} u_j + \frac{\partial}{\partial x_j} u_i \right] \\
 &= -\frac{\partial}{\partial x_i} p + \left(\zeta - \frac{2}{3}\mu\right) \frac{\partial}{\partial x_i} \frac{\partial}{\partial x_j} u_j + \mu \frac{\partial}{\partial x_i} \frac{\partial}{\partial x_j} u_j + \mu \frac{\partial^2}{\partial x_j^2} u_i \\
 &= -\frac{\partial}{\partial x_i} p + \left(\zeta + \frac{\mu}{3}\right) \frac{\partial}{\partial x_i} \frac{\partial}{\partial x_j} u_j + \mu \frac{\partial^2}{\partial x_j^2} u_i \\
 \Leftrightarrow \nabla \cdot \Xi &= -\nabla p + \left(\zeta + \frac{\mu}{3}\right) \nabla(\nabla \cdot \mathbf{u}) + \mu \nabla \cdot (\nabla \mathbf{u})
 \end{aligned} \tag{6.21}$$

Divergence of the stress flux,

$$\nabla \cdot (\Xi \cdot \mathbf{u}) = (\nabla \cdot \Xi) \cdot \mathbf{u} + \Xi : \nabla \mathbf{u} \tag{6.22}$$

Let us take a closer look at the second term of Equation (6.22),

$$\begin{aligned}
 \Xi : \nabla \mathbf{u} &= \Xi : (\mathbb{D} + \mathbb{R}) = \Xi : \mathbb{D} = -p \delta^{ij} D_{ij} + \left(\zeta - \frac{2}{3}\mu\right) \frac{\partial}{\partial x_k} u_k \delta^{ij} D_{ij} + 2\mu D_{ij} D_{ij} \\
 &= -p D_{ii} + \left(\zeta - \frac{2}{3}\mu\right) \frac{\partial}{\partial x_k} u_k D_{ii} + 2\mu D_{ij} D_{ij} \\
 &= -p \nabla \cdot \mathbf{u} + \left(\zeta - \frac{2}{3}\mu\right) (\nabla \cdot \mathbf{u})^2 + 2\mu \mathbb{D} : \mathbb{D}.
 \end{aligned} \tag{6.23}$$

The pressure term $-p \nabla \cdot \mathbf{u}$, is responsible for reversible internal to mechanical (expansion) or reverse (compression) energy transfer, while the last two terms account for the irreversible dissipation of mechanical energy.

6.7 Balance of internal energy in terms of enthalpy

Let us transform the balance of internal energy into the balance on enthalpy,

$$\begin{aligned}
 \frac{\widehat{D}}{\widehat{D}t}(\rho h) &= \Xi : \nabla \mathbf{u} + \nabla \cdot (k \nabla T) + \rho \dot{q} \\
 \underbrace{\frac{\partial}{\partial t}(\rho h) + \nabla \cdot (\rho \mathbf{u} h)}_{\frac{\widehat{D}}{\widehat{D}t}(\rho h)} &= \underbrace{-p \nabla \cdot \mathbf{u} + \left(\zeta - \frac{2}{3}\mu\right) (\nabla \cdot \mathbf{u})^2 + 2\mu \mathbb{D} : \mathbb{D}}_{\Xi : \nabla \mathbf{u}} + \nabla \cdot (k \nabla T) + \rho \dot{q}.
 \end{aligned} \tag{6.24}$$

Moving the pressure term to the LHS, we obtain,

$$\begin{aligned} \frac{\partial}{\partial t}(\rho h) + \frac{\partial}{\partial t}p + \nabla \cdot (\rho \mathbf{u} i) + \overbrace{\nabla \cdot (p \mathbf{u}) - \mathbf{u} \cdot \nabla p}^{p \nabla \cdot \mathbf{u}} - \frac{\partial}{\partial t}p = \\ = (\zeta - \frac{2}{3}\mu)(\nabla \cdot \mathbf{u})^2 + 2\mu \mathbb{D} : \mathbb{D} + \nabla \cdot (k \nabla T) + \rho \dot{q}. \end{aligned} \quad (6.25)$$

Grouping terms together,

$$\begin{aligned} \frac{\partial}{\partial t} \left[\rho \left(h + \frac{p}{\rho} \right) \right] + \nabla \cdot \left[\rho \mathbf{u} \left(h + \frac{p}{\rho} \right) \right] - \mathbf{u} \cdot \nabla p - \frac{\partial}{\partial t}p = \\ = (\zeta - \frac{2}{3}\mu)(\nabla \cdot \mathbf{u})^2 + 2\mu \mathbb{D} : \mathbb{D} + \nabla \cdot (k \nabla T) + \rho \dot{q}. \end{aligned} \quad (6.26)$$

Recognizing the specific enthalpy as $\mathcal{H} = h + p/\rho$ allows us to express the LHS of the balance in terms of enthalpy,

$$\begin{aligned} \frac{\partial}{\partial t}(\rho \mathcal{H}) + \nabla \cdot (\rho \mathbf{u} \mathcal{H}) - \mathbf{u} \cdot \nabla p - \frac{\partial}{\partial t}p = \\ \frac{\widehat{D}}{\widehat{D}t}(\rho \mathcal{H}) - \mathbf{u} \cdot \nabla p - \frac{\partial}{\partial t}p = (\zeta - \frac{2}{3}\mu)(\nabla \cdot \mathbf{u})^2 + 2\mu \mathbb{D} : \mathbb{D} + \nabla \cdot (k \nabla T) + \rho \dot{q}. \end{aligned} \quad (6.27)$$

6.8 Balance of total energy in terms of enthalpy

Now, we will repeat the analysis to see how the balance of total energy transforms to a form which contains enthalpy,

$$\begin{aligned} \frac{\widehat{D}}{\widehat{D}t}(\rho h) + \frac{\widehat{D}}{\widehat{D}t}(\rho \kappa) &= \nabla \cdot (\Xi \cdot \mathbf{u}) + \nabla \cdot (k \nabla T) + \rho \dot{q} \\ \frac{\partial}{\partial t}(\rho h) + \nabla \cdot (\rho \mathbf{u} h) + \frac{\widehat{D}}{\widehat{D}t}(\rho \kappa) &= \nabla \cdot \underbrace{(\mathbb{Z} \cdot \mathbf{u} - p \mathbf{u})}_{\Xi \cdot \mathbf{u}} + \nabla \cdot (k \nabla T) + \rho \dot{q} \end{aligned} \quad (6.28)$$

Moving the pressure part to the LHS allows to collect the terms in the form of enthalpy,

$$\begin{aligned}
 \frac{\partial}{\partial t}(\rho h) + \frac{\partial}{\partial t}p + \nabla \cdot (\rho \mathbf{u} h) + \nabla \cdot (p \mathbf{u}) - \frac{\partial}{\partial t}p + \frac{\widehat{D}}{\widehat{D}t}(\rho \kappa) &= \nabla \cdot (\boldsymbol{\Sigma} \cdot \mathbf{u}) + \nabla \cdot (k \nabla T) + \rho \dot{q} \\
 \frac{\partial}{\partial t} \left[\rho \left(h + \frac{p}{\rho} \right) \right] + \nabla \cdot \left[\rho \mathbf{u} \left(h + \frac{p}{\rho} \right) \right] - \frac{\partial}{\partial t}p + \frac{\widehat{D}}{\widehat{D}t}(\rho \kappa) &= \\
 \frac{\partial}{\partial t}(\rho \mathcal{H}) + \nabla \cdot (\rho \mathbf{u} \mathcal{H}) - \frac{\partial}{\partial t}p + \frac{\widehat{D}}{\widehat{D}t}(\rho \kappa) &= \\
 \frac{\widehat{D}}{\widehat{D}t}(\rho \mathcal{H}) - \frac{\partial}{\partial t}p + \frac{\widehat{D}}{\widehat{D}t}(\rho \kappa) &= \nabla \cdot (\boldsymbol{\Sigma} \cdot \mathbf{u}) + \nabla \cdot (k \nabla T) + \rho \dot{q}.
 \end{aligned} \tag{6.29}$$

Reminding Equations (6.21) and (6.23) which describe divergence of the stress flux Equation (6.22), the $\nabla \cdot (\boldsymbol{\Sigma} \cdot \mathbf{u})$ term responsible for viscous dissipation can be explicitly written as,

$$\nabla \cdot (\boldsymbol{\Sigma} \cdot \mathbf{u}) = \underbrace{\left[\left(\zeta + \frac{\mu}{3} \right) \nabla (\nabla \cdot \mathbf{u}) + \mu \nabla \cdot (\nabla \mathbf{u}) \right] \cdot \mathbf{u}}_{(\nabla \cdot \boldsymbol{\Sigma}) \cdot \mathbf{u}} + \underbrace{\left(\zeta - \frac{2}{3} \mu \right) (\nabla \cdot \mathbf{u})^2 + 2\mu \mathbb{D} : \mathbb{D}}_{\boldsymbol{\Sigma} : \nabla \mathbf{u}}. \tag{6.30}$$

Chapter 7

Recovering Energy transfer

“Creativity is just connecting things. When you ask creative people how they did something, they feel a little guilty because they didn’t really do it, they just saw something. It seemed obvious to them after a while.”

– Steve Jobs

Contents

7.1 Macroscopic equation	105
7.1.1 Way I: The ‘basic’ approach	106
7.2 Conjugate Heat Transfer — future outlook	112
7.2.1 Way II: Why variable ρc_v causes problem	112
7.2.2 Way III: Calculate the right moments (or correction by weights)	114
7.2.3 Way IV: Correction by source term	118
7.2.4 Way V: Two passive scalar worlds tied by BC at the interface.	120

In this chapter a procedure of recovering the selected macroscopic advection-diffusion equations is presented.

7.1 Macroscopic equation

For an incompressible and inviscid fluid, i.e. skipping the pressure work and viscous heat production, the balance of internal energy, (see Equation (6.14)), can be simplified as,

$$\int \frac{\partial}{\partial t}(\rho c_v T) dV + \oint (\rho c_v T \mathbf{u}) \cdot \mathbf{n} dS = - \oint \mathbf{n} \cdot \mathbf{q} dS + \int \dot{q} dV \quad (7.1)$$

$$\text{where } \mathbf{q} = -k \nabla T \quad (7.2)$$

The heat flux \mathbf{q} is related to the thermal conductivity coefficient $k[W/mK]$.

Applying GGO theorem, we obtain,

$$\frac{\partial}{\partial t}(\rho c_v T) + \nabla \cdot (\mathbf{u} \rho c_v T) = \nabla \cdot (k \nabla T) + \dot{q}. \quad (7.3)$$

This is the differential form of the internal energy balance. In this chapter we show how to recover the above equation or its simplified version using LBM. We adapt the multiple-scale analysis of the NS equations from Łaniewski-Wołk [153]. In this chapter, the ϕ will be used to denote the advected field.

The procedure of recovering the NS equations can be also found in textbooks [9, 10]. A comparison of other analysis methods like Chapman-Enskog analysis, Maxwell iteration, direct Taylor expansion, and recurrence equations approaches has been presented in [35].

7.1.1 Way I: The 'basic' approach

Thermal LB models, which do not deal with Conjugate Heat Transfer (CHT) problems simply assume $c_v = \text{const} = 1$. We will implement and benchmark such a model in Chapter 9.

Equilibrium distribution function (EDF) - second order in \mathbf{u} ,

$$h_i^{\text{eq}} = w_i \phi \left[1 + \frac{\mathbf{e}_i \mathbf{u}}{\theta e^2} + \frac{(\mathbf{e}_i \mathbf{u})^2}{2\theta^2 e^4} - \frac{\mathbf{u}^2}{2\theta e^2} \right]. \quad (7.4)$$

where $\theta = c_s^2 = R_{gas} T_0$ is a constant non-dimensional lattice temperature (see Section 2.1.1 for short discussion) Moments of EDF,

$$\begin{cases} \sum h_i^{\text{eq}} &= \phi = \rho T \\ \sum e_i^j h_i^{\text{eq}} &= u^j \phi \\ \sum e_i^j e_i^k h_i^{\text{eq}} &= \Pi_{eq}^{jk} = \delta^{jk} \theta \phi + u^j u^k \phi \end{cases} \quad (7.5)$$

Moments of distribution function (DF),

$$\begin{cases} \sum h_i &= \phi = \rho T \\ \sum e_i^j h_i &= u^j \phi + Q_{neq}^j \\ \sum e_i^j e_i^k h_i &= \Pi_{eq}^{jk} + \Pi_{neq}^{jk} = \delta^{jk} \theta \phi + u^j u^k \phi + \Pi_{neq}^{jk} \end{cases} \quad (7.6)$$

The Q_{neq}^j can be viewed as a diffusive flux. It is interesting to observe, that the first order central moments of h , corresponds to diffusive flux Q_{neq}^j which is a temperature gradient $\tilde{k}_{10}^H = \sum_i (e_i^x - u^x) = k \partial_x T$. Discrete Boltzmann equation (DBE) reads,

$$\frac{\partial}{\partial t} h_i + e_i^j \frac{\partial}{\partial x_j} h_i = \frac{1}{\tau} (h_i^{\text{eq}} - h_i). \quad (7.7)$$

Zeroth moment of DBE = $\sum_i DBE_i$,

$$\begin{aligned} \frac{\partial}{\partial t} \phi + \frac{\partial}{\partial x_j} (u^j \phi + Q_{neq}^j) &= 0 \Leftrightarrow \\ \Leftrightarrow \frac{\partial}{\partial t} \phi + \frac{\partial}{\partial x_j} (u^j \phi) &= -\frac{\partial}{\partial x_j} Q_{neq}^j. \end{aligned} \quad (7.8)$$

First moment of DBE = $\sum_i e_i^k DBE_i$,

$$\begin{aligned} \frac{\partial}{\partial t} (u^k \phi + Q_{neq}^k) + \frac{\partial}{\partial x_j} (\delta^{jk} \theta \phi + u^j u^k \phi + \Pi_{neq}^{jk}) &= -\frac{1}{\tau_\phi} Q_{neq}^k \Leftrightarrow \\ \Leftrightarrow \frac{\partial}{\partial t} (u^k \phi) + \frac{\partial}{\partial t} Q_{neq}^k + \frac{\partial}{\partial x_j} (\delta^{jk} \theta \phi) + \frac{\partial}{\partial x_j} (u^j u^k \phi) + \frac{\partial}{\partial x_j} \Pi_{neq}^{jk} &= -\frac{1}{\tau_\phi} Q_{neq}^k \\ \Leftrightarrow \frac{\partial}{\partial t} (u^k \phi) + \frac{\partial}{\partial t} Q_{neq}^k + \frac{\partial}{\partial x_k} (\theta \phi) + \frac{\partial}{\partial x_j} (u^j u^k \phi) + \frac{\partial}{\partial x_j} \Pi_{neq}^{jk} &= -\frac{1}{\tau_\phi} Q_{neq}^k. \end{aligned} \quad (7.9)$$

Product rule:

$$\begin{aligned} (abc)' &= abc' + ab'c + a'bc. \\ a(bc)' + (ab)'c - a'bc &= ab'c + abc' + a'bc + ab'c - a'bc = (abc)'. \end{aligned}$$

Applying product rule to identities from Equation (7.9):

$$\frac{\partial}{\partial t} (u^k \phi) = u^k \frac{\partial}{\partial t} \phi + T \frac{\partial}{\partial t} (\rho u^k) - T u^k \frac{\partial}{\partial t} \rho. \quad (7.10)$$

$$\frac{\partial}{\partial x_k} (\theta \phi) = \rho \frac{\partial}{\partial x_k} (\theta T) + T \frac{\partial}{\partial x_k} (\theta \rho). \quad (7.11)$$

$$\frac{\partial}{\partial x_j} (u^j u^k \phi) = T \frac{\partial}{\partial x_j} (u_j \rho u_k) + u_k \frac{\partial}{\partial x_j} (u_j \phi) - u_k T \frac{\partial}{\partial x_j} (\rho u_j). \quad (7.12)$$

Substituting Equations (7.10) to (7.12) into Equation (7.9),

$$\begin{aligned}
 & u^k \frac{\partial}{\partial t} \phi + T \frac{\partial}{\partial t} (\rho u^k) - T u^k \frac{\partial}{\partial t} \rho + \\
 & \quad + \rho \frac{\partial}{\partial x_k} (\theta T) + T \frac{\partial}{\partial x_k} (\theta \rho) + \\
 & + T \frac{\partial}{\partial x_j} (u_j \rho u_k) + u_k \frac{\partial}{\partial x_j} (u_j \phi) - u_k T \frac{\partial}{\partial x_j} (\rho u_j) + \\
 & \quad + \frac{\partial}{\partial t} Q_{neq}^k + \frac{\partial}{\partial x_j} \Pi_{neq}^{jk} = -\frac{1}{\tau_\phi} Q_{neq}^k.
 \end{aligned} \tag{7.13}$$

Grouping terms,

$$\begin{aligned}
 & \text{Equation (7.8)} = -\frac{\partial}{\partial x_j} Q_{neq}^j \\
 & \quad \overbrace{u^k \left(\frac{\partial}{\partial t} \phi + \frac{\partial}{\partial x_j} (u_j \phi) \right)}^{\text{momentum eq.}} + \\
 & + T \overbrace{\left(\frac{\partial}{\partial t} (\rho u^k) + \frac{\partial}{\partial x_j} (u_j \rho u_k) + \frac{\partial}{\partial x_k} (\theta \rho) \right)}^{\text{continuity eq.}} + \\
 & \quad - T u^k \overbrace{\left(\frac{\partial}{\partial t} \rho + \frac{\partial}{\partial x_j} (\rho u_j) \right)}^{\text{continuity eq.}} + \\
 & \quad + \rho \frac{\partial}{\partial x_k} (\theta T) + \\
 & \quad + \frac{\partial}{\partial t} Q_{neq}^k + \frac{\partial}{\partial x_j} \Pi_{neq}^{jk} = -\frac{1}{\tau_\phi} Q_{neq}^k.
 \end{aligned} \tag{7.14}$$

Next, we apply Equation (7.8), continuity ($\sum_i DBE_i^{hydrodynamics} = 0$) and momentum ($\sum_i e_i^k DBE_i^{hydrodynamics} = -\hat{\Pi}^{jk}$) equations,

$$\begin{aligned}
 & -u^k \frac{\partial}{\partial x_j} Q_{neq}^j - T \frac{\partial}{\partial x_j} \hat{\Pi}^{jk} - T u^k 0 + \rho \frac{\partial}{\partial x_k} (\theta T) + \frac{\partial}{\partial t} Q_{neq}^k + \frac{\partial}{\partial x_j} \Pi_{neq}^{jk} = -\frac{1}{\tau_\phi} Q_{neq}^k \Leftrightarrow \\
 & \quad \Leftrightarrow -u^k \frac{\partial}{\partial x_j} Q_{neq}^j - T \frac{\partial}{\partial x_j} \hat{\Pi}^{jk} + \rho \frac{\partial}{\partial x_k} (\theta T) + \frac{\partial}{\partial t} Q_{neq}^k + \frac{\partial}{\partial x_j} \Pi_{neq}^{jk} = -\frac{1}{\tau_\phi} Q_{neq}^k \\
 & \quad \Leftrightarrow -Q_{neq}^k = \tau_\phi \rho \frac{\partial}{\partial x_k} (\theta T) + \tau_\phi \left(u^k \frac{\partial}{\partial x_j} Q_{neq}^j - T \frac{\partial}{\partial x_j} \hat{\Pi}^{jk} + \frac{\partial}{\partial t} Q_{neq}^k + \frac{\partial}{\partial x_j} \Pi_{neq}^{jk} \right).
 \end{aligned} \tag{7.15}$$

To recover the macroscopic equation we insert the Q_{neq}^k from Equation (7.15) back to Equation (7.8),

$$\begin{aligned} \frac{\partial}{\partial t}\phi + \frac{\partial}{\partial x_j}(u^j\phi) &= \frac{\partial}{\partial x_j}\tau_\phi\rho\frac{\partial}{\partial x_k}(\theta T) + \\ &+ \underbrace{\tau_\phi\left(u^k\frac{\partial}{\partial x_j}Q_{neq}^j - T\frac{\partial}{\partial x_j}\hat{\Pi}^{jk} + \frac{\partial}{\partial t}Q_{neq}^k + \frac{\partial}{\partial x_j}\Pi_{neq}^{jk}\right)}_{\text{error terms}}. \end{aligned} \quad (7.16)$$

To match the macroscopic conductivity coefficient, k , with a relaxation time, τ_ϕ , the relationship must hold as

$$\boxed{\tau_\phi = \frac{k}{\rho\theta}}. \quad (7.17)$$

Recall, that at the beginning of Section 7.1.1 we assumed that $\theta = c_s^2$ is constant.

7.1.1.1 Scaling

Let us introduce a scaling factor $\varepsilon \rightarrow 0$, which can be interpreted as Knudsen number (**Kn**). For **diffusive scaling**:

$$\left\{ \begin{array}{ll} t = \frac{1}{\varepsilon^2}t^* & \\ x = \frac{1}{\varepsilon}x^* & \\ u = \varepsilon u^* & \text{the scale of velocity is [m/s], thus } u^* \sim \frac{x^*}{t^*} \\ \tau_\phi = \tau_\phi^* & \text{the scale of diffusivity is [m}^2\text{/s], thus } \tau_\phi^* \sim \frac{(x^*)^2}{t^*} \end{array} \right. \quad (7.18)$$

Based on Equations (7.5) and (7.6) the scale of non-equilibrium terms is analogous to the velocity scale, thus

$$\left\{ \begin{array}{l} Q_{neq} = \varepsilon Q_{neq}^* \\ \Pi_{neq} = \varepsilon^2 \Pi_{neq}^* \end{array} \right. \quad (7.19)$$

Substituting into Equation (7.16),

$$\begin{aligned} \varepsilon^2 \frac{\partial}{\partial t^*} \phi + \varepsilon^2 \frac{\partial}{\partial x_j^*} (u^{*j} \phi) &= \varepsilon^2 \frac{\partial}{\partial x_j^*} \tau_\phi \rho \frac{\partial}{\partial x_k^*} (\theta T) + \\ &+ \tau_\phi \left(\varepsilon^3 u^{*k} \frac{\partial}{\partial x_j^*} Q_{neq}^{*j} - \varepsilon^3 T \frac{\partial}{\partial x_j^*} \hat{\Pi}^{*jk} + \varepsilon^3 \frac{\partial}{\partial t^*} Q_{neq}^{*k} + \varepsilon^3 \frac{\partial}{\partial x_j^*} \Pi_{neq}^{*jk} \right). \end{aligned} \quad (7.20)$$

Dividing both sides by ε^2 ,

$$\begin{aligned} \frac{\partial}{\partial t^*} \phi + \frac{\partial}{\partial x_j^*} (u^{*j} \phi) &= \frac{\partial}{\partial x_j^*} \tau_\phi \rho \frac{\partial}{\partial x_k^*} (\theta T) + \\ &+ \underbrace{\varepsilon \tau_\phi \left(u^{*k} \frac{\partial}{\partial x_j^*} Q_{neq}^{*j} - T \frac{\partial}{\partial x_j^*} \hat{\Pi}^{*jk} + \frac{\partial}{\partial t^*} Q_{neq}^{*k} + \frac{\partial}{\partial x_j^*} \Pi_{neq}^{*jk} \right)}_{\text{cancels out as } \varepsilon \rightarrow 0}. \end{aligned} \quad (7.21)$$

The (recursive) scale of Q_{neq}^k term based on Equation (7.15) is,

$$-\varepsilon Q_{neq}^{*k} = \tau_\phi \varepsilon \rho \frac{\partial}{\partial x_k^*} (\theta T) + \tau_\phi \left(\varepsilon^3 u^{*k} \frac{\partial}{\partial x_j^*} Q_{neq}^{*j} - \varepsilon^3 T \frac{\partial}{\partial x_j^*} \hat{\Pi}^{*jk} + \varepsilon^3 \frac{\partial}{\partial t^*} Q_{neq}^{*k} + \varepsilon^3 \frac{\partial}{\partial x_j^*} \Pi_{neq}^{*jk} \right). \quad (7.22)$$

Dividing both sides by ε ,

$$-Q_{neq}^{*k} = \tau_\phi \rho \frac{\partial}{\partial x_k^*} (\theta T) + \underbrace{\varepsilon^2 \tau_\phi \left(u^{*k} \frac{\partial}{\partial x_j^*} Q_{neq}^{*j} - T \frac{\partial}{\partial x_j^*} \hat{\Pi}^{*jk} + \frac{\partial}{\partial t^*} Q_{neq}^{*k} + \frac{\partial}{\partial x_j^*} \Pi_{neq}^{*jk} \right)}_{\text{cancels out as } \varepsilon \rightarrow 0}. \quad (7.23)$$

For **acoustic scaling**:

$$\left\{ \begin{array}{ll} t = \frac{1}{\varepsilon} t^* & \\ x = \frac{1}{\varepsilon} x^* & \\ u = u^* & \text{the scale of velocity is [m/s], thus } u^* \sim \frac{x^*}{t^*} \\ \tau_\phi = \frac{1}{\varepsilon} \tau_\phi^* & \text{the scale of diffusivity is [m}^2\text{/s], thus } \tau_\phi^* \sim \frac{(x^*)^2}{t^*} \end{array} \right.$$

Again, the scale of non-equilibrium terms is analogous to the velocity scale, thus

$$\begin{cases} Q_{neq} = Q_{neq}^* \\ \Pi_{neq} = \Pi_{neq}^* \end{cases} \quad (7.24)$$

Substituting into Equation (7.16),

$$\varepsilon \frac{\partial}{\partial t^*} \phi + \varepsilon \frac{\partial}{\partial x_j^*} (u^{*j} \phi) = \varepsilon \frac{\partial}{\partial x_j^*} \tau_\phi^* \rho \frac{\partial}{\partial x_k^*} (\theta T) + \quad (7.25)$$

$$+ \frac{1}{\varepsilon} \tau_\phi^* \left(\varepsilon u^{*k} \frac{\partial}{\partial x_j^*} Q_{neq}^{*j} - \varepsilon T \frac{\partial}{\partial x_j^*} \hat{\Pi}^{*jk} + \varepsilon \frac{\partial}{\partial t^*} Q_{neq}^{*k} + \varepsilon \frac{\partial}{\partial x_j^*} \Pi_{neq}^{*jk} \right). \quad (7.26)$$

Dividing both sides by ε ,

$$\begin{aligned} \frac{\partial}{\partial t^*} \phi + \frac{\partial}{\partial x_j^*} (u^j \phi) &= \frac{\partial}{\partial x_j^*} \tau_\phi^* \rho \frac{\partial}{\partial x_k^*} (\theta T) + \\ &+ \underbrace{\frac{1}{\varepsilon} \tau_\phi^* \left(u^{*k} \frac{\partial}{\partial x_j^*} Q_{neq}^{*j} - T \frac{\partial}{\partial x_j^*} \hat{\Pi}^{*jk} + \frac{\partial}{\partial t^*} Q_{neq}^{*k} + \frac{\partial}{\partial x_j^*} \Pi_{neq}^{*jk} \right)}_{\text{cancels out as } \varepsilon \rightarrow \infty}. \end{aligned} \quad (7.27)$$

The scale of Q_{neq}^k term is,

$$-Q_{neq}^{*k} = \tau_\phi^* \rho \frac{\partial}{\partial x_k^*} (\theta T) + \tau_\phi^* \left(u^* \frac{\partial}{\partial x_j^*} Q_{neq}^{*j} - T \frac{\partial}{\partial x_j^*} \hat{\Pi}^{*jk} + \frac{\partial}{\partial t^*} Q_{neq}^{*k} + \frac{\partial}{\partial x_j^*} \Pi_{neq}^{*jk} \right). \quad (7.28)$$

Observe that the acoustic scaling does not converge to the target macroscopic equation (see Figure 4.5)!

Central moments

To present the concept, the central moments for a D2Q9 lattice are calculated below,

$$\begin{aligned}
 \sum h_i^{\text{eq}} &= \phi = \rho T \\
 \sum (e_i^j - u^j) h_i^{\text{eq}} &= u^j \phi - u^j \phi = 0 \\
 \sum (e_i^j - u^j)(e_i^k - u^k) h_i^{\text{eq}} &= \sum e_i^j e_i^k h_i^{\text{eq}} - \sum e_i^j u^k h_i^{\text{eq}} - \sum u^j e_i^k h_i^{\text{eq}} + \sum u^j u^k h_i^{\text{eq}} = \\
 &= \delta^{jk} \theta \phi + u^j u^k \phi - u^k u^j \phi - u^j u^k \phi + u^j u^k \phi = \\
 &= \delta^{jk} \theta \phi \\
 \sum (e_i^j - u^j)^2 (e_i^k - u^k) h_i^{\text{eq}} &= (\delta^{jj} \theta)(0) \phi = 0 \\
 \sum (e_i^j - u^j)^2 (e_i^k - u^k)^2 h_i^{\text{eq}} &= (\delta^{jj} \theta)(\delta^{kk} \theta) \phi = \theta^2 \phi.
 \end{aligned}$$

7.2 Conjugate Heat Transfer — future outlook

In this section we would like to account for variable ρ and c_v to simulate Conjugate Heat Transfer (CHT) flow. Up to the author's best knowledge, no model concerning cumulants or central moments for CHT has been presented in the LBM literature. The analysis is analogous as in the previous Section 7.1.1. We will start by showing origin of the problems related to modelling of the CHT in the LBM framework.

7.2.1 Way II: Why variable ρc_v causes problem

EDF - second order, same as Equation (7.4).

Moments of DF,

$$\begin{cases} \sum h_i &= \phi = \rho c_v T \\ \sum e_i^j h_i &= u^j \phi + Q_{neq}^j \\ \sum e_i^j e_i^k h_i &= \delta^{jk} \theta \phi + u^j u^k \phi + \Pi_{neq}^{jk} \end{cases} \quad (7.29)$$

DBE - same as Equation (7.7).

Zeroth moment of DBE = $\sum_i DBE_i$ - same as Equation (7.8).

First moment of DBE = $\sum_i e_i^k DBE_i$ - same as Equation (7.9).

Identities:

$$\begin{cases} \frac{\partial}{\partial t}(u^k \phi) &= u^k \frac{\partial}{\partial t} \phi + T \frac{\partial}{\partial t}(\rho c_v u^k) - T u^k \frac{\partial}{\partial t}(\rho c_v) \\ \frac{\partial}{\partial x_k}(\theta \phi) &= \rho \frac{\partial}{\partial x_k}(\theta c_v T) + T \frac{\partial}{\partial x_k}(\theta \rho c_v) \\ \frac{\partial}{\partial x_j}(u^j u^k \phi) &= T \frac{\partial}{\partial x_j}(u_j \rho c_v u_k) + u_k \frac{\partial}{\partial x_j}(u_j \phi) - u_k T \frac{\partial}{\partial x_j}(\rho c_v u_j) \end{cases} \quad (7.30)$$

Substituting,

$$\begin{aligned} & u^k \frac{\partial}{\partial t} \phi + T \frac{\partial}{\partial t}(\rho c_v u^k) - T u^k \frac{\partial}{\partial t}(\rho c_v) + \\ & \quad + \rho \frac{\partial}{\partial x_k}(\theta c_v T) + T \frac{\partial}{\partial x_k}(\theta \rho c_v) + \\ & + T \frac{\partial}{\partial x_j}(u_j \rho c_v u_k) + u_k \frac{\partial}{\partial x_j}(u_j \phi) - u_k T \frac{\partial}{\partial x_j}(\rho c_v u_j) + \\ & \quad + \frac{\partial}{\partial t} Q_{neq}^k + \frac{\partial}{\partial x_j} \Pi_{neq}^{jk} = -\frac{1}{\tau_\phi} Q_{neq}^k. \end{aligned} \quad (7.31)$$

Grouping terms,

$$\begin{aligned} & u^k \left(\frac{\partial}{\partial t} \phi + \frac{\partial}{\partial x_j}(u_j \phi) \right) + \\ & + T \left(\frac{\partial}{\partial t}(\rho c_v u^k) + \frac{\partial}{\partial x_k}(\theta \rho c_v) + \frac{\partial}{\partial x_j}(u_j \rho c_v u_k) \right) + \\ & - T u_k \left(\frac{\partial}{\partial t}(\rho c_v) + \frac{\partial}{\partial x_j}(\rho c_v u_j) \right) + \\ & \quad + \rho \frac{\partial}{\partial x_k}(\theta c_v T) + \\ & \quad + \frac{\partial}{\partial t} Q_{neq}^k + \frac{\partial}{\partial x_j} \Pi_{neq}^{jk} = -\frac{1}{\tau_\phi} Q_{neq}^k. \end{aligned} \quad (7.32)$$

This time, due to the presence of c_v the equations can not be simplified. The only thing we can do is to make a step back and calculate Q_{neq}^k from Equation (7.9),

$$Q_{neq}^k = -\tau_\phi \left[\frac{\partial}{\partial t}(u^k \phi) + \frac{\partial}{\partial t} Q_{neq}^k + \frac{\partial}{\partial x_k}(\theta \phi) + \frac{\partial}{\partial x_j}(u^j u^k \phi) + \frac{\partial}{\partial x_j} \Pi_{neq}^{jk} \right], \quad (7.33)$$

and insert it to Equation (7.8),

$$\frac{\partial}{\partial t} \phi + \frac{\partial}{\partial x_j}(u^j \phi) = \frac{\partial}{\partial x_j} \tau_\phi \left[\frac{\partial}{\partial t}(u^k \phi) + \frac{\partial}{\partial t} Q_{neq}^k + \frac{\partial}{\partial x_k}(\theta \phi) + \frac{\partial}{\partial x_j}(u^j u^k \phi) + \frac{\partial}{\partial x_j} \Pi_{neq}^{jk} \right].$$

Rearranging,

$$\begin{aligned} \frac{\partial}{\partial t}\phi + \frac{\partial}{\partial x_j}(u^j\phi) &= \frac{\partial}{\partial x_j}\tau_\phi \frac{\partial}{\partial x_k}(\theta\phi) \\ &+ \frac{\partial}{\partial x_j}\tau_\phi \left[\frac{\partial}{\partial t}(u^k\phi) + \frac{\partial}{\partial t}Q_{neq}^k + \frac{\partial}{\partial x_k}(\theta\phi) + \frac{\partial}{\partial x_j}(u^j u^k \phi) + \frac{\partial}{\partial x_j}\Pi_{neq}^{jk} \right]. \end{aligned} \quad (7.34)$$

Recalling that $\phi = \rho c_v T$, the recovered diffusive term $\frac{\partial}{\partial x_j}\tau_\phi \frac{\partial}{\partial x_k}(\theta\rho c_v T)$ does not coincide with the target macroscopic Equation (7.3)!

7.2.2 Way III: Calculate the right moments (or correction by weights)

Chen *et al.* [154] followed by Hosseini *et al.* [62] noticed that to recover the energy transport with physical diffusive term, a right set of moments of EDF is required. In [154] the EDF is modified, while in [62] a set of corrective weights is applied. Both approaches lead to the same result.

From a broader perspective, it is enough to say, that the right moments shall be relaxed. This is a well-know fact: using LBM to solve NS equations we relax the moments responsible for shear stresses. Unfortunately, in [154, 62] the SRT scheme is applied for both fluid and thermal DF. To circumvent the issue, the authors introduced the *special* weights η or modified EDF. Furthermore, to improve the stability (for $\tau_H \rightarrow 0.5$) the γ coefficient is introduced in [62].

Here, we will enhance the derivation from [62] by expressing the result in the central moments space (CMS)

Moments of DF with *special* weights,

$$\begin{cases} \sum [h_i + \eta_i \theta(\gamma T - \phi)] &= \phi = \rho c_v T \\ \sum e_i^j [h_i + \eta_i \theta(\gamma T - \phi)] &= u^j \phi + Q_{neq}^j \\ \sum e_i^j e_i^k [h_i + \eta_i \theta(\gamma T - \phi)] &= \delta^{jk} \theta \gamma T + u^j u^k \phi + \Pi_{neq}^{jk} \end{cases} \quad (7.35)$$

Weights have to fulfil,

$$\begin{cases} \sum \eta_i &= 0 \\ \sum e_i^j \eta_i &= 0 \\ \sum e_i^j e_i^k \eta_i &= \delta^{jk} \theta \end{cases} \quad (7.36)$$

It can be simply achieved by defining them as,

$$\begin{aligned} \eta_0 &= - \sum_{i \neq 0} w_i \\ \forall i \neq 0, \eta_i &= w_i \end{aligned} \quad (7.37)$$

Zeroth moment of DBE = $\sum_i DBE_i$

$$\begin{aligned} \frac{\partial}{\partial t} \phi + \frac{\partial}{\partial x_j} (u^j \phi + Q_{neq}^j) &= 0 \Leftrightarrow \\ \Leftrightarrow \frac{\partial}{\partial t} \phi + \frac{\partial}{\partial x_j} (u^j \phi) &= - \frac{\partial}{\partial x_j} Q_{neq}^j. \end{aligned} \quad (7.38)$$

First moment of DBE = $\sum_i e_i^k DBE_i$

$$\begin{aligned} \frac{\partial}{\partial t} (u^k \phi + Q_{neq}^k) + \frac{\partial}{\partial x_j} (\delta^{jk} \theta \gamma T + u^j u^k \phi + \Pi_{neq}^{jk}) &= - \frac{1}{\tau_\phi} Q_{neq}^k \Leftrightarrow \\ \Leftrightarrow \frac{\partial}{\partial t} (u^k \phi) + \frac{\partial}{\partial t} Q_{neq}^k + \frac{\partial}{\partial x_j} (\delta^{jk} \theta \gamma T) + \frac{\partial}{\partial x_j} (u^j u^k \phi) + \frac{\partial}{\partial x_j} \Pi_{neq}^{jk} &= - \frac{1}{\tau_\phi} Q_{neq}^k \\ \Leftrightarrow \frac{\partial}{\partial t} (u^k \phi) + \frac{\partial}{\partial t} Q_{neq}^k + \frac{\partial}{\partial x_k} (\theta \gamma T) + \frac{\partial}{\partial x_j} (u^j u^k \phi) + \frac{\partial}{\partial x_j} \Pi_{neq}^{jk} &= - \frac{1}{\tau_\phi} Q_{neq}^k \\ \Leftrightarrow Q_{neq}^k &= - \tau_\phi \left[\frac{\partial}{\partial t} (u^k \phi) + \frac{\partial}{\partial t} Q_{neq}^k + \frac{\partial}{\partial x_k} (\theta \gamma T) + \frac{\partial}{\partial x_j} (u^j u^k \phi) + \frac{\partial}{\partial x_j} \Pi_{neq}^{jk} \right]. \end{aligned} \quad (7.39)$$

As usual, we insert Q_{neq}^k to Eq.(7.38):

$$\begin{aligned} \frac{\partial}{\partial t} \phi + \frac{\partial}{\partial x_j} (u^j \phi) &= \frac{\partial}{\partial x_j} \tau_\phi \frac{\partial}{\partial x_k} (\theta \gamma T) \\ &+ \frac{\partial}{\partial x_j} \tau_\phi \left[\frac{\partial}{\partial t} (u^k \phi) + \frac{\partial}{\partial t} Q_{neq}^k + \frac{\partial}{\partial x_j} (u^j u^k \phi) + \frac{\partial}{\partial x_j} \Pi_{neq}^{jk} \right]. \end{aligned} \quad (7.40)$$

Finally, the desired macroscopic Equation (7.3) is recovered.

7.2.2.1 The EDF in CMS

We need to transform the *special* terms to the central moments space,

$$h'_i = \eta_i \theta (\gamma T - \phi). \quad (7.41)$$

Resulting moments,

$$\kappa^{H,eq} = \begin{bmatrix} \kappa_{00}^{eq} \\ \kappa_{10}^{eq} \\ \kappa_{01}^{eq} \\ \kappa_{20}^{eq} \\ \kappa_{02}^{eq} \\ \kappa_{11}^{eq} \\ \kappa_{21}^{eq} \\ \kappa_{12}^{eq} \\ \kappa_{22}^{eq} \end{bmatrix} = \sum_i (e_{ix} - u_x)^m (e_{iy} - u_y)^n [h_i^{eq} + h'_i] = \begin{bmatrix} \phi + 0 \\ 0 + 0 \\ 0 + 0 \\ \theta\phi + \theta(\gamma T - \phi) \\ \theta\phi + \theta(\gamma T - \phi) \\ 0 + 0 \\ 0 + 0 \\ 0 + 0 \\ \theta^2\phi + \theta^2(\gamma T - \phi) \end{bmatrix} = \begin{bmatrix} \phi \\ 0 \\ 0 \\ \theta\gamma T \\ \theta\gamma T \\ 0 \\ 0 \\ 0 \\ \theta^2\gamma T \end{bmatrix}. \quad (7.42)$$

Example of calculations for D2Q9:

$$\begin{aligned} \sum e_i^j e_i^k \eta_i &= \eta_5 - \eta_6 + \eta_7 - \eta_8 = 0 \\ \sum e_i^j e_i^j \eta_i &= \eta_1 + \eta_3 + \eta_5 + \eta_6 + \eta_7 + \eta_8 = 2/9 + 4/36 = 1/3 = \theta \\ \sum (e_i^j)^2 e_i^k \eta_i &= \eta_5 + \eta_6 - \eta_7 - \eta_8 = 0 \\ \sum (e_i^j)^2 (e_i^k)^2 \eta_i &= \eta_5 + \eta_6 + \eta_7 + \eta_8 = 4/36 = 1/9 = \theta^2 \end{aligned}$$

A more LB-native approach would be to tune the variance of the distribution,

$$\boxed{\sigma^2 = \frac{\gamma\theta}{\rho c_v}} \quad (7.43)$$

and the equilibrium distribution function would follow as,

$$\begin{aligned}
 \Psi_{CHT}^{M-B, eq} &= \Psi_{CHT}^{M-B, eq}(\phi, \sigma, \boldsymbol{\xi}, \mathbf{u}) = \\
 &= \frac{\phi}{(2\pi\sigma^2)^{D/2}} \exp \left[-\frac{(\boldsymbol{\xi} - \mathbf{u})^2}{2\sigma^2} \right] \\
 &= \frac{\rho c_v T}{\left(2\pi \frac{\gamma\theta}{\rho c_v} \right)^{D/2}} \exp \left[-\frac{(\boldsymbol{\xi} - \mathbf{u})^2}{2 \frac{\gamma\theta}{\rho c_v}} \right].
 \end{aligned} \tag{7.44}$$

Then the moments would read,

$$\begin{aligned}
 \Upsilon_{CHT}^{H,eq} &= \begin{bmatrix} \phi \\ \phi u_x \\ \phi u_y \\ \phi(\sigma^2 + u_x^2) \\ \phi(\sigma^2 + u_y^2) \\ \phi u_x u_y \\ \phi u_y(\sigma^2 + u_x^2) \\ \phi u_x(\sigma^2 + u_y^2) \\ \phi(\sigma^4 + \sigma^2 u_x^2 + \sigma^2 u_y^2 + u_x^2 u_y^2) \end{bmatrix} = \\
 &= \begin{bmatrix} T\rho c_v \\ T\rho c_v u_x \\ T\rho c_v u_y \\ T(\rho c_v u_x^2 + \gamma c_s^2) \\ T(\rho c_v u_y^2 + \gamma c_s^2) \\ T\rho c_v u_x u_y \\ T u_y(\gamma c_s^2 + \rho c_v u_x^2) \\ T u_x(\gamma c_s^2 + \rho c_v u_y^2) \\ T [c_v \rho (u_x^2 u_y^2 c_v \rho + (u_x^2 + u_y^2) c_s^2 \gamma) + c_s^4 \gamma^2] / (c_v \rho) \end{bmatrix}, \tag{7.45}
 \end{aligned}$$

and central moments,

$$\boldsymbol{\kappa}_{CHT}^{H,eq} = \begin{bmatrix} \kappa_{00}^{eq} \\ \kappa_{10}^{eq} \\ \kappa_{01}^{eq} \\ \kappa_{20}^{eq} \\ \kappa_{02}^{eq} \\ \kappa_{11}^{eq} \\ \kappa_{21}^{eq} \\ \kappa_{12}^{eq} \\ \kappa_{22}^{eq} \end{bmatrix} = \begin{bmatrix} \phi \\ 0 \\ 0 \\ \phi\sigma^2 \\ \phi\sigma^2 \\ 0 \\ 0 \\ 0 \\ \phi\sigma^4 \end{bmatrix} = \begin{bmatrix} \rho c_v T \\ 0 \\ 0 \\ \gamma\theta T \\ \gamma\theta T \\ 0 \\ 0 \\ 0 \\ \gamma^2\theta^2 T / (\rho c_v) \end{bmatrix}. \quad (7.46)$$

The same concept can be expressed in the cumulants' space,

$$\boldsymbol{c}_{CHT}^{H,eq} = \begin{bmatrix} c_{00}^{eq} \\ c_{10}^{eq} \\ c_{01}^{eq} \\ c_{20}^{eq} \\ c_{02}^{eq} \\ c_{11}^{eq} \\ c_{10}^{eq} \\ c_{22}^{eq} \end{bmatrix} = \begin{bmatrix} \phi \\ u_x \\ u_y \\ \sigma^2 \\ \sigma^2 \\ 0 \\ 0 \\ \sigma^4 \end{bmatrix} = \begin{bmatrix} \rho c_v T \\ u_x \\ u_y \\ \gamma\theta / (\rho c_v) \\ \gamma\theta / (\rho c_v) \\ 0 \\ 0 \\ (\gamma\theta / (\rho c_v))^2 \end{bmatrix}. \quad (7.47)$$

The γ coefficient plays a role of *numerical* stability enhancement. It achieves its goal by tuning the variance of the distribution closer to 1/3 (see Section 3.3.1).

7.2.3 Way IV: Correction by source term

In the next approach, instead of weights [62] or modified EDF [154], the terms in advection-diffusion equation are re-arranged to obtain the form of energy balance. This idea was expressed for the first time by Karani and Huber [60], then revisited by Chen *et al.* [61] with a better FD stencil.

Let us remind the target equation, which is a simplified balance of internal energy given by Equation (7.3):

$$\frac{\partial}{\partial t}(\rho c_v T) + \nabla \cdot (\mathbf{u} \rho c_v T) = \nabla \cdot k \nabla T.$$

And, an advection-diffusion equation (ADE):

$$\frac{\partial}{\partial t} \phi + \nabla \cdot (\mathbf{u} \phi) = \nabla \cdot (\alpha \nabla \phi). \quad (7.48)$$

We set $\phi = T$, then the re-arrangement of Equation (7.48) begins.

The advective term,

$$\begin{aligned} \nabla \cdot (\mathbf{u} T) &= \nabla \cdot \left(\mathbf{u} \frac{\rho c_v}{\rho c_v} T \right) \\ &= \frac{1}{\rho c_v} \nabla \cdot (\mathbf{u} \rho c_v T) + \mathbf{u} \rho c_v T \cdot \nabla \left(\frac{1}{\rho c_v} \right). \end{aligned} \quad (7.49)$$

The diffusive term,

$$\begin{aligned} \nabla \cdot (\alpha \nabla T) &= \nabla \cdot \left(\frac{k}{\rho c_v} \nabla T \right) \\ &= \frac{1}{\rho c_v} \nabla \cdot (k \nabla T) + k \nabla T \cdot \nabla \left(\frac{1}{\rho c_v} \right). \end{aligned} \quad (7.50)$$

We divide both sides of Equation (7.3) by ρc_v (assuming that ρc_v is time-independent),

$$\frac{\partial}{\partial t} T + \frac{1}{\rho c_v} \nabla \cdot (\mathbf{u} \rho c_v T) = \frac{1}{\rho c_v} \nabla \cdot (k \nabla T). \quad (7.51)$$

Next, we plug the expanded terms,

$$\begin{aligned} \frac{\partial}{\partial t} T + \overbrace{\nabla \cdot (\mathbf{u} T) - \mathbf{u} \rho c_v T \cdot \nabla \left(\frac{1}{\rho c_v} \right)}^{Eq.(7.49)} &= \overbrace{\nabla \cdot (\alpha \nabla T) - k \nabla T \cdot \nabla \left(\frac{1}{\rho c_v} \right)}^{Eq.(7.50)} \Leftrightarrow \\ \Leftrightarrow \frac{\partial}{\partial t} T + \nabla \cdot (\mathbf{u} T) &= \nabla \cdot (\alpha \nabla T) + \underbrace{[\mathbf{u} \rho c_v T - k \nabla T] \cdot \nabla \left(\frac{1}{\rho c_v} \right)}_{S_{conj}}. \end{aligned} \quad (7.52)$$

Finally, the S_{conj} term is discretized using FD stencil and added during the collision step as a source term.

7.2.4 Way V: Two passive scalar worlds tied by BC at the interface.

This approach states that the interfaces between heterogeneous media should be handled explicitly. The continuity of temperature Equation (7.53) and heat flux Equation (7.54) at the boundary must be satisfied:

$$T^{I,+} = T^{I,-} \quad (7.53)$$

$$\mathbf{n} \cdot (k\nabla T + \rho c_v \mathbf{u}T)^{I,+} = \mathbf{n} \cdot (k\nabla T + \rho c_v \mathbf{u}T)^{I,-} \quad (7.54)$$

where $+$ and $-$ indicates the side of the interface I . As a result, a straightforward implementation of such BC is limited to cases restricted by straight-interface geometry [155]. To model conjugate problems with arbitrary interfaces, an interpolation and/or extrapolation scheme are required [156, 157, 158]. The formulas are complicated and lose the intrinsic advantage of local computing of the standard LB method.

Chen *et al.* [61] believe that the explicit treatment of interfaces can be avoided:

"Especially, as it is a particle-based numerical solver, the LB method can guarantee, automatically, the continuity of a certain macroscopic quantity and of its flux across an arbitrary interface within the investigated domain, if the macroscopic quantity and its flux can be recovered from the zeroth- and first-order moment of the corresponding pseudo-particle distribution function, respectively, in the LB framework. This feature is a potential great advantage for conjugate heat transfer research as in the LB framework one need not explicitly treat the topology of the interface where the conjugated boundary condition should be strictly satisfied."

Chapter 8

Boundary Conditions in LBM

“Smooth sea never made a skilled sailor.”

– Franklin D. Roosevelt

Contents

8.1	Link-wise approach: the bounce-back (BB)	122
8.2	The magic (Ginzburg) parameter	124
8.2.1	Velocity inlet or a moving wall	124
8.2.2	Pressure inlet/outlet	125
8.2.3	Concentration	125
8.2.4	Gradient at the boundary	126
8.3	Moments of a link-wise BC	126
8.3.1	Future outlook: heat flux boundary condition	131
8.4	Interpolated (anti)-bounce-back BC	135
8.5	Summary	137

The main problem with the boundary condition (BC) in LBM emerges from the fact that there are more degrees of freedom (g_i populations) than the corresponding macroscopic equations. This gives birth to a “zoo” of approaches, documented by more than 160 publications until 2015 [9, pp. 166]. A closer look of a so-called “link-wise” boundary condition will be taken. In this chapter a contribution to the textbooks’ knowledge [8, 9, 10] is done by analysis of moments of the aforementioned BC.

In general, there are two main families of boundary condition (BC). The *link-wise* BC recovers macroscopic solution where the boundary is located midway between the fluid and boundary node. The *wet node* BC assumes the boundary lie on a boundary node. A

quick comparison is given in Tab. 8. Reader interested in more detailed discussion of the BC implementations is referred to the regular textbook [9] and references therein.

	<i>link-wise</i>		<i>wet-note</i>		
	HBB	FBB	ES	NEEM	NEBB
Boundary location	Midway	Midway	On node	On node	On node
Accuracy	2nd-order ^a	1st-order	1st-order	2nd-order	3rd-order
Exactness	Linear	Linear	Constant	Linear	Parabolilc
Stability	High	High	High	Moderate	Low
Locality	✓	✓	✓	✗	✓
Viscosity independent	✗	✗	✗	✗	✓
Mass conservation	Exact	Exact	Non-exact	Non-exact	Non-exact
Algorithm simplicity	Simple	Simple	Simple	Moderate	Complex
Application to moving objects	✗	✗	✗	✗	✗

TABLE 8.1: Comparison of common BC (table from [9, pp. 157]). The abbreviations read: **HBB** - half-way bounce-back; **ES** - equilibrium scheme; **NEEM** - non-equilibrium extrapolation method; **NEBB** - non-equilibrium bounce-back.

^aOnly for straight boundaries.

8.1 Link-wise approach: the bounce- back (BB)

The bounce-back boundary conditions acts as a rigid wall, it reverses the particles velocity which fall onto it. The implementation can be done in two ways:

- *half-way bounce-back* HBB - the inversion of the particle's velocity happens during the streaming step, thus it comes back in the next iteration as it would travel only half of the link distance between nodes.
- *full-way bounce-back* FBB - the inversion of the particle's velocity happens during the collision step within the node, thus it takes two iterations for the particle to come back.

The Figure 8.1 shows the conceptual difference between HBB and FBB. It may happen

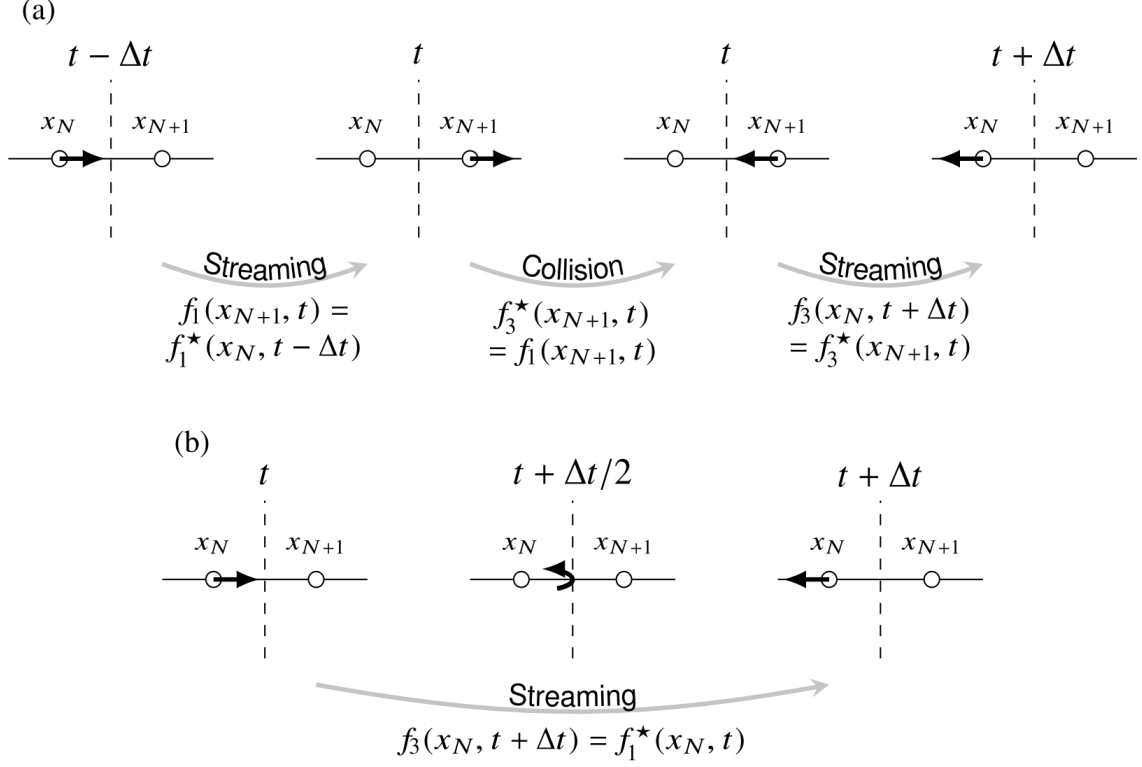


FIGURE 8.1: Comparison of (a) full-way bounce-back and (b) half-way bounce-back. The dashed line shows boundary location. (from [9, p. 177]).

that for the turbulent flows the lack of *lag* in half-way bounce back, compared to the full-way version, is crucial for the resolution of both turbulent boundary layer and correct value of forces (even if there is no separation).

Unfortunately, both bounce-back methods suffer from a dependence of the effective boundary location on the fluid viscosity in a SRT collision scheme, which can be viewed as an unphysical slip at the boundary. It has been shown in [159], that the bounce back condition is in fact a condition for 3rd order hydrodynamic moment ($\Upsilon_{xyy} = \frac{1}{3}\rho u_x + \Upsilon_{xyy}^{neq}$ in this case). From a Chapman-Enskog analysis, one can find the relaxation rate to minimize the error [160, 161].

In the upcoming sections, we will add an additional term, B_i , to modify the bounced-back distributions in order to obtain a more specific BC.

8.2 The magic (Ginzburg) parameter

The no-slip wall is positioned by the bounce-back rule exactly halfway between the boundary and solid nodes. However, the solution is viscosity-independent. The *numerical slip* caused by the bounce-back BC strongly depends on the value of numerical viscosity ν_{LB} . This effect particularly obscures simulations of the porous media, since the effective wall location directly affects the permeability parameter [162, 163, 160].

When odd and even moments are relaxed with appropriate relaxation rate, the numerical slip caused by the bounce-back BC can be alleviated or at least kept constant for different values of ν_{LB} . Detailed analyses done by the group of I. Ginzburg [164, 165] have shown that in the case of linear, steady flows the value of the magic parameter, λ , (see Equation (3.37)) is crucial for proper results. The research was continued by Khirevich *et al.* [166] who studied different formulation of interpolated bounce-back and variations of the MRT collision operator.

Unfortunately, there is not much literature available regarding non-creeping flows. The issue was investigated in the PhD thesis of Regulski [167] who simulated higher Re-number flows in porous media by incorporating the *magic* parameter into the cumulant model [43]. It was found, that the interpolated bounce back proposed in [43] does not allow to obtain a viscosity independent model despite of claims given in [168]. Moreover, introduction of the *magic* parameter into the cumulant model reduces its stability. The desired behaviour of permeability independent from viscosity was observed only for selected values of Λ . However, it was achievable in a simpler MRT model without problems. Finally, an ad-hoc solution was proposed. First, the unstable but accurate MRT-TRT model was utilized to produced a reference solution, then the geometry was modified (thinned) together with calibrated ν_{LB} for the cumulant model.

8.2.1 Velocity inlet or a moving wall

The extension of the half/full-way bounce-back method to moving wall or inlet/outlet is achieved by adding additional momentum to the outgoing distributions [169, 170, 171],

$$f_i(\mathbf{x}_b, t + \Delta t) = f_i^*(\mathbf{x}_b, t) - \underbrace{2w_i\rho_w \frac{\mathbf{e}_i \cdot \mathbf{u}_w}{c_s^2}}_{B_i}. \quad (8.1)$$

Obviously, the exact value of density at the wall ρ_w is unknown. To estimate it, either system average density or local density at the node is used. Unfortunately, both approaches

lead to violation of mass conservation. The only solution is to use incompressible-LB or a different formulation of BC.

One may wonder where does the (multiplication by) “2” coefficient in Equations (8.1) to (8.3), (8.8) and (8.9) comes from. Although the first idea of averaging ($\frac{1}{2}(Node_A + Node_B)$) between nodes may appear sufficient, the change of flux/momentum is a better explanation as it holds for interpolation when the boundary is not located exactly between nodes (see Section 8.4). To exemplify, consider a transformation to the frame of the wall, bounce-back there and back transform to the initial frame of reference (think of bouncing a ball against a train while riding in a car).

8.2.2 Pressure inlet/outlet

In case of a pressure inlet/outlet, the momentum component (the first moment of the equilibrium distribution function, which is prescribed in case velocity inlet/moving wall as in Equation (8.1)) is removed from the equilibrium distribution:

$$f_{\bar{i}}(\mathbf{x}_b, t + \Delta t) = -f_i^*(\mathbf{x}_b, t) + \underbrace{2w_i\rho_w \left[1 + \frac{(\mathbf{e}_i \cdot \mathbf{u}_w)^2}{2c_s^4} + \frac{\mathbf{u}_w^2}{2c_s^2} \right]}_{B_i}. \quad (8.2)$$

This time, the exact value of velocity at the wall \mathbf{u}_w is unknown. It is usually estimated by extrapolation, which does not influence the mass conservation of the system in case of pressure-type BC.

8.2.3 Concentration

The concentration (Dirichlet) BC for the thermal distribution ($\sum_h h_i = \rho T$) can be implemented as,

$$\begin{aligned} h_{\bar{i}}(\mathbf{x}_b, t + \Delta t) &= -h_i^*(\mathbf{x}_b, t) + 2h_{i,w}^{eq} \\ &= -h_i^*(\mathbf{x}_b, t) + \underbrace{2w_i\rho_w T_w \left[1 + \frac{\mathbf{e}_i \cdot \mathbf{u}_w}{c_s^2} + \frac{(\mathbf{e}_i \cdot \mathbf{u}_w)^2}{2c_s^4} - \frac{(\mathbf{u}_w)^2}{2c_s^2} \right]}_{B_i}. \end{aligned} \quad (8.3)$$

Since the post collision populations are given with a negative sign (e.g. $-h_i^*$), this approach is commonly called *Anti Bounce Back*.

8.2.4 Gradient at the boundary

The implementation of the Neumann BC can be done by imposition of the concentration (Dirichlet BC) required to obtain desired gradient. From a broader view point, a general concentration boundary condition can be formulated as [172],

$$b_1 \frac{\partial}{\partial \mathbf{n}} C_w + b_2 C_w = b_3. \quad (8.4)$$

Using the finite-difference scheme to approximate the concentration gradient,

$$b_1 \frac{\partial}{\partial \mathbf{n}} C_w \approx b_1 \frac{C_b - C_w}{|\mathbf{x}_b - \mathbf{x}_w|}, \quad (8.5)$$

the unknown concentration at the wall, C_w , can be found easily,

$$C_w = C_b + \frac{b_3 |\mathbf{x}_b - \mathbf{x}_w|}{b_2 |\mathbf{x}_b - \mathbf{x}_w| - b_1}. \quad (8.6)$$

The C_b is the concentration at the boundary (fluid) node neighboring the interface. Extension to dissolution or surface reaction is straightforward,

$$-k \frac{\partial}{\partial \mathbf{n}} C_w = \alpha (C_{eq} - C_w)^\beta, \quad (8.7)$$

where α is the reaction rate constant and β is the order of reaction kinetics.

There is an ongoing dispute regarding proper choice of the FD stencil required to calculate the concentration gradient [173, 174, 175] from macroscopic field.

Interestingly, Li et al., have develop an interpolation schemes on the level of distribution functions [156, 157, 176].

Alternatively, a simple yet effective method would be to smear a source term across the body to mimic the Neumann BC. Although not as precise from a mathematical point of view, this approach would easily result in the same heat flux submitted to the domain.

8.3 Moments of a link-wise BC

It is very instructive to calculate the moments of the already discussed, link-wise BC.

Here, it shall be noticed that the diffusive flux, Q_{neq}^j , in ADE is present in the non-equilibrium part of the first moments.

To obtain pressure type BC, the B_i coefficients have to act on the second order moments (stress tensor),

$$B_i = 2w_i\rho_w \left[1 + \frac{(\mathbf{e}_i \cdot \mathbf{u}_w)^2}{2c_s^4} - \frac{(\mathbf{u}_w)^2}{2c_s^2} \right]. \quad (8.8)$$

In case of a velocity type BC, the B_i coefficient have to contribute to the first order moments (flux of momentum),

$$B_i = 2w_i\rho_w \frac{\mathbf{e}_i \cdot \mathbf{u}_w}{c_s^2}. \quad (8.9)$$

It shall be noted, that the continuous moments of B_i result in a more accurate expressions (see bolded terms in Tables 8.2 and 8.4 and in Equation (8.10)).

For convenience of the study, let us list the hydrodynamics moments for a D2Q9 lattice:

$$\Upsilon^{eq} = \begin{bmatrix} \Upsilon_{00}^{eq} \\ \Upsilon_{10}^{eq} \\ \Upsilon_{01}^{eq} \\ \Upsilon_{20}^{eq} \\ \Upsilon_{02}^{eq} \\ \Upsilon_{11}^{eq} \\ \Upsilon_{21}^{eq} \\ \Upsilon_{12}^{eq} \\ \Upsilon_{22}^{eq} \end{bmatrix} = \begin{bmatrix} \rho \\ \rho u_x \\ \rho u_y \\ \rho(u_x^2 + c_s^2) \\ \rho(u_y^2 + c_s^2) \\ \rho u_x u_y \\ \rho u_y(c_s^2 + \mathbf{u}_x^2) \\ \rho u_x(c_s^2 + \mathbf{u}_y^2) \\ \rho(c_s^4 + c_s^2 u_x^2 + c_s^2 u_y^2 + \mathbf{u}_x^2 \mathbf{u}_y^2) \end{bmatrix}. \quad (8.10)$$

and the moments for thermal distribution (see Section 7.1.1, where $\Upsilon_{00}^H = \rho T$),

$$\Upsilon^{H,eq} = \begin{bmatrix} H \\ Hu_x \\ Hu_y \\ H(u_x^2 + c_s^2) \\ H(u_y^2 + c_s^2) \\ Hu_x u_y \\ Hu_y(c_s^2 + \mathbf{u}_x^2) \\ Hu_x(c_s^2 + \mathbf{u}_y^2) \\ H(c_s^4 + c_s^2 u_x^2 + c_s^2 u_y^2 + \mathbf{u}_x^2 \mathbf{u}_y^2) \end{bmatrix} = \begin{bmatrix} \rho T \\ \rho T u_x \\ \rho T u_y \\ \rho T(u_x^2 + c_s^2) \\ \rho T(u_y^2 + c_s^2) \\ \rho T u_x u_y \\ \rho T u_y(c_s^2 + \mathbf{u}_x^2) \\ \rho T u_x(c_s^2 + \mathbf{u}_y^2) \\ \rho T(c_s^4 + c_s^2 u_x^2 + c_s^2 u_y^2 + \mathbf{u}_x^2 \mathbf{u}_y^2) \end{bmatrix}, \quad (8.11)$$

and the moments for thermal distribution in Conjugate Heat Transfer model (see Section 7.2 and Equations (7.35), (7.43) and (7.45), where $\Upsilon_{00}^H = H = \rho c_v T$),

$$\begin{aligned} \mathfrak{Y}_{CHT}^{H,eq} &= \begin{bmatrix} H \\ Hu_x \\ Hu_y \\ H(\sigma^2 + u_x^2) \\ H(\sigma^2 + u_y^2) \\ Hu_x u_y \\ Hu_y(\sigma^2 + \mathbf{u}_x^2) \\ Hu_x(\sigma^2 + \mathbf{u}_y^2) \\ H(\sigma^4 + \sigma^2 u_x^2 + \sigma^2 u_y^2 + \mathbf{u}_x^2 \mathbf{u}_y^2) \end{bmatrix} = \\ &= \begin{bmatrix} T \rho c_v \\ T \rho c_v u_x \\ T \rho c_v u_y \\ T(\rho c_v u_x^2 + \gamma c_s^2) \\ T(\rho c_v u_y^2 + \gamma c_s^2) \\ T \rho c_v u_x u_y \\ T u_y(\gamma c_s^2 + \rho c_v \mathbf{u}_x^2) \\ T u_x(\gamma c_s^2 + \rho c_v \mathbf{u}_y^2) \\ T \left[c_v \rho \left(\mathbf{u}_x^2 \mathbf{u}_y^2 c_v \rho + (\mathbf{u}_x^2 + \mathbf{u}_y^2) c_s^2 \gamma \right) + c_s^4 \gamma^2 \right] / (c_v \rho) \end{bmatrix}. \end{aligned} \quad (8.12)$$

$\Upsilon_{jk} = \sum_i e_{ix}^j e_{iy}^k$	$f_i(x_b, t)$	$-f_i(x_s, t)$	$B_i = 2w_i \rho_w \left[1 + \frac{(\mathbf{e}_i \cdot \mathbf{u}_w)^2}{2c_s^4} - \frac{(\mathbf{u}_w)^2}{2c_s^2} \right]$	at $x_w = \frac{1}{2}[f_i(x_b, t) - f_i(x_s, t) + B_i]$
Υ_{00}	ρ	$-\rho$	$2\rho_w$	$0 + \rho_w$
Υ_{10}	ρu_x	ρu_x	0	ρu_x
Υ_{01}	ρu_y	ρu_y	0	ρu_y
Υ_{20}	Υ_{20}	$-\Upsilon_{20}$	$2\rho_w(c_s^2 + u_{x,w}^2)$	$0 + 2\rho_w(c_s^2 + u_{x,w}^2)$
Υ_{02}	Υ_{02}	$-\Upsilon_{02}$	$2\rho_w(c_s^2 + u_{y,w}^2)$	$0 + 2\rho_w(c_s^2 + u_{y,w}^2)$
Υ_{11}	Υ_{11}	$-\Upsilon_{11}$	$2\rho_w u_{x,w} u_{y,w}$	$0 + \rho_w u_{x,w} u_{y,w}$
Υ_{21}	Υ_{21}	Υ_{21}	0	Υ_{21}
Υ_{12}	Υ_{12}	Υ_{12}	0	Υ_{12}
Υ_{22}	Υ_{22}	$-\Upsilon_{22}$	$2\rho_w(c_s^4 + c_s^2 u_{x,w}^2 + c_s^2 u_{y,w}^2 + \mathbf{u}_{x,w}^2 \mathbf{u}_{y,w}^2)$	$0 + \rho_w(c_s^4 + c_s^2 u_{x,w}^2 + c_s^2 u_{y,w}^2 + \mathbf{u}_{x,w}^2 \mathbf{u}_{y,w}^2)$

TABLE 8.2: Moments of an Anti Bounce Back (pressure type) BC for D2Q9 lattice.

Note that the sign of even moments is reverted during the Anti Bounce Back procedure.

$\Upsilon_{jk} = \sum_i e_{ix}^j e_{iy}^k$	$f_i(x_b, t)$	$f_i(x_s, t)$	$B_i = 2w_i \rho_w \frac{\mathbf{e}_i \cdot \mathbf{u}_w}{c_s^2}$	at $x_w = \frac{1}{2}[f_i(x_b, t) + f_i(x_s, t) + B_i]$
Υ_{00}	ρ	ρ	0	ρ
Υ_{10}	ρu_x	$-\rho u_x$	$-2\rho_w u_{x,w}$	$0 - \rho_w u_{x,w}$
Υ_{01}	ρu_y	$-\rho u_y$	$-2\rho_w u_{y,w}$	$0 - \rho_w u_{y,w}$
Υ_{20}	Υ_{20}	Υ_{20}	0	Υ_{20}
Υ_{02}	Υ_{02}	Υ_{02}	0	Υ_{02}
Υ_{11}	Υ_{11}	Υ_{11}	0	Υ_{11}
Υ_{21}	Υ_{21}	$-\Upsilon_{21}$	$-2\rho_w u_{y,w}(c_s^2 + \mathbf{u}_{x,w}^2)$	$0 - c_s^2 \rho u_{y,w}$
Υ_{12}	Υ_{12}	$-\Upsilon_{12}$	$-2\rho_w u_{x,w}(c_s^2 + \mathbf{u}_{y,w}^2)$	$0 - c_s^2 \rho u_{x,w}$
Υ_{22}	Υ_{22}	Υ_{22}	0	Υ_{22}

TABLE 8.3: Moments of an Bounce Back (velocity inlet/moving wall) BC for D2Q9 lattice.

Note that the sign of odd moments is reverted during the Bounce Back procedure.

8.3.1 Future outlook: heat flux boundary condition

To impose a flux of some quantity, g , one have to modify its first order moments. Inspired by the forcing scheme proposed by He et al. [22] (see Equation (2.19)), we will show a theoretical derivation of a heat flux BC. To the best of the author's knowledge, both the implementation of the flux BC by adding required moments of the distribution as proposed in Table 8.5 and the role of the velocity truncation (bolded velocity terms) in the equilibrium distribution function on the accuracy of link-wise BC is not well covered in the literature. However, a detailed numerical benchmarks are beyond the scope of the current work. Let accommodate the Equation (2.19),

$$\begin{aligned} \mathbf{F}_{\text{lux of heat}}(\boldsymbol{\xi}) &= \left(\frac{\mathbf{H}_w}{\Upsilon_{00}^H} \cdot \nabla_{\boldsymbol{\xi}} \right) \overbrace{\Psi^{M-B, eq}(\Upsilon_{00}^H, \boldsymbol{\xi}, \mathbf{u})}^{h^{eq}} \\ &\approx \frac{\mathbf{H}_w}{\Upsilon_{00}^H} \cdot \nabla_{\boldsymbol{\xi}} h^{eq} = -\frac{\mathbf{H}_w}{\Upsilon_{00}^H} \frac{(\boldsymbol{\xi} - \mathbf{u})}{\sigma^2} h^{eq}. \end{aligned} \quad (8.13)$$

where \mathbf{H}_w is the heat flux imposed thorough the boundary per unit length (2D) or surface (3D). The Υ_{00}^H is the zeroth moment of the thermal distribution. Depending on the case, it can be interpreted as $\Upsilon_{00}^H = \rho T$ and $\sigma^2 = c_s^2$, while for the Conjugate Heat Transfer model (see Section 7.2 and Equations (7.35), (7.43) and (7.45)) $\Upsilon_{00}^H = \rho c_v T$ and $\sigma^2 = \frac{\gamma c_s^2}{\rho c_v}$. Calculating the central moments (if the wall is stationary then $\mathbf{u} = \mathbf{0}$) of Equation (8.13),

$$\Upsilon^{H_w} = H_w \begin{bmatrix} 0 \\ -n_{w,x} \\ -n_{w,y} \\ 0 \\ 0 \\ 0 \\ -n_{w,y}\sigma^2 \\ -n_{w,x}\sigma^2 \\ 0 \end{bmatrix}, \quad (8.14)$$

where \mathbf{n} is the normal to boundary surface.

Alternatively, an extension to the collision step (see Equations (4.3) to (4.5)) by means of the exact difference method [71] can be applied to obtain the desired flux,

$$\tilde{\mathbf{\Upsilon}}^* = (1 - s) \left(\tilde{\mathbf{\Upsilon}} - \mathbf{\Upsilon}^{\text{eq}}(\tilde{\phi}, \mathbf{u}) \right) + \mathbf{\Upsilon}^{\text{eq}} \left(\tilde{\phi}, \mathbf{u} + \mathbf{n} \frac{H^{\text{imposed}}}{\Upsilon_{00}^H} \right). \quad (8.15)$$

Finally, we can apply the calculated moments as BC in a link-wise (perform (Anti)-Bounce-Back then add moments) or wet-node (add/overwrite the desired moments to the incoming distributions) manner. Observe, that implementation of the aforementioned condition within the fluid would act as a heat pump BC.

$\Upsilon_{jk} = \sum_i e_{ix}^j e_{iy}^k$	$h_i(x_b, t)$	$-h_i(x_s, t)$	$B_i = 2w_i H_w$	$\left[1 + \frac{e_i \cdot \mathbf{u}_w}{c_s^2} + \frac{(e_i \cdot \mathbf{u}_w)^2}{2c_s^4} - \frac{(\mathbf{u}_w)^2}{2c_s^2}\right]$	at $x_w = \frac{1}{2}[h_i(x_b, t) - h_i(x_s, t) + B_i]$
Υ_{00}	H	$-H$		$2H_w$	$0 + H_w$
Υ_{10}	$Hu_x + Q_x$	$Hu_x + Q_x$		$2H_w u_{x,w}$	$Hu_x + Q_x + H_w u_{x,w}$
Υ_{01}	$Hu_y + Q_y$	$Hu_y + Q_y$		$2H_w u_{y,w}$	$Hu_y + Q_y + H_w u_{y,w}$
Υ_{20}	Υ_{20}	$-\Upsilon_{20}$		$2H_w(c_s^2 + u_{x,w}^2)$	$0 + H_w(c_s^2 + u_{x,w}^2)$
Υ_{02}	Υ_{02}	$-\Upsilon_{02}$		$2H_w(c_s^2 + u_{y,w}^2)$	$0 + H_w(c_s^2 + u_{y,w}^2)$
Υ_{11}	Υ_{11}	$-\Upsilon_{11}$		$2H_w u_{x,w} u_{y,w}$	$0 + H_w u_{x,w} u_{y,w}$
Υ_{21}	Υ_{21}	Υ_{21}		$2H_w u_y(c_s^2 + \mathbf{u}_x^2)$	$\Upsilon_{21} + H_w u_y(c_s^2 + \mathbf{u}_x^2)$
Υ_{12}	Υ_{12}	Υ_{12}		$2H_w u_x(c_s^2 + \mathbf{u}_y^2)$	$\Upsilon_{12} + H_w u_x(c_s^2 + \mathbf{u}_y^2)$
Υ_{22}	Υ_{22}	$-\Upsilon_{22}$	$2H_w(c_s^4 + c_s^2 u_{x,w}^2 + c_s^2 u_{y,w}^2 + \mathbf{u}_{x,w}^2 \mathbf{u}_{y,w}^2)$		$0 + H_w(c_s^4 + c_s^2 u_{x,w}^2 + c_s^2 u_{y,w}^2 + \mathbf{u}_{x,w}^2 \mathbf{u}_{y,w}^2)$

TABLE 8.4: Moments of an Anti Bounce Back BC for D2Q9 lattice (Dirichlet BC for temperature, where $\Upsilon_{00}^H = \rho T$ and $\sigma = c_s^2$).
Note that the sign of even moments is reverted during the Anti Bounce Back procedure.

$\Upsilon_{jk} = \sum_i e_{ix}^j e_{iy}^k$	$h_i(x_b, t)$	$h_i(x_s, t)$	$B_i = -2w_i H_w \frac{e_i \cdot \mathbf{n}_w}{c_s^2}$	at $x_w = \frac{1}{2}[h_i(x_b, t) + h_i(x_s, t) + B_i]$
Υ_{00}	H	H	0	H
Υ_{10}	$Hu_x + Q_x$	$-(Hu_x + Q_x)$	$-2H_w n_x$	$0 - H_w n_x$
Υ_{01}	$Hu_y + Q_y$	$-(Hu_y + Q_y)$	$-2H_w n_y$	$0 - H_w n_y$
Υ_{20}	Υ_{20}	Υ_{20}	0	Υ_{20}
Υ_{02}	Υ_{02}	Υ_{02}	0	Υ_{02}
Υ_{11}	Υ_{11}	Υ_{11}	0	Υ_{11}
Υ_{21}	Υ_{21}	$-\Upsilon_{21}$	$-2c_s^2 H_w n_y$	$0 - c_s^2 H_w n_y$
Υ_{12}	Υ_{12}	$-\Upsilon_{12}$	$-2c_s^2 H_w n_x$	$0 - c_s^2 H_w n_x$
Υ_{22}	Υ_{22}	Υ_{22}	0	Υ_{22}

TABLE 8.5: Moments of a Bounce Back BC for D2Q9 lattice and central moments of B_i (impose flux BC for the thermal field, where $\Upsilon_{00}^H = \rho T$ and $\sigma = c_s^2$). Note that the sign of odd moments is reverted during the Bounce Back procedure.

$\Upsilon_{jk} = \sum_i e_{ix}^j e_{iy}^k$	$h_i(x_b, t)$	$-h_{\bar{i}}(x_s, t)$	$B_i = 2\Upsilon_i^{H_w}$	at $x_w = \frac{1}{2}[h_i(x_b, t) - h_{\bar{i}}(x_s, t) + B_i]$
Υ_{00}	H	$-H$	$2H_w$	$0 + H_w$
Υ_{10}	$Hu_x + Q_x$	$Hu_x + Q_x$	$2H_w u_{x,w}$	$Hu_x + Q_x + H_w u_{x,w}$
Υ_{01}	$Hu_y + Q_y$	$Hu_y + Q_y$	$2H_w u_{y,w}$	$Hu_y + Q_y + H_w u_{y,w}$
Υ_{20}	Υ_{20}	$-\Upsilon_{20}$	$2H_w(\sigma^2 + u_{x,w}^2)$	$0 + H_w(\sigma^2 + u_{x,w}^2)$
Υ_{02}	Υ_{02}	$-\Upsilon_{02}$	$2H_w(\sigma^2 + u_{y,w}^2)$	$0 + H_w(\sigma^2 + u_{y,w}^2)$
Υ_{11}	Υ_{11}	$-\Upsilon_{11}$	$2H_w u_{x,w} u_{y,w}$	$0 + H_w u_{x,w} u_{y,w}$
Υ_{21}	Υ_{21}	Υ_{21}	$2H_w u_y(\sigma^2 + \mathbf{u}_x^2)$	$\Upsilon_{21} + H_w u_y(\sigma^2 + \mathbf{u}_x^2)$
Υ_{12}	Υ_{12}	Υ_{12}	$2H_w u_x(\sigma^2 + \mathbf{u}_y^2)$	$\Upsilon_{12} + H_w u_x(\sigma^2 + \mathbf{u}_y^2)$
Υ_{22}	Υ_{22}	$-\Upsilon_{22}$	$2H_w(\sigma^4 + \sigma^2 u_{x,w}^2 + \sigma^2 u_{y,w}^2 + \mathbf{u}_{x,w}^2 \mathbf{u}_{y,w}^2)$	$0 + H_w(\sigma^4 + \sigma^2 u_{x,w}^2 + \sigma^2 u_{y,w}^2 + \mathbf{u}_{x,w}^2 \mathbf{u}_{y,w}^2)$

TABLE 8.6: Moments of an Anti Bounce Back BC for D2Q9 lattice (Dirichlet BC for temperature, where $\Upsilon_{00}^{CHT} = \rho c_v T$ and $\sigma^2 = \frac{\gamma c_s^2}{\rho c_v}$).

Note that the sign of even moments is reverted during the Anti Bounce Back procedure.

$\Upsilon_{jk} = \sum_i e_{ix}^j e_{iy}^k$	$h_i(x_b, t)$	$h_{\bar{i}}(x_s, t)$	$B_i = 2\Upsilon_i^{H_w}$	at $x_w = \frac{1}{2}[h_i(x_b, t) + h_{\bar{i}}(x_s, t) + B_i]$
Υ_{00}	H	H	0	H
Υ_{10}	$Hu_x + Q_x$	$-(Hu_x + Q_x)$	$-2H_w n_x$	$0 - H_w n_x$
Υ_{01}	$Hu_y + Q_y$	$-(Hu_y + Q_y)$	$-2H_w n_y$	$0 - H_w n_y$
Υ_{20}	Υ_{20}	Υ_{20}	0	Υ_{20}
Υ_{02}	Υ_{02}	Υ_{02}	0	Υ_{02}
Υ_{11}	Υ_{11}	Υ_{11}	0	Υ_{11}
Υ_{21}	Υ_{21}	$-\Upsilon_{21}$	$-2\sigma^2 H_w n_y$	$0 - \sigma^2 H_w n_y$
Υ_{12}	Υ_{12}	$-\Upsilon_{12}$	$-2\sigma^2 H_w n_x$	$0 - \sigma^2 H_w n_x$
Υ_{22}	Υ_{22}	Υ_{22}	0	Υ_{22}

TABLE 8.7: Moments of a Bounce Back BC for D2Q9 lattice and central moments of B_i (impose flux BC for the thermal field, where $\Upsilon_{00}^{CHT} = \rho c_v T$ and $\sigma^2 = \frac{\gamma c_s^2}{\rho c_v}$). Note that the sign of odd moments is reverted during the Bounce Back procedure.

8.4 Interpolated (anti)-bounce-back BC

The simple bounce-back (BB) rule reduces the convergence of the LBM to first order if the wall is not located exactly between lattice nodes. The higher-order boundary condition allows to circumvent this issue and recover the second order convergence.

Bouzidi *et al.* [177] proposed the interpolated-bounce-back (IBB) scheme to represent a non-slip wall on a curved boundary. It is assumed that during each streaming step, the distributions travels a distance $|\mathbf{e}_i|\Delta t$. The walls are modelled by a bounce back of said distributions back into the domain. As the wall is not necessarily half-way between lattice nodes, the algorithm employs a linear interpolation scheme between boundary node \mathbf{x}_b and neighbouring fluid node \mathbf{x}_f ,

$$f_{\bar{i}}(\mathbf{x}_b, t + \Delta t) = \begin{cases} 2qf_i^*(\mathbf{x}_b, t) + (1 - 2q)f_i^*(\mathbf{x}_f, t) & \text{for } q \in [0, 0.5] \\ \frac{1}{2q} [f_i^*(\mathbf{x}_b, t) + (2q - 1)f_i^*(\mathbf{x}_f, t)] & \text{for } q \in (0.5, 1], \end{cases} \quad (8.16)$$

where q is the distance (along lattice link) between the boundary node and the actual boundary and \bar{i} denotes direction opposite to i . The idea is depicted in Figure 8.2. Inter-

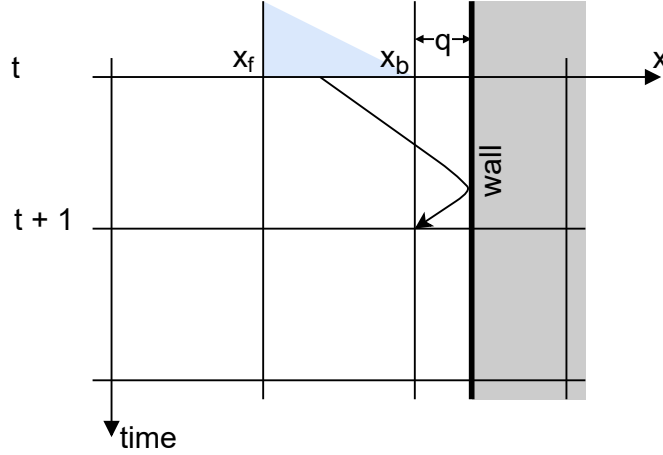


FIGURE 8.2: Interpolated (Anti-)Bounce Back in the time-space diagram. The blue triangle indicates the intensity of the interpolation function between $g_i^*(\mathbf{x}_b, t)$ and $g_i^*(\mathbf{x}_f, t)$ for $q \in [0, 0.5]$.

estingly, Geier *et al.* [43] noticed that the algorithm can be implemented locally. Observing that the bounce-back populations are in fact the ones from the previous time step, the

costly operation of accessing neighbour's value can be substituted by storing the past value locally or recovering it from the pre-collision state as in the original work of [43].

The intuitive interpolation as in Equation (8.16) has been improved to third order by Ginzburg and D'Humières [161], who used second-order Chapman-Enskog expansion to find the appropriate coefficients. Their scheme is called *multi-reflection* BC, as it utilizes five populations to interpolate from and is viscosity independent when TRT/MRT collision kernel is applied.

The interpolation scheme proposed by Bouzidi *et al.* [177] can be modified [178, 164, 179, 180] to obtain Dirichlet boundary conditions for advection-diffusion problems. Due to change in sign of the post-collision distribution function, the scheme is refereed as interpolated-anti-bounce-back (IABB),

$$h_i^-(\mathbf{x}_b, t + \Delta t) = \begin{cases} -[2qh_i^*(\mathbf{x}_b, t) + (1 - 2q)h_i^*(\mathbf{x}_f, t)] + 2h_i^{eq}(\mathbf{x}_w, \mathbf{u}, t) & \text{for } q \in [0, 0.5] \\ \frac{1}{2q} [-h_i^*(\mathbf{x}_b, t) + (2q - 1)h_i^*(\mathbf{x}_b, t) + 2h_i^{eq}(\mathbf{x}_w, \mathbf{u}, t)] & \text{for } q \in (0.5, 1], \end{cases} \quad (8.17)$$

where $h_i^{eq}(\mathbf{x}_w, \mathbf{u}, t)$ is a source term designed to impose the desired temperature at the wall, \mathbf{x}_w . If the interpolation is skipped, then the scheme simplifies to the so called anti-bounce-back (ABB) [82, 181, 182]. In the simplest form of the Dirichlet boundary condition, known as the equilibrium scheme (EQ) [183, 184, 185], only the equilibrium part of the above equation is prescribed to the outgoing distributions.

Pros	Cons
Second-order accurate.	Not mass conserving (due to interpolations)
As the scheme is aware of boundary's normal, the turbulent boundary layer shall have more physical profile than in the case of immersed boundary method [186] or partially saturated method [187] where <i>interpolating kernel</i> is isotropic.	Adoption of TRT/MRT can not cure the issue slip is always viscosity dependent slip (due to interpolations). Viscosity independent IBB has been proposed by the group of I. Ginzburg [188, 181, 189] and Chun and Ladd [190].
	Non-local implementation may cause problems in narrow geometries (like porous media), because it may happen that there will be not enough nodes to interpolate from.
	HBB, which can be viewed as special case of IBB does not suffer from a <i>lag</i> as a regular BB, thus the IBB scheme is expected to be more accurate in turbulent flows.

TABLE 8.8: Pros and cons of the Interpolated Bounce Back

8.5 Summary

Is is difficult to select proper BC, as each candidate has its own pros and cons. The problem is case specific, and the criteria such as overall robustness, mass conservation, convergence order, locality/computational effort, applicability to moving boundaries, applicability to resolve turbulent boundary layer, stability, satisfaction of exact no slip condition at the wall, applicability to relatively small particles/objects or porous media shall be considered.

Chapter 9

Thermal Flows in high Prandtl number regime

“Good judgment comes from experience, and a lot of that comes from bad judgment.”

– Will Rogers

Contents

9.1	Introduction	140
9.2	Model description	145
9.2.1	Moments of the distribution functions	145
9.3	Model verification and validation	149
9.3.1	Advection-Diffusion of a Gaussian hill	150
9.3.2	Advection-diffusion of a square indicator function	152
9.3.3	Heat conduction between two concentric cylinders	155
9.3.4	Steady, forced convective heat transfer from a confined cylinder	156
9.4	Future outlook	163
9.5	Conclusions	164
9.6	Source term treatment	164

Content of this chapter is based on the article “A comparative study of 3D cumulant and central moments lattice Boltzmann schemes with interpolated boundary conditions for the simulation of thermal flows in high Prandtl number regime” [4].

Thermal flows characterized by high Prandtl number are numerically challenging as the transfer of momentum and heat occurs at different time scales. To account for very

low thermal conductivity and obey the Courant-Friedrichs-Lewy condition, the numerical diffusion of the scheme has to be reduced. As a consequence, the numerical artefacts are dominated by the dispersion errors commonly known as wiggles. In this chapter, we explore possible remedies for these issues in the framework of lattice Boltzmann method by means of applying novel collision kernels, lattices with large number of discrete velocities, namely D3Q27, and a second-order boundary conditions.

For the first time, the cumulant-based collision operator is utilised to simulate both the hydrodynamic and the thermal field. Alternatively, the advected field is computed using the central moments' collision operator. Different relaxation strategies have been examined to account for additional degrees of freedom introduced by a higher order lattice.

To validate the proposed kernels for a pure advection-diffusion problem, the numerical simulations are compared against analytical solution of a Gaussian hill. The structure of the numerical dispersion is shown by simulating advection and diffusion of a square indicator function. Next, the influence of the interpolated boundary conditions on the quality of the results is measured in the case of the heat conduction between two concentric cylinders. Finally, a study of steady forced heat convection from a confined cylinder is performed and compared against a Finite Element Method solution.

It is known from the literature, that the higher order moments contribute to the solution of the macroscopic advection-diffusion equation. Numerical results confirm that to profit from lattice with a larger number of discrete velocities, like D3Q27, it is not sufficient to relax only the first-order central moments/cumulants of the advected field. In all of the performed benchmarks, the kernel based on the two relaxation time approach has been shown to be superior or at least as good as counter-candidating kernels.

9.1 Introduction

The Prandtl number (\mathbf{Pr}) defines the ratio of kinematic viscosity to thermal diffusivity. Modelling high \mathbf{Pr} flows rises numerical difficulties due to different time scales of the physical phenomena occurring in the hydrodynamic and thermal field. Briefly, three distinct approaches to model thermal flows within the lattice Boltzmann method (LBM) framework can be distinguished in the literature [191].

In a *fully coupled double distribution function* approach, a second distribution function evolving between the same lattice nodes, at the same as the hydrodynamic one, is introduced to simulate the evolution of the energy field [31]. Due to tight coupling, many

benchmarks published for this type of LBM models are restricted to $\mathbf{Pr} \leq 100$ [192, 193, 194] or $\mathbf{Pr} \simeq 1$ [31, 50, 45, 90, 102, 195, 95, 196, 63, 52, 55, 62, 197, 198, 199, 200]. Limits of this way of modelling, are explored in the current paper.

Another approach, called multispeed LBM uses single distribution function, but utilises a lattices with a large velocity set [66]. The expanded velocity set allows to eliminate the aliasing of the higher order moments of the distribution. As a result, the internal energy can be incorporated as a quantity solved by LBM. This is not possible for standard lattices, as the limited number of independent moments results in a fixed relation between the internal energy and the pressure, which is referred as *isothermal LBM*. The use of the multispeed method with the SRT collision operator would lead to the \mathbf{Pr} being a constant of the model, as the relaxation rate corresponding to the thermal conductivity could not be set independently of from the kinematic viscosity [201, 202]. Successful decoupling has been achieved by Chen *et al.* [76] followed by Shan [203]. A collision operator with multiple relaxation frequencies in a moving reference frame has been proposed and validated for $\mathbf{Pr} \in \{0.5, 1, 2\}$.

In the hybrid approach, two distinct numerical methods are used to solve the hydrodynamics and the advected field. Examples of this approach include studies, where LBM solver was used for the Navier Stokes (NS) equations and a finite difference [204, 205] or finite volume [197] method for the thermal field.

Finally, some researches attempt to take advantage of high \mathbf{Pr} regime to decouple NS and advection-diffusion equation (ADE) solvers. In this method, both fields can be computed using LBM solver, but on separated lattices [206, 207]. Parmigiani *et al.* [206] notes that either the timestep or grid spacing of the second distribution can be decoupled. Although the spatial decoupling demands interpolations between lattices, the overall computational cost is reduced. The group managed to simulate flow with \mathbf{Pr} up to 1000. However, when the heat transport becomes velocity controlled, the advantages of decoupling deteriorate [206].

The Q_F and Q_H subscripts will be used in the present chapter to distinguish the lattices used for hydrodynamic and thermal distribution functions, hence defining the lattice as DdQ_FxQ_Hy . To solve the advection-diffusion equations, a lower order lattices like $D2Q_H5$ [95, 196, 63, 55] and $D3Q_H7$ [58, 157, 59, 60, 154, 61, 198, 200] are frequently used. However, to properly recover complex thermal flows (e.g. measure the critical Rayleigh number), a higher-order lattice is required [45]. According to Huang *et al.* [208], the accuracy of $D2Q_H4$, $D2Q_H5$ and $D2Q_H9$ lattices can be comparable, but the effects of low diffusivity were not considered in their study. Additionally, lattices such as $D3Q15$

shall be avoided, as it is not feasible to derive the shift matrix from the raw moment space (discussed in next section) following the procedure presented by Asinari [47]. Apart from increasing the number of discrete velocities, it is possible to take advantage of a specific geometry of the problem by either scaling a lattice into cuboidal one [209] or by adding a correction terms to account for axisymmetric flows [210]. Interestingly, when the relaxation frequency is exactly equal to one, a memory efficient LBM scheme can be implemented, by eliminating the storage of the distribution function. From the theoretical perspective, a memory savings of up to $\sim 86\%$ can be achieved for the D3Q27 lattice [211].

In this work, a linear interpolation scheme [177] is implemented to represent a boundary located between lattice nodes and improve the representation of the geometry. Readers interested in a more detailed studies on the application of an interpolated-anti-bounce-back boundary condition are referred to [178, 164, 179, 180].

Application of standard lattices, such as D2Q_H9 [212] and D3Q_H15 [213], -19 or -27, raises the question of the appropriate relaxation of higher-order moments. Due to its simplicity, the SRT collision operator is frequently applied [50, 20, 53, 90, 93, 154, 45, 60, 214, 54, 56, 192, 193]. When it comes to use a more advanced multiple relaxation time (MRT) [58, 215, 59, 90, 102, 26, 216, 200, 198] or central moments (CM) [95, 196, 212, 213, 63, 68, 210] collision operator, various relaxation strategies can be identified. Some authors [58, 59, 102, 26, 213, 212, 200] relax first-order moments only, setting the rest of moments to their corresponding equilibrium values. The two relaxation time (TRT) approach was adopted to moment space [215, 90, 198] and central moment space in [196, 63, 68], however in [68, 213, 212] the relaxation of higher-order moments is said to be tunable.

It has been shown by different authors [66, 67, 68, 69, 5], that truncation of the equilibrium distribution function deteriorates Galilean invariance of the flow model. Chopard *et al.* [65] have discussed the role of the second-order velocity terms in the equilibrium distribution function on the error of the recovered macroscopic equation and proposed a correction term. Nie *et al.* [66] noticed that the error appears as spurious dependence of the macroscopic diffusion coefficient (i.e. viscosity or thermal conductivity) on velocity. A similar effect has been observed by Fei *et al.* [68] who used a cascaded collision operator with full order equilibrium to show that thermal diffusivity is independent of Mach number as opposed to works where MRT with truncated equilibrium [217, 216] were used. To avoid the above-mentioned issues, a full order equilibrium distribution function is used in the present work.

The Table 9.1 presents a concise summary of the models present in the literature, to

put the collision operators chosen in this work in a context. Features such as the type of collision kernel, order of equilibrium, utilized lattice and the range of reported Prandtl numbers has been extracted. The publications were usually focused only on selected properties from the aforementioned set. Usage of SRT collision and truncated equilibrium distribution is prevalent, as is the relaxation of only first raw, or central moments. It is expected that to some extend, the models listed in Table 9.1 would work for Prandtl numbers other than reported.

In this study, the role of different relaxation approaches for the advection-diffusion problems is investigated. To the best of the author's knowledge a cumulant collision kernel is applied to simulate the advection-diffusion equation for the first time. A set of benchmarks with different complexity has been conducted, to isolate the factors which can affect the numerical simulations. For the set of numerically investigated cases, specified for a range of non-dimensional numbers, the relaxation of higher-order moments has to be adjusted to achieve the benefits of lattice with a large stencil. Concluding, current work is focused on the numerical limits of the central moment and cumulant collision operators applied to the variant of advection-diffusion equation, namely transport of internal energy in a homogeneous, isotropic medium with first and second-order boundary conditions using a fully coupled double distribution function approach on a $D3Q_F27Q_H27$ lattice.

This chapter is organised as follows. In the Section 9.2, the LBM routine and the investigated collision kernels are described. The validation and tests of the model is discussed in Section 9.3. The future outlook is given in Section 9.4. Finally, the summary and conclusions are formulated in Section 9.5. For clarity of the manuscript, some of the derivations regarding discretisation of the distribution function, two relaxation time approach, the transformation matrices and the source treatment have been listed in 3.4, 3.6, 3.5 and 9.6 respectively.

Year	Reference	Notes	Collision	h^{eq} ord.	Lattice	Pr
1998	[31]		SRT	2^{nd}	D2Q9	$0.25 \div 0.71$
2007	[50]		SRT	2^{nd}	D2Q9	$0.71 \div 1$
2009	[206]	(a)	SRT	1^{st}	D2Q5	$10 \div 1000$
2013	[53]		SRT	2^{nd}	D2Q9	0.02
2013	[51]		Entropic	2^{nd}	DdQq	1
2013	[215]		MRT-TRT	1^{st}	D2Q5	$0.71 \div 7$
2014	[76]	(b)	CM-TRT	4^{th}	D2Q27	$0.5 \div 2$
2015	[90]		MRT-TRT	2^{nd}	D2Q9	0.2
2015	[45]		SRT	2^{nd}	D3Q15/19/27	0.71
2016	[102]	(c)	MRT- 1^{st}	1^{st}	D3Q7	0.71
2017	[95]		CM-TRT	∞	D2Q5	0.71
2017	[218]	(e)	MRT-TRT	1^{st}	D2Q5	0.71
2017	[54]		SRT	2^{nd}	D2Q9	1
2018	[196]		CM-TRT	∞	D2Q5	0.71
2018	[52]		SRT	2^{nd}	D2Q9	0.71
2018	[197]		SRT	2^{nd}	D2Q9	0.71
2018	[213]		CM- 1^{st}	∞	D3Q15	0.71
2018	[212]		CM- 1^{st}	∞	D2Q9	$0.71 \div 1$
2018	[63]	(d)	CM-TRT	∞	D2Q5	0.71
2018	[55]		MRT-TRT	2^{nd}	D2Q9	$0.7 \div 1$
2018	[62]		SRT	1^{st}	D2Q9	$0.7 \div 1$
2019	[203]	(b)	CM-TRT	9^{th}	D2Q37	0.5
2019	[198]		MRT-TRT	1^{st}	D3Q7	$0.7 \div 7$
2019	[200]	(c)	MRT- 1^{st}	1^{st}	D3Q7	0.73
2019	[57]		MRT-TRT	2^{nd}	D2Q9/D3Q7	0.02
2019	[199]		SRT	1^{st}	D2Q5	0.2
2020	[192]		SRT	1^{st}	D2Q9	50
2021	[193]		SRT	2^{nd}	D2Q9	50
2021	[194]		SRT	1^{st}	D3Q7	100
2021	[207]	(a)	SRT	1^{st}	D2Q9	$0.01 \div 100$
2022	current model		CM-TRT	∞	D3Q27	$10 \div 1000$

TABLE 9.1: The summary of models present in the literature. h^{eq} ord. - Order of equilibrium distribution function used for the advection-diffusion equation (value ∞ means that equilibrium is not truncated, **Pr** - Prandtl number. Notes: (a) - NS and ADE were computed on decoupled lattices, (b) - multispeed model, (c) - collision based on [58], (d) - collision based on [216], (e) - collision based on [215]. The \div sign is used to indicate the range of **Pr** for which the model has been benchmarked.

9.2 Model description

The flow of fluid and the internal energy balance is modelled by the Navier-Stokes and advection-diffusion equation respectively. Only one-way coupling between these equations will be considered. The hydrodynamics is described by the continuity and momentum equations,

$$\frac{\partial \rho}{\partial t} + \nabla \cdot \rho \mathbf{u} = 0, \quad (9.1)$$

$$\rho \left(\frac{\partial \mathbf{u}}{\partial t} + (\mathbf{u} \cdot \nabla) \mathbf{u} \right) = -\nabla p + \nabla \cdot (\mu [\nabla \mathbf{u} + (\nabla \mathbf{u})^\top]), \quad (9.2)$$

where \mathbf{u} is the fluid velocity, ρ is the density, p is pressure, and μ is the viscosity coefficient. Although the LBM is a weakly compressible method, it is used in this study in the incompressible regime ($\rho \simeq \text{const}$).

The heat transfer is described using an internal energy field expressed as $H = \rho c_v T$, where c_v is a specific heat capacity at constant volume and T is the temperature. Omitting viscous heat production and assuming that the flow is incompressible, the conservation of internal energy (see Chapter 6) can be written as [219, 191, 220],

$$\frac{\partial}{\partial t}(\rho c_v T) + \nabla \cdot (\mathbf{u} \rho c_v T) = \nabla \cdot (k \nabla T), \quad (9.3)$$

with thermal conductivity of the fluid being denoted by k . As the conjugate heat transfer in the surrounding medium is not considered in this study, the c_v is set to 1. Having calculated the velocity field from Equations (9.1) and (9.2), the advection-diffusion of i can be solved independently. Readers interested in the Chapman-Enskog procedure for the advected field are referred to the work of Shi *et al.* [219].

9.2.1 Moments of the distribution functions

The fluid flow and temperature field in the present LBM framework is described with two distributions functions, f_i and h_i , with the corresponding set of velocity vectors \mathbf{e}_i . The

connection between \mathbf{f} and \mathbf{h} , and macroscopic flow fields is described by,

$$\rho = \sum_i f_i, \quad (9.4)$$

$$\rho \mathbf{u} = \sum_i \mathbf{e}_i f_i, \quad (9.5)$$

$$\rho c_v T = \sum_i h_i. \quad (9.6)$$

The density and internal energy correspond to the zeroth order moments of hydrodynamic and energy distribution functions respectively. The momentum $\rho \mathbf{u}$ corresponds to the first moment of \mathbf{f} . According to the probabilistic definition, the central moments (see Section 3.3) or cumulants [43] of some quantity \mathbf{g} shall be calculated basing on \mathbf{g} itself. Observe, that the *cascaded* or central moments, defined here, would correspond to the probabilistic definition of central moments in case hydrodynamics distributions, \mathbf{f} , but do not for the advected ones, \mathbf{h} . Strictly speaking, the macroscopic velocity, \mathbf{u} , being used to compute the shift matrix, $\mathbb{N} = \mathbb{N}(\mathbf{u})$, is related to the first order moment of \mathbf{f} not \mathbf{h} .

A detail presentation of the cumulant transformation, \mathcal{C} , and the use of cumulants in LBM, can be found in the works of Geier [43, 44] and Coreixas [12, 13]. Here, the cumulant transform for both the advected and hydrodynamic field is the same and follows the rules described in [43]. Generally, one can think of cumulants as of intensive and statistically independent quantities as opposed to (central) moments, being extensive ones. In case of the hydrodynamic field, the first order moment correspond to momentum, $\rho \mathbf{u}$, as opposed to first order cumulant which is just the velocity, \mathbf{u} .

9.2.1.1 Considered collision kernels

The general evolution equation of \mathbf{f} and \mathbf{h} distributions can be decomposed into two steps: collision and streaming. The collision is a nonlinear operator Ω acting on the distribution function at a specific time and location, while the streaming spreads this distribution function along the velocity vectors \mathbf{e}_i . This is expressed as,

$$f_i(\mathbf{x} + \mathbf{e}_i \delta t, t + \delta t) = \Omega_{F,i}(\mathbf{f}(\mathbf{x}, t)), \quad (9.7)$$

$$h_i(\mathbf{x} + \mathbf{e}_i \delta t, t + \delta t) = \Omega_{H,i}(\mathbf{h}(\mathbf{x}, t)). \quad (9.8)$$

The collision operator Ω is considered to consist of three steps: some transformation \mathcal{W} (see Section 3.3), relaxation to equilibrium, and inverse of the transformation,

$$\Omega_G(\mathbf{g}) = \mathcal{W}^{-1} \left(\mathcal{W}(\mathbf{g}) + \mathbb{S}(\mathcal{W}(\mathbf{g}^{\text{eq}}) - \mathcal{W}(\mathbf{g})) \right), \quad (9.9)$$

where \mathbb{S} is the relaxation matrix and g_i is the distribution function of interest (either hydrodynamic or advected field i.e., f_i, h_i) and. The operator \mathcal{W} can be the transformation to the space of *moments*, *central moments* or *cumulants*.

Now, four different collision kernels being investigated in the present study will be described. In all cases, the hydrodynamics collision operator Ω_F is always based on cumulant transform \mathcal{C} and follows the formulas described in [43]. Denoting cumulants as $\mathcal{C}^G = \mathcal{C}(\mathbf{g})$, the cumulant collision kernel can be written as,

$$\Omega_F(\mathbf{f}) = \mathcal{C}^{-1} \left(\mathcal{C}^F + \mathbb{S}^F (\mathcal{C}^{F,\text{eq}} - \mathcal{C}^F) \right) \quad (9.10)$$

On the other hand, different kernels are used for the internal energy field, based on either central moments or cumulants,

$$\Omega_H(\mathbf{h}) = \mathbb{M}^{-1} \mathbb{N}^{-1} \left(\boldsymbol{\kappa}^H + \mathbb{S}^H (\boldsymbol{\kappa}^{H,\text{eq}} - \boldsymbol{\kappa}^H) \right), \quad (9.11)$$

or

$$\Omega_H(\mathbf{h}) = \mathcal{C}^{-1} \left(\mathcal{C}^H + \mathbb{S}^H (\mathcal{C}^{H,\text{eq}} - \mathcal{C}^H) \right), \quad (9.12)$$

The analytical form of the Maxwell-Boltzmann equilibrium distribution is used to calculate the central moments for the internal energy field (see 3.4). The non-zero elements of equilibrium vector for \mathbf{h}^{eq} are,

$$\begin{aligned} \boldsymbol{\kappa}^{H,\text{eq}} &= [\Upsilon_{000}^{\text{eq}}, \dots 0, \dots, \Upsilon_{200}^{\text{eq}}, \Upsilon_{020}^{\text{eq}}, \Upsilon_{002}^{\text{eq}}, \dots 0, \dots, \Upsilon_{220}^{\text{eq}}, \Upsilon_{202}^{\text{eq}}, \Upsilon_{022}^{\text{eq}}, \dots 0, \dots, \Upsilon_{222}^{\text{eq}}]^\top \\ &= [H, \dots 0, \dots, Hc_s^2, Hc_s^2, Hc_s^2, \dots 0, \dots, Hc_s^4, Hc_s^4, Hc_s^4, \dots 0, \dots, Hc_s^6]^\top. \end{aligned} \quad (9.13)$$

In case of cumulants, the collision kernel which has been originally implemented for the hydrodynamic field [43] requires adjustments to reflect the macroscopic advection-diffusion equation. Since the first and second-order cumulants corresponds to the mean and variance

of the distribution, the equilibrium cumulants in case of an advected field read,

$$\begin{aligned}\mathcal{C}^{\text{H,eq}} &= [c_{000}^{eq}, c_{100}^{eq}, c_{010}^{eq}, c_{001}^{eq}, c_{110}^{eq}, c_{101}^{eq}, c_{011}^{eq}, c_{200}^{eq}, c_{020}^{eq}, c_{002}^{eq}, \dots c_{ijk}^{eq} \dots, c_{122}^{eq}, c_{212}^{eq}, c_{221}^{eq}, c_{222}^{eq}]^\top \\ &= [H, u_x, u_y, u_z, 0, 0, 0, c_s^2, c_s^2, c_s^2, \dots 0 \dots, 0, 0, 0, 0]^\top,\end{aligned}\tag{9.14}$$

where c_s refers to the lattice speed of sound and is set to $\sqrt{1/3}$.

The diagonal relaxation matrix is used for the advection-diffusion equation and can be formulated in a general form as,

$$\mathbb{S}^{\text{H}} = \text{diag}([s_{000}, s_{100}, s_{010}, s_{001}, s_{110}, \dots s_{ijk} \dots, s_{222}]),\tag{9.15}$$

where three-indexes ijk correspond to the choice of moment three-indexes. The main relaxation frequency, s^H , corresponds to the macroscopic thermal conductivity [10]. As the density fluctuations are negligible ($\ll 0.01\%$) for the cases being investigated, the main relaxation frequency can be expressed as [219]:

$$s^H = \frac{1}{\frac{k}{c_s^2 \delta t} + 1/2}.\tag{9.16}$$

Based on this framework, four collision operators are formulated. Three of them use the central moment transform and different choices of relaxation frequencies s_{ijk} , and one uses the cumulant transform.

CM-SRT is obtained by setting $s_{ijk} = s^H$. Thanks to \mathbb{S}^{H} being diagonal, the CM-single relaxation time (SRT) relaxation scheme is equivalent to the well known single relaxation time (SRT) scheme in the space of distribution functions,

$$\begin{aligned}\mathbf{h}^*(\mathbf{x}, t) &= \mathbb{M}^{-1} \mathbb{N}^{-1} \boldsymbol{\kappa}^{\text{H},*}(\mathbf{x}, t) \\ &= \mathbb{M}^{-1} \mathbb{N}^{-1} [(\mathbb{1} - \mathbb{S}^{\text{H}}) \mathbb{N} \mathbf{M} \mathbf{h} + \mathbb{S}^{\text{H}} \boldsymbol{\kappa}^{\text{H, eq}}] \\ &= (1 - s^H) \mathbf{h} + \underbrace{\mathbb{1} s^H}_{\mathbb{S}^{\text{H}}} \underbrace{\mathbb{M}^{-1} \mathbb{N}^{-1} \boldsymbol{\kappa}^{\text{H, eq}}}_{\mathbf{h}^{\text{eq}}} \\ &= (1 - s^H) \mathbf{h} + s^H \mathbf{h}^{\text{eq}}.\end{aligned}\tag{9.17}$$

CM-1st is the basic approach for (central) moment based scheme for advection diffusion equation. Only the first order moments are relaxed ($s_{ijk} = s^H$ for $i + j + k = 1$), while the higher order central moments are set to equilibrium ($s_{ijk} = 1$ for $i + j + k > 1$).

Similar relaxation approach has been adopted in [213, 212], although it has been presented in a generalized framework, indicating that the remaining relaxation rates can be tuned independently to influence numerical stability. Benchmarks conducted in the current chapter confirm, that the relaxation rates responsible for the higher order moments must be adjusted to mitigate *wiggles* occurring at numerically low conductivities.

CM-TRT originates from the two relaxation time (TRT) scheme which has been derived by Ginzburg in 2005 [40, 81], and extended in the subsequent years [82, 83, 84, 85]. The basic idea is to separate the relaxation rate of the odd and even moments. Usually, the specific combination of the relaxation rates, known as a *magic parameter* is kept constant. As a result, the stationary, non-dimensional solution of NS or ADE is exactly controlled by the similarity numbers [85]. One of the beneficial consequences is that the transport coefficients (like viscosity, conductivity) shall not influence the apparent location of the boundary condition [82, 216]. It has been shown in [90, 57] that the TRT allows to eliminate an unphysical numerical diffusion in solid-liquid phase change model. However, it has been decided to not set the *magic parameter* (see Section 3.6) in the current chapter for the following reasons:

- (a) The central moments' relaxation scheme does not collapse to the TRT defined in the space of distribution functions (see Section 3.6).
- (b) The second order boundary conditions based on the linear interpolation schemes [177, 180] (see Section 8.4), which have been used in the current study do not preserve the effect of the magic parameter [133, 166]. According to [221, 82], application of *magic* boundary schemes allows to obtain viscosity independent permeability, however such extension is beyond the scope of the present work.
- (c) There is no universal, most accurate magic number [164].

In this chapter, the odd-moments are relaxed with a common rate ($s_{odd} = s^H$), while the even moments are set to equilibrium ($s_{even} = 1$). For further discussion regarding the relation with the original TRT model, the interested reader is referred to Section 3.6.

Cumulants-1st follows the statistical independence of cumulants, thus only the first order cumulants are relaxed with $s_{ijk} = s^H$ (for $i + j + k = 1$), while the higher order ones are set to equilibrium values ($s_{ijk} = 1$ for $i + j + k > 1$).

9.3 Model verification and validation

In this section, a set of numerical experiments used to evaluate the accuracy of the investigated kernels is described. The benchmarks starts with advection-diffusion problems

in a fixed, external velocity field. Next, the second order boundary conditions are tested. Finally, a comprehensive study of a flow with forced convection is performed.

To assure consistency all cases are calculated with the same 3D code. In the 2D cases, the z-direction is periodic and it is cut to three elements. This is technical minimum in our solver [6, 222], because a message passing layer is used for domain decomposition. In such a setup, the 3D model reduce itself to 2D one (of course, with a higher computational cost). Observe, that the LBM weights of D3Q27 lattice, when summed over the z-direction, give the standard LBM weights for D2Q9.

The normalized L_2 norm of error is utilised to compare the results between the simulations. It is defined as,

$$L_2 = \sqrt{\frac{\sum_i \left(T_i^{\text{analytical}} - T_i^{\text{numerical}}\right)^2}{\sum_i \left(T_i^{\text{analytical}}\right)^2}} \quad (9.18)$$

where the sum \sum_i goes over all lattice nodes and T_i is the temperature in the i -th node.

9.3.1 Advection-Diffusion of a Gaussian hill

To avoid the influence of boundary conditions, the first benchmarks investigates behaviour of the collision kernels in a periodic domain. In the case of an isotropic diffusion, and convection with constant velocity, the analytical solution describing the evolution of a Gaussian hill can be derived [223, 58, 9]. The formula can be expressed as,

$$C(\mathbf{x}, t) = \frac{(2\pi\sigma_0^2)^{N/2}}{(2\pi(\sigma_0^2 + 2kt))^{N/2}} C_0 \exp\left(-\frac{(\mathbf{x} - \mathbf{x}_0 - \mathbf{u}t)^2}{2(\sigma_0^2 + 2kt)}\right) \quad (9.19)$$

where N is the number of spatial dimensions, t is time and σ_0 represents the initial variance of the distribution.

Given the initial condition, the same physical case (defined by physical time, t_{SI} , physical length, L_{SI} , and physical conductivity k_{SI}), can be simulated numerically using different time steps $\delta t = (\delta x)^2 k_{LB} / k_{SI}$. The δx denotes ratio of the physical length to the number of lattice nodes and has been fixed as $\delta x = L_{SI} / L = 1$. Since $t_{SI} = n\delta t$, where n is the number of iterations, the k_{LB} can be expressed as $k_{LB} = (t_{SI} k_{SI}) / (n(\delta x)^2)$. The domain was a square, $256 \times 256 \times 3$, with periodic boundaries. Each case has been initialised with a 2D Gaussian distribution, according to Equation (9.19), with initial

variance, $\sigma_0 = 100$. The simulations were executed for n iterations, ranging from 2400 (corresponding to $k_{LB} = 1/6$) to 40×10^6 ($k_{LB} = 10^{-5}$). Once the simulation reached the prescribed number of iterations, the result was compared against the analytical solution. The L_2 error norm has been plotted in Figure 9.1 for each of the investigated kernels. For

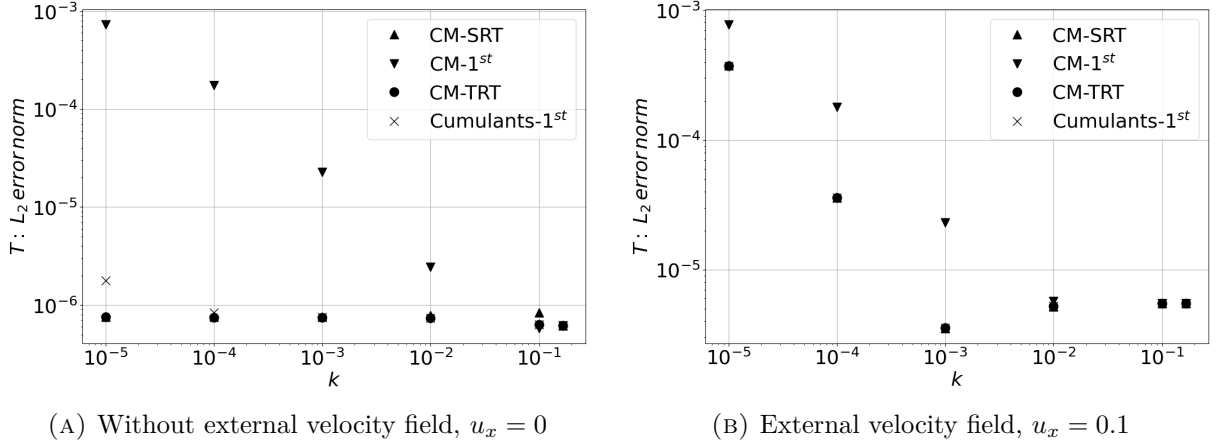


FIGURE 9.1: Advection-diffusion of a Gaussian hill has been calculated analytically for the physical time $t_{SI} = 100$ and physical conductivity $k_{SI} = 4$. To benchmark the investigated collision kernels, the same physical case has been simulated using different numerical conductivities k on a $256 \times 256 \times 3$ lattice.

pure diffusion, the error of all collision kernels is small and of similar level, for k ranging from $1/6$ to 10^{-4} (see Figure 9.1a), except for CM-1st model, for which the error strongly depends on k . In the case of constant velocity $\mathbf{u} = [1, 0]$, the error of all collision kernels depend on k , as artefacts resulting from numerical dispersion dominates the ones related to diffusion (see Figure 9.1b). The geometrical structure of errors (*wiggles*) caused by the numerical dispersion is shown in Section 9.3.2.

To show the behaviour of the investigated kernels in 3D, and the geometry of the introduced error, a spherical Gaussian hill was investigated on a $D3Q_F27Q_H27$ lattice. The domain has initialised according to Equation (9.19) with initial variance of $\sigma_0^2 = 100$. The domain was a box, $256 \times 256 \times 256$, with periodic boundary conditions. Conductivity of the stationary medium has been set to moderate value, namely $k_{LB} = 10^{-3}$ and the simulation was run for $n = 400000$ iterations. Again, the results were compared with analytical solution. All the collision kernels resulted in error with spherical symmetry, except for the CM-1st kernel. The geometrical structure of the absolute error for this collision operator is shown Figure 9.2. It is immediately evident that when only first-order central moments are relaxed, a considerable amount of spurious, mesh aligned, structures

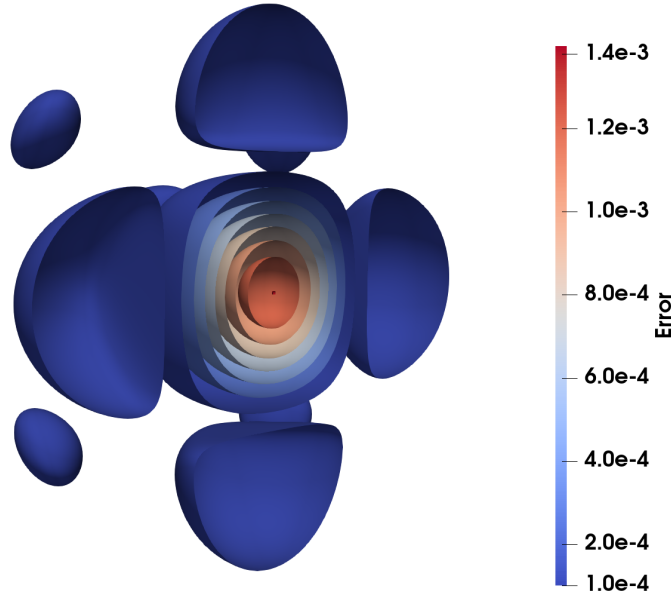


FIGURE 9.2: The iso-contours of the absolute error of the 3D Gaussian hill for the CM-1st kernel. The simulation has been run for 400000 iterations with conductivity being set to $k_{LB} = 10^{-3}$.

arise. Contrastingly, the other collision operators provided nearly identical results, with spherical symmetry and an order of magnitude smaller maximum errors, compared to CM-1st.

9.3.2 Advection-diffusion of a square indicator function

To depict the character of wiggles caused by both external velocity field and a jump in the value of a scalar field, a simple advection-diffusion study with uniform velocity field and periodic boundary conditions has been done. The qualitative results are presented in Table 9.2. The dimensions of the domain were $128 \times 128 \times 3$ [lu]. In the middle of the domain, a $48 \times 48 \times 3$ square has been initialised with $T = 11$, while $T_0 = 10$. The conductivity has been set to 10^{-5} . Each simulation has been run for 12 800 iterations. To store the scalar field, the D3Q_H7 lattice has been benchmarked against D3Q_H27. It is easy to observe that the D3Q7 lattice is a subset of D3Q27. It can be obtained by limiting the set of discrete velocities, \mathbf{e} , to its first seven elements. Only the first seven central moments can be represented: the zeroth, first and second order, non-diagonal ones. As a

consequence, it is not possible to distinguish between CM-1st and CM-TRT. The shape of the square advected on this lattice is distorted and strong wiggles are evident.

For the D3Q_H27 lattice, all four collision kernels were compared. The CM-1st and Cumulants-1st kernels generates diffusive artefacts that appears at the corners of the resting square. The issue can be alleviated using the CM-SRT or CM-TRT kernel, which relax the higher-order moments.

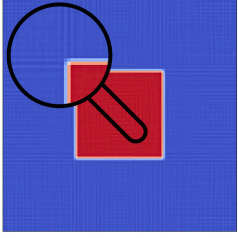
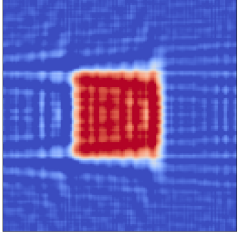
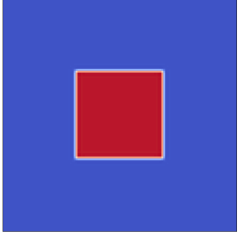
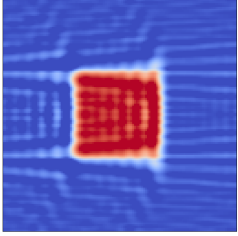
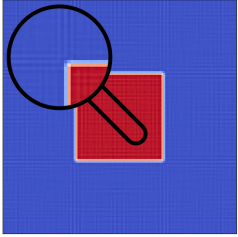
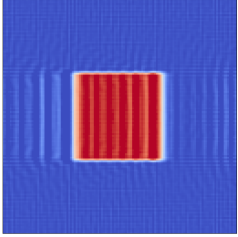
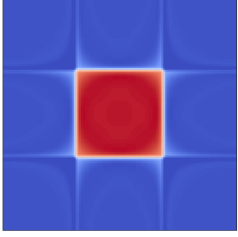
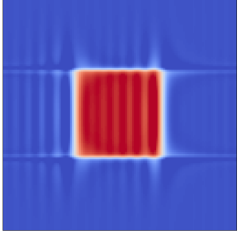
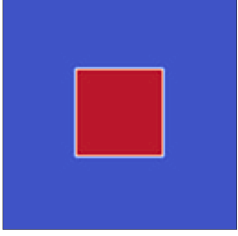
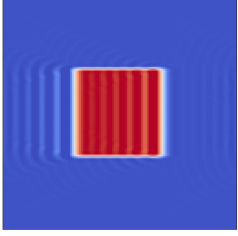
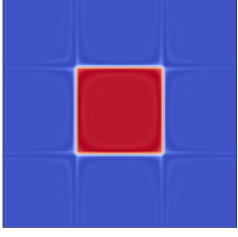
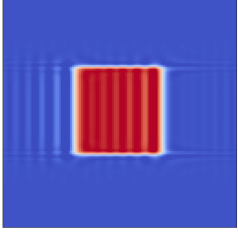
D3Q7	CM-SRT		
	CM-1 st = CM-TRT		
D3Q27	CM-SRT		
	CM-1 st		
	CM-TRT		
	Cumulants-1 st		
Lattice	Kernel	$\mathbf{u} = \mathbf{0}$	$u_x = 0.1$

TABLE 9.2: The square has been initialised with $T = 11$, while $T_0 = 10$. The color map on all images has been clipped to range $T \in (9.98 - 11.02)$. The region inside the loupe has been magnified by 175%. Notice the onset of numerical noise in the background when the CM-SRT kernel is used. For the D3Q7 lattice the CM-TRT kernel collapses to CM-1st.

9.3.3 Heat conduction between two concentric cylinders

To assess the accuracy of a curved boundary representation, steady state heat conduction between two concentric cylinders (without flow) is studied. The geometry is shown in Figure 9.3.

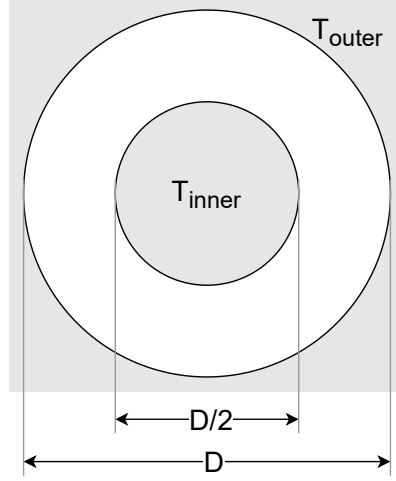


FIGURE 9.3: The inner cylinder was a heater with diameter $\frac{1}{2}D$, while the outer one with diameter D was a cooler.

Heat conduction in the cylindrical coordinate system can be described by a partial differential equation,

$$\rho c_v \frac{\partial}{\partial t} T = \frac{1}{r} \frac{\partial}{\partial r} \left(k r \frac{\partial}{\partial r} T \right) + \frac{1}{r^2} \frac{\partial}{\partial \phi} \left(k \frac{\partial}{\partial \phi} T \right) + \frac{\partial}{\partial z} \left(k \frac{\partial}{\partial z} T \right) + \dot{q}. \quad (9.20)$$

The general solution for a 2D, steady-state case is,

$$T(r) = \frac{\lambda_1}{k} \ln \left(\frac{r}{r_{inner}} \right) + \lambda_2. \quad (9.21)$$

Applying the Dirichlet boundary condition for $T(r_{inner}) = T_{inner}$ and $T(r_{outer}) = T_{outer}$, the unknown coefficients, λ_1, λ_2 are found and the solution reads,

$$T(r) = (T_{outer} - T_{inner}) \frac{\ln \left(\frac{r}{r_{inner}} \right)}{\ln \left(\frac{r_{outer}}{r_{inner}} \right)} + T_{inner}. \quad (9.22)$$

In Figure 9.4, three different implementations of Dirichlet's boundary condition (see Section 8.4) for the internal energy field have been assessed in a circular geometry. As

expected, only the interpolated-anti-bounce-back (IABB) exhibited the second order convergence rate.

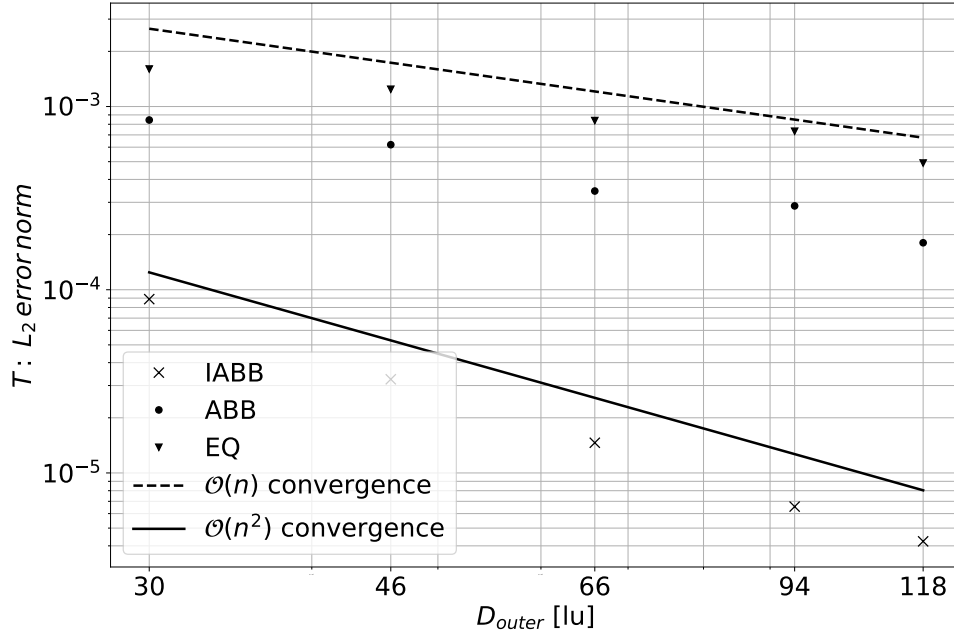


FIGURE 9.4: Grid convergence study for the Dirichlet boundary condition. The CM-TRT collision Kernel has been used and the conductivity was set to $k = 0.1$. Three different implementations of boundary conditions were benchmarked. The abbreviations reads: interpolated-anti-bounce-back (IABB), anti-bounce-back (ABB), equilibrium scheme (EQ).

9.3.4 Steady, forced convective heat transfer from a confined cylinder

From an engineering perspective, the temperature of the fluid is usually controlled by a presence of a heat exchanger. Here, a mesh dependence study of a steady forced convection from a confined cylinder is performed to illustrate the effect of the various implementation of the boundary conditions, collision kernels at different Prandtl number (\mathbf{Pr}) numbers. Figure 9.5 presents parametrisation of the domain. All simulations have been performed on a $D3Q_F27Q_H27$ lattice. To refine the lattice, a geometry scaling factor has been defined as $S \in \{1, 2, 4\}$. The height, length and cylinder's diameter of the *coarse* ($S = 1$) lattice are $H = 150$ [lu], $L = 1000$ [lu] and $D = 30$ [lu] respectively. On the inlet, the *Zou-He* [224] boundary condition (BC) also know as *non equilibrium bounce-back* method, with $T_{inlet} = 10$, has been imposed. The Neumann BC has been placed at the outlet as

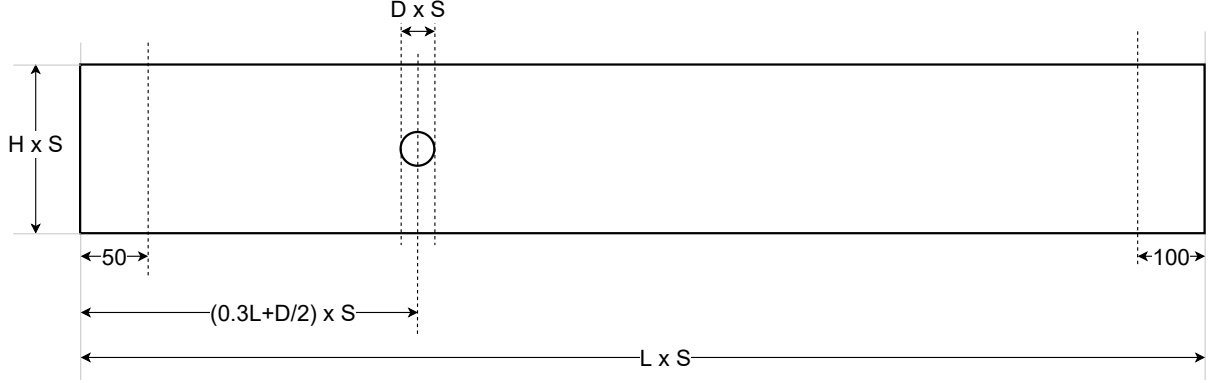


FIGURE 9.5: Channel with hot cylinder and cross-sections used for the heat flux measurements.

described in [225]. Top and bottom of the domain utilised symmetry BC. The Dirichlet BC has been prescribed on walls of the cylinder, $T_{cylinder} = 11$, using either first or second order implementation. In case of the first order BC, the bounce-back (BB) rule for hydrodynamics and equilibrium scheme (EQ) for internal energy field has been used. For the second order BC, the interpolated-bounce-back (IBB) and interpolated-anti-bounce-back (IABB), as described in Section 8.4 were employed. The LBM simulation has been iterated until heat flux calculated thorough the heater's surface, $\dot{q}_{surface}$, matched the outflow flux, $\dot{q}_x = \dot{q}_x^{inlet} - \dot{q}_x^{outlet}$, or the iterations limit has been reached. The heat flux thorough the heater's surface has been calculated as,

$$\dot{q}_{surface} = q_{out} - q_{in} = \sum_i h_i^* - \sum_i h_i, \quad (9.23)$$

while the heat flux thorough a section as,

$$\dot{q}_x^{section} = \int \rho c_v T \mathbf{u} \cdot \mathbf{n} dA = \sum_i e_i^x h_i. \quad (9.24)$$

To limit the effect of a boundary condition, the heat flux measurements' sections for the inlet and outlet have been defined 50 and 100 [lu] away from the boundary (see Figure 9.5).

The flow around a hot cylinder can be defined by two dimensionless numbers, namely Reynolds number (**Re**) and Prandtl number (**Pr**). The well known **Re** describes the ratio of inertia to viscous forces within the fluid, $Re = \frac{uD}{\nu}$. Subsequently, the **Pr** describes the relative thickness of the momentum to thermal boundary layer, $Pr = \frac{\nu}{\alpha} = \frac{\nu \rho c_v}{k}$. As mentioned in the Section 9.1, it can be also viewed as a property of a medium, which describes the ratio of time scales at which physical phenomena related to hydrodynamic

and thermal field occurs. For fluids characterised by high Pr (e.g. oil), the heat diffuses much slower than the momentum and the thermal boundary layer is contained within the velocity boundary layer. In the case of liquid metals, the opposite happens. The Pr is low, heat diffuses much faster than momentum, and the velocity boundary layer is fully contained within the thermal boundary layer. Finally, the Nusselt number (Nu) has been chosen to assess quality of the simulations. It represents the enhancement of heat transfer through a fluid as a result of convection relative to conduction across the same fluid layer. It is defined as $Nu = \frac{\varsigma D}{k}$, where ς is the average convective heat transfer coefficient, $\varsigma = \dot{q}/(A(T_{cylinder} - T_{inlet}))$ and $A = \pi D$ is the area of the cylinder. The heat flux, \dot{q} , is calculated as an average of $\dot{q}_{surface}$ and $\dot{q}_x^{section}$.

In the numerical study, 72 LBM simulations were performed. The resulting Nu are compared against a high-quality solution obtained with Bubnov-Galerkin finite element method (FEM) solver from QuickerSim CFD Toolbox for MATLAB. The FEM structural mesh consisted of 392704 second order triangular elements. Figure 9.6 presents discretization of the domain behind the cylinder. Four collision kernels were tested with first and

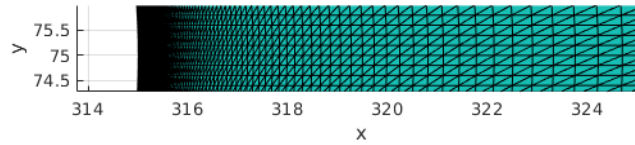


FIGURE 9.6: The FEM mesh in the vicinity of the cylinder.

second order BC for $Pr \in \{10, 100, 1000\}$. To lower the computational effort, the Reynolds number was set to 10 thus, the flow pattern could be assumed to be two-dimensional. As a consequence, the result obtained on the $D3Q_F 27Q_H 27$ lattice would correspond to the one obtained on $D2Q_F 9Q_H 9$. The coarse lattice $1000 \times 150 \times 3$ was refined two times resulting in a medium $2000 \times 300 \times 3$ and a fine $4000 \times 600 \times 3$ one. The Table 9.3, defines the Case-ID using lattice size, input parameters. It is followed by Table 9.4, which presents the outcomes for each combination of the kernel, boundary conditions and Case-ID.

mesh	Pr	Lattice size	D	U	Re	ν	k
coarse	10	1000×150×3	30	0.01	10	3×10^{-2}	3×10^{-3}
medium	10	2000×300×3	60	0.005	10	3×10^{-2}	3×10^{-3}
fine	10	4000×600×3	120	0.0025	10	3×10^{-2}	3×10^{-3}
coarse	100	1000×150×3	30	0.01	10	3×10^{-2}	3×10^{-4}
medium	100	2000×300×3	60	0.005	10	3×10^{-2}	3×10^{-4}
fine	100	4000×600×3	120	0.0025	10	3×10^{-2}	3×10^{-4}
coarse	1000	1000×150×3	30	0.01	10	3×10^{-2}	3×10^{-5}
medium	1000	2000×300×3	60	0.005	10	3×10^{-2}	3×10^{-5}
fine	1000	4000×600×3	120	0.0025	10	3×10^{-2}	3×10^{-5}

TABLE 9.3: The summary of executed cases. The variables, D, U, ν and k are expressed in lattice units.

mesh	Pr	CM-1 st		CM-SRT		CM-TRT		Cumulants-1 st		FEM
		1 st	2 nd	1 st	2 nd	1 st	2 nd	1 st	2 nd	
coarse	10	3.44	4.91	4.94	4.81	4.91	4.81	5.04	4.83	4.82
	10	5.03	4.84	4.87	4.81	4.86	4.81	4.92	4.82	4.82
	10	4.92	4.83	4.84	4.81	4.83	4.81	4.87	4.81	4.82
coarse	100	20.68	14.75	10.64	10.20	10.66	10.27	14.50	11.52	10.10
	100	15.87	11.84	10.33	10.11	10.32	10.13	11.82	10.36	10.10
	100	12.96	10.64	10.20	10.09	10.19	10.08	10.83	10.13	10.10
coarse	1000	166.42	102.27	-71.52	-57.02	27.09	24.58	94.31	58.33	21.43
	1000	111.76	62.52	22.75	21.78	22.73	21.84	53.97	34.19	21.43
	1000	74.00	40.47	21.87	21.38	21.84	21.37	34.04	24.56	21.43

TABLE 9.4: The **Nu** number, computed for different collision kernels and boundary conditions (see Table 9.3). The columns 1st and 2nd refer to the order of BC. 1st order BC – BB (hydrodynamics) & EQ (thermodynamics), 2nd order BC – IBB (hydrodynamics) & IABB (thermodynamics). The FEM has been used to obtain reference solution.

As far as the numerical conductivity is relatively high ($k = 3 \times 10^{-3}$), all kernels provided good results even with first order BC on each lattice. Once the conductivity is lowered by order of magnitude, ($k = 3 \times 10^{-4}$), discrepancies occur for the CM-1st and Cumulants-1st kernel on the coarse lattice. The mismatching results origin from relaxing first-order central moments or cumulants with frequencies corresponding to thermal conductivity, while higher-order quantities were relaxed towards equilibrium. Although benefits from the second-order boundary conditions can be clearly observed, they are not sufficient to counterweight the aforementioned effect. For the most numerically challenging case ($k = 3 \times 10^{-5}$), the CM-TRT kernel provided results with highest quality. Interestingly, the CM-SRT kernel performed reasonably well, except the coarsest lattice for which the wiggles in the temperature field reached the inlet (Figure 9.7b), causing the heat flux to be spurious. Notice that the behaviour of numerical artefacts for kernel pairs { CM-SRT, CM-TRT } and { CM-1st, Cumulants-1st } is similar. In Figure 9.7, the flow is computed, on a coarse mesh: $1000 \times 150 \times 3$, using 1st order boundary conditions. The cylinder diameter is $D=30$ [lu] and the inlet velocity is $U=0.01$ [lu/ts]. The relaxation frequencies corresponds to $\nu = 3 \times 10^{-2}$ and $k = 3 \times 10^{-5}$ ($\mathbf{Re} = 10$, $\mathbf{Pr} = 1000$). Following the imposed BC, the physical temperature range shall be contained within the values of 10 and 11. Other values are undoubtedly artefacts (see Figure 9.7, in which the temperature range has been clipped to highlight the issue). In the case of second-order boundary conditions, the shape of the artefacts was preserved, but the magnitude was decreased.

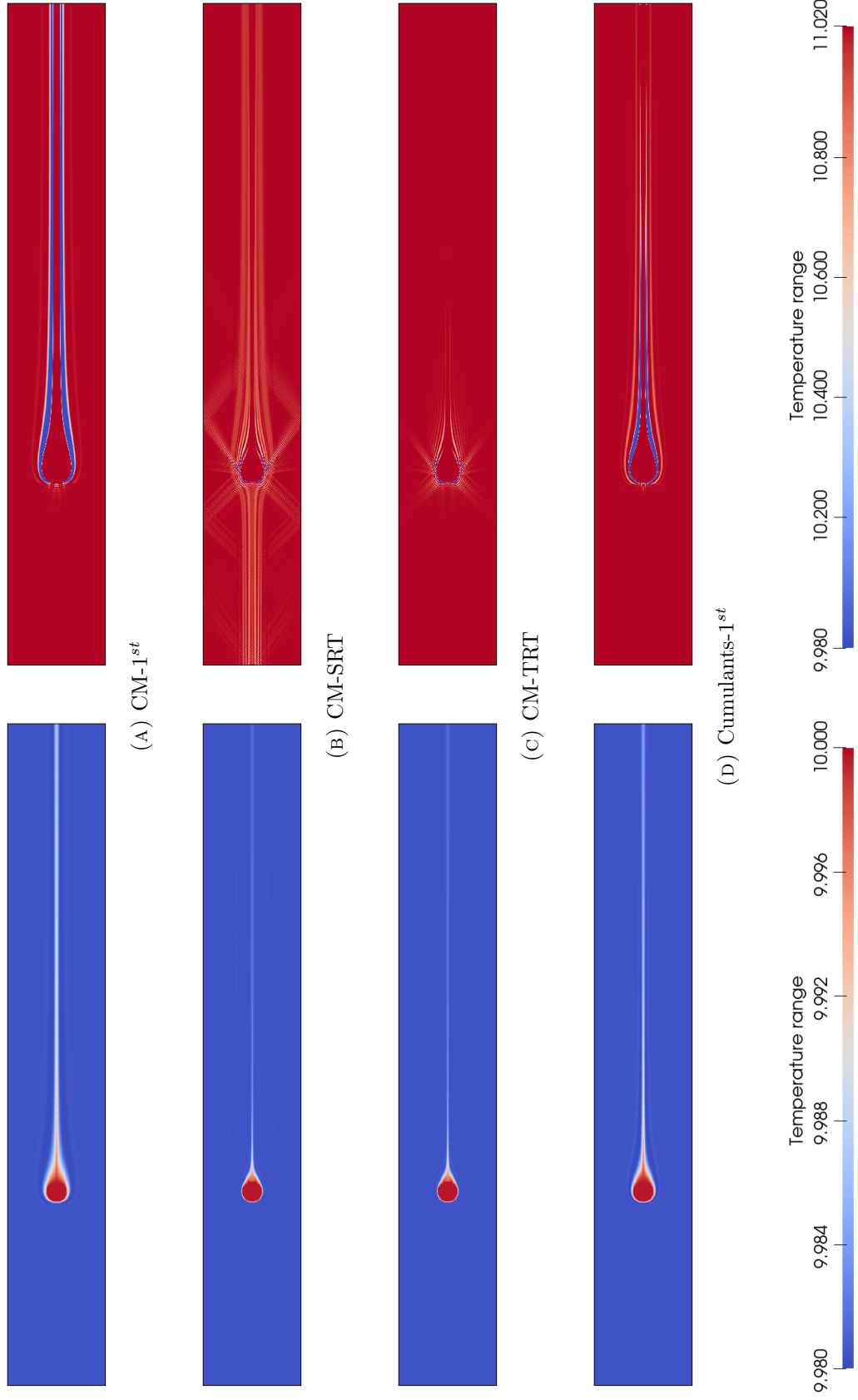


FIGURE 9.7: The temperature field is simulated using four different collision kernels. Left: the color scale is restricted to $T \in [9.98, 11.02]$. Right: the color scale is restricted to $T \in [9.98, 10.00]$, to highlight the numerical artefacts.

9.4 Future outlook

We decided to skip the benchmarks involving buoyancy force (natural convection inside a heated cavity or Rayleigh-Bernard convection) to limit the number of factors which can influence the results. Readers interested in the proper treatment of the forcing term are referred to discussions in [27, 43, 123, 124, 73, 79, 5].

Although an increase of the resolution might be enough to break the necessity of a larger stencil for the investigated cases, it is not obvious whether such an approach would be computationally cheaper, especially that both lattices responsible for the hydrodynamics and the advected field must be refined.

The seek of optimal relaxation frequencies for central moments, or cumulant collision kernel responsible for the advected field deserves further study. The relationship between higher order cumulants and central moments is non-linear, thus the conclusions related to the relaxation of higher-order central moments can not be projected to cumulants in a straightforward fashion. Due to the similarity between central moments and cumulants for order lower than fourth [43, 12], one may expect improvements by relaxing third-order cumulants. However, such extension is beyond the scope of the current research. As a good starting point, research regarding parametrisation of the cumulant kernel responsible for the hydrodynamic field [44] can be recommended. In terms collision operators which can be expressed in a matrix form, a comprehensive method for recovering equivalent partial differential equations has been recently proposed by Fučík and Straka [36].

As already mentioned, the central moments are calculated with respect to the macroscopic velocity, \mathbf{u} , which is the first order moment of the hydrodynamic distribution. According to the probabilistic definition of central moments, the shift matrix shall be computed with respect to the first order moments of the field being investigated. In case of the advected field, this points to the thermal distributions i.e. $\mathbb{N} = \mathbb{N}(\sum_i \mathbf{e}_i h_i)$. Next, two options exists.

First option is to relax the advected central moments, $\boldsymbol{\kappa}^H$, towards the mean of the hydrodynamic distribution, for example $\kappa_{10}^{H,*} = H(\kappa_{10}^H - u_x)s^H + \kappa_{10}(1 - s^H)$. Next concept, which follows immediately, is that the higher order moments of the advected field can also be relaxed towards their hydrodynamic counterparts.

Second option is to relax $\boldsymbol{\kappa}^H$ as proposed in the CM-SRT or CM-TRT approach, for example $\kappa_{10}^{H,*} = \kappa_{10}^H(1 - s^H)$, then backtransform the post-collision distributions using hydrodynamic velocity $\mathbb{N}(\mathbf{u})$.

9.5 Conclusions

In this work, an analysis of the state of the art collision kernels applied to both hydrodynamic and the advected field with a focus on the relaxation of the higher-order moments has been presented. To isolate features which may affect the accuracy of the proposed kernels a set of simple benchmarks was conducted. The tests have been performed in a numerically challenging, high Prandtl number regime. To alleviate the numerical artefacts raised by low conductivity, a D3Q27 lattice has been utilized for the advected field. However, lattices with large number of discrete velocities introduce additional degrees of freedom to the relaxation scheme. We demonstrated that proper treatment of the collision kernel plays a more important role than the application of second-order boundary conditions to represent a curved geometry. To sum up, for the set of investigated benchmarks, characterized by specific grid resolution and a range of non-dimensional numbers, the beneficial effect of tuning of the relaxation coefficients corresponding to the higher order moments has been confirmed numerically and the CM-TRT followed by CM-SRT kernel has been shown to be superior to the kernels that relax only first-order central moments/cumulants.

9.6 Source term treatment

For completeness of the study, the addition of the source term to the cumulant collision kernel is described in this appendix from the theoretical point of view. It is known in the literature [9], that the integration of the discrete Boltzmann equation with trapezoidal rule leads to implicit evolution equation,

$$h_i(\mathbf{x} + \mathbf{e}_i \delta t, t + \delta t) = \Omega_{H,i}(\mathbf{h}(\mathbf{x}, t)) + \frac{1}{2} \left[q_i(\mathbf{x} + \mathbf{e}_i \delta t, t + \delta t) + q_i(\mathbf{x}, t) \right]. \quad (9.25)$$

To remove the implicitness, a shift of variables is conducted and denoted with tilde,

$$\tilde{h}_i = h_i - \frac{1}{2} q_i \quad (9.26)$$

$$\tilde{H} = \sum_i \tilde{h}_i = H - \frac{1}{2} Q. \quad (9.27)$$

The q_i and Q denote the discretized source term and its zeroth moment respectively. A more detailed discussion of this procedure has been discussed in Chapters 2 and 4.

By transforming source term to the cumulant space, where the collision is performed, the augmented form of Equation (9.12) can be written as,

$$\Omega_{\mathbf{H}}(\tilde{\mathbf{h}}) = \mathcal{C}^{-1} \left(\tilde{\mathbf{c}}^{\mathbf{H}} + \mathbb{S}^{\mathbf{H}} \left(\tilde{\mathbf{c}}^{\mathbf{H},\text{eq}} - \tilde{\mathbf{c}}^{\mathbf{H}} \right) + \left(1 - \mathbb{S}^{\mathbf{H}}/2 \right) \mathbf{c}^Q \right). \quad (9.28)$$

The simplicity of the source term in the cumulants space is noteworthy,

$$\begin{aligned} \mathbf{c}^Q = \mathcal{C}(Q) &= \left[c_{000}^Q, c_{100}^Q, c_{010}^Q, c_{001}^Q, c_{110}^Q, c_{101}^Q, c_{011}^Q, c_{200}^Q, c_{020}^Q, c_{002}^Q, \dots, c_{ijk}^{eq}, \dots, c_{222}^Q \right]^{\top} \\ &= [Q, \quad 0, \quad 0, \quad 0, \quad 0, \quad 0, \quad 0, \quad 0, \quad 0, \quad 0, \quad \dots 0 \dots, \quad 0 \quad]^{\top}. \end{aligned} \quad (9.29)$$

Chapter 10

Multiphase Flows

“Learn the rules like a pro, so you can break them like an artist.”

– Pablo Picasso

Contents

10.1 The separation flux	167
10.2 Phase field - modified EDF	169
10.3 Phase field - forcing term	171
10.4 Phase field - forcing term - anti diffusion	173

This chapter shows how to adjust the advection-diffusion equation to model multiphase flows.

10.1 The separation flux

The separation flux, \mathbf{j}_S , is supposed to counteract the diffusion and reach a predefined interface profile in the equilibrium state [226, 227, 228],

$$\frac{\partial \phi}{\partial t} + \nabla \cdot \phi \mathbf{u} = \nabla \cdot (\underbrace{M \nabla \phi}_{\mathbf{j}_D} - \mathbf{j}_S). \quad (10.1)$$

To obtain the anti-diffusive effect, we require,

$$\mathbf{j}_S = \mathbf{j}_D^{eq} = M \nabla \phi^{eq}. \quad (10.2)$$

Let us use the \tanh function to smooth the step interface,

$$\phi^{eq} = \frac{1}{2} \tanh \left(\frac{2(\mathbf{x} - \mathbf{x}_0)}{\gamma} \right), \quad (10.3)$$

where γ is the thickness of the interface.

Evaluate diffusive flux in the equilibrium,

$$\mathbf{j}_D^{eq} = M \nabla \left[\overbrace{\frac{1}{2} \tanh \left(\frac{2(\mathbf{x} - \mathbf{x}_0)}{\gamma} \right)}^{\phi^{eq}} \right] = \frac{M}{2} \mathbf{n} \frac{\partial}{\partial \mathbf{x}_n} \tanh \left[\left(\frac{2(\mathbf{x} - \mathbf{x}_0)}{\gamma} \right) \right] \quad (10.4)$$

$$= \frac{M}{\gamma} \mathbf{n} \left[\underbrace{1 - \tanh^2 \left(\frac{2(\mathbf{x} - \mathbf{x}_0)}{\gamma} \right)}_{1 - 4(\phi^{eq})^2} \right] = M \mathbf{n} \frac{1 - 4(\phi^{eq})^2}{\gamma}. \quad (10.5)$$

Therefore,

$$\mathbf{j}_S = M \mathbf{n} \frac{1 - 4\phi^2}{\gamma} \quad \text{where} \quad \mathbf{n} = \frac{\nabla \phi}{|\nabla \phi|}. \quad (10.6)$$

Plugging in Equation (10.6) into Equation (10.1), we obtain the phase field evolution equation:

$$\frac{\partial \phi}{\partial t} + \nabla \cdot \phi \mathbf{u} = \nabla \cdot M \left(\nabla \phi - \frac{\nabla \phi}{|\nabla \phi|} \frac{[1 - 4(\phi - \phi_0)^2]}{\gamma} \right) \quad (10.7)$$

The interface is located in the middle between high and low value of ϕ : $\phi_0 = (\phi_H + \phi_L)/2$. Next, the macroscopic quantities like density or viscosity can be calculated based on the value of the phase field at particular location. For example, the density can be found using a linear interpolation between ρ_H and ρ_L ,

$$\rho = \rho_L + \frac{\phi - \phi_L}{\phi_H - \phi_L} (\rho_H - \rho_L). \quad (10.8)$$

10.2 Phase field - modified EDF

The target macroscopic equation is the Allen-Cahn equation. It consist of ADE, tweaked with an anti-diffusive (phase-separation) flux,

$$\frac{\partial \phi}{\partial t} + \vec{\nabla} \cdot (\phi \vec{u}) = \vec{\nabla} \cdot \left[M \left(\vec{\nabla} \phi - \frac{\vec{\nabla} \phi}{|\vec{\nabla} \phi|} \frac{1 - 4\phi^2}{W} \right) \right]. \quad (10.9)$$

Geier *et al.* [229] proposed a following EDF,

$$h_i^{\text{eq}} = w_i \phi \left[1 + \frac{\mathbf{e}_i \mathbf{u}}{\theta \mathbf{e}^2} + \frac{(\mathbf{e}_i \mathbf{u})^2}{2\theta^2 \mathbf{e}^4} - \frac{\mathbf{u}^2}{2\theta \mathbf{e}^2} \right] + \underbrace{B w_i (\mathbf{e}_i \mathbf{n})}_{\Gamma_i}. \quad (10.10)$$

where,

$$B = \frac{M}{\theta} \frac{1 - 4\phi^2}{W} \quad (10.11)$$

and the normal vector, \mathbf{n} , is defined as,

$$\mathbf{n} = [n_x, n_y] = \left[\left(\frac{\nabla \phi}{|\nabla \phi|} \right)_x, \left(\frac{\nabla \phi}{|\nabla \phi|} \right)_y \right]. \quad (10.12)$$

The raw moments of Γ_i read,

$$\begin{aligned} \sum_i (e_i^x)^m (e_i^y)^n \Gamma_i &= \begin{bmatrix} \Gamma_{00} & \Gamma_{10} & \Gamma_{01} & \Gamma_{20} & \Gamma_{02} & \Gamma_{11} & \Gamma_{21} & \Gamma_{12} & \Gamma_{22} \end{bmatrix}^\top \\ &= \begin{bmatrix} 0 & \theta B n_x & \theta B n_y & 0 & 0 & 0 & \theta^2 B n_y & \theta^2 B n_x & 0 \end{bmatrix}^\top. \end{aligned}$$

Moments of equilibrium distribution function (EDF) are,

$$\begin{cases} \sum h_i^{\text{eq}} &= \phi \\ \sum e_i^j h_i^{\text{eq}} &= u^j \phi + B \theta n^j \\ \sum e_i^j e_i^k h_i^{\text{eq}} &= \underbrace{\delta^{jk} \theta \phi + u^j u^k \phi}_{\Pi_{\phi, \text{eq}}^{jk}} \end{cases} \quad (10.13)$$

Moments of distribution function (DF) are,

$$\begin{cases} \sum h_i &= \phi \\ \sum e_i^j h_i &= u^j \phi + B\theta n^j + Q_{neq}^j \\ \sum e_i^j e_i^k h_i &= \underbrace{\delta^{jk} \theta \phi + u^j u^k \phi}_{\Pi_{\phi,eq}^{jk}} + \Pi_{\phi,neq}^{jk} \end{cases}$$

Let us remind, the discrete Boltzmann equation (DBE) (see Equation (7.7)),

$$\frac{\partial}{\partial t} h_i + e_i^j \frac{\partial}{\partial x_j} h_i = \frac{1}{\tau} (h_i^{\text{eq}} - h_i). \quad (10.14)$$

Zeroth moment of DBE = $\sum_i DBE_i$ are,

$$\begin{aligned} \frac{\partial}{\partial t} \phi + \frac{\partial}{\partial x_j} (u^j \phi + B\theta n^j + Q_{neq}^j) &= 0 \Leftrightarrow \\ \Leftrightarrow \frac{\partial}{\partial t} \phi + \frac{\partial}{\partial x_j} (u^j \phi) &= -\frac{\partial}{\partial x_j} Q_{neq}^j - \frac{\partial}{\partial x_j} B\theta n^j. \end{aligned} \quad (10.15)$$

First moment of DBE = $\sum_i e_i^k DBE_i$ are,

$$\begin{aligned} \frac{\partial}{\partial t} (u^k \phi + B\theta n^k + Q_{neq}^k) + \frac{\partial}{\partial x_j} (\delta^{jk} \theta \phi + u^j u^k \phi + \Pi_{\phi,neq}^{jk}) &= -\frac{1}{\tau_\phi} Q_{neq}^k \Leftrightarrow \\ \Leftrightarrow Q_{neq}^k &= -\tau_\phi \left[\frac{\partial}{\partial x_j} (\delta^{jk} \theta \phi + u^j u^k \phi + \Pi_{\phi,neq}^{jk}) + \frac{\partial}{\partial t} (u^k \phi + B\theta n^k + Q_{neq}^k) \right] \\ \Leftrightarrow Q_{neq}^k &= -\tau_\phi \left[\frac{\partial}{\partial x_k} \theta \phi + \frac{\partial}{\partial x_j} (u^j u^k \phi + \Pi_{\phi,neq}^{jk}) + \frac{\partial}{\partial t} (u^k \phi + B\theta n^k + Q_{neq}^k) \right]. \end{aligned} \quad (10.16)$$

As usual, we insert Q_{neq}^k to Equation (10.15) and we obtain,

$$\begin{aligned} \frac{\partial}{\partial t} \phi + \frac{\partial}{\partial x_j} (u^j \phi) &= \frac{\partial}{\partial x_j} \tau_\phi \frac{\partial}{\partial x_k} \theta \phi \\ &+ \frac{\partial}{\partial x_j} \tau_\phi \left[\frac{\partial}{\partial x_j} (u^j u^k \phi + \Pi_{\phi,neq}^{jk}) + \frac{\partial}{\partial t} (u^k \phi + B\theta n^k + Q_{neq}^k) \right] \\ &- \frac{\partial}{\partial x_j} B\theta n^k. \end{aligned} \quad (10.17)$$

Assuming that θ is spatially independent, we can conclude that $\tau_\phi \theta = M$. Next, we have to plugging in the definitions for B and \mathbf{n} , given by Equations (10.11) and (10.12),

$$\begin{aligned} \frac{\partial}{\partial t} \phi + \frac{\partial}{\partial x_j} (u^j \phi) &= \frac{\partial}{\partial x_j} \underbrace{\tau_\phi \theta}_{=M} \frac{\partial}{\partial x_k} \phi \\ &\quad - \frac{\partial}{\partial x_j} M \frac{1 - 4\phi^2}{W} \frac{\partial_{x_k} \phi}{|\partial_x \phi|} \\ &\quad + \frac{\partial}{\partial x_j} \tau_\phi \left[\frac{\partial}{\partial x_j} (u^j u^k \phi + \Pi_{\phi, neq}^{jk}) + \frac{\partial}{\partial t} (u^k \phi + M \frac{1 - 4\phi^2}{W} \frac{\partial_{x_k} \phi}{|\partial_x \phi|} + Q_{neq}^k) \right]. \end{aligned} \quad (10.18)$$

Finally the desired macroscopic equation is recovered,

$$\begin{aligned} \frac{\partial}{\partial t} \phi + \frac{\partial}{\partial x_j} (u^j \phi) &= \frac{\partial}{\partial x_j} M \left[\frac{\partial}{\partial x_k} \phi - \frac{1 - 4\phi^2}{W} \frac{\partial_{x_k} \phi}{|\partial_x \phi|} \right] \\ &\quad + \frac{\partial}{\partial x_j} \tau_\phi \left[\frac{\partial}{\partial x_j} (u^j u^k \phi + \Pi_{\phi, neq}^{jk}) + \frac{\partial}{\partial t} (u^k \phi + M \frac{1 - 4\phi^2}{W} \frac{\partial_{x_k} \phi}{|\partial_x \phi|} + Q_{neq}^k) \right]. \end{aligned} \quad (10.19)$$

10.3 Phase field - forcing term

Here, we will recover the conservative Allen-Cahn equation (10.9) again. Instead of modifying the EDF, a forcing term will be applied (see Equation (2.21))

$$\frac{\partial}{\partial t} h_i + e_i^j \frac{\partial}{\partial x_j} h_i = \frac{1}{\tau} (h_i^{eq}(\phi, \mathbf{u}) - h_i) + \underbrace{\frac{F^j (e_i^j - u^j)}{\phi c_s^2} h_i^{eq}(\phi, \mathbf{u})}_{\Gamma_i}. \quad (10.20)$$

Moments of EDF are,

$$\begin{cases} \sum h_i^{eq} &= \phi \\ \sum e_i^j h_i^{eq} &= u^j \phi \\ \sum e_i^j e_i^k h_i^{eq} &= \underbrace{\delta^{jk} \theta \phi + u^j u^k \phi}_{\Pi_{\phi, eq}^{jk}} \end{cases} \quad (10.21)$$

Moments of DF are,

$$\begin{cases} \sum h_i &= \phi \\ \sum e_i^j h_i &= u^j \phi + Q_{neq}^j \\ \sum e_i^j e_i^k h_i &= \underbrace{\delta^{jk} \theta \phi + u^j u^k \phi}_{\Pi_{\phi,eq}^{jk}} + \Pi_{\phi,neq}^{jk} \end{cases} \quad (10.22)$$

Moments of the forcing term, Γ_i , are,

$$\begin{cases} \sum \Gamma_i &= 0 \\ \sum e_i^j \Gamma_i &= F^j \\ \sum e_i^j e_i^k \Gamma_i &= F^j u^k + F^k u^j \end{cases} \quad (10.23)$$

Zeroth moment of ADBE = $\sum_i ADBE_i$ are,

$$\begin{aligned} \frac{\partial}{\partial t} \phi + \frac{\partial}{\partial x_j} (u^j \phi + Q_{neq}^j) &= 0 \Leftrightarrow \\ \Leftrightarrow \frac{\partial}{\partial t} \phi + \frac{\partial}{\partial x_j} (u^j \phi) &= -\frac{\partial}{\partial x_j} Q_{neq}^j. \end{aligned} \quad (10.24)$$

First moment of ADBE = $\sum_i e_i^k ADBE_i$ are,

$$\begin{aligned} \frac{\partial}{\partial t} (u^k \phi + Q_{neq}^k) + \frac{\partial}{\partial x_j} (\delta^{jk} \theta \phi + u^j u^k \phi + \Pi_{\phi,neq}^{jk}) &= -\frac{1}{\tau_\phi} Q_{neq}^k + F^k \Leftrightarrow \\ \Leftrightarrow Q_{neq}^k &= -\tau_\phi \left[\frac{\partial}{\partial t} (u^k \phi + Q_{neq}^k) + \frac{\partial}{\partial x_j} (\delta^{jk} \theta \phi + u^j u^k \phi + \Pi_{\phi,neq}^{jk}) - F^k \right] \\ \Leftrightarrow Q_{neq}^k &= -\tau_\phi \left[\frac{\partial}{\partial x_k} \theta \phi - F^k + \frac{\partial}{\partial t} (u^k \phi + Q_{neq}^k) + \frac{\partial}{\partial x_j} (u^j u^k \phi + \Pi_{\phi,neq}^{jk}) \right]. \end{aligned} \quad (10.25)$$

As usual, we insert Q_{neq}^k to Equation (10.24) and we get,

$$\begin{aligned} \frac{\partial}{\partial t} \phi + \frac{\partial}{\partial x_j} (u^j \phi) &= \frac{\partial}{\partial x_j} \tau_\phi \left[\frac{\partial}{\partial x_k} \theta \phi - F^k \right] \\ &+ \frac{\partial}{\partial x_j} \tau_\phi \left[\frac{\partial}{\partial t} (u^k \phi + Q_{neq}^k) + \frac{\partial}{\partial x_j} (u^j u^k \phi + \Pi_{\phi,neq}^{jk}) \right]. \end{aligned} \quad (10.26)$$

It is easy to observe that to recover Equation (10.9), the F^k shall have a following form:

$$F^k = \theta \frac{1 - 4\phi^2}{W} \frac{\partial_{x_k} \phi}{|\partial_x \phi|}. \quad (10.27)$$

10.4 Phase field - forcing term - anti diffusion

Now, suppose that we would like to create a LBM scheme without diffusion,

$$\frac{\partial \phi}{\partial t} + \vec{\nabla} \cdot (\phi \vec{u}) = \vec{\nabla} \cdot M \left(\vec{\nabla} \phi - \vec{\nabla} \phi \right). \quad (10.28)$$

Why we can not calculated gradient ($\sim \frac{\partial}{\partial x_k} \phi$) from first moment of DF? Following reasoning from Section 10.3, namely Equations (10.25) and (10.26), we have,

$$Q_{neq}^k = -\tau_\phi \left[\frac{\partial}{\partial x_k} \theta \phi - F^k + \frac{\partial}{\partial t} (u^k \phi + Q_{neq}^k) + \frac{\partial}{\partial x_j} (u^j u^k \phi + \Pi_{\phi, neq}^{jk}) \right]. \quad (10.29)$$

To counter act diffusion, the forcing term, F^k , shall have the following form,

$$F^k = \frac{\tau_\phi}{\tau_\phi} \frac{\partial}{\partial x_k} \theta \phi. \quad (10.30)$$

where τ_ϕ is the anti-diffusion relaxation parameter. Plugging F^k back to Q_{neq}^k we get,

$$Q_{neq}^k = -\tau_\phi \left[\frac{\partial}{\partial x_k} \theta \phi - \frac{\tau_\phi}{\tau_\phi} \frac{\partial}{\partial x_k} \theta \phi + garbage \right] \quad (10.31)$$

$$= \left[(\tau_\phi - \tau_\phi) \frac{\partial}{\partial x_k} \theta \phi + garbage \right] : (\tau_\phi - \tau_\phi) \quad (10.32)$$

$$\Rightarrow \frac{\partial}{\partial x_k} \theta \phi = \frac{Q_{neq}^k}{\tau_\phi - \tau_\phi} + garbage. \quad (10.33)$$

To counter act diffusion, τ_ϕ shall be equal to τ_ϕ , but this would cause division by 0. Concluding, such an approach will not work and it is not feasible to construct a LBM scheme without diffusion term.

Chapter 11

A cascaded phase-field lattice Boltzmann model for the simulation of incompressible, immiscible fluids with high density contrast

“You often feel tired, not because you’ve done too much, but because you’ve done too little of what sparks a light in you.”

– Alexander Den Heijer

Contents

11.1 Introduction	176
11.2 Model description	179
11.2.1 Macroscopic equations	179
11.2.2 Lattice Boltzmann equations	180
11.2.3 Forcing terms	183
11.3 Model verification and validation	185
11.3.1 Two phase Poiseuille flow	185
11.3.2 Interpolation of the relaxation rate in the diffuse interface	187
11.3.3 Effect of the moving reference frame	189
11.3.4 Planar Taylor bubble analysis	194
11.3.5 Planar Taylor bubble in a moving reference frame	197
11.3.6 Computational Efficiency	200
11.4 Remarks on orthogonalization of moments and relaxation	201

11.5 Remarks on discretization of the distribution functions . . .	202
11.6 Discretization of the force term	205
11.7 Conclusions	208
11.8 Future Outlook	208

Content of this chapter is based on the article “A cascaded phase-field lattice Boltzmann model for the simulation of incompressible, immiscible fluids with high density contrast” [5].

In this work, a conservative phase-field model for the simulation of immiscible multiphase flows is developed using an incompressible, velocity-based, cascaded lattice Boltzmann method (CLBM). Extensions are made to the lattice Boltzmann (LB) equations for interface tracking and incompressible hydrodynamics, proposed by Fakhari et al. [230], by performing relaxation operations in central moment space. This was motivated by the work of Fei et al. [48, 68], where promising results from such a transformation were observed. The relaxation of central moments is defined in a reference frame moving with the fluid, while the existing multiple-relaxation time [231, 232] scheme performs collision in a fixed frame of reference. Moreover, the derivations make use of continuous, Maxwellian distribution functions. As a result, the CLBM enhances the Galilean invariance and stability of the method when high lattice Mach numbers are evident. The cascaded scheme has been previously used in the literature to simulate multiphase flows based on the pseudo-potential model, where it allowed for high density and viscosity contrasts to be captured [233, 234]. Here, the CLBM is implemented within the phase-field framework and is verified through the analysis of a layered Poiseuille flow. The performance of the CLBM is then investigated in terms of spurious currents, Galilean invariance and computational efficiency. Finally, the work of Fakhari et al. [230] is extended by validating the model’s ability to capture the relation between surface tension and the rise velocity of a planar Taylor bubble, in both stagnant and flowing fluid. New counter-current results indicate that the rise velocity model of Ha-Ngoc and Fabre [235] also applies in this regime.

11.1 Introduction

Multiphase flows are frequently observed in a wide array of both engineering applications and environmental phenomena. However, challenges can arise when attempting to track the interface between different fluids due to the complex dynamics associated with phase

change, separation and coalescence. Additionally, the discontinuity created by such an interface can cause steep numerical gradients, which can further complicate the simulation of such flows. As a result of its mesoscopic nature, the lattice Boltzmann method (LBM) [236, 237], has proven to be a suitable candidate to simulate the intermolecular interactions responsible for interfacial behaviours. The LBM has seen a significant increase in popularity over the past few decades, due to its relative ease of implementation and its ability to handle complex geometries. The algorithm can generally be separated into non-linear computations that are performed locally and simple linear operations that require information from only neighbouring nodes, allowing favourable performance on parallel architectures. These features have seen the LBM enter mainstream computational fluid dynamics in both research and commercial software packages. Recent and comprehensive reviews of multiphase modelling with the LBM can be found in the literature [238, 239].

The approaches to mimicking interfacial dynamics in the simulation of multiphase flows can be separated into two overarching categories, namely, sharp and diffuse interface models [240, 241]. In the former, the multiphase interface is treated as a boundary where a discontinuous jump in fluid properties is evident. While the velocity must be continuous, there is a stress jump across the interface, which corresponds to the Laplace pressure. As a result, it is quite common that boundary fitted meshes are required for each phase and often interface reconstruction and or re-meshing between iterations may be required. The interfacial dynamics must be explicitly tracked by coupling a Navier-Stokes solver on each side of the boundary with a method to capture the spatial evolution of the interface through time. Within this class of methods, the volume-of-fluid [242, 243, 244], immersed boundary [245] and front-tracking method [246] are highlighted for the interested reader. On the other hand, the diffuse interface approach uses a region of finite width for the transition of fluid properties. In these methods, the interface does not need to be explicitly tracked, and the computational operation performed at each fluid node is equivalent. These methods are commonly observed in the LB framework in which the interface is smoothed across several lattice nodes allowing the fluid properties to vary continuously.

There exists two main philosophies when it comes to diffuse interface modelling, here, they are described in terms of a *bottom-up* and *top-down* approach [247, 128, 248]. The bottom-up approach, which is exemplified by the pseudo-potential model proposed by Shan and Chen [249, 250], describes the microscopic interactions between fluid elements to achieve macroscopic phase separation. Depending on the postulation, different equations-of-state can be achieved. The pseudo-potential model has been subsequently improved since its first appearance, with notable contributions by Lycett-Brown and Luo [233,

[234] who, in particular, introduced the cascaded collision operator into the method. This enabled the model to reproduce a wide range of coexistence curves correctly. One of the main drawbacks with the bottom-up approach, however, comes from the fact that there is no explicit way to derive physical parameters such as surface tension and or wetting contact angle from the lattice interaction constants. As such, numerical experiments need to be conducted to ascertain the fluid properties desired for a particular simulation [251]. The top-down approach formulates a free energy functional for the fluid system. It consists of a bulk term, a gradient term used to penalize variations of an order parameter, and a surface term describing interactions between fluid and solid media [252]. By design, this method is thermodynamically consistent, and the physical properties of interacting fluids can be explicitly derived. In the current study, the focus is on binary or immiscible fluids and their respective models. Following the idea of the energy functional approach, an order parameter or phase-field is introduced to differentiate the fluid phases within the domain. The phase-field can then be evolved according to Cahn-Hilliard [253] or Allen-Cahn [254] theory. Recent advances in the implementation of phase-field models within the LB framework can be found in Geier et al. [229], Fakhari et al. [230, 78] and Chiu et al. [255]. Although the locality of the original LBM collision process is slightly degraded in these models, they are able to simulate flows with large density and or viscosity contrasts while maintaining an explicit relationship between numerical and physical parameters.

In this work, the cascaded collision operator is incorporated into the model of Fakhari et al. [230] and its performance is benchmarked. To the best of the author's knowledge, this is the first time when a phase-field, velocity based CLBM has been proposed for the simulation of incompressible, multiphase flow. In order to do this, it was necessary to derive the central moments of the continuous equilibrium function for the incompressible, velocity based LBM. As a result, this work improves the velocity discretization of the equilibrium distribution function, being one of the conditions of the Galilean invariance (see Section 3.4). The formulation and implementation are first verified against the well-known layered Poiseuille flow case, for which an analytical solution can be obtained. Additionally, the results of the CLBM are compared with a high resolution finite difference solution, allowing the effect of the diffuse interface to be captured. Following this, the spurious currents related to the interpolation of the relaxation parameter from the phase-field are assessed. This includes the linear interpolation scheme used in the work of Fakhari et al. [230] and Mitchell et al. [78] as well as interpolation through the dynamic viscosity. To compare the Galilean invariance and stability of the cascaded relaxation to the previously used multiple relaxation time (MRT) scheme, a droplet is immersed in an

immiscible fluid and analyzed in a moving reference frame. This test was performed at both a low and high Mach number. Finally, the validity and practical use of the proposed model is shown by extending the planar Taylor bubble analysis presented in Fakhari et al. [230]. Here, the relation between surface tension and bubble rise velocity in a stagnant fluid is developed prior to investigating the effects of bulk fluid velocity on the Taylor bubble dynamics. To conclude the study, the computational efficiency of different collision operators is compared to show that the modifications to the model do not inhibit its applicability.

11.2 Model description

To simplify the model description, the formulation of the cascaded phase-field LBM is restricted to two-dimensions and builds on the work of Fakhari et al. [230]. In particular, a D2Q9 lattice is used for both the hydrodynamic and phase-field distribution functions. It is noted that generality is not lost as an extension to three-dimensions follows the theory presented.

11.2.1 Macroscopic equations

11.2.1.1 Navier-Stokes equations

The focus of this work is to implement a cascaded collision operator in the phase-field LBM and then benchmark its performance against existing formulations. Here, the objective is to simulate the flow dynamics of an incompressible, immiscible, multiphase fluid system. The governing hydrodynamics is described by the continuity and momentum equations,

$$\frac{\partial \rho}{\partial t} + \nabla \cdot \rho \mathbf{u} = 0, \quad (11.1)$$

$$\rho \left(\frac{\partial \mathbf{u}}{\partial t} + \mathbf{u} \cdot \nabla \mathbf{u} \right) = -\nabla p + \nabla \cdot (\mu [\nabla \mathbf{u} + (\nabla \mathbf{u})^\top]) + \mathbf{F}_s + \mathbf{F}_b, \quad (11.2)$$

where a volumetric force, \mathbf{F}_s , accounts for the interface interactions, and additional body forces are described by, \mathbf{F}_b .

11.2.1.2 Interface tracking

The phase-field models used in this study are built from the work of Cahn-Hilliard [253] and later Allen-Cahn [254]. Although both approaches can provide valid results, the Allen-Cahn equations are of the second order compared to the fourth order Cahn-Hilliard equations, which provides numerical benefits in implementation and computational efficiency [256]. Here, the conservative form of the Allen-Cahn equation proposed by Chiu and Lin [255] is used to track the evolution of the interface between fluids,

$$\frac{\partial \phi}{\partial t} + \nabla \cdot \phi \mathbf{u} = \nabla \cdot M \left(\nabla \phi - \frac{\nabla \phi}{|\nabla \phi|} \frac{[1 - 4(\phi - \phi_0)^2]}{\gamma} \right). \quad (11.3)$$

The interface is located in the middle of the extreme, ϕ_H and ϕ_L , phase-field values such that, $\phi_0 = (\phi_H + \phi_L)/2$. In this study $\phi_H = 1$ and $\phi_L = 0$. The interested reader is pointed to the work of Geier et al. [229] for further details regarding the conservative phase-field LBM.

11.2.2 Lattice Boltzmann equations

With the current framework [230], a double-distribution function approach is used in which one distribution function recovers the Navier-Stokes equations, and an additional one is used to resolve the conservative phase-field equation. Here, the components of the equilibrium distribution function and force vectors are also defined in central moment space. The system of equations is then closed by defining the relationship between LB and macroscopic parameters.

11.2.2.1 Physical interpretation of moments

The physical interpretation of the raw, zeroth order moments of the hydrodynamic and phase-field distribution function corresponds to the values of normalized pressure, $\bar{p} = p/(\rho c_s^2)$, and phase-field, ϕ ,

$$\phi = \Upsilon_{00}^\phi = \sum_i h_i, \quad (11.4)$$

respectively. The macroscopic fluid velocity, \mathbf{u} , is the first raw moment of the hydrodynamic distribution function and has a dependency on the forcing term, \mathbf{F} , that is described

in Sec. 11.2.3,

$$\mathbf{u} = \begin{bmatrix} u_x \\ u_y \end{bmatrix} = \begin{bmatrix} \Upsilon_{10} \\ \Upsilon_{01} \end{bmatrix} = \sum_i f_i \mathbf{e}_i + \frac{\mathbf{F}}{2\rho} \delta t. \quad (11.5)$$

11.2.2.2 Collision

The collision process and application of forcing terms is conducted in the central moment space (see Section 3.3) to improve computational efficiency [48, 68, 26],

$$\boldsymbol{\kappa}^*(\mathbf{x}, t) = (\mathbb{1} - \mathbb{S})\boldsymbol{\kappa} + \mathbb{S}\boldsymbol{\kappa}^{eq} + (\mathbb{1} - \mathbb{S}/2)\tilde{\mathbf{F}}, \quad (11.6)$$

$$\boldsymbol{\kappa}^{\phi,*}(\mathbf{x}, t) = (\mathbb{1} - \mathbb{S}^\phi)\boldsymbol{\kappa}^\phi + \mathbb{S}^\phi\boldsymbol{\kappa}^{\phi,eq} + (\mathbb{1} - \mathbb{S}^\phi/2)\tilde{\mathbf{F}}^\phi. \quad (11.7)$$

The relaxation matrices, \mathbb{S} and \mathbb{S}^ϕ , have a diagonal form specified as,

$$\mathbb{S} = \text{diag} \left([s_0, s_1, s_1], \begin{bmatrix} s_+ & s_- \\ s_- & s_+ \end{bmatrix}, [s_\nu, s_3, s_3, s_4] \right), \quad (11.8)$$

$$\mathbb{S}^\phi = \text{diag} \left([s_0^\phi, s_M^\phi, s_M^\phi, s_2^\phi, s_2^\phi, s_2^\phi, s_3^\phi, s_3^\phi, s_4^\phi] \right), \quad (11.9)$$

where $s_+ = (s_b + s_v)/2$ and $s_- = (s_b - s_v)/2$. The relation between current relaxation matrices and the ones used previously in the MRT scheme [231, 232, 230] is discussed in Section 11.4. Following the Chapman-Enskog expansion, the kinematic and bulk viscosities are used to calculate corresponding relaxation frequencies, s_v and s_b ,

$$s_v = \frac{1}{\tau} = \frac{1}{\frac{\nu}{c_s^2 \delta t} + 1/2}, \quad (11.10)$$

$$s_b = \frac{1}{\tau_b} = \frac{1}{\frac{\zeta}{c_s^2 \delta t} + 1/2}. \quad (11.11)$$

The bulk relaxation rate is specified as, $s_b = 1$. Such an approach results in a reduction of non-physical pressure oscillations, giving a *bulk equilibrium* after each collision and a more stable model. To satisfy conservation laws for density and momentum, the zeroth and first order relaxation constants are set to unity, $s_0 = s_1 = 1$. For this study, the tunable relaxation frequencies are specified as, $s_3 = s_4 = 1$. In the case of the phase-field

distribution function, the relaxation frequency, s_v , is replaced by,

$$s_M^\phi = \frac{1}{\tau_M} = \frac{1}{\frac{M}{c_s^2 \delta t} + 1/2}. \quad (11.12)$$

Here, s_M^ϕ is used to relax the first moments only (see [68]) while the remainder are conserved by setting the relaxation frequencies to unity, $s_0^\phi = s_2^\phi = s_3^\phi = s_4^\phi = 1$. The reader is referred to the in-depth numerical study conducted by Kusumaatmaja et al. [257] for details on the choice of the mobility parameter, M .

11.2.2.3 Central moments of equilibrium distribution functions and force vectors

The components of the equilibrium distribution function and force vectors in central moment space are presented in Equations 11.13-11.16. These are derived from the corresponding continuous distributions. As mentioned in Section 11.1, such a procedure enhances the stability and Galilean invariance of the scheme. Further details on the derivations are provided in Sections 11.5 and 11.6.

$$\boldsymbol{\kappa}^{eq} = \begin{bmatrix} \Upsilon_{00} \\ (\Upsilon_{00} - 1)(-u_x) \\ (\Upsilon_{00} - 1)(-u_y) \\ (\Upsilon_{00} - 1)(u_x^2 + c_s^2) + c_s^2 \\ (\Upsilon_{00} - 1)(u_y^2 + c_s^2) + c_s^2 \\ (\Upsilon_{00} - 1)u_x u_y \\ (\Upsilon_{00} - 1)(-u_y)(c_s^2 + u_x^2) \\ (\Upsilon_{00} - 1)(-u_x)(c_s^2 + u_y^2) \\ (\Upsilon_{00} - 1)(u_x^2 u_y^2 + c_s^2(u_x^2 + u_y^2) + c_s^4) + c_s^4 \end{bmatrix} \quad (11.13)$$

$$\boldsymbol{\kappa}^{\phi,eq} = [\Upsilon_{00}^\phi, 0, 0, c_s^2 \Upsilon_{00}^\phi, c_s^2 \Upsilon_{00}^\phi, 0, 0, 0, c_s^4 \Upsilon_{00}^\phi]^\top \quad (11.14)$$

$$\tilde{\mathbf{F}} = [0, F_x/\rho, F_y/\rho, 0, 0, 0, c_s^2 F_y/\rho, c_s^2 F_x/\rho, 0]^\top \quad (11.15)$$

$$\tilde{\mathbf{F}}^\phi = [0, F_x^\phi, F_y^\phi, 0, 0, 0, c_s^2 F_y^\phi, c_s^2 F_x^\phi, 0]^\top \quad (11.16)$$

11.2.2.4 Streaming

To perform the streaming step, the relaxed, post-collision central moments need to be transformed back into the velocity distribution space and streamed to neighbours,

$$\mathbf{f}(\mathbf{x} + \mathbf{e}\delta t, t + \delta t) = \mathbb{M}^{-1}\mathbb{N}^{-1}\boldsymbol{\kappa}^*(\mathbf{x}, t), \quad (11.17)$$

$$\mathbf{h}(\mathbf{x} + \mathbf{e}\delta t, t + \delta t) = \mathbb{M}^{-1}\mathbb{N}^{-1}\boldsymbol{\kappa}^{\phi,*}(\mathbf{x}, t). \quad (11.18)$$

11.2.3 Forcing terms

11.2.3.1 Forcing terms for hydrodynamics

The total hydrodynamic force, $\mathbf{F} = [F_x, F_y]^\top$, acting upon a fluid is the sum of all forcing components,

$$\mathbf{F} = \mathbf{F}_s + \mathbf{F}_b + \mathbf{F}_p + \mathbf{F}_\mu. \quad (11.19)$$

To exactly recover the macroscopic momentum equation in a velocity-based formulation, Zu and He [258] introduced two additional body forces. The first is related to pressure, \mathbf{F}_p ,

$$\mathbf{F}_p = -\bar{p}c_s^2\nabla\rho, \quad (11.20)$$

while the second describes the viscous stress, \mathbf{F}_μ , which can be recovered locally through the LBM,

$$F_{\mu,i}^{CM} = -\frac{\nu}{c_s^2\delta t} \left[\sum_{\beta} e_{\beta i} e_{\beta j} \times \sum_{\alpha} (\mathbb{M}^{-1}\mathbb{N}^{-1}\mathbb{S})_{\beta\alpha} (\kappa_{\alpha} - \kappa_{\alpha}^{eq}) \right] \frac{\partial\rho}{\partial x_j}. \quad (11.21)$$

The equation for \mathbf{F}_μ is implicit, because the \mathbb{N} matrix depends on \mathbf{u} , which depends on \mathbf{F} . However, it has been found that there is no need to apply a sub-iteration routine to determine the velocity more precisely because it does not affect the results. Concluding, the order of calculations can be presented as in Diagram 11.1.

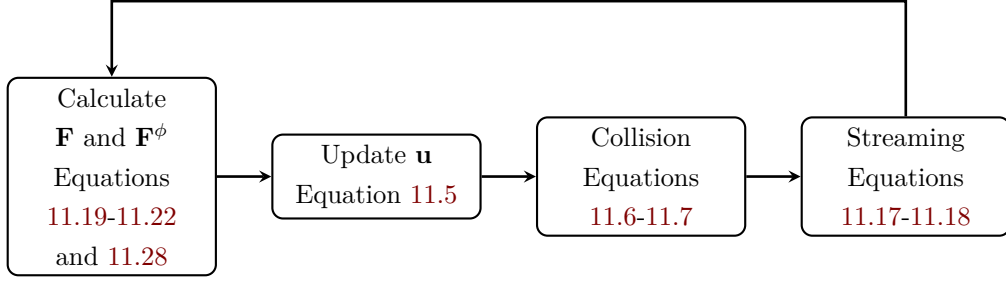


DIAGRAM 11.1: The order of operations performed within a normal lattice update, without the need for any sub-iteration routine.

The surface tension force and chemical potential follow the model presented in [230, 78],

$$\mathbf{F}_s = \mu_\phi \nabla \phi, \quad (11.22)$$

$$\mu_\phi = 4\beta(\phi - \phi_L)(\phi - \phi_H)(\phi - \phi_0) - \kappa \nabla^2 \phi. \quad (11.23)$$

The model coefficients, β and κ , are related to the surface tension, σ , and interface thickness, γ , as $\beta = 12\sigma/\gamma$ and $\kappa = 3\sigma\gamma/2$.

The fluid density at a particular point in space is determined from a linear interpolation between the light, ρ_L , and heavy, ρ_H , fluid densities,

$$\rho = \rho_L + \frac{\phi - \phi_L}{\phi_H - \phi_L}(\rho_H - \rho_L). \quad (11.24)$$

Due to this relation, the density gradient can be determined based on the gradient of the phase-field through,

$$\nabla \rho = \frac{\rho_H - \rho_L}{\phi_H - \phi_L} \nabla \phi. \quad (11.25)$$

Finally, the gradient of the phase-field and its Laplacian are calculated using isotropic central differences [259, 260],

$$\nabla \phi = \frac{c}{c_s^2 \delta x} \sum_i \mathbf{e}_i w_i \phi(\mathbf{x} + \mathbf{e}_i \delta t, t), \quad (11.26)$$

$$\nabla^2 \phi = \frac{2c^2}{c_s^2 (\delta x)^2} \sum_i w_i [\phi(\mathbf{x} + \mathbf{e}_i \delta t, t) - \phi(\mathbf{x}, t)]. \quad (11.27)$$

11.2.3.2 Forcing term for the phase-field

Discretization of the forcing term in Equation 11.3 is given in lattice units as,

$$\mathbf{F}^\phi = c_s^2 \frac{[1 - 4(\phi - \phi_0)^2]}{\gamma} \frac{\nabla \phi}{|\nabla \phi|} \delta t. \quad (11.28)$$

The force, \mathbf{F}^ϕ , acts to counteract the diffusion of the phase-field and drives it to reach a predefined interface profile in the equilibrium state. In the current model, the step function is approximated by a hyperbolic tangent. A derivation and detailed analysis of the forcing term can be found in [229, 256].

11.3 Model verification and validation

In this section, the model is verified and tested against a series of benchmark cases before being used to investigate the effect of flowing fluid on a planar Taylor bubble.

11.3.1 Two phase Poiseuille flow

The layered, two phase Poiseuille flow is a classical benchmark problem to assess the ability of a multiphase model to accurately simulate binary fluids with a density and or viscosity contrast. For this system, the Navier-Stokes equations can be simplified to,

$$0 = -\frac{dp}{dx} + \frac{d}{dy} \left(\mu \frac{du_x}{dy} \right) + \rho G_x. \quad (11.29)$$

By omitting the pressure term and using only a gravity force to drive the flow, the analytical solution becomes [261],

$$u(y) = \begin{cases} \frac{G_x h^2}{2\mu_T} \left[-\rho_T \frac{y^2}{h^2} - \frac{y}{h} \left(\frac{\mu_H \rho_L - \mu_L \rho_H}{\mu_H + \mu_L} \right) + \mu_T \frac{\rho_H + \rho_L}{\mu_H + \mu_L} \right] & \text{for } y \in [0, h] \\ \frac{G_x h^2}{2\mu_L} \left[-\rho_L \frac{y^2}{h^2} - \frac{y}{h} \left(\frac{\mu_H \rho_L - \mu_L \rho_H}{\mu_H + \mu_L} \right) + \mu_L \frac{\rho_H + \rho_L}{\mu_H + \mu_L} \right] & \text{for } y \in [-h, 0). \end{cases} \quad (11.30)$$

The velocity at the interface can be found as,

$$u_c = \frac{G_x (\mu_H + \mu_L) h^2}{2(\rho_H + \rho_L)}. \quad (11.31)$$

It is noted that the solution formulated in the work of Liang et al. et al. [262] was simplified by assuming no variation in density, $\rho_H = \rho_L = 1$, and as a result, is invalid for flow with a density contrast.

As the phase-field method belongs to the class of diffusive interface models, one needs to determine how the fluid properties vary in this region, as well as decide on appropriate values for the interface width and mobility. This is not the main topic of the current work, but here a number of alternative methods are introduced and tested for completeness. Firstly, the difference in behaviour for a Poiseuille flow is analysed using a diffuse and sharp change in fluid properties. For the diffuse case, the fluid viscosity and density are calculated using linear interpolation from the phase-field, while a step function is used in case of the sharp interface approach. Following [263], the step function acts as a simple switch between the viscosity of the different fluids, once the phase-field reaches a predefined value,

$$\begin{cases} \tau = \tau_L & \text{for } \phi < \phi_{avg} \\ \tau = \tau_H & \text{for } \phi \geq \phi_{avg} \end{cases} \quad \text{where } \phi_{avg} = (\phi_H + \phi_L)/2. \quad (11.32)$$

The interpolation can be realized using kinematic or dynamic viscosity. For simplicity, there is no density contrast between fluids in this benchmark, thus both schemes coincide.

Figure 11.2 shows the effect of the diffuse interface in a multiphase flow exhibiting viscosity contrast, where the domain size ($D/2 = h = 50$ [lu] - distance from the midline to the walls) is only an order of magnitude larger than the interface thickness ($\gamma = 5$ [lu]). Equation 11.29 is also solved using the finite difference (FD) method, where the density and dynamic viscosity profiles are [230],

$$\rho(y) = \frac{1}{2} \left[\rho_H + \rho_L - (\rho_H - \rho_L) \tanh \left(\frac{2y - D}{\gamma} \right) \right] \quad (11.33)$$

$$\mu(y) = \frac{1}{2} \left[\mu_H + \mu_L - (\mu_H - \mu_L) \tanh \left(\frac{2y - D}{\gamma} \right) \right]. \quad (11.34)$$

The results of the CLBM are observed to align with the expected diffuse and sharp interface results. It is noted here that the sharp interface implementation is impractical for flows with a density contrast as numerical instabilities can result in the calculation of the gradient and Laplacian of the phase-field.

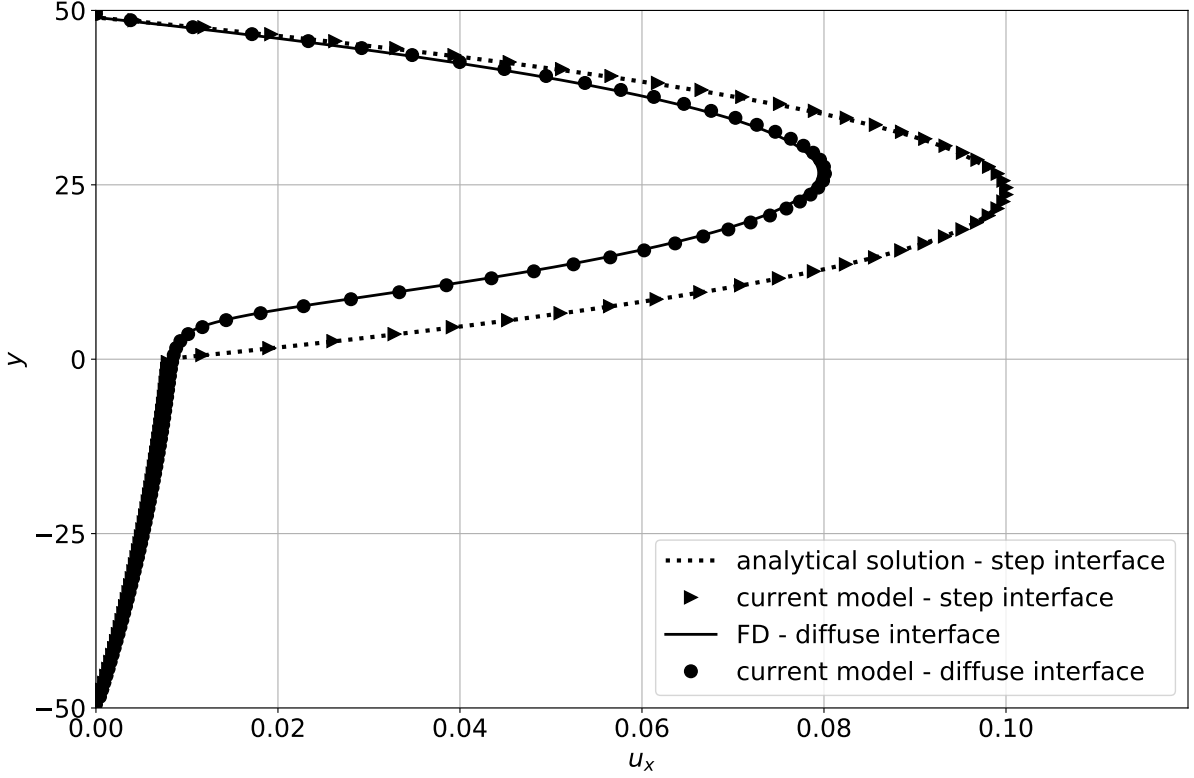


FIGURE 11.2: Effect of the interface diffusivity on the velocity profile in a two phase Poiseuille flow with $\rho_H = \rho_L = 1$, $\nu_H = 1$, $\nu_L = 100$, $h = 50$, $u_c = 0.0076$, and $\gamma = 5$.

11.3.2 Interpolation of the relaxation rate in the diffuse interface

Fakhari et al. [230] showed that the accuracy of results as well as the model stability was affected by the interpolation scheme used to determine the relaxation rate within the diffuse interface. It was shown that the most accurate method was to interpolate the dynamic viscosity of the fluid and use this to determine the relaxation parameter. However, a linear interpolation of the relaxation parameter was found to provide better stability properties. Here, this is investigated through an analysis of the spurious currents generated for each of these cases.

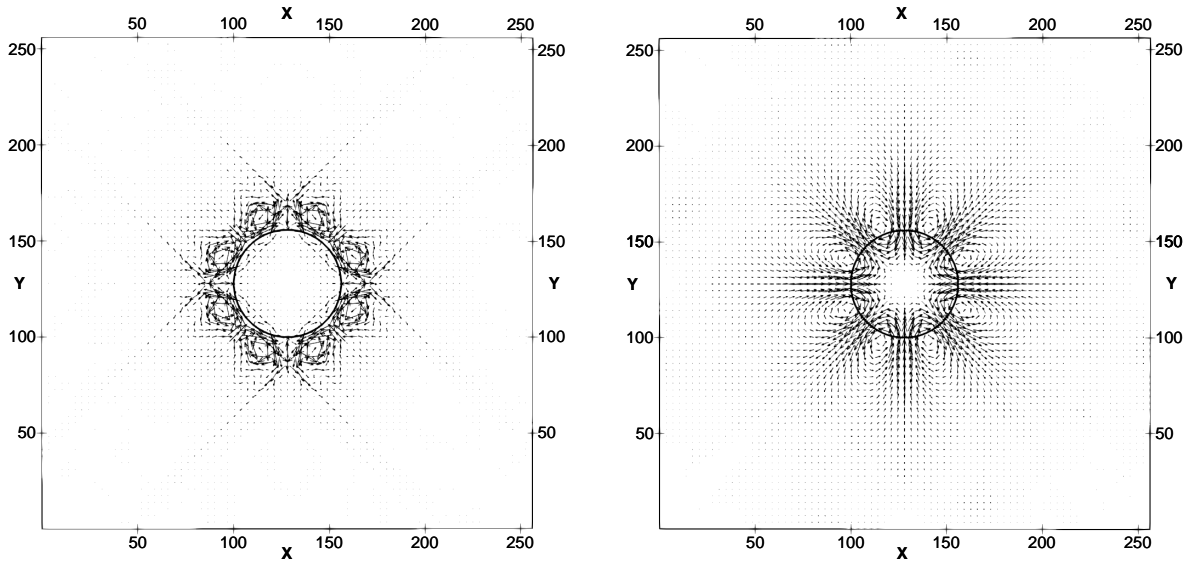
The first scheme interpolates the dynamic viscosity and then uses it to update the relaxation rate,

$$\begin{aligned}\mu &= \mu_L + \frac{\phi - \phi_L}{\phi_H - \phi_L}(\mu_H - \mu_L), \\ \tau &= \frac{\mu}{\rho c_s^2}.\end{aligned}\tag{11.35}$$

The second approach assumes that linear interpolation of the relaxation rate, τ , is directly proportional to the kinematic viscosity, ν ,

$$\tau = \tau_L + \frac{\phi - \phi_L}{\phi_H - \phi_L}(\tau_H - \tau_L).\tag{11.36}$$

It is hypothesized that the steeper gradients generated in the relaxation rate profile when interpolating the dynamic viscosity will result in an increase in spurious currents about the interface. To test this, a droplet of radius, $r = 56$ [lu], was initialized in a domain of size, 256×256 [lu]. The properties of the fluids and the interface parameters are given by $\rho_H = 10$, $\rho_L = 1$, $\nu_L = \nu_H = 1/6$, $\gamma = 5$, $M = 1/6$, and $\sigma = 10^{-4}$ for which the droplet is simulated for 10^6 iterations.



(A) Magnified by $1 \cdot 10^6$

(B) Magnified by $3 \cdot 10^8$

FIGURE 11.3: Comparison of the spurious currents when the interpolation of the relaxation rate is realized by Equation 11.35 (left) and Equation 11.36 (right).

The vector plot and the magnitude of spurious currents across the domain are presented in Figure 11.3 and 11.4, respectively. It is clearly visible that Equation 11.36 generates a spurious velocity distribution that is two orders of magnitude smaller than that produced by Equation 11.35. Therefore, it is believed that the more rapidly changing viscosity provided by Equation 11.35 across the interface improves the accuracy of the solution, but the corresponding increase in spurious currents degrades the model stability.

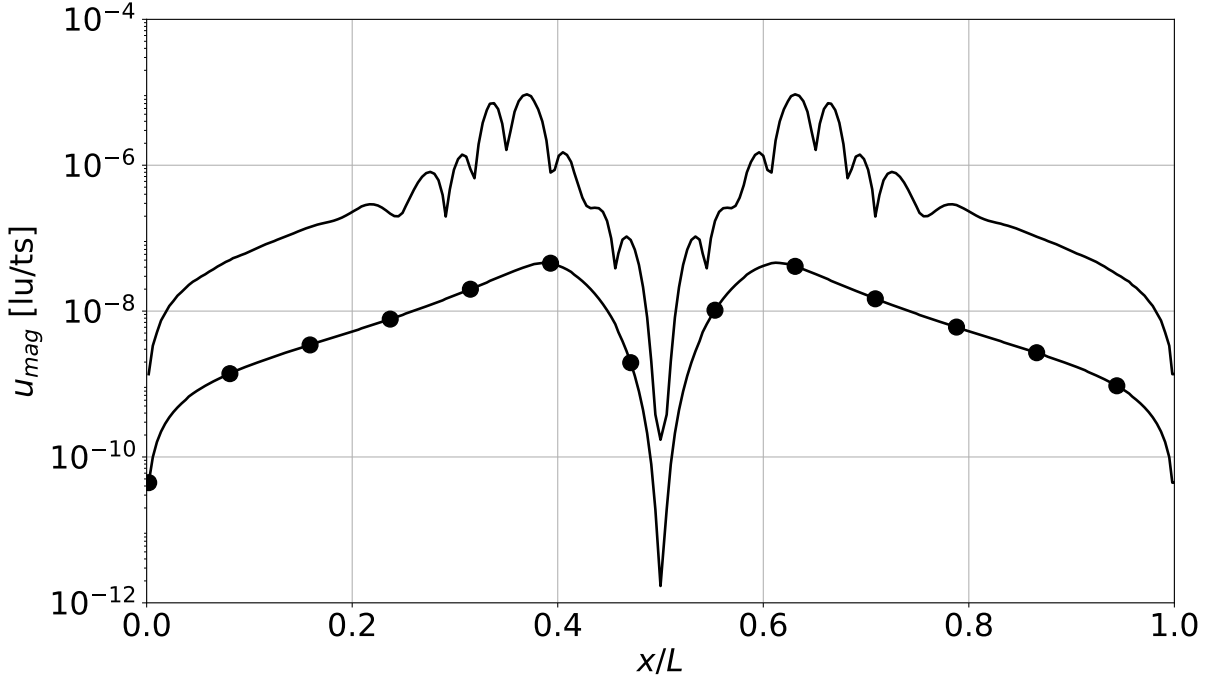


FIGURE 11.4: Cross-section of spurious currents at $y = 128$ [lu] for the static droplet presented in Figure 11.3. The difference due to relaxation rate interpolation by Equation 11.35 (solid line) and Equation 11.36 (solid line with markers) is evident.

11.3.3 Effect of the moving reference frame

In this subsection, the Galilean invariance of the MRT-LBM and CLBM is assessed and compared. The model of Fakhari et al. [230] is used for reference, in which an MRT collision kernel was employed in conjunction with truncated, discrete equilibria. For completeness, an explicit formulation of both raw and central moments of these equilibria is provided in 11.5.

To construct a suitable benchmark, a droplet of radius, $r = 56$ [lu], is placed into a moving reference frame. The domain is a periodic square of length, $L = 256$ [lu], and is initialized with a uniform velocity field, $\overline{u_x}$. The center of mass, CM_x , of the bubble is tracked through the simulation and compared to the expected theoretical location at various time increments. The fluid and model parameters defining the flow configuration are, $\rho_L = \rho_H = 1$, $\gamma = 5$, $M = 1/6$, and $\sigma = 10^{-4}$ and the simulation is run for 10^6 iterations.

To understand the effect under various conditions, the fluid viscosity and the initialized velocities were varied creating four total configurations, i.e. the permutations of $\nu_L = \nu_H \in \{0.01, 0.1\}$ and $\overline{u_x} \in \{0.01, 0.1\}$. It is noted here that the upper velocity range results in a Mach number, $Ma = \overline{u_x}/c_s$, of approximately 0.173. This value is higher than what would be recommended in a standard LBM simulation, but here it is chosen to highlight the capability of the CLBM.

It can be observed in Figure 11.5, that for the low velocity cases, both methods perform reasonably well with the droplet velocity well maintained. However, for a high Mach number, the Galilean invariance of the MRT scheme [230] can be seen to degrade, with the droplet center of mass diverging from theoretical expectations. In comparison, performing the relaxation in the moving frame of reference allows the CLBM to maintain invariance even with high lattice velocities. A similar discrepancy, expressed as a Euclidean norm of the droplet's kinetic energy, has been observed by Dzikowski et al. [264], who used the Kupershtokh [71] scheme with an MRT collision operator.

Figure 11.6 presents a comparison of the velocity field across the square domain for a stationary and moving frame of reference. Here, it is evident that the external velocity field has a noticeable influence when resolved with the MRT scheme. The reduction in droplet velocity is observed with the MRT model in the moving frame, and this is reflected in the velocity profile. The inconsistency here may be low relative to expected velocities if an external force was placed on the system, but for certain configurations, knowledge of this discrepancy could be essential.

The final test conducted here is completed to assess whether the minor deviations apparent in the MRT solutions are exaggerated in the presence of a density contrast. In order to assess this, the standard deviation of the x-velocity component, u_x , in comparison to the initial velocity is defined as,

$$\sigma_{u_x} = \sqrt{\frac{1}{N} \sum_i^N (u_{x_i} - \overline{u_x})^2}, \quad (11.37)$$

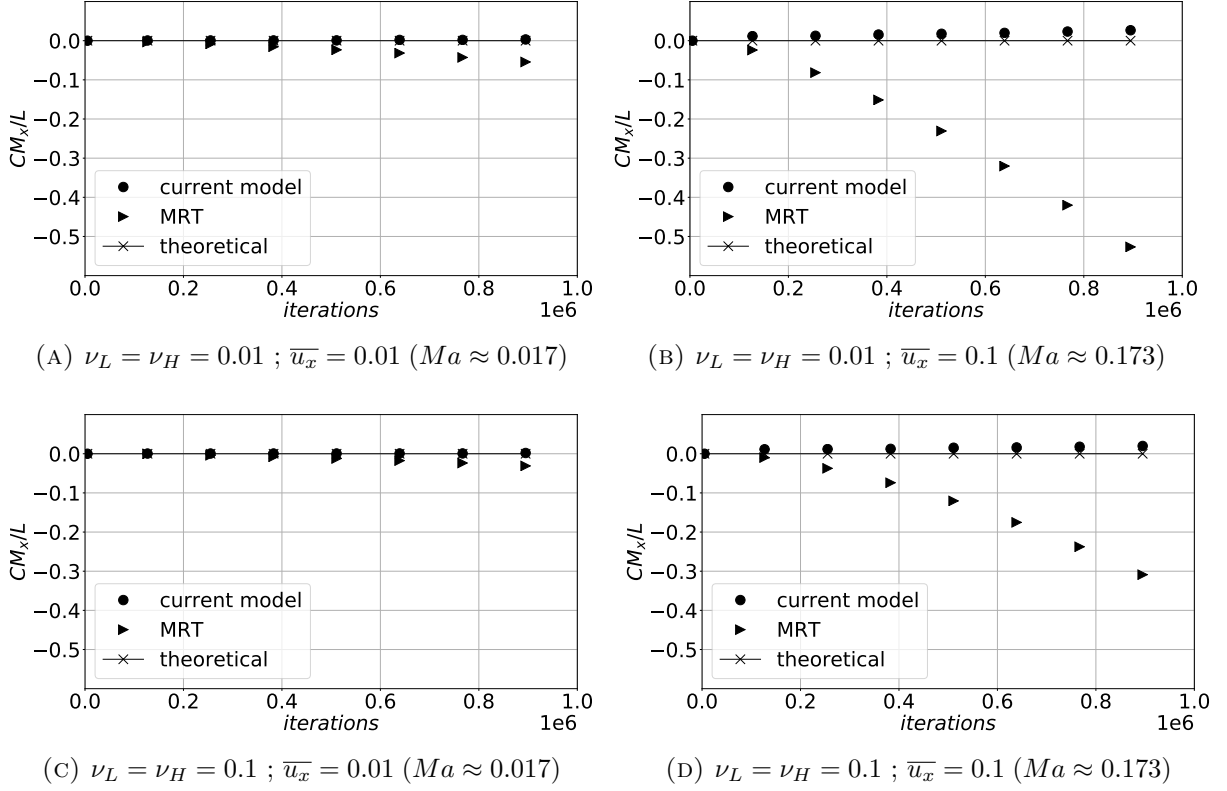


FIGURE 11.5: Lag of the center of the mass of the droplet due to viscosity and the initial velocity field.

where the summation is over the x-coordinates along the center line of the domain. Figure 11.7 shows the resultant error metric for a density ratio of 10 and 100 in a moving reference frame.

It is noted that when the density contrast between the droplet and the external flow is increased, a *checkerboard* pattern artefact is more likely to emerge in the velocity field. The onset of this discrepancy is observed in Figure 11.7b at approximately 1×10^5 iterations for the MRT scheme and then shortly after for the CLBM. The standard deviation of the x-velocity then reaches a plateau after approximately 2×10^5 iterations, yielding an unphysical solution. As the flow is symmetric, the accumulation of numerical error progresses without disturbance or cancellation, and as a result, the two lines in Figure 11.7a would ultimately converge to a plateau as well. The appearance of the *checkerboard* artefact is a known issue for isotropic central difference schemes (Equation 11.26 and 11.27), caused by the accumulation of numerical errors. These are likely to cancel out in a system with some degree of asymmetry in the flow profile. For this particular flow case, the onset of this detrimental effect was delayed further when using the CLBM in

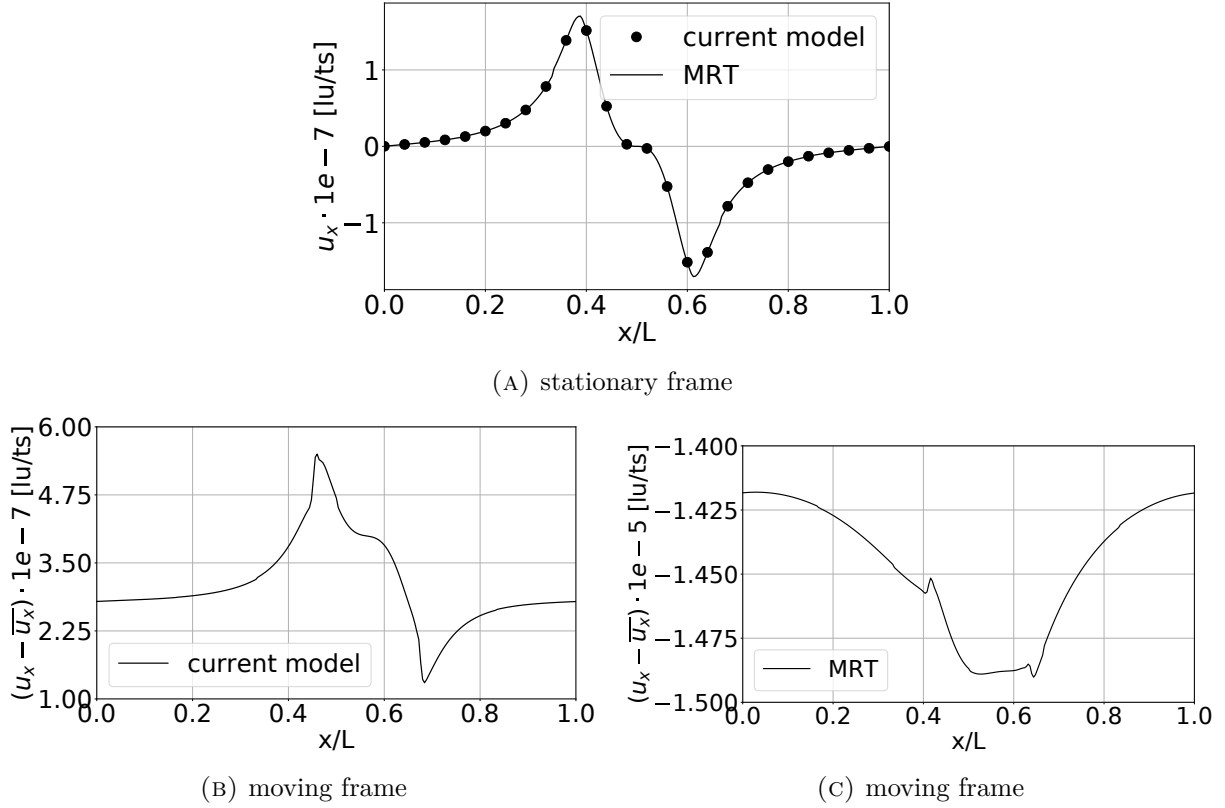


FIGURE 11.6: The effect of the initial velocity field on the spurious currents, u_x . Matched densities ($\rho_H = \rho_L = 1$) and matched viscosities ($\nu_H = \nu_L = 0.1$) were used with a background velocity of $\bar{u}_x = 0.01$, which resulted in $Ma \approx 0.017$.

comparison to the MRT scheme.

To further assess stability properties and Galilean invariance, the oscillation of an ovoid shaped droplet was considered. Figure 11.8 compares the frequency of pulsation between both schemes. In terms of frequency, no significant differences were found for low Ma (<0.1) flows. To repeat the experiment for $Ma \approx 0.17$ ($\bar{u} = 0.1$), the viscosity was increased to keep the MRT model stable. Again, there were no differences in the droplet's pulsation. On the other hand, in the study of shear wave decay performed by Fei et al. [67], the observed viscosity in the single relaxation time (SRT) and discrete CLBM schemes decreased for higher Ma number flows.

It was observed that to reconstruct the forces independent of the reference frame, conducting the collision operations in central moment space outperforms the MRT scheme. Moreover, when using two distribution functions to model a variation of the advection-diffusion equation, the equilibrium of the *advected* distribution function does not depend

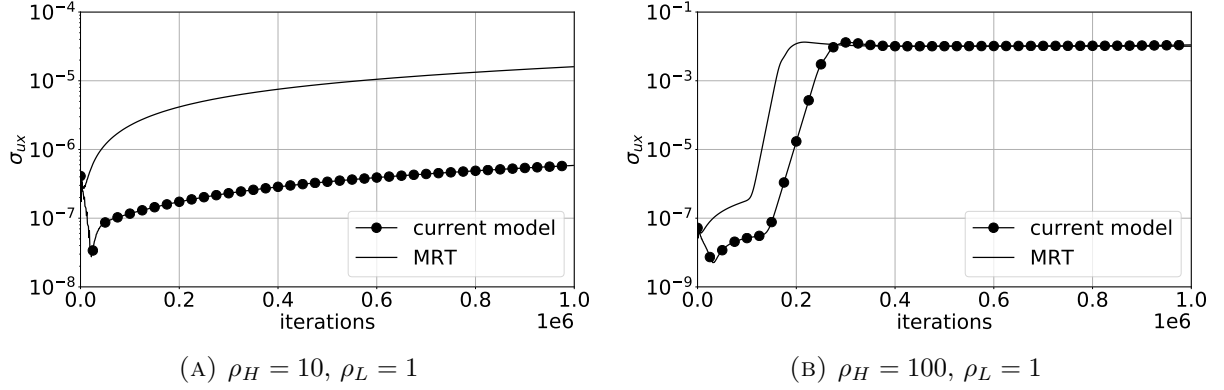


FIGURE 11.7: The effect of density ratio on the standard deviation of the x-velocity component in a moving reference frame. Matched viscosities ($\nu_H = \nu_L = 0.01$) were used with a background velocity of $\overline{u_x} = 0.01$, which resulted in $Ma \approx 0.017$.

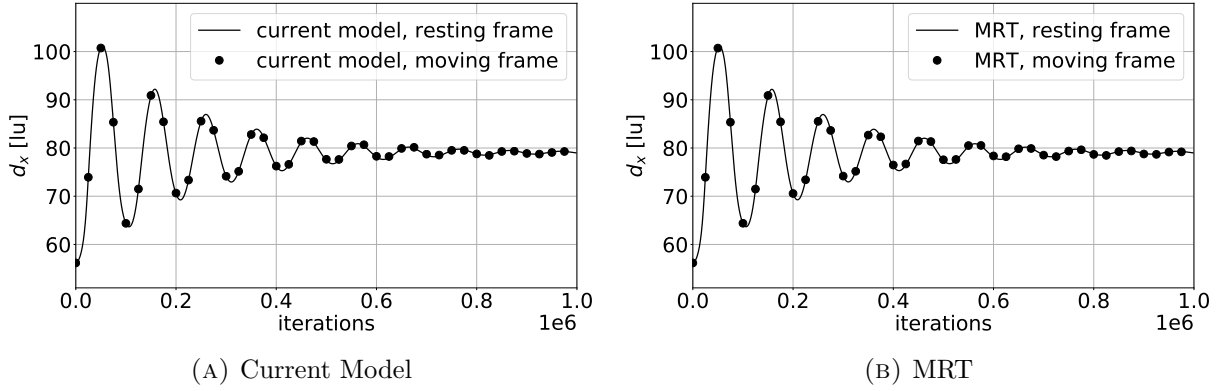


FIGURE 11.8: Comparison of the pulsation frequency of an ovoid-shaped droplet. Match densities ($\rho_H = \rho_L = 1$) and matched viscosities ($\nu_H = \nu_L = 0.001$) were used with a background velocity of $\overline{u_x} = 0.01$, which resulted in $Ma \approx 0.017$.

on the external velocity field as is the case for the discrete equilibrium distribution function (see Equation 11.56) used in either the SRT or MRT collision models. Since the moments of the equilibrium distribution function in CLBM are obtained from integration of the continuous Maxwell-Boltzmann distribution, they do not suffer from discretization errors. The continuous and discrete transformations differ by spurious $\mathcal{O}(\mathbf{u}^3)$ terms (see 11.5 for details). It has been shown in [66, 67, 69] that these terms are responsible for violation of Galilean invariance in the flow. More discussion of these issues and a Chapman-Enskog analysis can be found in [65, 26, 67]. The Chapman-Enskog analysis of an advection-diffusion equation using CLBM is given in [68], while the *phase-field forcing term*, Equation 11.28, has been already analyzed in [229, 256].

11.3.4 Planar Taylor bubble analysis

Having presented the implementation and benchmarking of the CLBM, the model was then used to extend the work of Fakhari et al. [230] on the simulation of planar Taylor bubbles. As per the work of Ha-Ngoc and Fabre [235], it is expected that a relation exists between the rise velocity of an elongated Taylor bubble and the Eötvös number,

$$Eo = \frac{(\rho_H - \rho_L)g_x D^2}{\sigma}, \quad (11.38)$$

when in an inertial regime. Ha-Ngoc and Fabre [235] define the inertial regime based on the Reynolds number of the Taylor bubble,

$$Re = \frac{U_{TB} D}{\nu_H} > 100, \quad (11.39)$$

where U_{TB} is the measured macroscopic rise velocity in a stationary fluid, D is the width of the channel and ν_H is the kinematic viscosity of the bulk fluid. Here, results are generally presented using a dimensionless velocity, namely, the Froude number,

$$Fr = \frac{U_{TB}}{\sqrt{g_x D}}. \quad (11.40)$$

This section aims to validate the CLBM over a large parameter space, highlighting its applicability to physically-relevant phenomena. Additionally, cases that do not meet the Re criterion used by Ha-Ngoc and Fabre [235] were investigated to analyse the resultant behaviour of the elongated planar bubble.

11.3.4.1 Problem definition

Following on from the work of Fakhari et al. [230], the computational domain is constructed according to Figure 11.9. Here, the length of the channel is 20 times the width, D , and the low density gas, ρ_L , μ_L , is initialized as a rectangular section with a semi-circular front inside the high density fluid, ρ_H , μ_H , for various Eo .

With this configuration, a set of relevant dimensionless parameters to generalize the flow configuration can be defined. To start with, a reference time scale is specified as, $t_0 = \sqrt{D/g_x}$, such that the dimensionless time is given by, $t^* = t/t_0$. The simulations presented here were conducted with a characteristic channel width, $D = 128$ [lu]. Given a specified geometry, the reference time scale defines the gravitational acceleration applied to the flow domain. Simulations were run for $20t_0$ iterations, with the measured rise

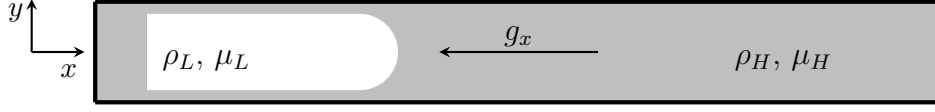


FIGURE 11.9: Domain schematic of the slug flow tests for the Taylor bubble rise, modified from [230]. The fluid domain size is $20D \times D$, and the initial bubble size has a rectangular section, $3D \times 3D/4$ with a semi-circular front of diameter $3D/4$.

velocity taken as an average of the bubble velocity over the final t_0 iterations. The desired Eu gives the lattice surface tension.

To ensure that the flow is in an inertial regime, a reference rise velocity is predicted, U_{ref} , from the work of Ha-Ngoc and Fabre [235] and a Reynolds number is defined,

$$Re_{ref} = \frac{U_{ref} D}{\nu_H} = 200. \quad (11.41)$$

Therefore, even if the measured rise velocity, U_{TB} , varies from the previous work, it is still expected that the system will be in an inertial regime. Another useful parameter when looking at multiphase flow is the Morton number,

$$Mo = \frac{g_x \mu_H^4 (\rho_H - \rho_L)}{\rho_H^2 \sigma^3}, \quad (11.42)$$

which along with Eu is often used to describe expected bubble topologies. To close the system of parameters, the density and dynamic viscosity ratios are set at 1000 and 100, respectively.

11.3.4.2 Results

Figure 11.10 indicates the measured rise velocity of the planar Taylor bubbles for various Eu and t_0 numbers and reference times. In this simulation, a higher reference time can be considered analogous to a smaller physical time-step between each iteration. It is observed from this figure, that a reference time of $t_0 = 16000$ was insufficient to capture the expected behaviour of the bubble. However, increasing the temporal resolution to $t_0 = 24000$ and $t_0 = 32000$, it was evident that the results agreed well with the work of Ha-Ngoc and Fabre [235]. This is particularly clear for $Eu < 100$, where the predicted rise velocity is a function of the surface tension prior to plateauing at $Fr \approx 0.225$.

The measured rise velocities for higher Eu can be seen to deviate slightly from the results of Ha-Ngoc and Fabre [235]. The loss in accuracy for these cases is believed to be a

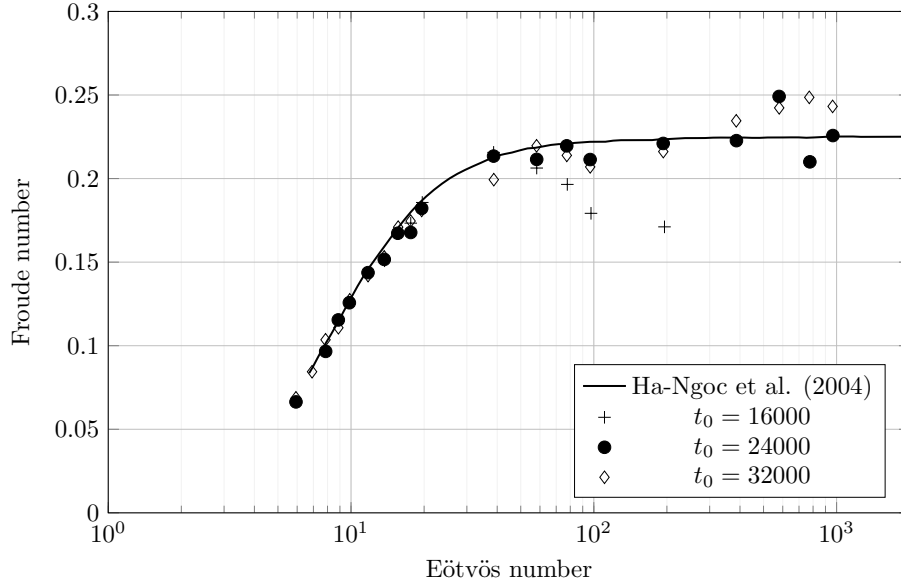


FIGURE 11.10: Dimensionless rise velocity (Fr), measured as the average velocity over the final t_0 iterations, as a function of Eo for various time resolutions.

result of the wake behaviour of the Taylor bubble. Figure 11.11 shows the Taylor bubble and wake region for various Eo . Here, it is evident that for a higher Eo , a continuous system of bubble detachment, break-up, coalescence and reattachment in the wake region is formed. The unsteadiness of this behaviour may have contributed to the minor variation from the predicted macroscopic rise velocity in this range.

In order to gain further insight into the behaviour of the Taylor bubble wake, simulations were conducted at various Mo . Figure 11.12 indicates the shape profiles of the Taylor bubble, with an initial symmetry observed prior to the wake region progressing to a more chaotic structure. As the simulations approach the inertial regime (decreasing Mo), it is evident that vortices in the continuous fluid shed from the tail of the Taylor bubble and strongly influence the behaviour of smaller bubbles that have detached into the wake. In Figure 11.12, it is clear that there is a variation in rise velocity for the different Morton numbers. This demonstrates that while not in an inertial regime, the rise velocity of a Taylor bubble with specified density and viscosity ratios, is at the least, a function of both the Eo and Mo (i.e. $Fr = Fr(Eo, Mo)$).

With relatively low lattice velocities, there was little difference observed between the MRT scheme and that of central moments displayed here. This is due to the fact that the shift matrix, \mathbb{N} , in 3.5 approaches the identity matrix for low velocities. However,

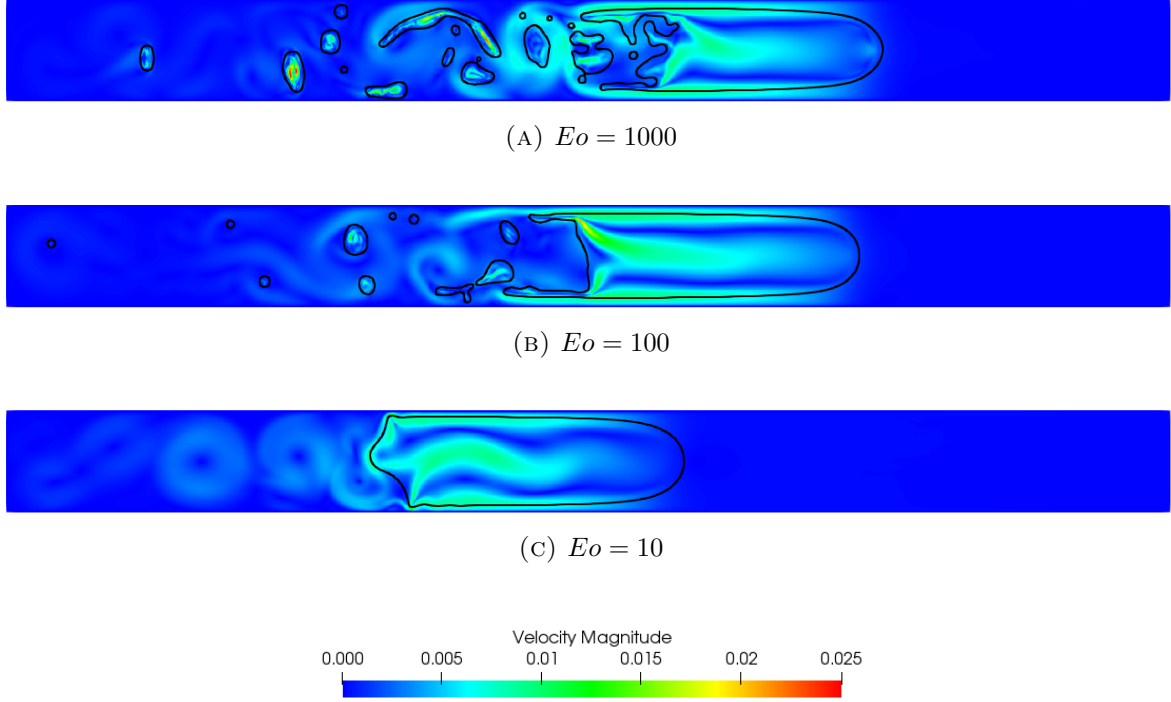


FIGURE 11.11: The shape profile of the Taylor bubbles at $t^* = 20$ for (a) $Eo = 1000$, (b) $Eo = 100$ and, (c) $Eo = 10$ displayed on a color (online) map of the lattice velocity.

from these results, one can conclude that the model is stable and accurate over a large parameter space (multiple orders of magnitude for both Eo and Mo) while maintaining a large viscosity and density contrast. To highlight the capability of the model and take advantage of the moving reference frame results in Sec. 11.3.3, the following section shifts the simulation into a reference frame moving with the Taylor bubble, allowing the impact of flowing liquid to be assessed.

11.3.5 Planar Taylor bubble in a moving reference frame

In order to transform to the bubble's frame of reference, Dirichlet velocity conditions were specified on all boundaries according to the work of Zu and He [258]. Implementing these conditions allows the dynamics of the Taylor bubble to be analyzed in both co- and counter-current liquid flows within the bubble's reference frame. In a flowing liquid, the complex interaction between liquid motion and buoyancy is observed and can be used to

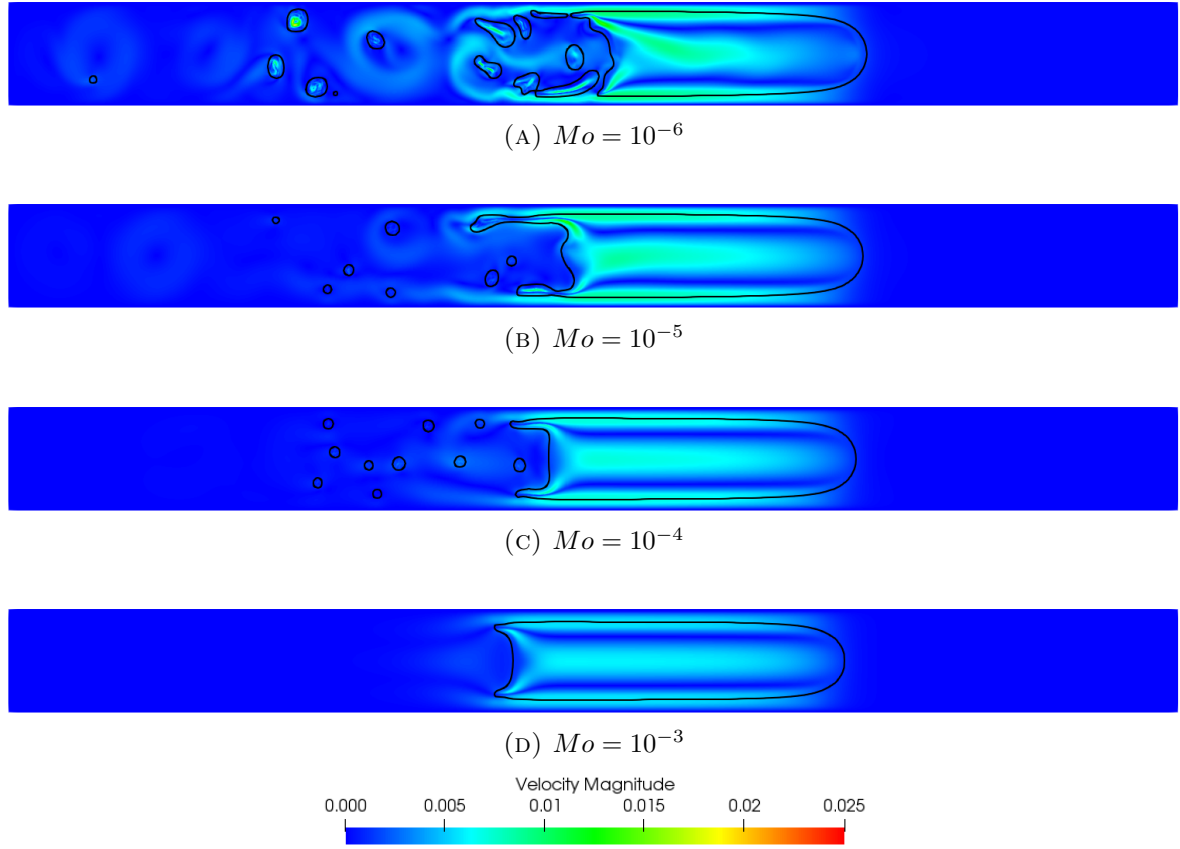


FIGURE 11.12: The shape profile and wake behaviour of the Taylor bubbles at $t^* = 20$ for $Eo = 100$ and (a) $Mo = 10^{-6}$, (b) $Mo = 10^{-5}$, (c) $Mo = 10^{-4}$ and, (d) $Mo = 10^{-3}$ displayed on a color (online) map of the lattice velocity.

predict the velocity of Taylor bubbles [265],

$$U_{TB} = C_0 U_\infty + U_{ref}, \quad (11.43)$$

$$Fr_{TB} = C_0 Fr_\infty + Fr_{ref}, \quad (11.44)$$

where U_{TB} is the bubble's measured velocity, U_∞ is the mean dimensional velocity of the far-field fluid, U_{ref} is the velocity of a Taylor bubble in stagnant fluid and C_0 is a dimensionless variable often empirically tuned with experimental findings. The Fr and respective subscripts correspond to the dimensionless forms of the relevant velocities.

11.3.5.1 Problem definition

With the motion of the fluid, another dimensionless number is required in order to characterize the system dynamics. Here the Froude number of the bulk liquid previously

introduced is defined as,

$$Fr_\infty = \frac{U_\infty}{\sqrt{g_x D}}. \quad (11.45)$$

In line with the stationary reference frame, the characteristic channel width at, $D = 128$ [lu], and domain size of, $20D \times D$, is specified. The bubble is initialized in the center of the domain with the bubble front at, $x = 10D$. The density and dynamic viscosity ratios of the system are 1000 and 100, respectively. The system definition is then completed by specifying $t^* = 24000$, $Eo = 100$ and $Mo = 10^{-3}$.

To simulate the incoming fluid flow, a Poiseuille flow profile (fully developed channel flow) is assumed for the inlet and outlet of the domain. In the moving reference frame, this is given by

$$U_{in/out}(y) = U_{TB} + 6U_\infty \frac{(yD - y^2)}{D^2}. \quad (11.46)$$

With this definition, a negative value of liquid velocity corresponds to counter-current flow while a positive value indicates a co-current configuration. The velocity of the top and bottom walls is prescribed based on the expected rise velocity of the Taylor bubble through the flowing fluid.

11.3.5.2 Results

Table 11.1 shows the results obtained for the rise velocity of the Taylor bubble in both co- and counter-current flow configurations. Here, one observes a relatively constant value for the empirical coefficient, C_0 , which agrees with common assumptions typically taken in the literature. To further validate the co-current dynamics determined in the moving reference frame, the values of C_0 were compared with the previous work of Ha-Ngoc and Fabre [266]. Interestingly, the value obtained for this parameter held relatively constant for both liquid flow configurations. Figure 11.13 presents the results obtained in comparison

Fr_∞	-0.25	-0.20	-0.15	-0.10	-0.05	0.05	0.10	0.15	0.20	0.25
Fr_U	-0.1022	-0.0386	0.0233	0.0856	0.1470	0.2714	0.3338	0.3984	0.4656	0.5294
C_0	1.2429	1.2355	1.2350	1.2297	1.2298	1.2574	1.2526	1.2656	1.2855	1.2836

TABLE 11.1: Resultant Taylor bubble rise velocity and empirical coefficient value in both co- and counter-current flowing configurations.

to Ha-Ngoc and Fabre [266] as well as the independence of C_0 with respect to the liquid

Froude number, Fr_∞ , and flow direction. It is noted here that future work will look to incorporate a broader range of pipe configurations (inclination angle, internal obstructions, etc.) to build a database of rise velocities for which correlations to dimensionless flow parameters can be made. This will enable otherwise difficult experiments to be conducted numerically to determine suitable models describing the rise velocity of Taylor bubbles. Such data are useful, for example, in predicting pressure drops through piping systems where simplified models are required to describe phase interactions due to the large scale of industrial systems.

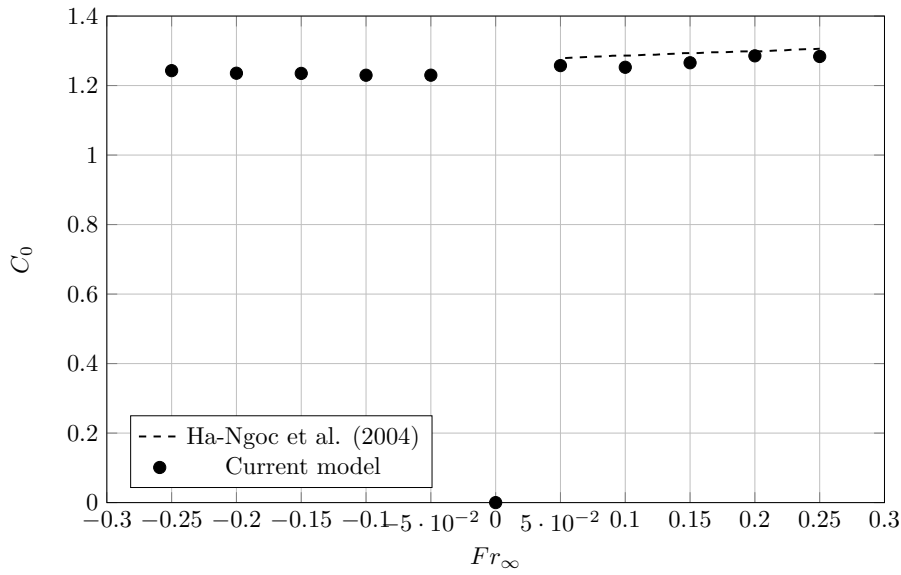


FIGURE 11.13: Comparison of the value of C_0 for various liquid Froude numbers, F_∞ , and the work of Ha-Ngoc and Fabre [266].

11.3.6 Computational Efficiency

Both the parallel scalability of the solver and the performance of the reference phase-field model have been previously investigated in [6] and [230], respectively. Although the results of computational efficiency may vary depending on the problem size as well as the architecture of the hardware, here, a set of identical simulations were conducted with an SRT, MRT [230] and CLBM collision kernel. This aims to assess the cost of the enhanced relaxation scheme and compare commonly used kernels to determine if their computational cost affects the usability of the model. All of the components of the solver and the simulation domain are held constant, with only the collision kernel varied. Each kernel was used to run five simulations for 5×10^6 iterations (~ 1 hour), on a 256×256

lattice. An Nvidia Tesla K40 XL GPU was used for the computations. From here, the run time of the simulations was averaged to determine the computational cost of the different relaxations. Surprisingly, the MRT collision kernel was found to be the most expensive of the three. The SRT scheme was the most efficient being on average approximately 14% faster than the MRT kernel, and approximately 2% quicker than the presented CLBM. Although the introduction of the central moments may appear to increase the amount of computation required with an additional transformation from raw moments, no significant overhead in computational time was observed. This is a result of the explicit formulation for the force and equilibrium distributions (see Equations 11.13-11.16) available in the CLBM, which were not employed in the reference MRT kernel.

11.4 Remarks on orthogonalization of moments and relaxation

Multiple-relaxation-time collision is frequently realized with the use of an orthogonalized moment transformation matrix, especially for the hydrodynamic distributions. This means that the matrix \mathbb{M} used for transformation from the velocity distribution space to the moment space is an orthogonal matrix (but not orthonormal). Another feature, typical for such scheme, is to have the sum of the raw second order moments ($k_{20} + k_{02}$ in 2D) as one of the vectors used early in the Gram-Schmidt orthogonalization procedure. This results in separation of the moments responsible for the pressure/bulk behaviour from the rest of the matrix. A commonly used orthogonalized matrix is [231],

$$\mathbb{M}_{\perp} = \begin{bmatrix} 1 & 1 & 1 & 1 & 1 & 1 & 1 & 1 & 1 \\ -4 & -1 & -1 & -1 & -1 & 2 & 2 & 2 & 2 \\ 4 & -2 & -2 & -2 & -2 & 1 & 1 & 1 & 1 \\ 0 & 1 & 0 & -1 & 0 & 1 & -1 & -1 & 1 \\ 0 & -2 & 0 & 2 & 0 & 1 & -1 & -1 & 1 \\ 0 & 0 & 1 & 0 & -1 & 1 & 1 & -1 & -1 \\ 0 & 0 & -2 & 0 & 2 & 1 & 1 & -1 & -1 \\ 0 & 1 & -1 & 1 & -1 & 0 & 0 & 0 & 0 \\ 0 & 0 & 0 & 0 & 0 & 1 & -1 & 1 & -1 \end{bmatrix} \quad (11.47)$$

The corresponding relaxation matrix for the orthogonalized moments may be [230],

$$\mathbb{S}_\perp = \text{diag}([1, 1, 1, 1, 1, 1, 1, s_\nu, s_\nu]). \quad (11.48)$$

Only the last two terms of the relaxation matrix corresponds to diagonal and off-diagonal components of the stress tensor, which are a non-conserved quantities (i.e. $k_{20} - k_{02}$ and k_{11}). For such matrices, the MRT collision operator is

$$\Omega_{MRT} = -\mathbb{M}_\perp^{-1} \mathbb{S}_\perp \mathbb{M}_\perp (\mathbf{g} - \mathbf{g}^{eq}). \quad (11.49)$$

In the present work (see Chapter 11), the raw and central moments have not been explicitly orthogonalized. However, it can be shown that the choice of the relaxation matrix, \mathbb{S} , recovers the properties of the MRT collision presented in Equation 11.49 (used in [232]).

To impose the equivalence of the two relaxation methods for any \mathbf{f} , the following condition has to be fulfilled:

$$-\mathbb{M}^{-1} \mathbb{S} \mathbb{M} (\mathbf{f} - \mathbf{f}^{eq}) = -\mathbb{M}_\perp^{-1} \mathbb{S}_\perp \mathbb{M}_\perp (\mathbf{f} - \mathbf{f}^{eq}). \quad (11.50)$$

Next, the relaxation matrix is obtained as $\mathbb{S} = \mathbb{M} \mathbb{M}_\perp^{-1} \mathbb{S}_\perp \mathbb{M}_\perp \mathbb{M}^{-1}$. This gives:

$$\mathbb{S} = \text{diag} \left([1, 1, 1], \begin{bmatrix} \frac{1+s_\nu}{2} & \frac{1-s_\nu}{2} \\ \frac{1-s_\nu}{2} & \frac{1+s_\nu}{2} \end{bmatrix}, [s_\nu, 1, 1, 1] \right), \quad (11.51)$$

which recovers Equation 11.8 and is equivalent to Equation 11.48 for $s_b = 1$.

The \mathbb{M}_\perp matrix has 60 non-zero elements, while there are only 49 such elements in \mathbb{M} , thus the numerical cost of the collision operator in the current model is reduced. The reduction is even more significant if one considers the inverse matrices.

11.5 Remarks on discretization of the distribution functions

In this section, the general discussion given in Section 3.4 will be extended to account for incompressible NS equations. It is interesting to observe, that performing the collision and forcing operations in the central moment space, not only improves the stability and

Galilean invariance, but also helps to reduce the discretization errors of both equilibrium distribution and force.

For hydrodynamics, a method to recover the incompressible Navier-Stokes equation from a velocity-based LBM was proposed by He and Luo [267], through a modification of the discrete equilibrium distribution function. Using the same idea for continuous distribution, the equilibrium distribution for hydrodynamics can be expressed as,

$$\Psi_{hydrodynamics}^{M-B, eq} = \underbrace{\Psi^{M-B, eq}(\Upsilon_{00} - 1, \boldsymbol{\xi}, 0)}_{\Psi_p^{M-B, eq}} + \underbrace{\Psi^{M-B, eq}(1, \boldsymbol{\xi}, \mathbf{u})}_{\Psi_u^{M-B, eq}}. \quad (11.52)$$

The central moments for the hydrodynamics are thus

$$\boldsymbol{\kappa}^{eq} = \begin{bmatrix} (\Upsilon_{00} - 1) & & & & & & & +1 \\ (\Upsilon_{00} - 1)(-u_x) & & & & & & & \\ (\Upsilon_{00} - 1)(-u_y) & & & & & & & \\ (\Upsilon_{00} - 1)(u_x^2 + c_s^2) & & & & & & +c_s^2 & \\ (\Upsilon_{00} - 1)(u_y^2 + c_s^2) & & & & & & +c_s^2 & \\ (\Upsilon_{00} - 1)u_x u_y & & & & & & & \\ (\Upsilon_{00} - 1)(-u_y)(c_s^2 + u_x^2) & & & & & & & \\ (\Upsilon_{00} - 1)(-u_x)(c_s^2 + u_y^2) & & & & & & & \\ (\Upsilon_{00} - 1)(u_x^2 u_y^2 + c_s^2(u_x^2 + u_y^2) + c_s^4) + c_s^4 & & & & & & & \end{bmatrix}. \quad (11.53)$$

The above central moments (Equations 3.22 and 11.53) are used in the present work without any truncation.

On the other hand, the discrete equilibria of hydrodynamic f_i^{eq} and phase field h_i^{eq} distributions used in [230] are

$$f_i^{eq} = w_i(\Upsilon_{00} - 1) + \Gamma_i, \quad (11.54)$$

$$h_i^{eq} = \Upsilon_{00}^\phi \Gamma_i, \quad (11.55)$$

where Γ is a truncated Taylor series expansion of the Equation 2.17,

$$\Gamma_i = w_i \left[1 + \frac{\mathbf{e}_i \cdot \mathbf{u}}{c_s^2} + \frac{(\mathbf{e}_i \cdot \mathbf{u})^2}{2c_s^4} - \frac{\mathbf{u} \cdot \mathbf{u}}{2c_s^2} \right]. \quad (11.56)$$

It can be observed, that the both raw and central moments for h_i^{eq} and f_i^{eq} differ from the ones above by spurious velocity terms of order \mathbf{u}^3 (bolded),

$$\mathbf{\Upsilon}_{\text{discrete}}^{\phi,eq} = \begin{bmatrix} \Upsilon_{00}^{\phi} \\ \Upsilon_{00}^{\phi} u_x \\ \Upsilon_{00}^{\phi} u_y \\ \Upsilon_{00}^{\phi} (u_x^2 + c_s^2) \\ \Upsilon_{00}^{\phi} (u_y^2 + c_s^2) \\ \Upsilon_{00}^{\phi} u_x u_y \\ \Upsilon_{00}^{\phi} c_s^2 u_y & + \Upsilon_{00}^{\phi} \mathbf{u}_y \mathbf{u}_x^2 \\ \Upsilon_{00}^{\phi} c_s^2 u_x & + \Upsilon_{00}^{\phi} \mathbf{u}_x \mathbf{u}_y^2 \\ \Upsilon_{00}^{\phi} c_s^4 + \Upsilon_{00}^{\phi} c_s^2 (u_x^2 + u_y^2) & + \Upsilon_{00}^{\phi} \mathbf{u}_x^2 \mathbf{u}_y^2 \end{bmatrix}, \quad (11.57)$$

$$\mathbf{\Upsilon}_{\text{discrete}}^{eq} = \begin{bmatrix} \Upsilon_{00} \\ u_x \\ u_y \\ \Upsilon_{00} c_s^2 + u_x^2 \\ \Upsilon_{00} c_s^2 + u_y^2 \\ u_x u_y \\ u_y c_s^2 & + \mathbf{u}_y \mathbf{u}_x^2 \\ u_x c_s^2 & + \mathbf{u}_x \mathbf{u}_y^2 \\ \Upsilon_{00} c_s^4 + c_s^2 (u_x^2 + u_y^2) & + \mathbf{u}_x^2 \mathbf{u}_y^2 \end{bmatrix}, \quad (11.58)$$

$$\mathbf{\kappa}_{\text{discrete}}^{\phi,eq} = \begin{bmatrix} \Upsilon_{00}^{\phi} \\ 0 \\ 0 \\ c_s^2 \Upsilon_{00}^{\phi} \\ c_s^2 \Upsilon_{00}^{\phi} \\ 0 \\ 0 & -\mathbf{u}_x^2 \mathbf{u}_y \Upsilon_{00}^{\phi} \\ 0 & -\mathbf{u}_x \mathbf{u}_y^2 \Upsilon_{00}^{\phi} \\ c_s^4 \Upsilon_{00}^{\phi} & + \mathbf{u}_x^2 \mathbf{u}_y^2 \Upsilon_{00}^{\phi} / c_s^2 \end{bmatrix}, \quad (11.59)$$

$$\boldsymbol{\kappa}_{\text{discrete}}^{eq} = \begin{bmatrix} (\Upsilon_{00} - 1) + 1 \\ (\Upsilon_{00} - 1)(-u_x) \\ (\Upsilon_{00} - 1)(-u_y) \\ (\Upsilon_{00} - 1)(u_x^2 + c_s^2) + c_s^2 \\ (\Upsilon_{00} - 1)(u_y^2 + c_s^2) + c_s^2 \\ (\Upsilon_{00} - 1)u_x u_y \\ (\Upsilon_{00} - 1)(-u_y)(c_s^2 + u_x^2) & -\mathbf{u}_y \mathbf{u}_x^2 \\ (\Upsilon_{00} - 1)(-u_x)(c_s^2 + u_y^2) & -\mathbf{u}_x \mathbf{u}_y^2 \\ (\Upsilon_{00} - 1)(u_x^2 u_y^2 + c_s^2(u_x^2 + u_y^2) + c_s^4) + c_s^4 & +\mathbf{u}_x^2 \mathbf{u}_y^2 / c_s^2 \end{bmatrix}. \quad (11.60)$$

It has been shown [66, 67, 69], that the usage of the discrete equilibria as in Equations 11.57 - 11.60 negatively affects the Galilean invariance of the scheme.

11.6 Discretization of the force term

In this subsection, a transformation of the forcing term to the central moments' space is analysed. There are several concepts as to what constitutes the incompressible LBM, thus we discuss several possibilities, which may be of interest to other researchers.

Scheme proposed by He et al. [22] was expressed in a continuous form by Premnath al. [72]. However, their derivation did not distinguish between the fluid density, ρ , and the zeroth moment, Υ_{00} , of the distribution. The general concept of the He's scheme is to approximate the gradient of unknown particle distribution function $a \cdot \nabla_\zeta f$ (where a is the acceleration) in continuous Boltzmann equation by its dominant, equilibrium part $-a \cdot \nabla_u f^{eq}$. In our case this would lead to

$$\mathbf{F}_{\text{He}}(\boldsymbol{\xi}) = \frac{\mathbf{F}}{\rho} \cdot \nabla_u \Psi^{eq}(\Upsilon_{00}, \boldsymbol{\xi}, \mathbf{u}).$$

For Ψ^{eq} defined by Equation 2.17, which is recognised as a density-based LBM, the He's scheme reads

$$\mathbf{F}_{He} = \frac{\mathbf{F}}{\rho} \cdot \frac{(\boldsymbol{\xi} - \mathbf{u})}{c_s^2} \Psi^{M-B, eq}(\Upsilon_{00}, \boldsymbol{\xi}, \mathbf{u}). \quad (11.61)$$

Central moments (Equation 3.18) of such a function are

$$\tilde{\mathbf{F}}_{\text{He, density-based}} = [0, F_x \Upsilon_{00} / \rho, F_y \Upsilon_{00} / \rho, 0, 0, 0, c_s^2 F_y \Upsilon_{00} / \rho, c_s^2 F_x \Upsilon_{00} / \rho, 0]^\top. \quad (11.62)$$

In a velocity based LBM, where the first raw moments of a distribution is equal to velocity, not momentum, the central moments differ. To take it into account, the $\Psi^{M-B, eq}(1, \boldsymbol{\xi}, \mathbf{u})$ has to be used. Otherwise, the result shall be divided by Υ_{00} . The obtained central moments of the forcing term are

$$\tilde{\mathbf{F}}_{\text{He, velocity based}} = [0, F_x/\rho, F_y/\rho, 0, 0, 0, c_s^2 F_y/\rho, c_s^2 F_x/\rho, 0]^\top. \quad (11.63)$$

Equations 11.62 and 11.63 take into account the density differences occurring in a multi-phase flows, thus they enhance the derivation done in [48, 72]. The case of the phase field distribution is special, as the zeroth moment, and the phase-field density are the same beings. As a result, the Equation 11.63 simplifies further, as in [48, 72],

$$\tilde{\mathbf{F}}_{\text{He, density based}}^\phi = [0, F_x, F_y, 0, 0, 0, c_s^2 F_y, c_s^2 F_x, 0]^\top. \quad (11.64)$$

To recover an incompressible Navier-Stokes equation, a modified equilibrium distribution function is used. In such a case, Ψ^{eq} is defined by Equation 11.52, which gives

$$\begin{aligned} \mathbf{F}_{\text{He, velocity based, incompressible}} &= \frac{\mathbf{F}}{\rho} \cdot \nabla_u \left[\Psi^{M-B, eq}(\Upsilon_{00} - 1, \boldsymbol{\xi}, 0) + \Psi^{M-B, eq}(1, \boldsymbol{\xi}, \mathbf{u}) \right] \\ &= \frac{\mathbf{F}}{\rho} \cdot \frac{(\boldsymbol{\xi} - \mathbf{u})}{c_s^2} \Psi^{M-B, eq}(1, \boldsymbol{\xi}, \mathbf{u}). \end{aligned} \quad (11.65)$$

The result is equivalent to Equation 11.63, so the central moments for this scheme will be the same.

The literature [27, 268, 71] suggest that the usage of the discrete version of the Guo's scheme [27] gives better results than the discrete He's scheme. Observing, that the discrete weights coefficients, w_i , correspond to $\Psi^{M-B, eq}(1, \boldsymbol{\xi}, 0)$, the Guo's scheme can be expressed as

$$\mathbf{F}_{Guo}(\boldsymbol{\xi}) = \frac{\mathbf{F}}{\rho} \cdot \left(\frac{\boldsymbol{\xi} - \mathbf{u}}{c_s^2} + \frac{(\boldsymbol{\xi} \cdot \mathbf{u})\boldsymbol{\xi}}{c_s^4} \right) \Psi^{M-B, eq}(1, \boldsymbol{\xi}, 0). \quad (11.66)$$

Integrating the above expression, the $\tilde{\mathbf{F}}_{Guo}$ can be found in the central moment space

$$\tilde{\mathbf{F}}_{Guo} = \begin{bmatrix} 0 \\ F_x/\rho \\ F_y/\rho \\ 0 \\ 0 \\ 0 \\ (F_y c_s^2 - 2F_x u_x u_y - F_y u_x^2)/\rho \\ (F_x c_s^2 - 2F_y u_x u_y - F_x u_y^2)/\rho \\ 4u_x u_y (F_x u_y + F_y u_x)/\rho \end{bmatrix}. \quad (11.67)$$

In the conducted tests, no significant differences in simulational results have been found using either Equation 11.67 or Equation 11.63. The discrete versions of the He's and the Guo's forcing schemes read as follows,

$$F_i^{\text{He}} = \frac{\mathbf{F}}{\rho} \cdot \frac{(\mathbf{e}_i - \mathbf{u})}{c_s^2} \underbrace{\Upsilon_{00}\Gamma_i}_{\Psi_i^{eq}}, \quad (11.68)$$

$$F_i^{\text{Guo}} = \frac{\mathbf{F}}{\rho} \cdot \left(\frac{\mathbf{e}_i - \mathbf{u}}{c_s^2} + \frac{(\mathbf{e}_i \cdot \mathbf{u})\mathbf{e}_i}{c_s^4} \right) w_i. \quad (11.69)$$

It is interesting to observe, that calculating discrete central moments (Equation 3.6) of the discrete version of Guo's scheme leads to the same result as in Equation 11.67. However, application of the discrete version of the He's scheme results in even more complicated expressions in the central moment space. Such central moments would further divert from the ones based on continuous distributions. Finally, Huang et al. [73] noticed that if higher order Hermite polynomials are used for approximation, then regardless of the approach, the result converges to the one obtained from the continuous equilibrium.

Using a different basis, another set of discrete equilibria and forcing terms has been computed by De Rosis [269, 270]. An interesting discussion regarding derivations and other forcing schemes can also be found in works of Fei et al. [48, 67], Huang et al. [73] and Premnath and Banerjee [72].

To conclude, the expressions for central moments derived from the continuous functions are both simpler and more accurate, than the commonly used, truncated, discrete equilibria.

11.7 Conclusions

In this work, the phase-field LBM proposed by Fakhari et al. [230] was extended by formulating the collision routine in central moment space. This was shown to improve the Galilean invariance of the model as well as reduce the associated discretization error and computational cost. It was found that for a higher Mach number, $Ma \approx 0.17$ ($u = 0.1$), the Galilean invariance of the MRT collision kernel degraded as a function of both velocity and viscosity while the presented CLBM does not. In this work, the continuous equilibrium distribution function was derived in central moment space for the velocity-based LBM with correction terms to recover the incompressible Navier-Stokes Equations. Moreover, the proper implementation, together with explicit formulations for the moments of the equilibrium distribution function and forcing terms in central moment space allowed the preservation of computational efficiency at the level of the single relaxation time scheme. Having formulated and presented the cascaded phase-field model, two simple benchmark cases were simulated to demonstrate the role of interface thickness and relaxation rate interpolation. Next, the model capability was demonstrated by extending previous investigations of planar Taylor bubbles by looking at scenarios with stagnant, co-current and counter-current liquid flows. Here, a new and interesting result was observed in that the dimensionless coefficient that adjusts bubble rise velocity based on fluid flow remained almost constant for all flow configurations.

11.8 Future Outlook

The hydrodynamic EDF expressed by Equation (11.53) is composed of two parts. Only one of them is velocity dependent, $\Psi_u^{M-B, eq}$. To account for the difference, the hydrodynamic collision kernel given by Equation (11.6) can be splitted. As a consequence, the $\Psi_u^{M-B, eq}$, can be relaxed in the central moments space, while the pressure (velocity independent) part, $\Psi_p^{M-B, eq}$, can be relaxed in the raw moments space,

$$\mathbf{f}^*(\mathbf{x}, t) = \mathbb{M}^{-1} \left[\mathbb{N}^{-1} \left((\mathbb{1} - \mathbb{S}) \boldsymbol{\kappa} + \mathbb{S} \boldsymbol{\kappa}_u^{eq} + (\mathbb{1} - \mathbb{S}/2) \tilde{\mathbf{F}} \right) + \mathbb{S} \Upsilon_p^{eq} \right] \quad (11.70)$$

The raw moment of the pressure part of hydrodynamics EDF, Υ_p^{eq} , and central moments velocity dependent part, κ_u^{eq} , are

$$\kappa_u^{eq} = \begin{bmatrix} 1 \\ 0 \\ 0 \\ c_s^2 \\ c_s^2 \\ 0 \\ 0 \\ 0 \\ c_s^4 \end{bmatrix}, \quad \Upsilon_p^{eq} = \begin{bmatrix} \Upsilon_{00} - 1 \\ 0 \\ 0 \\ c_s^2(\Upsilon_{00} - 1) \\ c_s^2(\Upsilon_{00} - 1) \\ 0 \\ 0 \\ 0 \\ c_s^4(\Upsilon_{00} - 1) \end{bmatrix}. \quad (11.71)$$

The relaxed EDFs read,

$$\mathbb{S}\kappa_u^{eq} = \begin{bmatrix} 1 \\ 0 \\ 0 \\ s_b c_s^2 \\ s_b c_s^2 \\ 0 \\ 0 \\ 0 \\ s_b c_s^4 \end{bmatrix}, \quad \mathbb{S}\Upsilon_p^{eq} = \begin{bmatrix} \Upsilon_{00} - 1 \\ 0 \\ 0 \\ s_b c_s^2(\Upsilon_{00} - 1) \\ s_b c_s^2(\Upsilon_{00} - 1) \\ 0 \\ 0 \\ 0 \\ s_b c_s^4(\Upsilon_{00} - 1) \end{bmatrix}. \quad (11.72)$$

Observe, that the relaxation of both parts of the hydrodynamic EDF in the central moment space, $\boldsymbol{\kappa}^{eq}$, results in unnecessary couplings (see Equations (11.6) and (11.53)),

$$\mathbb{S}\boldsymbol{\kappa}^{eq} = \begin{bmatrix} \Upsilon_{00} \\ u_x(1 - \Upsilon_{00}) \\ u_y(1 - \Upsilon_{00}) \\ (\Upsilon_{00} - 1)[u_x^2(s_b + s_\nu) + u_y^2(s_b - s_\nu)]/2 + s_b c_s^2 \Upsilon_{00} \\ (\Upsilon_{00} - 1)[u_y^2(s_b + s_\nu) + u_x^2(s_b - s_\nu)]/2 + s_b c_s^2 \Upsilon_{00} \\ s_\nu u_x u_y (\Upsilon_{00} - 1) \\ u_y(1 - \Upsilon_{00})(c_s^2 + u_x^2) \\ u_x(1 - \Upsilon_{00})(c_s^2 + u_y^2) \\ c_s^4 \Upsilon_{00} + (\Upsilon_{00} - 1)[u_x^2 u_y^2 + c_s^2(u_x^2 + u_y^2)] \end{bmatrix}. \quad (11.73)$$

To sum up, there is a place for improvement of the authors' original work [5].

Chapter 12

Summary

“Besides the noble art of getting things done, there is the noble art of leaving things undone.

– Lin Yutang

The following original achievements have been presented in this thesis:

1. Detailed derivation of the lattice Boltzmann method with focus on proper integration of the source (reaction) terms. Special care has been taken to study the connection between spatial and temporal refinement and its potential pitfalls (see Chapter 4).
2. The cumulant collision kernel has been implemented for advection-diffusion equation for the first time. It was benchmarked against kernels established in the literature on lattice with large number of discrete velocities (D3Q27) (see Chapter 9). Simulation of the flow in high Prandtl number regime has been conducted to find the numerical limits of the *standard* lattice Boltzmann method in low conductivity regime.
3. Novel (central-moments) collision kernel has been presented for incompressible lattice Boltzmann model based on the phase-field approach (see Chapter 11).

The potential for further research has been highlighted in *future outlook* sections. In short, these includes:

1. Numerical benchmark of the Conjugate Heat Transfer model in which the equilibrium distribution function has been presented in both central moments’ and cumulants’ space (see Section 7.2).
2. Numerical benchmark of an implicit system of reaction-diffusion equations with second order accuracy (see Section 4.7).
3. Influence of the velocity truncation in the equilibrium distribution function on the accuracy of link-wise boundary condition (BC) as indicated in Section 8.3.
4. Numerical benchmark of the heat flux BC as proposed in Section 8.3.1.

5. Improved relaxation of the cumulants of the advected field, for example in a two relaxation time fashion as indicated in Section 9.4.
6. Numerical benchmarks of the central moment transformation of the advected field according to its probabilistic definition as indicated in Section 9.4.
7. Numerical benchmark of the improved collision kernel for the incompressible multi-phase kernel (see Section 11.8). As the equilibrium distribution function is composed of two parts, the relaxation space can be splitted into raw and central moments' space depending on its velocity components.

Chapter 13

References

“If Americans obeyed every wrong law, they would have been ruled by a queen today and had slavery.”

– Alexandra Elbakyan

References

- [1] L. Allen, A. OConnell, and V. Kiermer, “How can we ensure visibility and diversity in research contributions? how the contributor role taxonomy (credit) is helping the shift from authorship to contributorship,” *Learned Publishing*, vol. 32, pp. 71–74, 1 2019.
- [2] Elsevier, *Credit author statement*, [Online; accessed X 3, 2022], 2022.
- [3] G. Gruszczyński, M. Dzikowski, and Ł. Łaniewski-Wołk, “Revisiting the second-order convergence of the lattice boltzmann method with reaction-type source terms,” *arXiv*, 2021.
- [4] G. Gruszczyński and Ł. Łaniewski-Wołk, “A comparative study of 3d cumulant and central moments lattice boltzmann schemes with interpolated boundary conditions for the simulation of thermal flows in high prandtl number regime,” *International Journal of Heat and Mass Transfer*, vol. 197, p. 123 259, 2022.
- [5] G. Gruszczyński, T. Mitchell, C. Leonardi, Ł. Łaniewski-Wołk, and T. Barber, “A cascaded phase-field lattice boltzmann model for the simulation of incompressible, immiscible fluids with high density contrast,” *Computers and Mathematics with Applications*, vol. 79, no. 4, pp. 1049–1071, 2020.

- [6] Ł. Łaniewski-Wołk and J. Rokicki, “Adjoint Lattice Boltzmann for topology optimization on multi-GPU architecture,” *Computers and Mathematics with Applications*, vol. 71, pp. 833–848, 2016.
- [7] Ł. Łaniewski-Wołk *et al.*, *CFD-GO/TCLB: Version 6.5*, version v6.5.0, 2020.
- [8] Z. Guo and C. Shu, *Lattice Boltzmann method and its application in engineering*. World Scientific, 2013, vol. 3.
- [9] T. Krüger, H. Kusumaatmaja, A. Kuzmin, O. Shardt, G. Silva, and E. M. Viggen, *The Lattice Boltzmann Method*. 2017.
- [10] S. Succi, *The Lattice Boltzmann Equation For Complex States of Flowing Matter*. Oxford University Press, 2019.
- [11] L. S. Luo, W. Liao, X. Chen, Y. Peng, and W. Zhang, “Numerics of the lattice Boltzmann method: Effects of collision models on the lattice Boltzmann simulations,” *Physical Review E - Statistical, Nonlinear, and Soft Matter Physics*, vol. 83, no. 5, p. 56710, 2011.
- [12] C. Coreixas, B. Chopard, and J. Latt, “Comprehensive comparison of collision models in the lattice boltzmann framework: Theoretical investigations,” *Physical Review E*, vol. 100, no. 3, p. 033305, 2019.
- [13] C. Coreixas, G. Wissocq, B. Chopard, and J. Latt, “Impact of collision models on the physical properties and the stability of lattice Boltzmann methods,” *Philosophical Transactions of the Royal Society A: Mathematical, Physical and Engineering Sciences*, vol. 378, no. 2175, 2020.
- [14] H. K. Versteeg and W. Malalasekera, *An introduction to computational fluid dynamics: the finite volume method*. Pearson education, 2007.
- [15] O. Zienkiewicz, R. Taylor, and P. Nithiarasu, “The finite element method for fluid dynamics, vol. 3,” *Elsiever: Oxford*, 2005.
- [16] A. Badarch, “Application of macro and mesoscopic numerical models to hydraulic problems with solid substances,” PhD thesis, Nagaoka University of Technology, 2017.
- [17] L. Boltzmann, *Further studies on the heat balance among gas molecules*. knight, 1970, pp. 115–225.

-
- [18] P. L. Bhatnagar, E. P. Gross, and M. Krook, “A model for collision processes in gases. i. small amplitude processes in charged and neutral one-component systems,” *Phys. Rev.*, vol. 94, pp. 511–525, 3 1954.
 - [19] Z. Guo, B. Shi, and C. Zheng, “A coupled lattice BGK model for the Boussinesq equations,” *International Journal for Numerical Methods in Fluids*, vol. 39, no. 4, pp. 325–342, 2002.
 - [20] Q. Li, K. H. Luo, Y. L. He, Y. J. Gao, and W. Q. Tao, “Coupling lattice Boltzmann model for simulation of thermal flows on standard lattices,” *Physical Review E - Statistical, Nonlinear, and Soft Matter Physics*, vol. 85, no. 1, pp. 1–16, 2012.
 - [21] M. Dzikowski, *Introduction to the lattice boltzmann method - lecture notes*, 2021.
 - [22] X. He, X. Shan, and G. D. Doolen, “Discrete Boltzmann equation model for non-ideal gases,” *Physical Review E - Statistical Physics, Plasmas, Fluids, and Related Interdisciplinary Topics*, vol. 57, no. 1, R13–R16, 1998.
 - [23] B. Shi, B. Deng, R. Du, and X. Chen, “A new scheme for source term in LBGK model for convection-diffusion equation,” *Computers and Mathematics with Applications*, vol. 55, no. 7, pp. 1568–1575, 2008.
 - [24] B. Shi and Z. Guo, “Lattice Boltzmann model for nonlinear convection-diffusion equations,” *Physical Review E - Statistical, Nonlinear, and Soft Matter Physics*, vol. 79, no. 1, 2009.
 - [25] T. Seta, “Implicit temperature-correction-based immersed-boundary thermal lattice Boltzmann method for the simulation of natural convection,” *Physical Review E - Statistical, Nonlinear, and Soft Matter Physics*, vol. 87, no. 6, p. 63 304, 2013.
 - [26] Z. Chai, B. Shi, and Z. Guo, “A Multiple-Relaxation-Time Lattice Boltzmann Model for General Nonlinear Anisotropic Convection–Diffusion Equations,” *Journal of Scientific Computing*, vol. 69, no. 1, pp. 355–390, 2016.
 - [27] Z. Guo, C. Zheng, and B. Shi, “Discrete lattice effects on the forcing term in the lattice Boltzmann method,” *Physical Review E - Statistical Physics, Plasmas, Fluids, and Related Interdisciplinary Topics*, vol. 65, no. 4, p. 6, 2002.
 - [28] X. He, X. Shan, and G. D. Doolen, “Discrete Boltzmann equation model for non-ideal gases,” en, *Physical Review E*, vol. 57, no. 1, R13–R16, 1998.
 - [29] T. Lee and C.-L. Lin, “A stable discretization of the lattice Boltzmann equation for simulation of incompressible two-phase flows at high density ratio,” *Journal of Computational Physics*, vol. 206, no. 1, pp. 16–47, 2005.

- [30] X. Guo, B. Shi, and Z. Chai, “General propagation lattice Boltzmann model for nonlinear advection-diffusion equations,” *Physical Review E*, vol. 97, no. 4, p. 043 310, 2018.
- [31] X. He, S. Chen, and G. D. Doolen, “A Novel Thermal Model for the Lattice Boltzmann Method in Incompressible Limit,” *Journal of Computational Physics*, vol. 146, no. 1, pp. 282–300, 1998.
- [32] A. Krämer, D. Wilde, K. Küllmer, D. Reith, H. Foysi, and W. Joppich, “Lattice boltzmann simulations on irregular grids: Introduction of the natrium library,” *Computers and Mathematics with Applications*, vol. 79, pp. 34–54, 1 2020.
- [33] D. Wilde, A. Krämer, K. Küllmer, H. Foysi, and D. Reith, “Multistep lattice boltzmann methods: Theory and applications,” *International Journal for Numerical Methods in Fluids*, vol. 90, pp. 156–169, 3 2019.
- [34] D. Strzelczyk and M. Matyka, “How nodes layout, refinement and velocity discretization influence convergence of the meshless lattice boltzmann method,” *SSRN Electronic Journal*, 2022.
- [35] Z. Chai and B. Shi, “Multiple-relaxation-time lattice Boltzmann method for the Navier-Stokes and nonlinear convection-diffusion equations: Modeling, analysis, and elements,” *Physical Review E*, vol. 102, no. 2, pp. 24–26, 2020.
- [36] R. Fučík and R. Straka, “Equivalent finite difference and partial differential equations for the lattice Boltzmann method,” *Computers & Mathematics with Applications*, vol. 90, pp. 96–103, 2021.
- [37] S. Simonis, M. Frank, and M. J. Krause, “Constructing relaxation systems for lattice boltzmann methods,” *Applied Mathematics Letters*, vol. 137, p. 108 484, 2023.
- [38] D. d’Humières, “Generalized lattice-boltzmann equations,” *Rarefied gas dynamics*, 1992.
- [39] M. Geier, A. Greiner, and G. Korvink, “Cascaded digital lattice Boltzmann automata for high Reynolds number flow,” *Physical Review E - Statistical, Nonlinear, and Soft Matter Physics*, vol. 73, no. 6, pp. 1–10, 2006.
- [40] I. Ginzburg, “Equilibrium-type and link-type lattice Boltzmann models for generic advection and anisotropic-dispersion equation,” *Advances in Water Resources*, vol. 28, no. 11, pp. 1171–1195, 2005.

-
- [41] F. Dubois, T. Février, and B. Graille, “On the stability of a relative velocity lattice Boltzmann scheme for compressible Navier-Stokes equations,” *Comptes Rendus Mécanique*, vol. 343, no. 10-11, pp. 599–610, 2015.
 - [42] D. d’Humières, “Multiple-relaxation-time lattice boltzmann models in three dimensions,” *Philosophical Transactions of the Royal Society of London. Series A: Mathematical, Physical and Engineering Sciences*, vol. 360, no. 1792, pp. 437–451, 2002.
 - [43] M. Geier, M. Schonherr, A. Pasquali, and M. Krafczyk, “The cumulant lattice Boltzmann equation in three dimensions: Theory and validation,” *Computers and Mathematics with Applications*, vol. 70, no. 4, pp. 507–547, 2015.
 - [44] M. Geier, A. Pasquali, and M. Schönherr, “Parametrization of the cumulant lattice Boltzmann method for fourth order accurate diffusion part I: Derivation and validation,” *Journal of Computational Physics*, vol. 348, pp. 862–888, 2017.
 - [45] Y. Feng, P. Sagaut, and W. Tao, “A three dimensional lattice model for thermal compressible flow on standard lattices,” *Journal of Computational Physics*, vol. 303, pp. 514–529, 2015.
 - [46] S. Suga, “Numerical Schemes Obtained From Lattice Boltzmann Equations for Advection Diffusion Equations,” *International Journal of Modern Physics C*, vol. 17, no. 11, pp. 1563–1577, 2006.
 - [47] P. Asinari, “Generalized local equilibrium in the cascaded lattice Boltzmann method,” *Physical Review E - Statistical, Nonlinear, and Soft Matter Physics*, vol. 78, no. 1, pp. 1–5, 2008.
 - [48] L. Fei and K. H. Luo, “Consistent forcing scheme in the cascaded lattice Boltzmann method,” *Physical Review E*, vol. 96, no. 5, 2017.
 - [49] L. Fei, K. H. Luo, and Q. Li, “Three-dimensional cascaded lattice Boltzmann method: Improved implementation and consistent forcing scheme,” *Physical Review E*, vol. 97, no. 5, pp. 1–12, 2018.
 - [50] Z. Guo, C. Zheng, B. Shi, and T. S. Zhao, “Thermal lattice Boltzmann equation for low Mach number flows: Decoupling model,” *Physical Review E - Statistical, Nonlinear, and Soft Matter Physics*, vol. 75, no. 3, pp. 1–15, 2007.
 - [51] I. V. Karlin, D. Sichau, and S. S. Chikatamarla, “Consistent two-population lattice Boltzmann model for thermal flows,” *Physical Review E - Statistical, Nonlinear, and Soft Matter Physics*, vol. 88, no. 6, pp. 1–13, 2013.

- [52] L. Fei and K. H. Luo, “Cascaded lattice Boltzmann method for thermal flows on standard lattices,” *International Journal of Thermal Sciences*, vol. 132, no. June, pp. 368–377, 2018.
- [53] R. Huang, H. Wu, and P. Cheng, “A new lattice Boltzmann model for solid-liquid phase change,” *International Journal of Heat and Mass Transfer*, vol. 59, no. 1, pp. 295–301, 2013.
- [54] J. H. Lu, H. Y. Lei, and C. S. Dai, “A lattice Boltzmann algorithm for simulating conjugate heat transfer through virtual heat capacity correction,” *International Journal of Thermal Sciences*, vol. 116, pp. 22–31, 2017.
- [55] J. H. Lu, H. Y. Lei, and C. S. Dai, “A unified thermal lattice Boltzmann equation for conjugate heat transfer problem,” *International Journal of Heat and Mass Transfer*, 2018.
- [56] J. W. McCullough, C. R. Leonardi, B. D. Jones, S. M. Aminossadati, and J. R. Williams, “Investigation of local and non-local lattice Boltzmann models for transient heat transfer between non-stationary, disparate media,” *Computers and Mathematics with Applications*, pp. 1–21, 2018.
- [57] J. H. Lu, H. Y. Lei, and C. S. Dai, “An optimal two-relaxation-time lattice Boltzmann equation for solid-liquid phase change: The elimination of unphysical numerical diffusion,” *International Journal of Thermal Sciences*, vol. 135, pp. 17–29, 2019.
- [58] H. Yoshida and M. Nagaoka, “Multiple-relaxation-time lattice Boltzmann model for the convection and anisotropic diffusion equation,” *Journal of Computational Physics*, vol. 229, no. 20, pp. 7774–7795, 2010.
- [59] H. Yoshida, T. Kobayashi, H. Hayashi, T. Kinjo, H. Washizu, and K. Fukuzawa, “Boundary condition at a two-phase interface in the lattice Boltzmann method for the convection-diffusion equation,” *Physical Review E - Statistical, Nonlinear, and Soft Matter Physics*, vol. 90, no. 1, p. 13 303, 2014.
- [60] H. Karani and C. Huber, “Lattice Boltzmann formulation for conjugate heat transfer in heterogeneous media,” *Physical Review E - Statistical, Nonlinear, and Soft Matter Physics*, vol. 91, no. 2, pp. 1–12, 2015.
- [61] S. Chen, Y. Y. Yan, and W. Gong, “A simple lattice Boltzmann model for conjugate heat transfer research,” *International Journal of Heat and Mass Transfer*, vol. 107, pp. 862–870, 2017.

-
- [62] S. Hosseini, N. Darabiha, and D. Thévenin, “Lattice Boltzmann formulation for conjugate heat transfer in heterogeneous media,” *International Journal of Heat and Mass Transfer*, pp. 906–919, 2018.
 - [63] L. Fei and K. H. Luo, “Cascaded lattice Boltzmann method for incompressible thermal flows with heat sources and general thermal boundary conditions,” *Computers and Fluids*, vol. 165, pp. 89–95, 2018.
 - [64] J. Wang, M. Wang, and Z. Li, “A lattice boltzmann algorithm for fluid-solid conjugate heat transfer,” *International Journal of Thermal Sciences*, vol. 46, no. 3, pp. 228–234, 2007.
 - [65] B. Chopard, J. L. Falcone, and J. Latt, “The lattice Boltzmann advection-diffusion model revisited,” *European Physical Journal: Special Topics*, vol. 171, no. 1, pp. 245–249, 2009.
 - [66] X. B. Nie, X. Shan, and H. Chen, “Galilean invariance of lattice Boltzmann models,” *EPL*, vol. 81, no. 3, p. 34 005, 2008.
 - [67] L. Fei, K. H. Luo, and Q. Li, “Three-dimensional cascaded lattice boltzmann method: Improved implementation and consistent forcing scheme,” *Physical Review E*, vol. 97, no. 5, p. 053 309, 2018.
 - [68] L. Fei, K. H. Luo, C. Lin, and Q. Li, “Modeling incompressible thermal flows using a central-moments-based lattice Boltzmann method,” *International Journal of Heat and Mass Transfer*, vol. 120, pp. 624–634, 2018.
 - [69] A. De Rosis and K. H. Luo, “Role of higher-order Hermite polynomials in the central-moments-based lattice Boltzmann framework,” *Physical Review E*, vol. 99, no. 1, 2019.
 - [70] N. I. Prasianakis and I. V. Karlin, “Lattice Boltzmann method for thermal flow simulation on standard lattices,” *Physical Review E*, vol. 76, 2007.
 - [71] A. L. Kupershtokh, D. A. Medvedev, and D. I. Karpov, “On equations of state in a lattice Boltzmann method,” *Computers and Mathematics with Applications*, vol. 58, no. 5, pp. 965–974, 2009.
 - [72] K. N. Premnath and S. Banerjee, “Incorporating forcing terms in cascaded lattice Boltzmann approach by method of central moments,” *Physical Review E - Statistical, Nonlinear, and Soft Matter Physics*, vol. 80, no. 3, 2009.

- [73] R. Huang, H. Wu, and N. A. Adams, “Eliminating cubic terms in the pseudopotential lattice Boltzmann model for multiphase flow,” *Physical Review E*, vol. 97, no. 5, p. 53308, 2018.
- [74] P. Dellar, “Nonhydrodynamic modes and a priori construction of shallow water lattice Boltzmann equations,” *Physical Review E*, vol. 65, p. 036309, 2002.
- [75] A. Fakhari, D. Bolster, and L. Luo, “A weighted multiple-relaxation-time lattice Boltzmann method for multiphase flows and its application to partial coalescence cascades,” *Journal of Computational Physics*, vol. 341, pp. 22–43, 2017.
- [76] H. Chen, P. Gopalakrishnan, and R. Zhang, “Recovery of Galilean Invariance in Thermal Lattice Boltzmann Models for Arbitrary Prandtl Number,” *International Journal of Modern Physics C*, vol. 25, no. 10, p. 1450046, 2014.
- [77] J. Latt and B. Chopard, “Lattice Boltzmann method with regularized pre-collision distribution functions,” *Mathematics and Computers in Simulation*, vol. 72, no. 2–6, pp. 165–168, 2006.
- [78] T. Mitchell, C. Leonardi, and A. Fakhari, “Development of a three-dimensional phase-field lattice Boltzmann method for the study of immiscible fluids at high density ratios,” *International Journal of Multiphase Flow*, vol. 107, pp. 1–15, 2018.
- [79] A. De Rosis, R. Huang, and C. Coreixas, “Universal formulation of central-moments-based lattice Boltzmann method with external forcing for the simulation of multiphysics phenomena,” *Physics of Fluids*, vol. 31, no. 11, p. 117102, 2019.
- [80] A. De Rosis, “Nonorthogonal central-moments-based lattice Boltzmann scheme in three dimensions,” *Physical Review E*, vol. 95, no. 1, p. 13310, 2017.
- [81] I. Ginzburg, “Generic boundary conditions for lattice Boltzmann models and their application to advection and anisotropic dispersion equations,” *Advances in Water Resources*, vol. 28, no. 11, pp. 1196–1216, 2005.
- [82] I. Ginzburg, F. Verhaeghe, and D. dHumières, “Two-relaxation-time lattice boltzmann scheme: About parametrization, velocity, pressure and mixed boundary conditions,” *Communications in computational physics*, vol. 3, no. 2, pp. 427–478, 2008.
- [83] B. Servan-Camas and F. T. Tsai, “Lattice Boltzmann method with two relaxation times for advection-diffusion equation: Third order analysis and stability analysis,” *Advances in Water Resources*, vol. 31, no. 8, pp. 1113–1126, 2008.

-
- [84] I. Ginzburg, D. D’Humières, and A. Kuzmin, “Optimal stability of advection-diffusion lattice boltzmann models with two relaxation times for positive/negative equilibrium,” *Journal of Statistical Physics*, vol. 139, no. 6, pp. 1090–1143, 2010.
- [85] A. Kuzmin, I. Ginzburg, and A. A. Mohamad, “The role of the kinetic parameter in the stability of two-relaxation-time advection-diffusion lattice Boltzmann schemes,” *Computers and Mathematics with Applications*, vol. 61, no. 12, pp. 3417–3442, 2011.
- [86] Y.-H. Fu, L. Bai, K.-H. Luo, Y. Jin, and Y. Cheng, “Modeling mass transfer and reaction of dilute solutes in a ternary phase system by the lattice boltzmann method,” *Phys. Rev. E*, vol. 95, p. 043 304, 4 2017.
- [87] C. Lin, A. Xu, G. Zhang, and Y. Li, “Double-distribution-function discrete Boltzmann model for combustion,” *Combustion and Flame*, vol. 164, pp. 137–151, 2016.
- [88] O. Aursjø and S. R. Pride, “Lattice boltzmann method for diffusion-limited partial dissolution of fluids,” *Phys. Rev. E*, vol. 92, p. 013 306, 1 2015.
- [89] S. An, H. Erfani, H. Hellevang, and V. Niasar, “Lattice-boltzmann simulation of dissolution of carbonate rock during co₂-saturated brine injection,” *Chemical Engineering Journal*, vol. 408, p. 127 235, 2021.
- [90] R. Huang and H. Wu, “Phase interface effects in the total enthalpy-based lattice Boltzmann model for solid-liquid phase change,” *Journal of Computational Physics*, vol. 294, pp. 346–362, 2015.
- [91] Z. Guo, T. S. Zhao, and Y. Shi, “A lattice boltzmann algorithm for electro-osmotic flows in microfluidic devices,” *The Journal of Chemical Physics*, vol. 122, no. 14, p. 144 907, 2005.
- [92] Z. Hashemi, O. Abouali, and R. Kamali, “Three dimensional thermal Lattice Boltzmann simulation of heating/cooling spheres falling in a Newtonian liquid,” *International Journal of Thermal Sciences*, vol. 82, no. 1, pp. 23–33, 2014.
- [93] A. Grucelski and J. Pozorski, “Lattice Boltzmann simulations of heat transfer in flow past a cylinder and in simple porous media,” *International Journal of Heat and Mass Transfer*, vol. 86, pp. 139–148, 2015.
- [94] F. M. Elseid, S. W. Welch, and K. N. Premnath, “A cascaded lattice boltzmann model for thermal convective flows with local heat sources,” *International Journal of Heat and Fluid Flow*, vol. 70, pp. 279–298, 2018.

- [95] K. V. Sharma, R. Straka, and F. W. Tavares, “New Cascaded Thermal Lattice Boltzmann Method for simulations of advection-diffusion and convective heat transfer,” *International Journal of Thermal Sciences*, vol. 118, pp. 259–277, 2017.
- [96] K. V. Sharma, R. Straka, and F. W. Tavares, “Natural convection heat transfer modeling by the cascaded thermal lattice Boltzmann method,” *International Journal of Thermal Sciences*, vol. 134, pp. 552–564, 2018.
- [97] P. J. Roache, “Code verification by the method of manufactured solutions,” *J. Fluids Eng.*, vol. 124, no. 1, pp. 4–10, 2002.
- [98] K. Salari and P. Knupp, “Code verification by the method of manufactured solutions,” Sandia National Lab.(SNL-NM), Albuquerque, NM (United States), Tech. Rep., 2000.
- [99] P. J. Roache, “The method of manufactured solutions for code verification,” *Computer Simulation Validation: Fundamental Concepts, Methodological Frameworks, and Philosophical Perspectives*. Cham: Springer International Publishing, 2019, pp. 295–318.
- [100] S. P. Dawson, S. Chen, and G. D. Doolen, “Lattice Boltzmann computations for reaction-diffusion equations,” *The Journal of Chemical Physics*, vol. 98, no. 2, pp. 1514–1523, 1993.
- [101] R. Blaak and P. M. A. Sloot, “Lattice dependence of reaction-diffusion in lattice Boltzmann modeling,” in *Computer Physics Communications*, vol. 129, no. 1, pp. 256–266, 2000.
- [102] Q. Li, K. H. Luo, Q. J. Kang, Y. L. He, Q. Chen, and Q. Liu, “Lattice Boltzmann methods for multiphase flow and phase-change heat transfer,” *Progress in Energy and Combustion Science*, vol. 52, pp. 62–105, 2016.
- [103] H. K. Jeong, H. S. Yoon, M. Y. Ha, and M. Tsutahara, “An immersed boundary-thermal lattice Boltzmann method using an equilibrium internal energy density approach for the simulation of flows with heat transfer,” *Journal of Computational Physics*, vol. 229, no. 7, pp. 2526–2543, 2010.
- [104] S. K. Kang and Y. A. Hassan, “A comparative study of direct-forcing immersed boundary-lattice Boltzmann methods for stationary complex boundaries,” *International Journal for Numerical Methods in Fluids*, vol. 66, no. 9, pp. 1132–1158, 2011.

-
- [105] S. K. Kang and Y. A. Hassan, “A direct-forcing immersed boundary method for the thermal lattice Boltzmann method,” *Computers and Fluids*, vol. 49, no. 1, pp. 36–45, 2011.
- [106] R. Huang and H. Wu, “An immersed boundary-thermal lattice Boltzmann method for solid-liquid phase change,” *Journal of Computational Physics*, vol. 277, pp. 305–319, 2014.
- [107] Y. Hu, D. Li, S. Shu, and X. Niu, “Study of multiple steady solutions for the 2D natural convection in a concentric horizontal annulus with a constant heat flux wall using immersed boundary-lattice Boltzmann method,” *International Journal of Heat and Mass Transfer*, vol. 81, pp. 591–601, 2015.
- [108] Z. Wang, Y. Wei, and Y. Qian, “A simple direct heating thermal immersed boundary-lattice Boltzmann method for its application in incompressible flow,” *Computers and Mathematics with Applications*, vol. 80, no. 6, pp. 1633–1649, 2020.
- [109] A. Eshghinejadfard and D. Thévenin, “Numerical simulation of heat transfer in particulate flows using a thermal immersed boundary lattice Boltzmann method,” *International Journal of Heat and Fluid Flow*, vol. 60, pp. 31–46, 2016.
- [110] S. Karimnejad, A. Amiri Delouei, M. Nazari, M. M. Shahmardan, M. M. Rashidi, and S. Wongwises, “Immersed boundarythermal lattice Boltzmann method for the moving simulation of non-isothermal elliptical particles,” *Journal of Thermal Analysis and Calorimetry*, vol. 138, no. 6, pp. 4003–4017, 2019.
- [111] K. Suzuki, T. Kawasaki, N. Furumachi, Y. Tai, and M. Yoshino, “A thermal immersed boundarylattice Boltzmann method for moving-boundary flows with Dirichlet and Neumann conditions,” *International Journal of Heat and Mass Transfer*, vol. 121, pp. 1099–1117, 2018.
- [112] D. Noble and J. Torczynski, “A lattice-boltzmann method for partially saturated computational cells,” *International Journal of Modern Physics C*, vol. 9, no. 08, pp. 1189–1201, 1998.
- [113] J. McCullough, S. Aminossadati, B. Jones, C. Leonardi, and J. Williams, “Lattice Boltzmann methods for the simulation of heat transfer in particle suspensions,” *International Journal of Heat and Fluid Flow*, vol. 62, pp. 150–165, 2016.
- [114] O. Aursjø, E. Jettestuen, L. Vinningland, and A. Hiorth, “An improved lattice Boltzmann method for simulating advective diffusive processes in fluids,” *Journal of Computational Physics*, vol. 332, pp. 363–375, 2017.

- [115] O. Aursjø, E. Jettestuen, L. Vinningland, and A. Hiorth, “On the inclusion of mass source terms in a single-relaxation-time lattice Boltzmann method,” *Physics of Fluids*, vol. 30, no. 5, 2018.
- [116] Q. Kang, P. C. Lichtner, and D. Zhang, “Lattice Boltzmann pore-scale model for multicomponent reactive transport in porous media,” en, *Journal of Geophysical Research: Solid Earth*, vol. 111, no. B5, 2006.
- [117] S. A. Hosseini, A. Eshghinejadfard, N. Darabiha, and D. Thévenin, “Weakly compressible Lattice Boltzmann simulations of reacting flows with detailed thermochemical models,” *Computers and Mathematics with Applications*, vol. 79, no. 1, pp. 141–158, 2020.
- [118] S. Dellacherie, “Construction and Analysis of Lattice Boltzmann Methods Applied to a 1D Convection-Diffusion Equation,” en, *Acta Applicandae Mathematicae*, vol. 131, no. 1, pp. 69–140, 2013.
- [119] M. Junk and Z. Yang, “L2 convergence of the lattice boltzmann method for one dimensional convection-diffusion-reaction equations,” *Communications in Computational Physics*, vol. 17, no. 5, pp. 1225–1245, 2015.
- [120] J. Onishi, Y. Chen, and H. Ohashi, “A Lattice Boltzmann model for polymeric liquids,” en, *Progress in Computational Fluid Dynamics, An International Journal*, vol. 5, no. 1/2, p. 75, 2005.
- [121] F. Osmanlic and C. Körner, “Lattice Boltzmann method for Oldroyd-B fluids,” en, *Computers & Fluids*, Special Issue for ICMES-2014, vol. 124, pp. 190–196, 2016.
- [122] V. E. Küng, F. Osmanlic, M. Markl, and C. Körner, “Comparison of passive scalar transport models coupled with the Lattice Boltzmann method,” *Computers & Mathematics with Applications*, 2018.
- [123] L. Fei and K. H. Luo, “Consistent forcing scheme in the cascaded lattice Boltzmann method,” *Physical Review E*, vol. 96, no. 5, p. 053 307, 2017, Publisher: American Physical Society.
- [124] L. Fei, K. H. Luo, and Q. Li, “Three-dimensional cascaded lattice Boltzmann method: Improved implementation and consistent forcing scheme,” *Physical Review E*, vol. 97, no. 5, p. 053 309, 2018, Publisher: American Physical Society.
- [125] H. P. Langtangen and G. K. Pedersen, *Scaling of Differential Equations* (Simula SpringerBriefs on Computing), en. Springer International Publishing, 2016.

-
- [126] M. Zhang, W. Zhao, and P. Lin, “Lattice Boltzmann method for general convection-diffusion equations: MRT model and boundary schemes,” *Journal of Computational Physics*, vol. 389, pp. 147–163, 2019.
- [127] J. W. Cahn and J. E. Hilliard, “Free Energy of a Nonuniform System. I. Interfacial Free Energy,” *The Journal of Chemical Physics*, vol. 28, no. 2, pp. 258–267, 1958.
- [128] D. Jacqmin, “Calculation of Two-Phase Navier–Stokes Flows Using Phase-Field Modeling,” *Journal of Computational Physics*, vol. 155, no. 1, pp. 96–127, 1999.
- [129] A. Logg and G. N. Wells, “Dolfin: Automated finite element computing,” *ACM Transactions on Mathematical Software*, vol. 37, no. 2, 2010.
- [130] M. S. Alnæs *et al.*, “The fenics project version 1.5,” *Archive of Numerical Software*, vol. 3, no. 100, 2015.
- [131] K. E. Skare, *Gryphon - a Module for Time Integration of Partial Differential Equations in FEniCS*. 2012.
- [132] I. Ginzburg, “Consistent lattice Boltzmann schemes for the Brinkman model of porous flow and infinite Chapman-Enskog expansion,” *Physical Review E - Statistical, Nonlinear, and Soft Matter Physics*, vol. 77, no. 6, 2008.
- [133] C. Pan, L. S. Luo, and C. T. Miller, “An evaluation of lattice Boltzmann schemes for porous medium flow simulation,” *Computers and Fluids*, vol. 35, no. 8-9, pp. 898–909, 2006.
- [134] W. Regulski *et al.*, “Pressure drop in flow across ceramic foams-A numerical and experimental study,” *Chemical Engineering Science*, vol. 137, pp. 320–337, 2015.
- [135] Wikipedia, the free encyclopedia, *Role of diffusion-reaction equations in epidemic modelling*, [Online; accessed X 3, 2022], 2021.
- [136] J. Graunt, *Natural and political observations made upon the bills of mortality*. The Johns Hopkins Press, 1939.
- [137] D. Bernoulli and S. Blower, “An attempt at a new analysis of the mortality caused by smallpox and of the advantages of inoculation to prevent it,” *Reviews in medical virology*, vol. 14, no. 5, p. 275, 2004.
- [138] W. O. Kermack and A. G. McKendrick, “A contribution to the mathematical theory of epidemics,” *Proceedings of the royal society of london. Series A, Containing papers of a mathematical and physical character*, vol. 115, no. 772, pp. 700–721, 1927.

- [139] M. Robinson, N. I. Stilianakis, and Y. Drossinos, “Spatial dynamics of airborne infectious diseases,” *Journal of theoretical biology*, vol. 297, pp. 116–126, 2012.
- [140] Q.-X. Liu and Z. Jin, “Formation of spatial patterns in an epidemic model with constant removal rate of the infectives,” *Journal of Statistical Mechanics: Theory and Experiment*, vol. 2007, no. 05, P05002, 2007.
- [141] G. Sun, Z. Jin, Q.-X. Liu, and L. Li, “Pattern formation in a spatial s-i model with non-linear incidence rates,” *Journal of Statistical Mechanics: Theory and Experiment*, vol. 2007, no. 11, P11011, 2007.
- [142] G.-Q. Sun, Z. Jin, Q.-X. Liu, and L. Li, “Chaos induced by breakup of waves in a spatial epidemic model with nonlinear incidence rate,” *Journal of Statistical Mechanics: Theory and Experiment*, vol. 2008, no. 08, P08011, 2008.
- [143] G.-Q. Sun, Z. Jin, Q.-X. Liu, and L. Li, “Spatial pattern in an epidemic system with cross-diffusion of the susceptible,” *Journal of Biological Systems*, vol. 17, no. 01, pp. 141–152, 2009.
- [144] Y. Cai and W. Wang, “Spatiotemporal dynamics of a reaction–diffusion epidemic model with nonlinear incidence rate,” *Journal of Statistical Mechanics: Theory and Experiment*, vol. 2011, no. 02, P02025, 2011.
- [145] A. Holko, M. Mdrek, Z. Pastuszak, and K. Phusavat, “Epidemiological modeling with a population density map-based cellular automata simulation system,” *Expert Systems with Applications*, vol. 48, pp. 1–8, 2016.
- [146] F. Rakowski, M. Gruziel, Ł. Bieniasz-Krzywiec, and J. P. Radomski, “Influenza epidemic spread simulation for polanda large scale, individual based model study,” *Physica A: Statistical Mechanics and its Applications*, vol. 389, no. 16, pp. 3149–3165, 2010.
- [147] R. N. Thompson, C. A. Gilligan, and N. J. Cunniffe, “Control fast or control smart: When should invading pathogens be controlled?” *PLoS computational biology*, vol. 14, no. 2, e1006014, 2018.
- [148] N. M. Ferguson, C. A. Donnelly, and R. M. Anderson, “The foot-and-mouth epidemic in great britain: Pattern of spread and impact of interventions,” *Science*, vol. 292, no. 5519, pp. 1155–1160, 2001.
- [149] Wikipedia, the free encyclopedia, *Herd immunity treshold*, [Online; accessed X 3, 2022], 2022.

-
- [150] S.-H. Paeng and J. Lee, “Continuous and discrete SIR-models with spatial distributions,” en, *Journal of Mathematical Biology*, vol. 74, no. 7, pp. 1709–1727, 2017.
- [151] A. De Rosis, “Modeling epidemics by the lattice Boltzmann method,” *PHYSICAL REVIEW E*, vol. 102, p. 23 301, 2020.
- [152] S. Brunton. “Control theory and covid-19 (youtube lecture).” (2020), (visited on 11/14/2021).
- [153] Ł Łaniewski-Wołk, “Adjoint lattice boltzmann for topology optimalization and optimal control on multi-gpu architecture,” PhD thesis, Warsaw University of Technology, Faculty of Power and Aeronautical Engineering, 2017.
- [154] S. Chen, B. Yang, and C. Zheng, “A lattice Boltzmann model for heat transfer in heterogeneous media,” *International Journal of Heat and Mass Transfer*, vol. 102, pp. 637–644, 2016.
- [155] A. A. Mohamad, Q. W. Tao, Y. L. He, and S Bawazeer, “Treatment of transport at the interface between multilayers via the lattice boltzmann method,” *Numerical Heat Transfer, Part B: Fundamentals*, vol. 67, no. 2, pp. 124–134, 2015.
- [156] L. Li, R. Mei, and J. F. Klausner, “Boundary conditions for thermal lattice Boltzmann equation method,” *Journal of Computational Physics*, vol. 237, pp. 366–395, 2013.
- [157] L. Li, C. Chen, R. Mei, and J. F. Klausner, “Conjugate heat and mass transfer in the lattice Boltzmann equation method,” *Physical Review E - Statistical, Nonlinear, and Soft Matter Physics*, vol. 89, no. 4, 2014.
- [158] G. Le, O. Oulaid, and J. Zhang, “Counter-extrapolation method for conjugate interfaces in computational heat and mass transfer,” *Physical Review E - Statistical, Nonlinear, and Soft Matter Physics*, vol. 91, no. 3, p. 33 306, 2015.
- [159] S. Bennett, “A lattice boltzmann model for diffusion of binary gas mixtures,” Ph.D. dissertation, University of Cambridge, 2010.
- [160] I. Ginzbourg and P. M. Adler, “Boundary flow condition analysis for the three-dimensional lattice Boltzmann model,” *Journal de Physique II*, vol. 4, no. 2, pp. 191–214, 1994.
- [161] I. Ginzburg and D. D’Humières, “Multireflection boundary conditions for lattice Boltzmann models,” *Physical Review E - Statistical Physics, Plasmas, Fluids, and Related Interdisciplinary Topics*, vol. 68, no. 6, 2003.

- [162] S. Chen, D. Martinez, and R. Mei, “On boundary conditions in lattice boltzmann methods,” *Physics of fluids*, vol. 8, no. 9, pp. 2527–2536, 1996.
- [163] R. Cornubert, D. d’Humières, and D. Levermore, “A knudsen layer theory for lattice gases,” *Physica D: Nonlinear Phenomena*, vol. 47, no. 1-2, pp. 241–259, 1991.
- [164] D. d’Humières and I. Ginzburg, “Viscosity independent numerical errors for lattice boltzmann models: From recurrence equations to magic collision numbers,” *Computers & Mathematics with Applications*, vol. 58, no. 5, pp. 823–840, 2009.
- [165] I. Ginzburg, “Une variation sur les propriétés magiques de modeles de boltzmann pour lécoulement microscopique et macroscopique,” Ph.D. dissertation, Université Pierre et Marie Curie, 2009.
- [166] S. Khirevich, I. Ginzburg, and U. Tallarek, “Coarse-and fine-grid numerical behavior of MRT/TRT lattice-Boltzmann schemes in regular and random sphere packings,” *Journal of Computational Physics*, vol. 281, pp. 708–742, 2015.
- [167] W. Regulski, “Investigation of hydrodynamic properties of structures with open porosity using the lattice Boltzmann method,” Ph.D. dissertation, Warsaw University of Technology, 2018.
- [168] X. Yang *et al.*, “Intercomparison of 3d pore-scale flow and solute transport simulation methods,” *Advances in water resources*, vol. 95, pp. 176–189, 2016.
- [169] A. J. C. Ladd, “Numerical simulations of particulate suspensions via a discretized boltzmann equation. part 1. theoretical foundation,” *Journal of Fluid Mechanics*, vol. 271, pp. 285309, 1994.
- [170] A. J. C. Ladd, “Numerical simulations of particulate suspensions via a discretized boltzmann equation. part 2. numerical results,” *Journal of Fluid Mechanics*, vol. 271, pp. 311339, 1994.
- [171] R. Verberg and A. Ladd, “Lattice-Boltzmann simulations of particle-fluid suspensions,” *Journal of statistical physics*, vol. 104, no. 5-6, pp. 1191–1251, 2001.
- [172] T. Zhang, B. Shi, Z. Guo, Z. Chai, and J. Lu, “General bounce-back scheme for concentration boundary condition in the lattice-Boltzmann method,” *Physical Review E - Statistical, Nonlinear, and Soft Matter Physics*, vol. 85, no. 1, p. 16 701, 2012.
- [173] G. Tang, W. Tao, and Y. He, “Thermal boundary condition for the thermal lattice boltzmann equation,” *Physical Review E*, vol. 72, no. 1, p. 016 703, 2005.

-
- [174] H. Huang, T. Lee, and C Shu, “Thermal curved boundary treatment for the thermal lattice boltzmann equation,” *International Journal of Modern Physics C*, vol. 17, no. 05, pp. 631–643, 2006.
- [175] C.-H. Liu, K.-H. Lin, H.-C. Mai, and C.-A. Lin, “Thermal boundary conditions for thermal lattice boltzmann simulations,” *Computers & Mathematics with Applications*, vol. 59, no. 7, pp. 2178–2193, 2010.
- [176] K. Guo, L. Li, G. Xiao, N. Auyeung, and R. Mei, “Lattice Boltzmann method for conjugate heat and mass transfer with interfacial jump conditions,” *International Journal of Heat and Mass Transfer*, vol. 88, pp. 306–322, 2015.
- [177] M. Bouzidi, M. Firdaouss, and P. Lallemand, “Momentum transfer of a Boltzmann-lattice fluid with boundaries,” *Physics of Fluids*, vol. 13, no. 11, pp. 3452–3459, 2001.
- [178] F. Dubois and P. Lallemand, “Towards higher order lattice boltzmann schemes,” *Journal of Statistical Mechanics: Theory and Experiment*, vol. 2009, no. 6, 2009.
- [179] L. Li, R. Mei, and J. F. Klausner, “Boundary conditions for thermal lattice Boltzmann equation method,” *Journal of Computational Physics*, vol. 237, pp. 366–395, 2013.
- [180] F. Dubois, P. Lallemand, and M. M. Tekitek, “On anti bounce back boundary condition for lattice Boltzmann schemes,” *Computers and Mathematics with Applications*, 2019.
- [181] I. Ginzburg, F. Verhaeghe, and D. dHumieres, “Study of simple hydrodynamic solutions with the two-relaxation-times lattice boltzmann scheme,” *Communications in computational physics*, vol. 3, no. 3, pp. 519–581, 2008.
- [182] S. Izquierdo and N. Fueyo, “Characteristic nonreflecting boundary conditions for open boundaries in lattice Boltzmann methods,” *Physical Review E - Statistical, Nonlinear, and Soft Matter Physics*, vol. 78, no. 4, 2008.
- [183] X. He, Q. Zou, L. S. Luo, and M. Dembo, “Analytic solutions of simple flows and analysis of nonslip boundary conditions for the lattice Boltzmann BGK model,” *Journal of Statistical Physics*, vol. 87, no. 1-2, pp. 115–136, 1997.
- [184] J. Latt, B. Chopard, O. Malaspinas, M. Deville, and A. Michler, “Straight velocity boundaries in the lattice Boltzmann method,” *Physical Review E - Statistical, Nonlinear, and Soft Matter Physics*, vol. 77, no. 5, 2008.

- [185] A. A. Mohamad and S Succi, “A note on equilibrium boundary conditions in lattice Boltzmann fluid dynamic simulations,” *European Physical Journal: Special Topics*, vol. 171, Springer-Verlag, 2009, pp. 213–221.
- [186] C. S. Peskin, “Numerical analysis of blood flow in the heart,” *Journal of computational physics*, vol. 25, no. 3, pp. 220–252, 1977.
- [187] D. Noble and J. Torczynski, “A lattice-boltzmann method for partially saturated computational cells,” *International Journal of Modern Physics C*, vol. 9, no. 08, pp. 1189–1201, 1998.
- [188] I. Ginzburg, F. Verhaeghe, and D. dHumieres, “Two-relaxation-time lattice boltzmann scheme: About parametrization, velocity, pressure and mixed boundary conditions,” *Communications in computational physics*, vol. 3, no. 2, pp. 427–478, 2008.
- [189] S. Khirevich, I. Ginzburg, and U. Tallarek, “Coarse-and fine-grid numerical behavior of mrt/trt lattice-boltzmann schemes in regular and random sphere packings,” *Journal of Computational Physics*, vol. 281, pp. 708–742, 2015.
- [190] B Chun and A. Ladd, “Interpolated boundary condition for lattice boltzmann simulations of flows in narrow gaps,” *Physical review E*, vol. 75, no. 6, p. 066 705, 2007.
- [191] Q. Li, K. H. Luo, Q. J. Kang, Y. L. He, Q. Chen, and Q. Liu, “Lattice Boltzmann methods for multiphase flow and phase-change heat transfer,” *Progress in Energy and Combustion Science*, vol. 52, pp. 62–105, 2016.
- [192] R. Mabrouk, H. Dhahri, H. Naji, S. Hammouda, and Z. Younsi, “Lattice Boltzmann simulation of forced convection melting of a composite phase change material with heat dissipation through an open-ended channel,” *International Journal of Heat and Mass Transfer*, vol. 153, p. 119 606, 2020.
- [193] W. Du, S. Chen, and G. Wu, “A new lattice Boltzmann method for melting processes of high Prandtl number phase change materials,” *Journal of Energy Storage*, vol. 41, p. 103 006, 2021.
- [194] S. Chen, W. Li, and H. I. Mohammed, “Heat transfer of large Prandtl number fluids in porous media by a new lattice Boltzmann model,” *International Communications in Heat and Mass Transfer*, vol. 122, p. 105 129, 2021.

-
- [195] Z. Chen, C. Shu, and D. Tan, “A simplified thermal lattice Boltzmann method without evolution of distribution functions,” *International Journal of Heat and Mass Transfer*, vol. 105, pp. 741–757, 2017.
- [196] K. V. Sharma, R. Straka, and F. W. Tavares, “Natural convection heat transfer modeling by the cascaded thermal lattice Boltzmann method,” *International Journal of Thermal Sciences*, vol. 134, pp. 552–564, 2018.
- [197] Y. L. Feng, S. L. Guo, W. Q. Tao, and P. Sagaut, “Regularized thermal lattice Boltzmann method for natural convection with large temperature differences,” *International Journal of Heat and Mass Transfer*, vol. 125, pp. 1379–1391, 2018.
- [198] A. Xu, L. Shi, and H. D. Xi, “Lattice Boltzmann simulations of three-dimensional thermal convective flows at high Rayleigh number,” *International Journal of Heat and Mass Transfer*, vol. 140, pp. 359–370, 2019.
- [199] Y. H. Yip, A. K. Soh, and J. J. Foo, “Flow-dynamics induced thermal management of crude oil wax melting: Lattice Boltzmann modeling,” *International Journal of Thermal Sciences*, vol. 137, pp. 675–691, 2019.
- [200] H. Sajjadi, A. Amiri Delouei, M. Sheikholeslami, M. Atashafrooz, and S. Succi, “Simulation of three dimensional MHD natural convection using double MRT Lattice Boltzmann method,” *Physica A: Statistical Mechanics and its Applications*, vol. 515, pp. 474–496, 2019.
- [201] X. He, S. Chen, and G. D. Doolen, “A Novel Thermal Model for the Lattice Boltzmann Method in Incompressible Limit,” *Journal of Computational Physics*, vol. 146, no. 1, pp. 282–300, 1998.
- [202] C. Cercignani, *The Boltzmann Equation and Its Application*. Springer, 1988.
- [203] X. Shan, “Central-moment-based Galilean-invariant multiple-relaxation-time collision model,” *Physical Review E*, vol. 100, no. 4, 2019.
- [204] P. Lallemand and L. S. Lou, “Hybrid finite-difference thermal lattice Boltzmann equation,” *International Journal of Modern Physics B*, vol. 17, no. 1-2, pp. 41–47, 2003.
- [205] S. Saito *et al.*, “Lattice Boltzmann modeling and simulation of forced-convection boiling on a cylinder,” *Physics of Fluids*, vol. 33, no. 2, p. 023307, 2021.

- [206] A. Parmigiani, C Huber, B Chopard, J Latt, and O Bachmann, “Application of the multi distribution function lattice Boltzmann approach to thermal flows,” *European Physical Journal: Special Topics*, vol. 171, Springer-Verlag, 2009, pp. 37–43.
- [207] S. A. Nabavizadeh, H. Barua, M. Eshraghi, and S. D. Felicelli, “A multiple-grid lattice boltzmann method for natural convection under low and high prandtl numbers,” *Fluids*, vol. 6, no. 4, 2021.
- [208] H. B. Huang, X. Y. Lu, and M. C. Sukop, “Numerical study of lattice Boltzmann methods for a convection-diffusion equation coupled with Navier-Stokes equations,” *Journal of Physics A: Mathematical and Theoretical*, vol. 44, no. 5, 2011.
- [209] E. Yahia, W. Schupbach, and K. N. Premnath, “Three-dimensional central moment lattice boltzmann method on a cuboid lattice for anisotropic and inhomogeneous flows,” *Fluids*, vol. 6, no. 9, p. 326, 2021.
- [210] F. Hajabdollahi, K. N. Premnath, and S. W. Welch, “Cascaded lattice Boltzmann method based on central moments for axisymmetric thermal flows including swirling effects,” *International Journal of Heat and Mass Transfer*, vol. 128, pp. 999–1016, 2019.
- [211] M. Matyka and M. Dzikowski, “Memory-efficient Lattice Boltzmann Method for low Reynolds number flows,” *Computer Physics Communications*, vol. 267, p. 108 044, 2021.
- [212] F. M. Elseid, S. W. Welch, and K. N. Premnath, “A cascaded lattice boltzmann model for thermal convective flows with local heat sources,” *International Journal of Heat and Fluid Flow*, vol. 70, pp. 279–298, 2018.
- [213] F. Hajabdollahi and K. N. Premnath, “Central moments-based cascaded lattice Boltzmann method for thermal convective flows in three-dimensions,” *International Journal of Heat and Mass Transfer*, vol. 120, pp. 838–850, 2018.
- [214] J. McCullough, S. Aminossadati, B. Jones, C. Leonardi, and J. Williams, “Lattice Boltzmann methods for the simulation of heat transfer in particle suspensions,” *International Journal of Heat and Fluid Flow*, vol. 62, pp. 150–165, 2016.
- [215] J. Wang, D. Wang, P. Lallemand, and L. S. Luo, “Lattice Boltzmann simulations of thermal convective flows in two dimensions,” *Computers and Mathematics with Applications*, vol. 65, no. 2, pp. 262–286, 2013.

-
- [216] S. Cui, N. Hong, B. Shi, and Z. Chai, “Discrete effect on the halfway bounce-back boundary condition of multiple-relaxation-time lattice Boltzmann model for convection-diffusion equations,” *Physical Review E*, vol. 93, p. 43311, 2016.
- [217] Q. Liu, Y. L. He, D. Li, and Q. Li, “Non-orthogonal multiple-relaxation-time lattice Boltzmann method for incompressible thermal flows,” *International Journal of Heat and Mass Transfer*, vol. 102, pp. 1334–1344, 2016.
- [218] A. Xu, L. Shi, and T. S. Zhao, “Accelerated lattice Boltzmann simulation using GPU and OpenACC with data management,” *International Journal of Heat and Mass Transfer*, vol. 109, pp. 577–588, 2017.
- [219] Y. Shi, T. S. Zhao, and Z. L. Guo, “Thermal lattice Bhatnagar-Gross-Krook model for flows with viscous heat dissipation in the incompressible limit,” *Physical Review E - Statistical Physics, Plasmas, Fluids, and Related Interdisciplinary Topics*, vol. 70, no. 6, p. 10, 2004.
- [220] O. Zikanov, *Essential computational fluid dynamics*. John Wiley & Sons, 2019.
- [221] D. D’Humières and I. Ginzburg, “Viscosity independent numerical errors for Lattice Boltzmann models: From recurrence equations to "magic" collision numbers,” *Computers and Mathematics with Applications*, vol. 58, no. 5, pp. 823–840, 2009.
- [222] Ł. Łaniewski-Wołk *et al.*, *CFD-GO/TCLB: Version 6.5*, version v6.5.0, 2020.
- [223] I. Ginzburg, “Equilibrium-type and link-type lattice boltzmann models for generic advection and anisotropic-dispersion equation,” *Advances in Water resources*, vol. 28, no. 11, pp. 1171–1195, 2005.
- [224] Q. Zou and X. He, “On pressure and velocity boundary conditions for the lattice boltzmann bgk model,” *Physics of Fluids*, vol. 9, no. 6, pp. 1591–1598, 1997.
- [225] Q. Lou, Z. Guo, and B. Shi, “Evaluation of outflow boundary conditions for two-phase lattice Boltzmann equation,” *Physical Review E - Statistical, Nonlinear, and Soft Matter Physics*, vol. 87, no. 6, pp. 1–16, 2013.
- [226] P.-H. Chiu and Y.-T. Lin, “A conservative phase field method for solving incompressible two-phase flows,” *Journal of Computational Physics*, vol. 230, no. 1, pp. 185–204, 2011.
- [227] Y. Sun and C. Beckermann, “Sharp interface tracking using the phase-field equation,” *Journal of Computational Physics*, vol. 220, pp. 626–653, 2 2007.

- [228] M. Geier, A. Fakhari, and T. Lee, “Conservative phase-field lattice Boltzmann model for interface tracking equation,” *Physical Review E - Statistical, Nonlinear, and Soft Matter Physics*, vol. 91, no. 6, pp. 1–11, 2015.
- [229] M. Geier, A. Fakhari, and T. Lee, “Conservative phase-field lattice Boltzmann model for interface tracking equation,” *Physical Review E - Statistical, Nonlinear, and Soft Matter Physics*, vol. 91, no. 6, 2015.
- [230] A. Fakhari, T. Mitchell, C. Leonardi, and D. Bolster, “Improved locality of the phase-field lattice-Boltzmann model for immiscible fluids at high density ratios,” *Physical Review E*, vol. 96, no. 5, pp. 1–14, 2017.
- [231] P. Lallemand and L.-S. Luo, “Theory of the lattice boltzmann method: Dispersion, dissipation, isotropy, galilean invariance, and stability,” *Physical Review E*, vol. 61, no. 6, p. 6546, 2000.
- [232] A. Fakhari and T. Lee, “Multiple-relaxation-time lattice Boltzmann method for immiscible fluids at high Reynolds numbers,” *Physical Review E - Statistical, Nonlinear, and Soft Matter Physics*, vol. 87, no. 2, pp. 1–8, 2013.
- [233] D. Lycett-Brown and K. H. Luo, “Multiphase cascaded lattice Boltzmann method,” *Computers and Mathematics with Applications*, vol. 67, no. 2, pp. 350–362, 2014.
- [234] D. Lycett-Brown and K. H. Luo, “Cascaded lattice Boltzmann method with improved forcing scheme for large-density-ratio multiphase flow at high Reynolds and Weber numbers,” *Physical Review E*, vol. 94, no. 5, pp. 1–20, 2016.
- [235] H. Ha-Ngoc and J. Fabre, “Test-case no 29A: The velocity and shape of 2D long bubbles in inclined channels or in vertical tubes (PA, PN) Part I: In a stagnant liquid,” *Multiphase Science and Technology*, vol. 16, no. 1-3, pp. 175–188, 2004.
- [236] S. Succi, *The lattice Boltzmann equation: for fluid dynamics and beyond*. Oxford university press, 2001.
- [237] T. Krüger, H. Kusumaatmaja, A. Kuzmin, O. Shardt, G. Silva, and E. M. Viggen, “The lattice boltzmann method,” *Springer International Publishing*, vol. 10, pp. 978–3, 2017.
- [238] Q. Li, K. H. Luo, Q. J. Kang, Y. L. He, Q. Chen, and Q. Liu, “Lattice Boltzmann methods for multiphase flow and phase-change heat transfer,” *Progress in Energy and Combustion Science*, vol. 52, pp. 62–105, 2016.
- [239] H. Huang, M. Sukop, and X. Lu, *Multiphase lattice Boltzmann methods: Theory and application*. John Wiley & Sons, 2015.

-
- [240] T. Wacawczyk, “On a relation between the volume of fluid, level-set and phase field interface models,” *International Journal of Multiphase Flow*, vol. 97, pp. 60–77, 2017.
- [241] B. S. Mirjalili, S. S. Jain, and M. S. Dodd, “Interface-capturing methods for two-phase flows : An overview and recent developments,” *Annual Research Briefs*, no. 1, pp. 117–135, 2017.
- [242] C. Hirt and B. Nichols, “Volume of fluid (VOF) method for the dynamics of free boundaries,” *Journal of Computational Physics*, vol. 39, no. 1, pp. 201–225, 1981.
- [243] Z. Wang, J. Yang, B. Koo, and F. Stern, “A coupled level set and volume-of-fluid method for sharp interface simulation of plunging breaking waves,” *International Journal of Multiphase Flow*, vol. 35, no. 3, pp. 227–246, 2009.
- [244] T. Waławczyk, “A consistent solution of the re-initialization equation in the conservative level-set method,” *J. Comp. Phys.*, vol. 299, pp. 487–525, 2015.
- [245] C. S. Peskin, “The immersed boundary method,” *Acta Numerica*, vol. 11, pp. 479–517, 2002.
- [246] G. Tryggvason *et al.*, “A front-tracking method for the computations of multiphase flow,” *Journal of Computational Physics*, vol. 169, no. 2, pp. 708–759, 2001.
- [247] D. M. Anderson, G. B. McFadden, and A. A. Wheeler, “Diffuse-interface methods in fluid mechanics,” *Annual Review of Fluid Mechanics*, vol. 30, no. 1, pp. 139–165, 1998.
- [248] A. Prosperetti and G. Tryggvason, *Computational methods for multiphase flow*. Cambridge University Press, 2009.
- [249] X. Shan and H. Chen, “Lattice Boltzmann model for simulating flows with multiple phases and components,” *Physical Review E*, vol. 47, no. 3, pp. 1815–1819, 1993.
- [250] X. Shan and H. Chen, “Simulation of nonideal gases and liquid-gas phase transitions by the lattice Boltzmann equation,” *Physical Review E*, vol. 49, no. 4, pp. 2941–2948, 1994.
- [251] J. Cui, W. Li, and W. H. Lam, “Numerical investigation on drag reduction with superhydrophobic surfaces by lattice-Boltzmann method,” *Computers and Mathematics with Applications*, vol. 61, no. 12, pp. 3678–3689, 2011.
- [252] M. R. Swift, W. R. Osborn, and J. M. Yeomans, “Lattice boltzmann simulation of nonideal fluids,” *Physical Review Letters*, vol. 75, pp. 830–833, 5 1995.

- [253] J. W. Cahn and J. E. Hilliard, “Free energy of a nonuniform system. I. Interfacial free energy,” *The Journal of Chemical Physics*, vol. 28, no. 2, pp. 258–267, 1958.
- [254] S. M. Allen and J. W. Cahn, “Mechanisms of phase transformations within the miscibility gap of Fe-rich Fe-Al alloys,” *Acta Metallurgica*, vol. 24, no. 5, pp. 425–437, 1976.
- [255] P. H. Chiu and Y. T. Lin, “A conservative phase field method for solving incompressible two-phase flows,” *Journal of Computational Physics*, vol. 230, no. 1, pp. 185–204, 2011.
- [256] H. Wang, Z. Chai, B. Shi, and H. Liang, “Comparative study of the lattice boltzmann models for allen-cahn and cahn-hilliard equations,” *Physical Review E*, vol. 94, no. 3, p. 033 304, 2016.
- [257] H. Kusumaatmaja, E. J. Hemingway, and S. M. Fielding, “Moving contact line dynamics: From diffuse to sharp interfaces,” *Journal of Fluid Mechanics*, vol. 788, pp. 209227, 2016.
- [258] Y. Q. Zu and S. He, “Phase-field-based lattice Boltzmann model for incompressible binary fluid systems with density and viscosity contrasts,” *Physical Review E - Statistical, Nonlinear, and Soft Matter Physics*, vol. 87, no. 4, pp. 1–23, 2013.
- [259] A. Kumar, “Isotropic finite-differences,” *Journal of Computational Physics*, vol. 201, no. 1, pp. 109–118, 2004.
- [260] K. K. Mattila, L. A. Hegele Júnior, and P. C. Philippi, “High-accuracy approximation of high-rank derivatives: Isotropic finite differences based on lattice-Boltzmann stencils,” *The Scientific World Journal*, vol. 2014, 2014.
- [261] A. Banari, “Lattice Boltzmann Simulation Of Multiphase Flows; Application To Wave Breaking And Sea Spray Generation,” PhD thesis, University of Rhode Island, 2014.
- [262] H. Liang, J. Xu, J. Chen, H. Wang, Z. Chai, and B. Shi, “Phase-field-based lattice Boltzmann modeling of large-density-ratio two-phase flows,” *Physical Review E*, vol. 97, no. 3, p. 33 309, 2018.
- [263] F. Ren, B. Song, M. C. Sukop, and H. Hu, “Improved lattice Boltzmann modeling of binary flow based on the conservative Allen-Cahn equation,” *Physical Review E*, vol. 94, no. 2, pp. 1–12, 2016.

-
- [264] M. Dzikowski, Ł. Łaniewski-Wołk, and J. Rokicki, “Single component multiphase lattice Boltzmann method for Taylor/Bretherton bubble train flow simulations,” *Communications in Computational Physics*, vol. 19, no. 4, pp. 1042–1066, 2016.
 - [265] D. Nicklin, J. Wilkes, and J. Davidson, “Two-phase flow in vertical tubes,” *Transactions of the Institution of Chemical Engineers*, vol. 40, pp. 61–68, 1962.
 - [266] H. Ha-Ngoc and J. Fabre, “Test-case no 29B: The velocity and shape of 2D long bubbles in inclined channels or in vertical tubes (PA, PN) part II: In a flowing liquid,” *Multiphase Science and Technology*, vol. 16, no. 1-3, pp. 189–204, 2004.
 - [267] X. He and L.-S. Luo, “Lattice Boltzmann Model for the Incompressible Navier-Stokes Equation,” *Journal of Statistical Physics*, vol. 88, no. 3/4, pp. 927–944, 1997.
 - [268] Z. Guo, C. Zheng, and B. Shi, “Force imbalance in lattice Boltzmann equation for two-phase flows,” *Physical Review E - Statistical, Nonlinear, and Soft Matter Physics*, vol. 83, no. 3, pp. 1–8, 2011.
 - [269] A. De Rosis, “Non-orthogonal central moments relaxing to a discrete equilibrium: A D2Q9 lattice Boltzmann model,” *EPL*, vol. 116, no. 4, 2016.
 - [270] A. De Rosis, “Central-moments-based lattice Boltzmann schemes with force-enriched equilibria,” *EPL*, vol. 117, no. 3, 2017.
